FACHBEREICH PHYSIK
BERGISCHE UNIVERSITÄT
GESAMTHOCHSCHULE WUPPERTAL

Measurement of $\pi^{\pm}$, $K^{\pm}$, p and $\overline{p}$ production in $Z^0 \rightarrow q\overline{q}$, $Z^0 \rightarrow b\overline{b}$ and $Z^0 \rightarrow u\overline{u}, d\overline{d}, s\overline{s}$

(Particle Identification with the DELPHI Barrel Ring Imaging Cherenkov Counter)

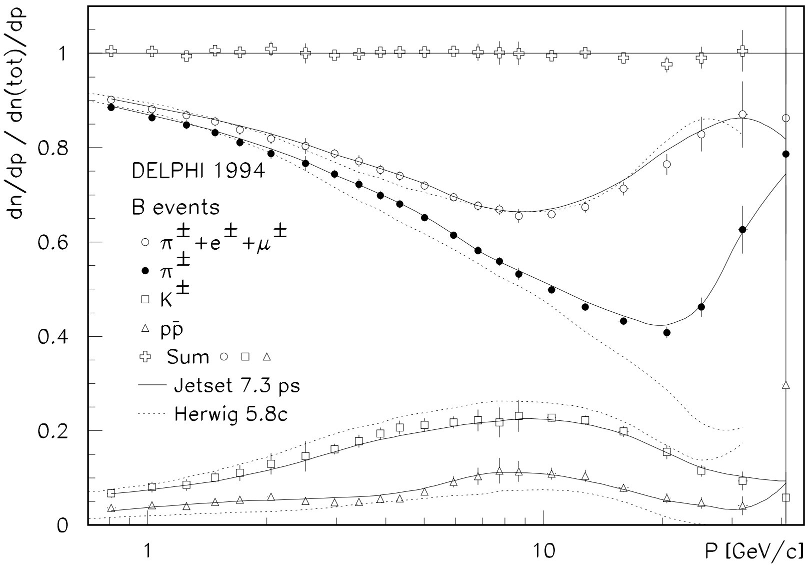

Dissertation

zur Erlangung des akademischen Grades eines
DOKTORS DER NATURWISSENSCHAFTEN
des Fachbereiches Physik
der Bergischen Universität Wuppertal

vorgelegt von

Emile Schyns

(Emile.Schyns@cern.ch)

WUB-DIS 96-22

Hauptreferent: Prof. Dr. J. Drees
Korreferent: Prof. Dr. K.-H. Becks

for you

DIESES ist das Bild der Welt,
Die man für die beste hält:
Fast wie eine Mördergrube,
Fast wie eines Burschen Stube,
Fast so wie ein Opernhaus,
Fast wie ein Magisterschmaus,
Fast wie Köpfe von Poeten,
Fast wie schöne Raritäten,
Fast wie abgesetztes Geld
Sieht sie aus, die beste Welt.
(Risum teneatis amici! Horatius.)

Es hat der Autor, wenn er schreibt,
So was Gewisses, das ihn treibt.
Der Trieb zog auch den Alexander
Und alle Helden miteinander.
Drum schreib ich auch allhier mich ein:
Ich möcht nicht gern vergessen sein.

Frankfurt am Main den 28. August 1765.

Goethe d.s. W. Liebhaber.

Abstract

The DELPHI experiment at LEP contains RICH detectors for particle identification. The good understanding of the RICH detectors allows the identification of charged pions, kaons and protons, covering the full momentum window from $0.7 < p < 45.6\,\mathrm{GeV}/c$. The RICH performance and the good agreement between the data and the detector simulation is illustrated through the reconstruction of resonances $\mathrm{K^0_S}$, ρ^0, $\mathrm{f_0}(980) \to \pi^+\pi^-$, $\Lambda^0 \to \mathrm{p}\pi^-$, $\mathrm{K}^*(892)^0 \to \mathrm{K}^+\pi^-$, $\phi(1020) \to \mathrm{K^+K^-}$, and $\Lambda^0(1520) \to \mathrm{pK}^-$.

The $\pi^\pm$, $\mathrm{K}^\pm$, p and $\overline{\mathrm{p}}$ differential cross sections and normalised production rates are measured for three event samples i.e. $\mathrm{Z}^0 \to q\overline{q}$, $\mathrm{Z}^0 \to b\overline{b}$ and $\mathrm{Z}^0 \to u\overline{u}, d\overline{d}, s\overline{s}$, selected from 1 400 000 Z^0 decays collected by DELPHI in 1994. The results are compared to the predictions of the JETSET parton shower model and the HERWIG cluster fragmentation model. The prediction by JETSET in general is better than HERWIG. The latter fails to describe the proton production for all three samples whereas the $\pi^\pm$, $\mathrm{K}^\pm$ production is over-estimated for $\mathrm{Z}^0 \to b\overline{b}$ and under-estimated for $\mathrm{Z}^0 \to u\overline{u}, d\overline{d}, s\overline{s}$.

The model of LPHD-MLLA provides a good distorted Gaussian description of the shape of the ξ_p distributions ($\xi_p = \ln(\sqrt{s}/2p)$). Only for protons in $\mathrm{Z}^0 \to b\overline{b}$ the contribution from B-decays becomes explicitly visible and the LPHD-MLLA fails. It is shown that a double-Gaussian approach performs better. The $\pi^\pm$, $\mathrm{K}^\pm$, p and $\overline{\mathrm{p}}$ multiplicities obtained by integration of the outcome of the LPHD-MLLA, performed on the measured distributions for the three event samples are enlisted below. Results with an improved accuracy compared to previous measurements are indicated by a '$*$' and newly obtained results are indicated by '$**$'.

	$\mathrm{Z}^0 \to q\overline{q}$	$\mathrm{Z}^0 \to b\overline{b}$	$\mathrm{Z}^0 \to u\overline{u}, d\overline{d}, s\overline{s}$
$< \pi^\pm >$	17.00±0.43	**18.47±1.06	**16.56±0.82
$< \mathrm{K}^\pm >$	*2.11±0.08	*2.54±0.16	**1.88±0.10
$< \mathrm{p}\overline{\mathrm{p}} >$	*1.04±0.04	*1.03±0.06	**1.02±0.05

A postscript version of this thesis (in colour or black/white) can be found via the following Homepages:
– Wuppertal University (Dissertationen), http://www.uni-wuppertal.de/FB8/groups/Drees
– DELPHI Experiment (Physics Results, Theses), http://www.cern.ch/Delphi/Welcome.html

Contents

1 Introduction **1**

2 Theory **3**

2.1 Introduction to the Standard Model 3

2.2 From Quarks to Hadrons 8

2.3 The Prediction of Particle Spectra 11

3 The LEP Collider **13**

4 The DELPHI Experiment **17**

4.1 The Tracking Detectors 18

4.2 The Calorimeters 24

4.3 Particle Identification 26

4.4 Data Taking and Control Systems 27

4.5 The Data Analysis Chain 29

5 DELPHI RICH Detectors **34**

5.1 Introduction 34

5.2 The Barrel RICH 36

5.3 The Forward RICH 42

5.4 Monitoring and Control 42

5.5 The RICH UV-Monochromator Systems 45

5.5.1 UV-Transparency of C_6F_{14} 48

5.5.2 UV-Transparency of C_5F_{12} 49

5.5.3 UV-Transparency of C_4F_{10} 49
5.5.4 Photon Conversion in TMAE-Loaded Drift Gas 50
5.6 Operational Experiences 51
5.6.1 Treatment of the RICH Cherenkov Fluids 51
5.6.2 Barrel RICH Commissioning Procedures 55

6 Particle Identification with the Barrel RICH 58
6.1 Raw Data Handling and Alignment 58
6.2 RICH Fixing 61
6.3 Ring-Finding Algorithms for RICH Data 64
6.4 The RIBMEAN Algorithm 65

7 The NEWTAG Package 71
7.1 The REMIGU Tagging Routine 73
7.2 Pion Tag 75
7.3 Kaon Tag 75
7.4 Proton Tag 76
7.5 Heavy Tag 77
7.6 Tag/Track Quality 77
7.7 Adaptations for Forward RICH Tagging 78
7.8 Appropriate Tagging and Alternatives 79
7.9 Efficiency, Purity, Rejection 81

8 NEWTAG Performance on Data and Monte Carlo 87
8.1 Data versus Detector Simulation 87
8.2 Reconstruction of Some Resonances in $Z^0 \to q\overline{q}$ 91
8.2.1 Reconstruction of $\phi(1020) \to K^+K^-$ 91
8.2.2 Reconstruction of K^0_S, ρ^0, $f_0(980) \to \pi^+\pi^-$ 95
8.2.3 Reconstruction of $K^*(892)^0 \to K^+\pi^-$ 96
8.2.4 Reconstruction of $\Lambda^0 \to p\pi^-$ 97

8.2.5 Reconstruction of $\Lambda^0(1520) \to \mathrm{pK}^-$ 98

8.3 Reconstruction of Some Resonances in $\mathrm{Z}^0 \to b\bar{b}$ 99

8.3.1 Reconstruction of $\phi(1020) \to \mathrm{K}^+\mathrm{K}^-$ 99

8.3.2 Reconstruction of K^0_S, ρ^0, $\mathrm{f}_0(980)$, $\mathrm{K}^*(892)^0$ and Λ^0 100

9 $\pi^\pm$, $\mathrm{K}^\pm$ and $\mathrm{p}\bar{\mathrm{p}}$ Production in $\mathrm{Z}^0 \to q\bar{q}$, $\mathrm{Z}^0 \to b\bar{b}$, $\mathrm{Z}^0 \to u\bar{u}, d\bar{d}, s\bar{s}$ 101

9.1 Event and Charged Particle Selection Criteria 101

9.2 Tagging $b\bar{b}$ and $u\bar{u}, d\bar{d}, s\bar{s}$ Events 105

9.3 The Analysis Method 108

9.4 Corrections and Uncertainties 112

9.4.1 Local Corrections 112

9.4.2 Global Corrections 114

9.4.3 Systematic Uncertainties 115

9.5 Normalised Production Rates 121

9.6 Differential Cross-sections 129

9.7 Particle Multiplicities 131

9.8 Comparison with Other Experimental Results 135

9.9 Fragmentation versus Decays in Flavour Tagged Events 138

10 Summary and Outlook 142

A RIBMEAN Quality Bits 146

B Differential Cross-sections in $\mathrm{Z}^0 \to q\bar{q}$ 147

C Differential Cross-sections in $\mathrm{Z}^0 \to b\bar{b}$ 150

D Differential Cross-sections in $\mathrm{Z}^0 \to u\bar{u}, d\bar{d}, s\bar{s}$ 153

List of Figures 156

List of Tables 159

References 160

Acknowledgements 165

Flapout 167

Chapter 1

Introduction

Our present knowledge about the elementary particles and their natural behaviour is formulated by the Standard Model of electroweak and strong interactions. Amongst others, the Standard Model provides a description of the formation of hadrons in the electron-positron annihilation $e^+e^- \to \mathrm{Z}^0/\gamma \to q\overline{q} \to$ hadrons, which is the underlying process of the study presented in this thesis. At the short distance range of the process, the momentum transfer is high and the formation of quarks and gluons can be calculated exactly, on the basis of perturbation theory. However, at the range of increasing distances, one enters the domain of the transition of quarks and gluons into hadrons. Here, the momentum transfer is rather small and only non-perturbative phenomenological models can be used to describe this phase of the process.

An excellent opportunity to test these models and to improve the understanding of the hadronisation process, can be provided by the measurement of the spectra of final state charged hadrons for different Z^0 decays. The precise measurement of these spectra and the sophisticated particle detection technique through which the measurement is possible, are the key topics of this thesis.

In chapter 2 the main features of the Standard Model are introduced, followed by a brief overview of the theoretical background concerning the different phases of the process $e^+e^- \to \mathrm{Z}^0/\gamma \to q\overline{q} \to$ hadrons. The production of hadrons and the prediction of the shape of their spectra will be discussed in some more detail.

Experimental data have become available through the Large Electron-Positron collider LEP at the European Laboratory for Particle Physics CERN. At LEP, electrons and positrons are accelerated up to 45.6 GeV/c, to produce Z^0 bosons in e^+e^- collisions. The high cross section at the Z^0 resonance allows the recording of large statistics data samples of hadronic Z^0 decays. In chapter 3, the LEP collider is presented.

One of the four experiments at LEP is named DELPHI. Chapter 4 describes the experimental setup of the DELPHI detector. Here, a short overview is given of the different DELPHI tracking devices, the calorimeters and the sub-detectors for particle identification. Furthermore, the DELPHI data taking and control systems as well as the DELPHI data analysis chain and the detector simulation is discussed.

The DELPHI experiment is the only LEP-experiment which contains Ring Imaging Cherenkov (RICH) detectors, the Barrel RICH (BRICH) and the Forward RICH (FRICH).

The RICH detectors allow the identification of charged hadrons i.e. charged pions ($\pi^{\pm}$), kaons ($\mathrm{K}^{\pm}$), and protons[1] (p,$\overline{\mathrm{p}}$). The elegant application of the RICH technique in DELPHI and its necessary complex realisation through a number of interlinked subsystems, are described in chapter 5. The RICH detector from the technical point of view, is the central topic in this chapter. Special attention is given to the treatment and the quality monitoring of the different Cherenkov fluids. Additionally, the computer control and the monitoring of the different detector parameters is discussed. Finally, a layout of the commissioning procedures with respect to the detector start-up and shut-down operations is presented.

In the next three chapters, the detector performance from the physics point of view is the main topic. In chapter 6, the raw data handling and the detector alignment are pictured together with the resulting detector resolutions. The tracing and understanding of different sources of background and their impact on the detector simulation is illustrated by detailed examples. A short overview is given on the different ring-finding algorithms which have been used for physics analyses. Extensive details are presented on the algorithm which has been applied for the measurement of the spectra, by making the comparison of the data with the detector simulation and by illustrating its particle separating power. Due to the increased understanding of the detector response, supplementary implementations in the RICH software delivered the first significant proof of positive identified high momentum protons ($16 < p < 45.6\,\mathrm{GeV}/c$). A new stand-alone software package was developed to tag $\pi^{\pm}$, $\mathrm{K}^{\pm}$ and $\mathrm{p}\overline{\mathrm{p}}$, covering the full detection range between $0.7 < p < 45.6\,\mathrm{GeV}/c$. Chapter 7 discusses the motivations and the technical details of this tagging package, which was initially developed for this work, but later has been applied for several other DELPHI physics analyses. Additionally, an overview is given of the different efficiencies, purities and rejections which can be obtained. The particle identifying power of the BRICH detector is presented in greater detail in chapter 8. Amongst others, the reconstruction of a number of resonances in $\mathrm{Z}^0 \to q\overline{q}$ and $\mathrm{Z}^0 \to b\overline{b}$ is performed and compared to the Monte Carlo simulation.

Chapter 8.1 presents the above discussed precision measurements of the $\pi^{\pm}$, $\mathrm{K}^{\pm}$ and $\mathrm{p}\overline{\mathrm{p}}$ spectra for different samples of Z^0 decays: for inclusive Z^0 decays i.e. $\mathrm{Z}^0 \to q\overline{q}$ ($q = u, d, s, c, b$), and for two sub-samples i.e. $\mathrm{Z}^0 \to b\overline{b}$ and $\mathrm{Z}^0 \to u\overline{u}, d\overline{d}, s\overline{s}$. The results are obtained from 1 400 000 Z^0 decays collected by DELPHI in 1994. First, the selection procedures and the analysis method are introduced, followed by a detailed study of the statistic and systematic uncertainties. The obtained results for the normalised production rates, the differential cross sections and the particle multiplicities are presented and compared with predictions obtained from different models. Most of the spectra are either measured for the first time, or show a significant improvement in accuracy compared to older measurements. The interesting outcome obtained for proton production in $\mathrm{Z}^0 \to b\overline{b}$, indicating that a possible distinction can be made between fragmentation and decay products, is studied in greater detail.

Finally, chapter 10 gives a summary of this work and an outlook on future perspectives of the RICH detectors and their contribution to the DELPHI particle identification.

[1] as of here, protons and anti-protons (i.e. p,$\overline{\mathrm{p}}$), simply will be symbolised by $\mathrm{p}\overline{\mathrm{p}}$.

Chapter 2

Theory

2.1 Introduction to the Standard Model

During the late 1960's, Glashow, Salam and Weinberg (GWS) combined electromagnetic interactions –based on Feynman's Quantum Electro Dynamic Theory (QED)– with weak interactions into the $SU(2)_L \otimes U(1)_\gamma$ gauge theory [1–3]. At an earlier stage, in 1964, Gell-Mann [4] and Zweig [5] proposed (independent of each other) three hypothetical fundamental particles called *quarks* (q), the up (u), down (d) and strange (s) quark (*flavours*), which could describe the –at that time– existing i.e. observed zoo of particles, by separating them into two classes. The *baryons*, consisting of three quarks (qqq) or three anti-quarks ($\bar{q}\bar{q}\bar{q}$) and the *mesons* consisting of a quark and an anti-quark ($q\bar{q}$). Each class can be divided into different groups (*multiplets*). With this approach it was found that certain groups were not complete. As a consequence for example, Gell-Mann predicted the existence of a particle containing three s-quarks, the Ω^- particle, which was discovered at Brookhaven National Laboratory in 1964. This discovery confirmed Gell-Mann's and Zweig's assumptions on the quark model but created yet another problem: the three s-quarks in the Ω^-, violated the Pauli exclusion principle which forbids bound spin-1/2-particles to be in the same state (i.e. have identical quantum numbers). Promptly Greenberg proposed that the problem of the quark statistics could be solved by assigning *colour* degrees of freedom to the quark flavours. It was convenient to choose three colours (e.g. red, green, blue) which would add up to a colour-less state (white) when mixed. In baryons and mesons i.e. *hadrons*, the quarks are forced together through the exchange of *gluons*. Quarks and gluons are the basic constituents of hadrons and are often referred to as *partons*.

The developments which started in the 1960's lead to what now is known as the Standard Model of particles and forces ($SU(3)_c \otimes SU(2)_L \otimes U(1)_\gamma$). It covers the electromagnetic, weak and strong interactions by interpreting a force as an exchange of a gauge boson between fermions. Strong interactions are described by Quantum Chromo Dynamics (QCD) while the behaviour of electromagnetic and weak interactions is described by the Electroweak Theory (GWS). The Standard Model of electroweak and

Table 2.1: The bosons describing the fundamental forces in the Standard Model. The Higgs boson (H^0) has not (yet) been experimentally observed. Gravity has not yet been quatised.

	interactions		
	strong	electroweak	gravity
gauge bosons	$g_1 \cdots g_8$	γ, $W^{\pm}$, Z^0, (H^0?)	graviton ?
theory	QCD	GWS	general relativity
gauge group	$SU(3)$	$SU(2) \otimes U(1)$	?
masses	0	0, M_W, M_Z	0
charge	colour	weak isospin weak hypercharge	mass
coupling	α_s	α, $\sin^2 \theta_W$	G

helicity	fermions	generations 1.	2.	3.	quantum numbers Q/e	I_3	Y
L	quarks	$\begin{pmatrix} u \\ d' \end{pmatrix}_L$	$\begin{pmatrix} c \\ s' \end{pmatrix}_L$	$\begin{pmatrix} t \\ b' \end{pmatrix}_L$	$2/3$ $-1/3$	$1/2$ $-1/2$	$1/3$ $-1/3$
	leptons	$\begin{pmatrix} \nu_e \\ e \end{pmatrix}_L$	$\begin{pmatrix} \nu_\mu \\ \mu \end{pmatrix}_L$	$\begin{pmatrix} \nu_\tau \\ \tau \end{pmatrix}_L$	0 -1	$1/2$ $-1/2$	-1 -1
R	quarks	$\begin{pmatrix} u \\ d \end{pmatrix}_R$	$\begin{pmatrix} c \\ s \end{pmatrix}_R$	$\begin{pmatrix} t \\ b \end{pmatrix}_R$	$2/3$ $-1/3$	0 0	$4/3$ $-2/3$
	leptons	$(e)_R$	$(\mu)_R$	$(\tau)_R$	-1	0	-2

Table 2.2: The fundamental fermions and their electroweak quantum numbers. The quarks, up (u), down (d), strange (s), charm (c), bottom (b) and top (t) also carry colour charge. The neutrinos ν_e, ν_μ and ν_τ respectively belong to the electron (e), muon (μ) and tau (τ) leptons.

strong interactions uses two different kinds of fundamental point like particles: fermions (i.e. quarks and leptons) and bosons (i.e. Higgs, g_i, γ, $W^{\pm}$, Z^0).

The complex scalar *Higgs boson* (H^0), is attributed to be responsible for the masses of fermions and gauge bosons. The Higgs boson has not yet been observed and the understanding of the mechanism remains one of the most fundamental problems particle physicists are facing nowadays. The *gauge bosons* (g_i, γ, $W^{\pm}$, Z^0) are the mediators of the different forces. If symmetry breaking $SU(2) \otimes U(1) \to U'(1)$ is done by the simplest Higgs mechanism, it results in three massive vector bosons ($W^{\pm}$, Z^0) and one Higgs scalar. The charged weak current is associated purely to $SU(2)$ while the neutral currents from $U(1)$ and $SU(2)$ undergo mixing, producing a massless photon and a massive Z^0 boson. The strength of this mixing is given by the weak mixing angle θ_W. The gluon field of the unbroken $SU(3)$ has eight different colour states. Table 2.1 gives an overview of the bosons and the interactions particles are subject to, α_s is the strong coupling constant, α is the fine structure constant and θ_W is the weak mixing angle.

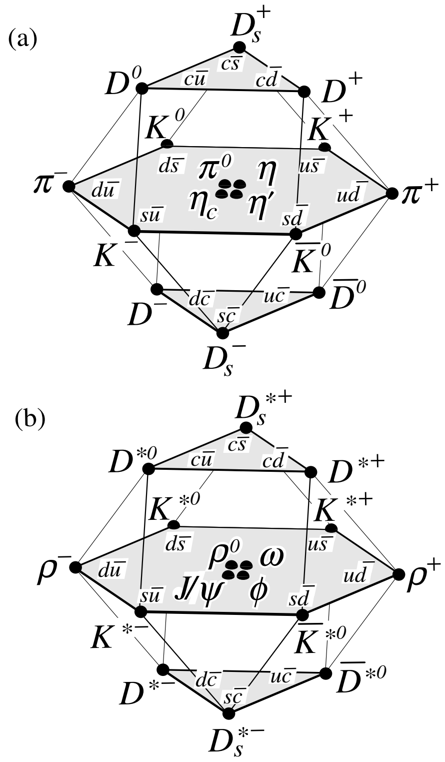

Figure 2.1: $SU(4)$ 16-plets for the pseudoscalar (a) and vector (b) mesons made of u, d, s, and c quarks. The nonets of light mesons occupy the central planes, to which the $c\bar{c}$ states have been added. The neutral mesons at the centres of these planes are mixtures of $u\bar{u}$, $d\bar{d}$, $s\bar{s}$ and $c\bar{c}$ states [6].

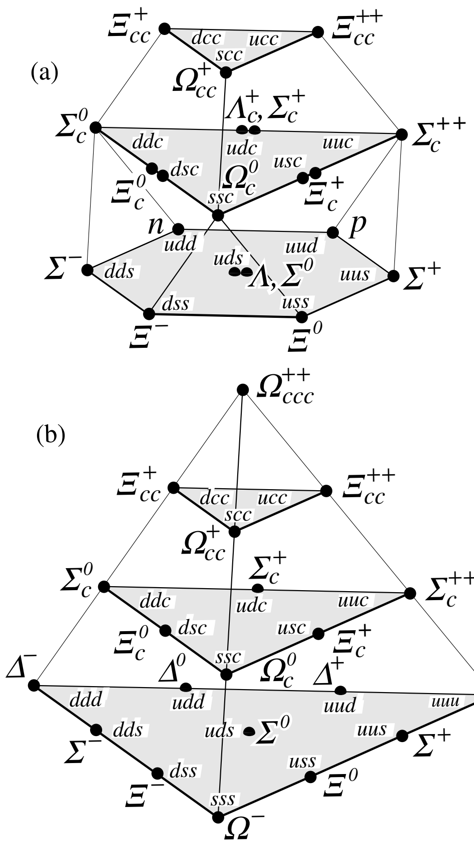

Figure 2.2: $SU(4)$ multiplets for baryons made of u, d, s, and c quarks. The 20-plet with an $SU(3)$ octet (a) and a 20-plet with an $SU(3)$ decuplet (b) [6].

The *quarks* and *leptons*, can be considered as the fundamental *fermions*. They are the basic constituents of matter and can be separated into three generations, as is indicated in table 2.2. The electrical charge of the fermions is related to the weak hypercharge Y and the third component of the weak isospin I_3 by the Gell-Mann-Nishijima relation $Q = I_3 + Y/2$. Apart from fractional electrical charge, quarks also carry colour charge whereas leptons do not. Thus leptons are not sensitive to the strong force. For each quark three colour states have been defined: red, green and blue. Quarks can appear in bound states as mesons ($q\bar{q}$) or as baryons (qqq or $\bar{q}\bar{q}\bar{q}$) in different multiplets. An illustration of such multiplets is shown in figures 2.1 for mesons made of u, d, s, c quarks. The equivalent for baryons is shown in figure 2.2.

In QCD, flavour changing forces do not exist i.e. quark flavour is conserved. However, they are allowed in the GSW theory. The quark mass eigenstates are not equal to the weak eigenstates. In other words, the charge $-1/3$ weak eigenstates d', s', b' (see table 2.2) are mixtures of the strong mass eigenstates d, s, b, thus one has decays consisting of transitions between generations. The mixed eigenstates are related to the flavour eigenstates by the Cabibbo-Kobayashi-Maskawa (CKM) matrix of which each of the (3x3) elements represents a coupling of a charge 2/3 quark to a charge $-1/3$ quark [7]. The elements of the CKM-matrix are fundamental parameters of matter.

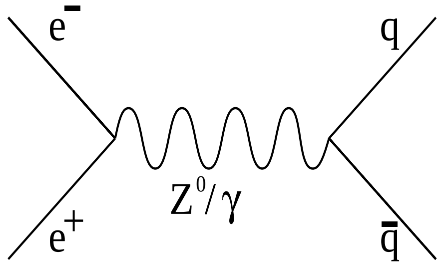

Figure 2.3: The lowest order electron-positron annihilation into a quark pair, $e^+e^- \to Z^0/\gamma \to q\bar{q}$. For Z^0 exchange, the coupling at the fermion vertex is given in equation 2.1.

$$\frac{e}{\sin\theta_W \cos\theta_W}\gamma^\mu(V_f - A_f\gamma_5) \quad (2.1)$$

where

$$A_f = a_f \cdot \sin\theta_W \cos\theta_W \quad (2.2)$$
$$= I_3 - 2Q_f \sin^2\theta_W,$$
$$V_f = v_f \cdot 2\sin\theta_W \cos\theta_W \quad (2.3)$$
$$= I_3$$

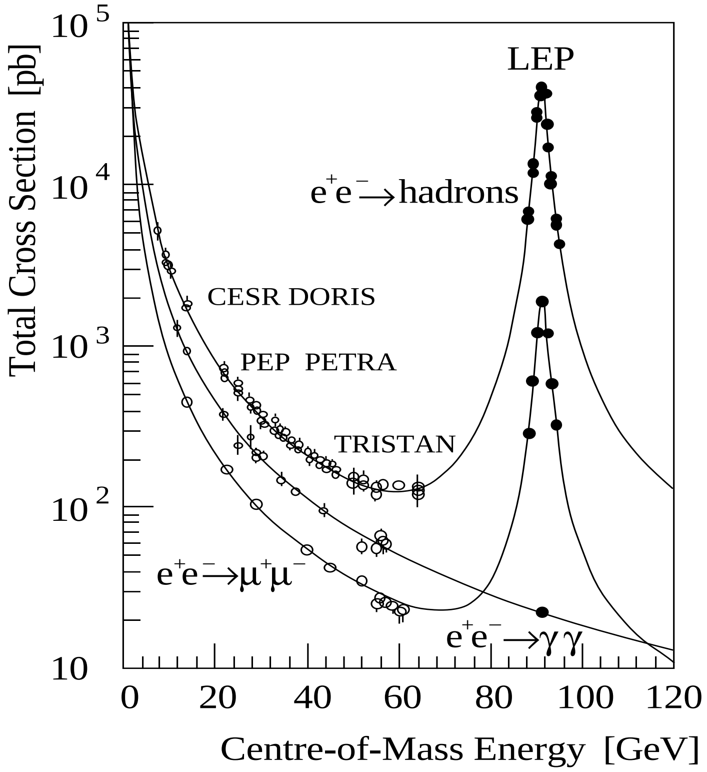

Figure 2.4: e^+e^- cross-section vs centre-of-mass energy. The lines indicate the prediction of the Standard Model [8].

The weak force violates parity (i.e. space-inversion symmetry). It has different couplings to fermion states of different chirality i.e. handedness[1]. Left-handed fermions belong to isospin doublets ($I = 1/2$) whereas right-handed fermions states are singlets ($I = 0$). The $W^\pm$ bosons couple only to fermions with opposite values of I_3 and thus couple only to left-handed fermions or right-handed anti-fermions. The CKM-matrix acts on d-type quarks to produce weak eigenstates that interact with u-type quarks. Mixing of generations between leptons has never been observed. Right-handed neutrinos completely decouple from all other fermions in the Standard Model. It can be assumed that they do not exist at all.

For photon exchange, the coupling at the fermion vertex is $eQ_f\gamma^\mu$, where Q_f is the electrical charge of fermion f and where the Dirac γ-matrices are represented by γ^μ. The Born-graph of the lowest order contribution for Z^0 exchange is illustrated in figure 2.3. The vertex factor is given by equation 2.1 [9]. Here, θ_W is the above discussed weak mixing angle, V_f and A_f represent the vector and axial vector couplings and I_3 is the third component of the weak isospin. The weak mixing angle θ_W is given by the Z^0 and $W^\pm$ masses according to the following relation:

$$\sin^2\theta_W = 1 - {M_W}^2/{M_Z}^2 \quad (2.4)$$

The coupling in equation 2.1 determines the Z^0 boson production at LEP through electron-positron annihilation into a quark pair. The total cross-section as a function of the centre-of-mass energy is shown in figure 2.4.

[1]Left-right handedness is defined by the chirality operator γ_5. For massless fermions this operator is equivalent to the helicity.

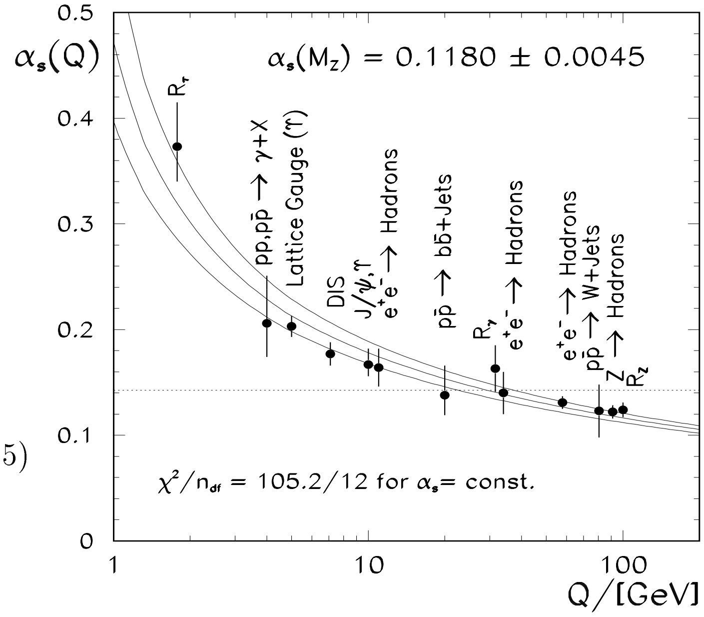

Figure 2.5: The running of the strong coupling constant α_s. The solid lines represent the fit for $\alpha_s(M_Z) = 0.1180 \pm 0.0045$ and the one standard deviation uncertainties. The dotted line indicates the mean value of α_s under the assumption of α_s being constant [8].

$$\alpha_s(Q^2) = \frac{\alpha_s(\mu^2)}{1 + \frac{\alpha_s(\mu^2)}{4\pi}(11 - \frac{2}{3}N_f)\ln(\frac{Q^2}{\mu^2})} \tag{2.5}$$

A significant difference between photons and gluons is that gluons themselves carry colour charge which enables not only quark-gluon coupling but also gluon-gluon coupling. The QCD coupling constant, α_s, in reality is not a constant but depends on the squared four-momentum Q^2 of the process (*running* α_s). Once α_s is known for a certain value $Q^2 = \mu^2$, one can calculate its value perturbatively for any other value of Q^2. In leading order one obtains the above expression 2.5 [10], where μ is called the *renormalisation scale* and N_f is the number of contributing quark flavours. The crucial point in the above equation is the behaviour of α_s for large values of Q^2 (i.e. small distances): $\lim_{Q^2\to\infty} \alpha_s = 0$. This allows the interpretation that quarks behave as weakly bound particles at very small distances e.g. as in hadrons: they are *asymptotic free*. At increasing distances (smaller Q^2-values) the quarks are subject to a constant force (*confinement*, discussed in more detail in section 2.2 below). Hence, free quarks can not exist. Figure 2.5 shows a compilation of different measurements of α_s versus Q [8]. The value of Q^2 for which the denominator in equation 2.5 disappears is often defined as Λ:

$$\Lambda^2 = \mu^2 \exp\left(\frac{-12\pi}{(33 - 2N_f)\,\alpha_s(\mu^2)}\right) \implies \alpha_s = \frac{12\pi}{(33 - 2N_f)\ln(Q^2/\Lambda^2)} \tag{2.6}$$

The Λ-parameter can be pictured as the QCD ‘cut-off’ parameter, i.e. the limit beyond which quarks become ‘free’. The value of Λ can not be obtained from calculations and its measurement is an important topic for particle physics experiments today.

For single photon exchange, taking gluon radiation into account, the total hadronic cross section has been calculated up to third order in α_s [11] i.e. $\sigma_{tot} = \sigma_0(1 + \delta_{\mathrm{QCD}})$:

$$\sigma_{tot}(Q^2) = \sigma_0(Q^2)\left(1 + \frac{\alpha_s}{\pi} + 1.409\left(\frac{\alpha_s}{\pi}\right)^2 - 12.805\left(\frac{\alpha_s}{\pi}\right)^3\right), \tag{2.7}$$

$$\sigma_0(Q^2) \;=\; \frac{4N_c\pi\alpha^2}{3Q^2}\sum_f Q_f^2\,, \qquad N_c = \text{ the number of colours.} \tag{2.8}$$

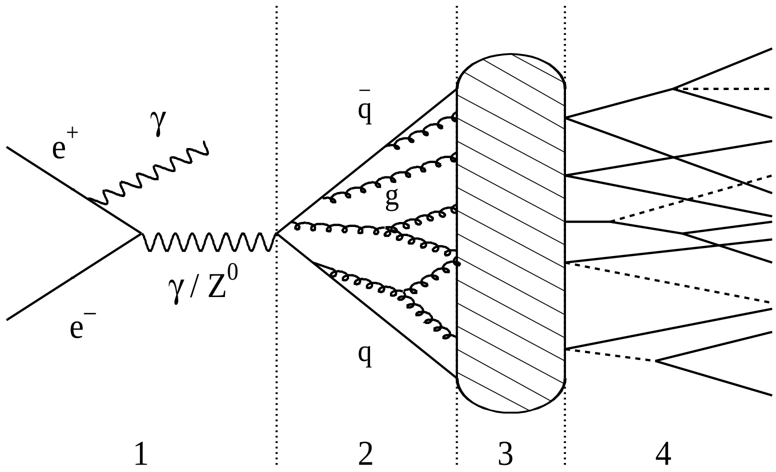

Figure 2.6: The schematic illustration of the four phases in e^+e^- annihilation i.e. $e^+e^- \to Z^0/\gamma \to q\bar{q} \to$hadrons.
1. electroweak phase with initial state radiation.
2. perturbative QCD phase with gluon radiation off the the leading quarks.
3. confinement phase, production of colour singlet hadrons.
4. decay of hadron resonances into final state particles.

It is often more convenient to express σ_{tot} as the ratio of hadronic to electronic width (for γ and Z^0 exchange, taking into account that this ratio does not factorise [12]):

$$R_{\mathrm{QCD}} = \frac{\Gamma(Z^0 \to q\bar{q})}{\Gamma(Z^0 \to e^+e^-)} = 19.943\left(1 + 1.060\frac{\alpha_s}{\pi} + 0.90\left(\frac{\alpha_s}{\pi}\right)^2 - 15\left(\frac{\alpha_s}{\pi}\right)^3\right) \quad (2.9)$$

The third order parameterisation leads to an $\alpha_s(M_Z) = 0.126 \pm 0.007$ which is higher than the world average of 0.118 ± 0.005 [8] or 0.117 ± 0.006 [13]. In e^+e^- annihilation at the Z^0 resonance, quark pair production is the dominating decay-channel: $\Gamma_{q\bar{q}}/\Gamma_{\mathrm{tot}} = 69.90\% \pm 0.15\%$ [6].

2.2 From Quarks to Hadrons

The formation of quarks and gluons i.e. the hard process, can be calculated perturbatively. On the other hand, the transition from quarks and gluons to hadrons, which occurs with a small momentum transfer where α_s is large (see fig. 2.5), can only be estimated non-perturbatively. Calculations concerning hadron production become even more complex when attempting to account for changes in phase space, differences in flavour composition and particle decays. In this respect, one has to rely on a model which describes the formation of hadrons from high energetic quarks.

A model should combine the parts which can be calculated in an exact way, with phenomenological algorithms and a series of experimentally observed hadron properties. An overview of the four basic phases in e^+e^- annihilation for a model is given in figure 2.6 in which the first phase, the e^+e^- annihilation, is ruled by the GSW theory of electroweak interactions.

The second phase is the phase of short distance strong interactions (often referred to as 'parton cascade') which can be calculated using perturbative QCD. Here, two methods can be applied. Firstly, the QCD matrix element (ME) calculations (up to second order in α_s) and secondly, the parton shower (PS) model, which uses a leading logarithmic approximation (LLA). The main difference between the two methods is that ME can not account for higher order effects (it is restricted to maximum four partons)

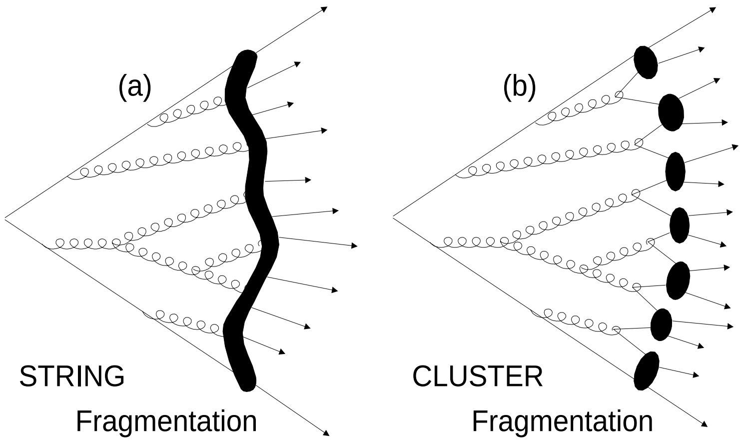

Figure 2.7: An illustration of string fragmentation (a) and cluster fragmentation (b).

whereas PS generates multi-gluon events with an average of nine (soft) gluons per Z^0 event. The LLA uses a certain quantity $R(\rho, \alpha_s(s))$ which depends on the centre-of-mass energy s, $\alpha_s(s)$ and the squared (heavy) jet-mass ($\rho = M_h^2/s$). For $M_h^2 < \rho s$, $R(\rho, \alpha_s(s))$ exponentiates at small ρ [14]:

$$R(\rho, \alpha_s(s)) = C(\alpha_s(s))\ e^{\left(\sum_{n=1}^{\infty} \alpha_s^n \sum_{m=1}^{n+1} G_{nm} \ln^m \rho\right)} + F(\rho, \alpha_s(s)) \tag{2.10}$$

where $C(\alpha_s(s)) = 1 + \sum_{n=1}^{\infty} \alpha_s^n C_n$ and $F(\rho, \alpha_s(s)) = \sum_{n=1}^{\infty} \alpha_s^n F_n(\rho)$. Here C_n and G_{nm} are constants and $F_n(\rho)$ are functions that vanish at small ρ. The exponential terms with $m = n+1$ are called *leading* (LLA) and for $m = n$ *next-to-leading* (NLLA). For $n < m$, the *sub-leading* approximations are called 'modified' (MLLA) or 'double' (DLLA), depending on the way how the sub-leading terms are taken into account.

The third phase in figure 2.6 represents the domain of long distance strong interactions (linear confinement) and hadron formation. As shortly discussed above, no perturbative computations are possible for this phase. Here one has to rely on fragmentation models such as JETSET (string fragmentation) and HERWIG (cluster fragmentation) which will be discussed below.

During the fourth and final phase, the primary hadron resonances produced in the previous phase, decay into final state leptons, photons and hadrons which can be detected in particle physics experiments.

String and Cluster Fragmentation Models

Since the fragmentation can not be computed exactly, one has to rely on phenomenological models to describe the process. Three models are commonly used for this purpose, the *Independent* Model, the *String* Model and the *Cluster* Model.

The approach applied in the Independent Model [15] assumes that the fragmentation of any system of partons can be described for each parton separately as an incoherent sum of independent fragmentation procedures.

The String Model is motivated by QCD confinement [16]. An illustration is shown in figure 2.7(a). It combines fragmentation with the concept of a colour string (i.e. a colour

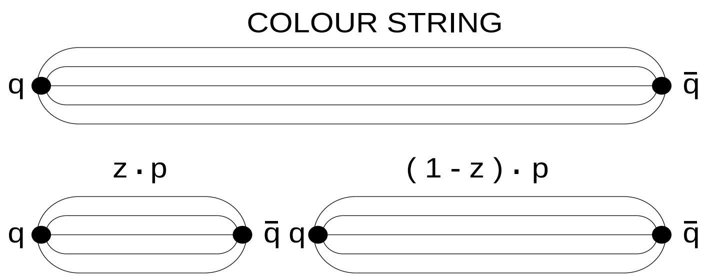

Figure 2.8: An illustration of the breaking of a colour string between a quark-anti-quark pair.

flux tube, see fig. 2.8), which is stretched via a gluon from a quark to an anti-quark. The string has a linearly rising potential $V(r) = \kappa r$, which leads to confinement. The string tension $\kappa \approx 1$ GeV/fm. With the increase of the distance between the quark and anti-quark, this colour string is envisaged to break, producing a new quark-anti-quark pair which carries a sizable fraction of the gluon energy. The remaining energy of the gluon is shared between the two pieces of the broken string. Each of the two pieces then fragments independently in their own centre-of-mass system. Baryon production takes place through the direct production of di-quark-anti-di-quark pairs, equivalent to the quark-anti-quark pairs.

Both the Independent and the String Model employ an iterative ansatz and fragmentation stops when only on shell hadrons remain. At each step, the sharing of energy and momentum is obtained from a probability function $f(z)$ (*fragmentation function*). For u, d and s quarks, in the String Model, the Lund parametrisation [17] is commonly used (a and b are tuning parameters):

$$f(z) = \frac{(1-z)^a}{z} \exp\left(-\frac{bm_t^2}{z}\right) \quad \text{where} \quad z = \frac{(E+p_{||})_{\text{hadron}}}{(E+p_{||})_{\text{quark}}}. \tag{2.11}$$

Here, the finite mass of quarks is taken into account, which basically means that the newly created quark and anti-quark need to travel a certain distance (tunneling) to pick up energy from the string to materialise. The tunneling probability is given by

$$\exp((-m_q^2 - p_t^2)\pi/\kappa), \tag{2.12}$$

causing a suppression of heavy quark pair production: $u\overline{u}:d\overline{d}:s\overline{s}:c\overline{c} \approx 1:1:0.3:10^{-11}$. For c and b quarks a harder fragmentation function is needed (Peterson parametrisation [18]):

$$f(z) = \frac{1}{z}\left(1 - \frac{1}{z} - \frac{\epsilon_q}{1-z}\right)^{-2}, \tag{2.13}$$

where ϵ_q is a free parameter which value is expected to decrease with increasing quark mass i.e. $\epsilon_q \sim 1/m_q^2$.

In the Cluster Model [19] the gluons from the perturbative phase are forced to split into quark-anti-quark pairs which form colourless clusters (fig. 2.7(b)). These clusters either decay into lower class clusters or they decay directly into hadrons, depending on the mass of the cluster. Baryon production is performed through the di-quarks or anti-di-quarks. The distribution of the particle momenta is determined by the momentum of the parent cluster and its decay properties.

The Cluster Model fragmentation is implemented in a Monte Carlo event generator programme called HERWIG [20]. In the HERWIG version 5.8c, the parton cascade is based on the PS model using an extened LLA (coherent parton branching). The String Model fragmentation has been applied in a Monte Carlo event generator called JETSET [17]. The parton cascade in JETSET version 7.3, is also based on the PS model (JETSET 7.3 PS) and uses a coherent LLA. In other words, the parton shower evolves in the centre-of-mass frame of the partons, ruled at each step by energy and momentum conservation. This leads to an angular ordering i.e. the later the gluon emission takes place in the parton shower, the smaller will be its emission angle. HERWIG does not need extra parameters for the hadronisation process and therefore has fewer parameters than JETSET. The JETSET 7.3 PS event generator programme is used for the DELPHI Monte Carlo simulation. A recent report on the DELPHI tuning of the JETSET (versions 7.3 PS, 7.4 PS and 7.4 ME) and HERWIG (5.8 c) generators can be found in reference [21].

2.3 The Prediction of Particle Spectra

The fact that in multi-hadronic events the hadrons are collimated in jets, indicates a duality between the parton level and the hadron level of the process (i.e. phase 2. and 3. in fig. 2.6). Furthermore, it can be assumed that this duality only occurs locally. The model of *Local Parton Hadron Duality* (LPHD) [22] is based on the assumption that hadron spectrum is proportional to the parton spectrum. In the framework of the MLLA, the assumption of LPHD allows a quantitative prediction of hadron spectra. This prediction can be tested by making the comparison with the measured spectra obtained by particle physics experiments. The measurement of these spectra is one of the key themes of the work presented below.

In the LPHD-MLLA, the above discussed coherence –leading to angular ordering– causes the production of low momentum partons to be suppressed. Consequently, the production of low momentum hadrons is also suppressed. This leads to the fact that the differential cross-section of the observable $\xi_p = \ln(1/X_p) = \ln(\sqrt{s}/2p)$ (for conversion see page 167) reaches a maximum for a certain value $\xi_p \equiv \xi_p^*$. The numerical prediction of the hadron spectrum by the LPHD-MLLA, as a function of the ratio of the centre-of-mass energy to the effective QCD-scale parameter ($E_{\mathrm{cm}}/\Lambda_{eff}$) is [8,23,24]:

$$\frac{1}{\sigma}\frac{\mathrm{d}\sigma}{\mathrm{d}\xi_p} = K_{\mathrm{LPHD}} \cdot f_{\mathrm{MLLA}}(\xi_p,\ E_{\mathrm{cm}}/\Lambda_{eff}). \tag{2.14}$$

The factor K_{LPHD} only depends on the produced hadron (mass) and thus basically is a constant. The above equation simply expresses that the relation between the cross sections at the hadron level and the parton level (f_{MLLA}) is determined by a constant K_{LPHD}. The ξ_p dependence of f_{MLLA} can be computed on parton level. A prediction of the mean value $\overline{\xi}_p$ of the ξ_p distribution, assuming that only light flavours (i.e. $u,\ d,\ s$) contribute to the fragmentation, can be expressed as follows:

$$\overline{\xi}_p = \frac{1}{2}\ln\frac{E_{\rm cm}}{2\Lambda_{eff}} + \frac{101}{324}\sqrt{3}\sqrt{\ln\frac{E_{\rm cm}}{2\Lambda_{eff}}} \tag{2.15}$$

Here the QCD cut-off parameter Λ_{eff} is the only free parameter. The differential hadronic cross section can be expressed according to [8]:

$$\frac{d\sigma}{d\xi_p} = 1 + \alpha_{\rm s}\,\xi_p\left(\ln\frac{E_{\rm cm}}{2\Lambda_{eff}} - \frac{\xi_p}{k}\right) \tag{2.16}$$

The parameter k determines whether the evolution of the parton shower is coherent i.e. $k = 1$ or incoherent i.e. $k = 2$. The value ξ_p^* for the maximum of the ξ_p distribution, with a slope $\mathcal{S}$, is computed to be:

$$\xi_p^* = \frac{k}{2}\ln\frac{E_{\rm cm}}{2\Lambda_{eff}} \quad\Longrightarrow\quad \mathcal{S} = \frac{d\xi_p^*}{d\ln E_{\rm cm}} = \frac{k}{2}. \tag{2.17}$$

The determination of the slope offers the possibility to verify whether the parton shower is coherent or incoherent.

The shape of the ξ_p distribution in the region around ξ_p^* is almost Gaussian. Therefore, the differential cross section can be expanded around the mean value $\overline{\xi}_p$, which is expected to be close to the value of ξ_p^*. By defining the quantity $\delta = (\xi_p - \overline{\xi}_p)/\sigma$ and using the expectation values μ_n of the central moments of the ξ_p distribution i.e. $\mu_n = E((\xi_p - \overline{\xi}_p)^n)$, one can compute the following distorted Gaussian expression [23,24]:

$$\frac{1}{\sigma}\frac{d\sigma}{d\xi_p}(\delta,\sigma,s,\kappa,N) = \frac{N}{\sigma\sqrt{2\pi}}\cdot\exp\left(\frac{1}{8}\kappa - \frac{1}{2}s\delta - \frac{1}{4}(2+\kappa)\delta^2 + \frac{1}{6}s\delta^3 + \frac{1}{24}\kappa\delta^4\right) \tag{2.18}$$

where
$$\begin{array}{rcl}
\delta &:=& (\xi_p - \overline{\xi}_p)/\sigma \\
\overline{\xi}_p &:=& \text{mean of the distribution} \\
\sigma &:=& \text{width of the distribution} = \sqrt{\mu_2} \\
s &:=& \text{skewness of the distribution} = \mu_3/\sigma^3 \\
\kappa &:=& \text{kurtosis}^2 \text{ of the distribution} = -3 + \mu_4/\sigma^4 \\
N &:=& \text{normalisation factor}
\end{array}$$

The prediction of the shape of the ξ_p distributions for hadrons can be tested on real data by using the above five parameter expression. Moreover, one can apply this expression to estimate the production rates of the hadrons, by integration over the total ξ_p range.

The measurement of the charged hadron spectra in Z^0 decays and the determination of their production rates is one of the main topics of the work presented below. The above expression will be tested on the measured ξ_p distributions. Furthermore, the comparison will be made with the predictions produced by the (DELPHI tuned [21]) JETSET and HERWIG Monte Carlo event generators. A recent review on measurements of inclusive particle production in hadronic Z^0 decays can be found in reference [25].

[2] The kurtosis is defined as the peakedness or flatness of the graph of a distribution especially with respect to the concentration of values near the mean as compared with the normal distribution.

Chapter 3

The LEP Collider

The Large Electron-Positron collider LEP [26] is located at the Swiss-French border between the Jura mountains and the town of Geneva (fig. 3.1). Being mounted in a ring of 26.7 km circumference makes the LEP collider the biggest accelerator in the world. It is positioned in a 3.8 m diameter tunnel about 100 m underground and was constructed between September 1983 and July 1989 under the management of the European Laboratory for Particle Physics (CERN). For geological reasons the tunnel is inclined by 1.42%. In eight bending sections, the electron and positron beams are kept in orbit by 3392 dipole magnets (B=0.48 T at a beam energy of 45.6 GeV). Furthermore there are 876 quadrupole, 520 sextupole and about 700 correction magnets for focusing purposes. All around the accelerator, over 500 monitors are installed to survey the horizontal and vertical beam position.

For the production of Z^0 particles, e^+e^- beam energies of 45.6 GeV ($\sqrt{s} = m_Z$) are required. These beams are obtained through a multi-step process (creation, accumulation and acceleration) as illustrated in figure 3.2. For positron production, electrons are accelerated up to ~ 200 MeV at the LEP Injector Linacs (LIL) where they collide onto a high mass target, producing positrons with a mean energy of 10 MeV. Approximately 0.1% of these positrons are captured and accelerated up to about 600 MeV in the second stage of LIL. For electron production, an electron gun is used to inject 10 MeV electrons directly into the second stage of LIL, accelerating them -like the positrons- up to 600 MeV. Then, to increase the current of the beams, the electrons and positrons are accumulated in the Electron Positron Accumulator (EPA). After the EPA, the beams are accelerated to 3.5 GeV by the Proton Synchrotron (PS), directly followed by the Super Proton Synchrotron (SPS) which takes the energy up to 20 GeV before injection into LEP. To increase the energy up to the required 45.6 GeV, radio-frequency (RF) cavities have been installed on two straight sections of LEP. These cavities also provide the 130 MeV energy which is lost per revolution due to synchrotron radiation. To compensate for this loss, the RF cavities consume about 1.2 MW, when LEP is in physics mode.

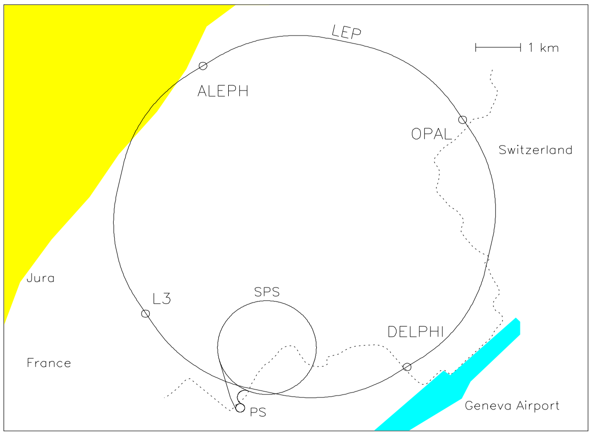

Figure 3.1: The map of the local area around the LEP collider.

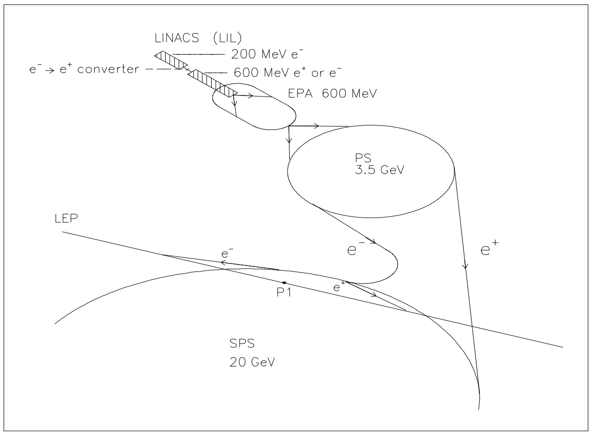

Figure 3.2: Schematic overview of the LEP injection systems.

In order to obtain stable beam energies for physics, online corrections are applied for various effects such as temperature variations, oscillations of the beam around its optimal orbit in the machine (betatron-oscillations) and electromagnetic interactions between the beams (beam-beam interactions) causing an increase of the betatron frequency. Also some remarkable influences caused by the outside world are accounted for. These influences originate for example from gravity, ground water and trains. The gravitational attraction of the moon on the earth surface changes the circumference of LEP by about 1 mm. This is especially the case when the moon is full whilst it is positioned at the low horizon, in the plane of LEP. As a consequence, the beam energy is shifted by about 14 MeV [27]. The alternating water level of Lake Geneva affects the ground-water level in the LEP area (at 4 km linea recta), causing similar variations on circumference and beam energies. The electro-power driven French high speed trains (TGV) produce fluctuating leak currents which escape via the rails to ground. These currents find their way 100 m down underground into the LEP tunnel and charge the beam-pipe, destabilising the beam control and affecting the beam energy.

The event-rate per second (n) of a given process can be defined as in equation 3.1, depending on the cross section (σ) and the luminosity $\mathcal{L}$.

$$n = \sigma \cdot \mathcal{L} \quad [\mathrm{s}^{-1}] \tag{3.1}$$

The luminosity can be expressed in machine parameters according to equation 3.2, where f_{rev} is the LEP revolution frequency (11.25 kHz), k is the number of bunches (4 or 8), N^+ and N^- are the number of positrons and electrons per bunch ($\sim 2.5 \cdot 10^{11}$) and finally $\sigma_x (\approx 100\mu\mathrm{m})$ and $\sigma_y (\approx 10\mu\mathrm{m})$ are the bunch dimensions in the plane perpendicular to the beam direction[1].

$$\mathcal{L} = f_{rev} \cdot k \cdot \frac{N^+ N^-}{4\pi\sigma_x\sigma_y} \quad [\mathrm{cm}^{-2}\mathrm{s}^{-1}] \tag{3.2}$$

[1] x, y, z is defined such that electrons circulate (anti-clockwise) in positive z direction, positive y is vertical (upwards) and positive x points to the centre of LEP.

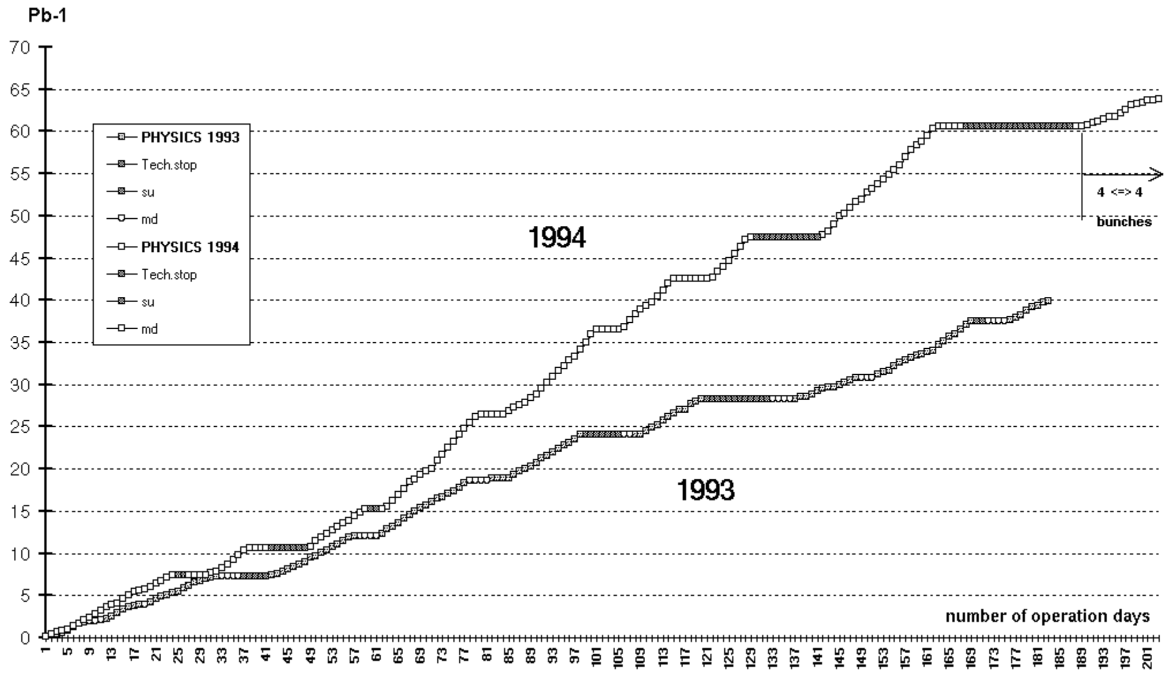

Figure 3.3: The time-integrated luminosity averaged over the four LEP experiments in 1993 and 1994. The flat periods correspond to technical stops and machine developments [28].

Initially LEP was operated with four bunches per beam (k=4). During the 1993 running period, the number of bunches per beam could be doubled (k=8, 'pretzel mode'). Later LEP was also operated using four bunches each consisting of four sub-bunches (k=4x4, 'bunch-train mode'). The bunch systems are synchronised such that they cross at four interaction points, each of which being surrounded by one of the detectors ALEPH, DELPHI, L3 and OPAL. To optimise the Z^0 production rate, the bunches are transversely squeezed by powerful super-conducting quadrupole magnets at each interaction point.

$$I^{\pm} = N^{\pm} \cdot k \cdot f_{rev} \cdot q \quad [\text{mA}] \tag{3.3}$$

The beam currents for e^+e^- can be defined as in equation 3.3, where q is the elementary electron (positron) charge. During the 1994 LEP operation the beam currents were typically of the order of 2.5 mA.

The LEP luminosities typically are of the order of 10^{30} cm^{-2}s^{-1} up to a few times 10^{31} cm^{-2}s^{-1}. During normal operation this yields about 10 000 hadronic Z^0 events per day. The time-integrated luminosity seen by the LEP experiments during 1993 (40 pb^{-1}) and 1994 (64.4 pb^{-1}) are presented in figure 3.3.

Applying an accurate energy calibration and including corrections for the variations discussed above, the total uncertainty of the LEP beam energy can be translated into an uncertainty on the Z mass of ~ 1.5 MeV/c^2 [29]. Combined with the high event statistics, this makes the LEP collider a unique machine.

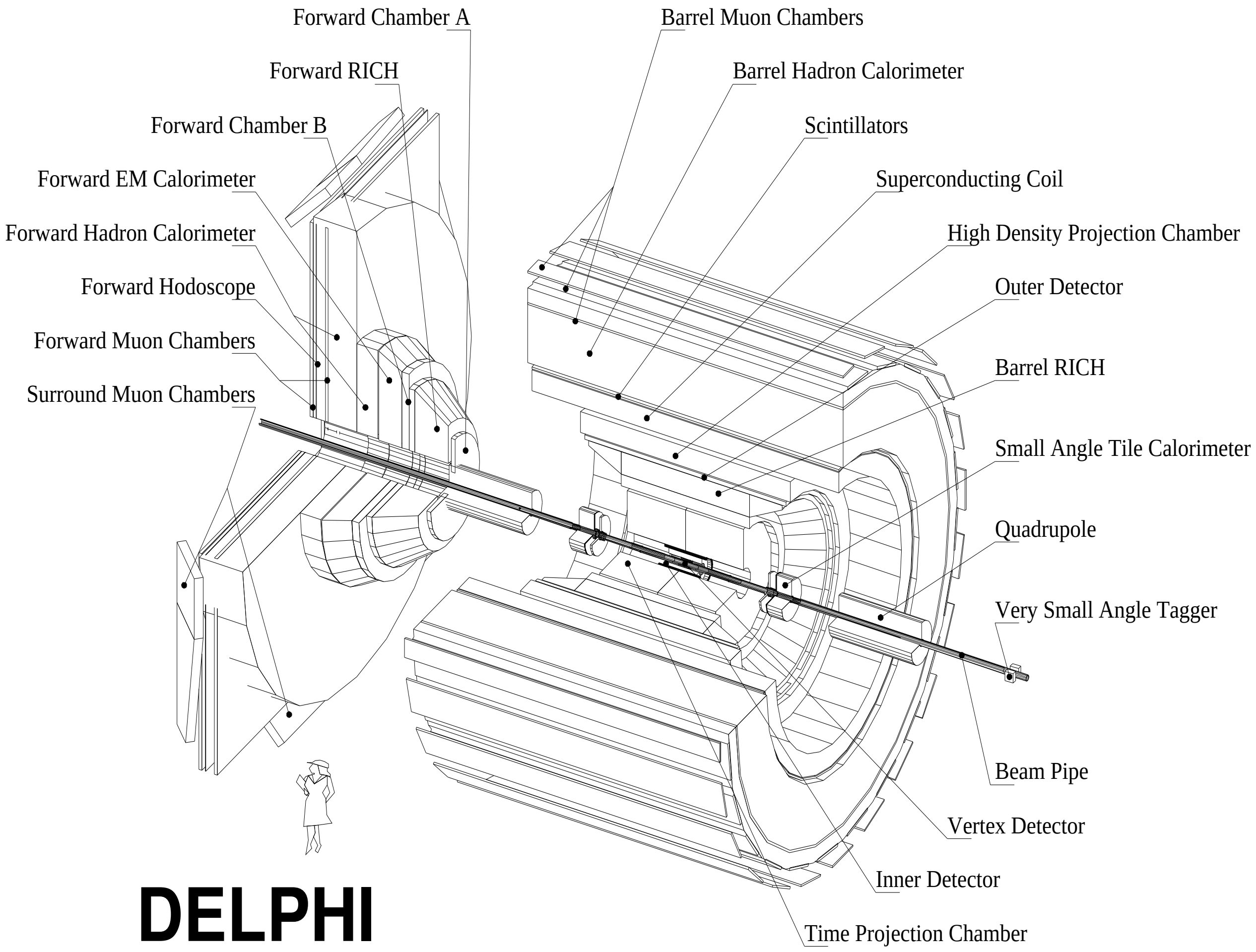

Figure 4.1: The DELPHI detector.

Chapter 4

The DELPHI Experiment

The DELPHI detector (DEtector with Lepton, Photon and Hadron Identification) is one of the four experiments for e^+e^- physics at LEP. The DELPHI detector is designed as a full 4π solid angle apparatus with emphasis on particle identification, three-dimensional information, high granularity and precise vertex determination. As such, it distinguishes itself from the other detectors at LEP. The design and construction by about 550 physicists (from 56 universities and research institutes in 22 countries world-wide) was finished by the end of 1989. Its length and diameter are over 10 m and its gross weight is 3500 tons. It total, the construction took 7 years and costed about 150 million Swiss Francs (excluding manpower). An artist's impression of the detector layout is given in figure 4.1.

The DELPHI experiment is an ensemble of 19 sub-detectors and a super-conducting magnet. It can be divided into three geometrical sections: a barrel section and two end-cap sections. Figure 4.2 shows a more schematic view of the barrel section in the beam direction. The end-caps can be moved axially to allow access to the detectors. Most of these sub-detectors[1] provide three-dimensional information via in total about 250 thousand channels, controlled by 14 dedicated computers and one main computer. From the start at end of 1989 until 1995, DELPHI has recorded over 3.4 million hadronic Z^0 events.

The DELPHI detector and its basic performance have been described in greater detail elsewhere ([30][31][32]). In this chapter, the main DELPHI devices for tracking, calorimetry and particle identification will be shortly discussed as well as the monitoring and control systems, the general data handling and the detector Monte Carlo simulation.

[1] as of here, 'sub-detectors' may also be called 'detectors'.

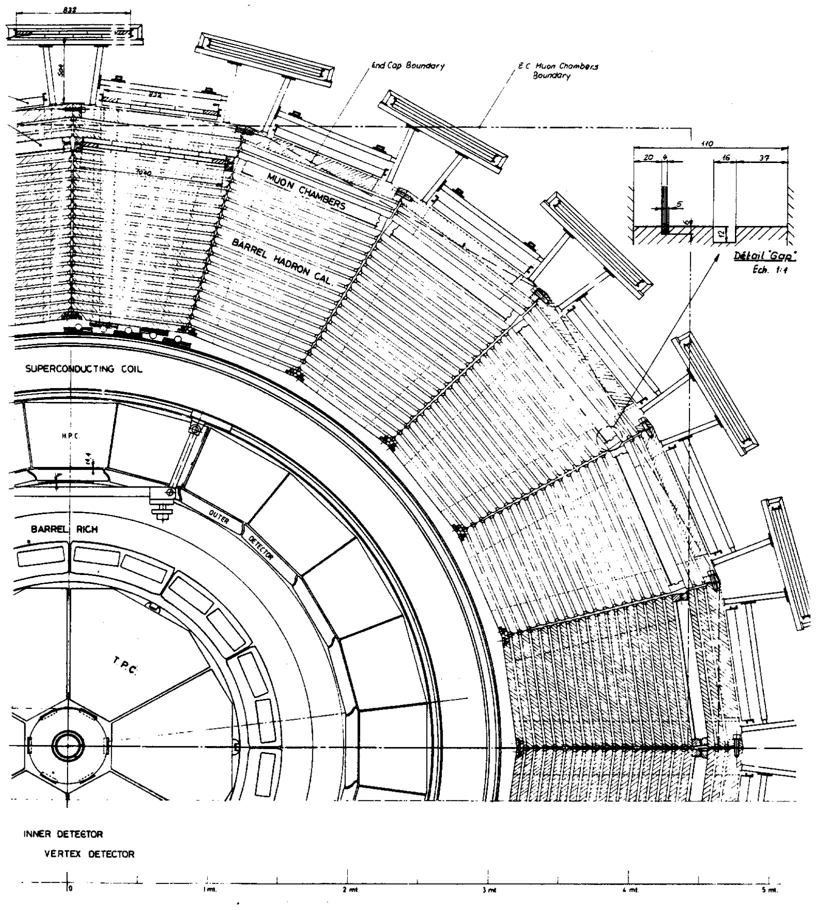

Figure 4.2: The schematic overview of the DELPHI detector along the beam-pipe.

4.1 The Tracking Detectors

The Super-conducting Solenoid

The barrel section contains a super-conducting solenoid of 7.2 m length and an inner diameter of 5.2 m. The conductor, made of copper-packed Nb-Ti, is operated at a temperature of 4.5 °K and carries a current of 5000 A. This leads to a magnetic field of 1.2 T which allows an accurate momentum determination of charged particles from their curved trajectory. To ensure the homogeneity of the field, compensating coils are mounted on both end flanges of the main coil. The magnetic field also plays an important role for those sub-detectors whose design is based on charge drift in the z-direction[2] The drift parallel to the magnetic field strongly reduces transverse diffusion. This is the case for the Time Projection Chamber, the barrel Ring Imaging Cherenkov counter as well as the High density Projection Chamber. The radial component of the magnetic field is of the order of 4.10^{-4}.

[2]DELPHI mostly uses cylindrical coordinates, $(r\phi,z)$ the z-axis is defined identical to the LEP definition (page 14).

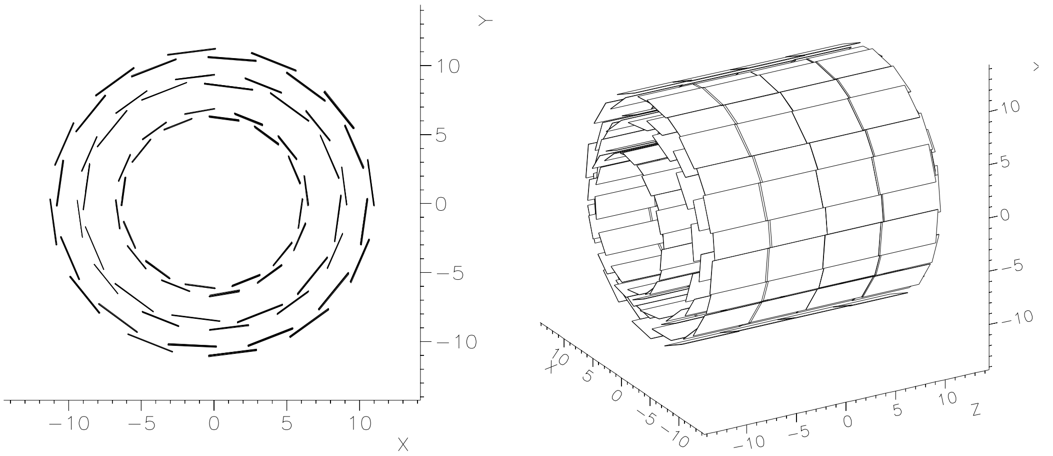

Figure 4.3: Schematic layout of the micro vertex detector (x, y, z in cm).

The Micro Vertex Detector

The Micro Vertex Detector (VD) is positioned closest to the interaction point and consists of three layers of silicon micro-strips which are placed along the beam–pipe at radii of 6.3, 9.0 and 10.9 cm. Every layer consists of 24 modules and covers track polar angles in θ between 31° and 149° . The VD layout is illustrated in figure 4.3. For the 1994 LEP running period, the most inner and the most outer layers were equipped with double sided micro-strips, allowing measurements both in $r\phi$ and z direction. To obtain a good resolution, it is necessary to perform a precise alignment of each layer. High momentum muons from $Z^0 \rightarrow \mu^+\mu^-$ are selected for this purpose. Muons which hit two overlapping modules of the same layer are the most useful. For perpendicular tracks, the intrinsic resolution is 7.6 μm in $r\phi$ and 9 μm in z.

Being situated closely to the interaction point, track impact parameters[3] can be determined with very high accuracy. The total uncertainty on the impact parameter basically finds its origin in three independent sources:

$$\sigma_{\mathrm{ip}}^2 = \sigma_0^2 + \sigma_{\mathrm{ms}}^2 + \sigma_{\mathrm{pvx}}^2 \tag{4.1}$$

The first source being the measurement error of the micro-strips causing a geometric extrapolation uncertainty (σ_0). The second source is multiple-scattering (σ_{ms}) in the beam-pipe and the micro-strips. Finally, the third source is the uncertainty on the position primary vertex (σ_{pvx}). The uncertainties in $r\phi$ and z direction have been parametrised depending on momentum p and the polar angle θ of the track as expressed in equations 4.2 and 4.3, after subtraction of σ_{pvx}^2 [33].

$$\sigma_{\mathrm{ip}}(r\phi) \quad = \quad \sqrt{20^2 + \left(\frac{\alpha_{\mathrm{ms}}}{p \cdot (\sin\theta)^{2/3}}\right)^2} \quad [\mu\mathrm{m}] \quad \wedge \quad \alpha_{\mathrm{ms}} = 65\ \mu\mathrm{m} \cdot \mathrm{GeV}/c \tag{4.2}$$

[3]the impact parameter is defined as the distance of closest approach of the track to the primary vertex.

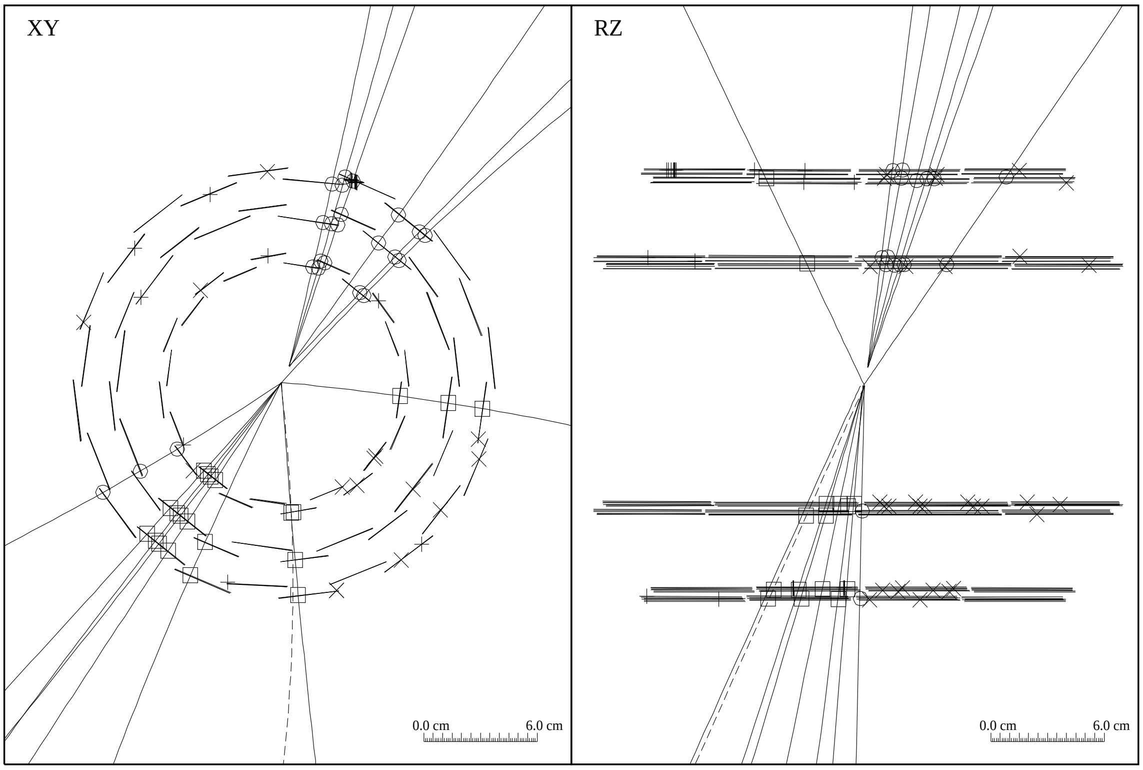

Figure 4.4: The xy and rz projection of a hadronic Z^0 decay (event 48758/2666 2/Jul/94) observed in the DELPHI micro vertex detector.

$$\sigma_{\mathrm{ip}}(z) = \sqrt{34^2 + \left(\frac{\alpha'_{\mathrm{ms}}}{p \cdot (\sin\theta)^{5/2}}\right)^2} \; [\mu\mathrm{m}] \quad \wedge \quad \alpha'_{\mathrm{ms}} = 71 \; \mu\mathrm{m} \cdot \mathrm{GeV}/c \tag{4.3}$$

(4.4)

The reconstruction of a hadronic Z^0 event is illustrated in figure 4.4. The crosses indicate unassociated VD hits whereas circles and boxes indicate associated VD hits.

For particle momenta below $\sim$1 GeV/c, the VD can also provide a measurement of the specific energy loss dE/dx. This will be discussed in more detail in section 4.3.

The Inner Detector

The 1 m long Inner Detector (ID) is situated in the barrel sector along the VD at a inner radius of 12 cm and an outer radius of 28 cm ($23° < \theta <157°$). It provides an accurate track measurement in both $r\phi$ and z direction. Additionally, the ID information is used for fast trigger decisions. The ID consists of two parts: the Jet Chamber and the Trigger Layers (see fig. 4.5).

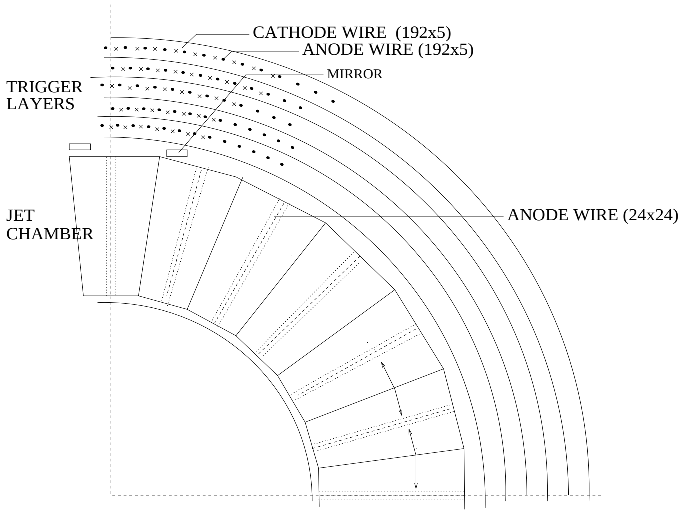

Figure 4.5: The schematic overview of one quarter of the Inner Detector.

The Jet Chambers are located at the most inner side up to a radius of 22 cm. The drift gas used is CO_2 with a small admixture of isobutane (iC_4H_{10}, 4.7%) and isopropanol (iC_3H_7, 0.7%). There are 24 sectors of 15° in ϕ, each of which contains 24 anode wires stretched along z, radially mounted in a row. The drift voltages are chosen such that they increase linearly in r, i.e. the longer the drift distance, the higher the field. Therefore, the ionisation electrons from tracks originating from the interaction point all arrive at the same time at one of the 24 wires. This feature is exploited for the fast trigger, which typically needs 5 μs to decide if a track originated from the interaction point or not.

Surrounding the Jet Chamber, there are 5 Trigger Layers of Multi-Wire-Proportional-Chambers at radii between 23 cm and 28 cm. They are filled with an admixture of argon (70%) and CO_2 (30%). Mounted along the beam-pipe, each layer consists of 192 sense wires, 192 field-shaping wires and 192 circular cathode strips (5 mm pitch). The sense wires solve the left-right ambiguity of the Jet Chambers whereas the cathode strips provide z-information. After corrections for effects such as temperature and pressure variations, the resolution for muons from $Z^0 \to \mu^+\mu^-$ is 50 μm in $r\phi$ and 1.5 mrad in ϕ.

Since the start of the 1995 LEP running period, a longer ID has been operational, extending its acceptance in polar angle down to 15° and 165° .

The Time Projection Chamber

The Time Projection Chamber (TPC) is 260 cm long and located around the ID at radii between 35 cm and 111 cm and is filled with an admixture of argon (80%) and methane (CH_4, 20%). The TPC fulfils two important tasks. Firstly, the TPC is the main tracking detector in DELPHI. Secondly, the TPC provides particle identification through the measurement of the characteristic energy loss per path length in the form

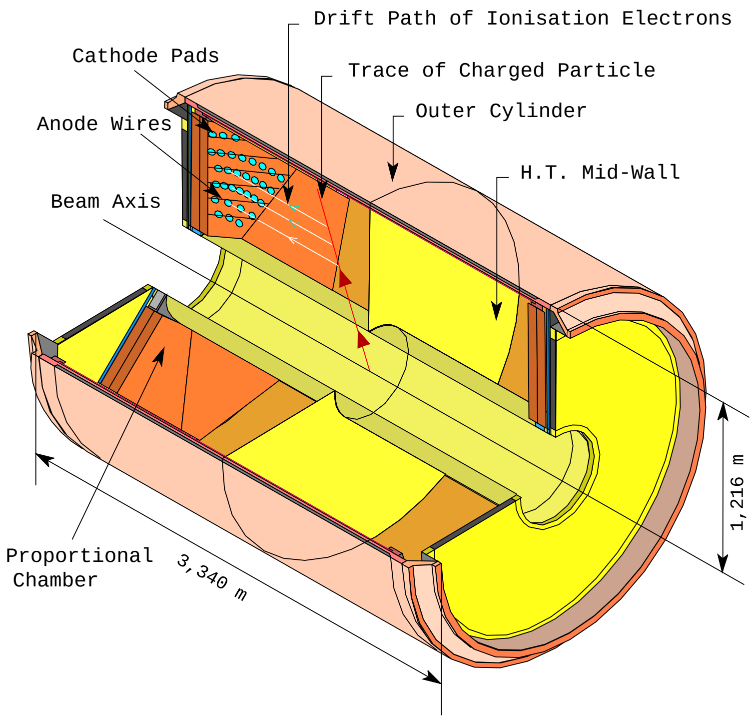

Figure 4.6: The schematic overview of the TPC.

of gas ionisation ($\mathrm{d}E/\mathrm{d}x$) [34]. As is shown in figure 4.6, at $z = 0$ the TPC is divided by a mid-wall into two hemispheres each of which having six 60° sectors in ϕ. The mid-wall carries the high-voltage (22kV), generating oppositely directed symmetric electric fields. A charged particle will ionise the gas on its way through the TPC and the resulting electrons will drift (parallel with the magnetic field) towards the end-plates with a velocity $v_d = 6.7$ cm/μs. Both end-plates contain MWPCs in segments of 60° , each of which having 192 anode wires and 16 concentric cathode pad-rows. The dead zones between the 60° segments corresponds to 4% of the $r\phi$-plane. The signals are collected by flash ADC's which provide information on the time of arrival as well as the shape of the signal. From the latter, the energy loss $\mathrm{d}E/\mathrm{d}x$ is determined, which is used for particle identification. Depending on the polar angle of the track, the TPC can provide up to 16 points with three-dimensional information. For tracks in hadronic Z^0 events the single point resolution is 250 μm in $r\phi$ and 880 μm in the rz plane, whereas the two-point resolution is of the order of 10 mm.

The Outer Detector

The Outer Detector (OD) covers 4.7 m along the beam-axis at radii between 198 cm and 206 cm ($42° < \theta < 138°$). The OD consists of 24 modules, each of which has 5 layers of drift tubes operated in limited streamer mode. It is flushed with an admixture of argon (50%), isobuthane (48%) and isopropanol (2%). Each layer provides three-dimensional information. The resolution in $r\phi$ is 110 μm. The z information is obtained from the measurement of the arrival time of the signal at both ends, with a resolution of 3.5 cm.

The OD provides fast trigger information in both $r\phi$ and z direction. Since it is positioned ~ 2 m away from the interaction point, the OD points increase the lever-arm for the track reconstruction and thus enable a precise determination of the momentum of a charged particle.

The Forward Chambers

On each end flange of the TPC, at a distance of 155 cm in $|z|$from the interaction point, the Forward Chambers A (FCA) are mounted. The FCA consists of three double layers of drift chambers which are operated in limited streamer mode. It is filled with an admixture of argon, isobuthane and ethanol (C_2H_5OH) (48.75% : 48.75% : 2.5%). The chamber covers polar angles $11° < \theta < 32°$ ($148° < \theta < 169°$). To obtain optimal reconstruction of space points and a good resolution, the 3 layers are rotated by 120° with respect to each other. In normal conditions, the precision on the reconstructed track elements are $\sigma(x) = 290\ \mu$m, $\sigma(y) = 240\ \mu$m, $\sigma(\theta) = 8.5$ mrad and $\sigma(\phi) = 24$ mrad (averaged over θ).

The Forward Chamber B (FCB) is a conventional drift chamber consisting of 4 independent modules, 2 at each end-cap, at a distance of 275 cm in $|z|$ from the interaction point. Each module is divided into 12 sense-wire planes. Like the FCA, 3 groups of 4 planes are rotated by 120° with respect to each other. They are filled with argon (50%), ethane (48%) and isopropanol (2%). The precision obtained on the reconstructed track elements are $\sigma(x, y) = 150\ \mu$m, $\sigma(\theta) = 3.5$ mrad and $\sigma(\phi) = 4/\sin\theta$ mrad.

FCA and FCB are the main DELPHI tracking detectors in the forward region. Apart from tracking information, both chambers also provide trigger information.

The DELPHI Combined Tracking

Some of the DELPHI tracking detectors are restricted in size due to the fact that both in the barrel and in the forward region the available space is shared with the Ring Imaging Cherenkov Counters (for particle identification). For two reasons it is essential that all available tracking information is combined for the track reconstruction. Firstly, because one is aiming for the best possible momentum resolution. Secondly, because the performance of the RICH particle identification depends very much on the quality of the track reconstruction. DELPHI is designed such that, in the limited space available, one obtains both an optimal momentum resolution and an excellent particle identification.

In combining information of different detectors, it is of vital importance to have them globally well aligned. This is achieved by using 45.6 GeV/c muons from $Z^0 \rightarrow \mu^+\mu^-$. In the DELPHI barrel region a combination of track components obtained from the VD, the ID, the TPC and the OD is used, the TPC being the main tracking device. Here, the total momentum resolution for muons from $Z^0 \to \mu^+\mu^-$ was measured to be:

$$\sigma(1/p) = 0.57 \times 10^{-3} \quad [(\mathrm{GeV}/c)^{-1}]. \tag{4.5}$$

In the forward region for muons from $Z^0 \to \mu^+\mu^-$ with ($20^\circ < \theta < 35^\circ$) for which at least track information of the VD (inner layer) and FCB was available, the total resolution was measured to be:

$$\sigma(1/p) = 1.31 \times 10^{-3} \quad [(\mathrm{GeV}/c)^{-1}]. \tag{4.6}$$

4.2 The Calorimeters

The High Density Projection Chamber

The High density Projection Chamber (HPC) is the DELPHI electromagnetic calorimeter in the barrel region. It is situated between the OD and the super-conducting coil (inner radius = 208 cm, outer radius = 260 cm) and is arranged in a set of 6 rings along the beam-pipe, each ring consisting of 24 individual modules. A module provides a three-dimensional reconstruction of an electromagnetic shower. As such, the HPC is the one of the largest time-projecting gas calorimeters of its kind.

Each module consists of a series of layers of dense material inside the gas volume where electromagnetic showers develop. An illustration is shown in figure 4.7. In reality, one module consists of 40 lead layers each 3 mm thick. Depending on the track angle of incidence, the lead converter thickness varies between 18 and 22 radiation lengths. The interleaved 8 mm gaps are flushed with an admixture of argon (80%) and CH_4 (20%). A traversing particle 'showers' in the lead converter. The large amount of particles created during the process, ionise the gas in the gaps. The resulting cloud of electrons drifts in a homogeneous electric field ($v_d = 5.5$ cm/μs parallel to the magnetic field) towards the end of the module where they are detected by a planar MWPC. The MWPCs consist of 39 sense wires and 128 pads, each pad being read out by flash ADC's with a sampling time of about 70 ns. Using photons from $\pi^0 \to 2\gamma$, having accurately reconstructed one photon which converted before the TPC, for the other photon, reconstructed in the HPC, one obtains an energy resolution of:

$$\frac{\sigma_E}{E} = \frac{32\%}{\sqrt{E}} + 4.3\ \% \quad [E \text{ in GeV}]. \tag{4.7}$$

The segmentation of the readout defines the angular resolution of $\sigma_\phi = 3.1$ mrad. The resolution in θ, depending on the drift time measurement, has been determined to be $\sigma_\theta = 1.0$ mrad.

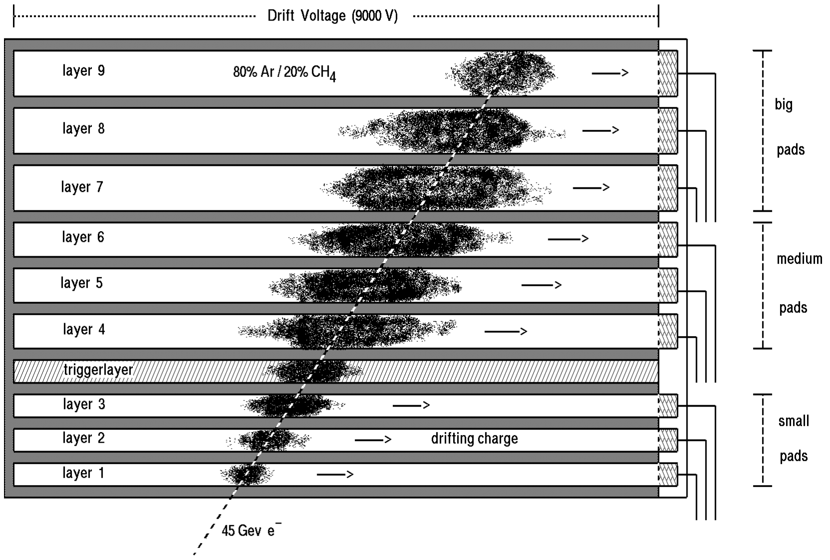

Figure 4.7: Schematic view of the layer structure of an HPC module.

The Hadron Calorimeters

Both in the barrel and the forward regions, the return yoke of the super-conducting magnet has been designed as an iron-gas Hadron Calorimeter (HCAL). The angular acceptance is between $43^\circ < \theta < 137^\circ$ in the barrel region and between $11^\circ < \theta < 50^\circ$ and $130^\circ < \theta < 169^\circ$ in the forward regions. It consists of successive layers of 5 cm iron and 2 cm wire chambers, 20 layers in the barrel and 19 in the forward regions. The chambers are filled with an admixture of CO_2 (59%), isobuthane (30%) and argon (11%). For hadronic Z^0 events in the barrel region ($52^\circ < \theta < 128^\circ$), the the energy precision in the HCAL is found to be:

$$\frac{\sigma_E}{E} = \frac{112\%}{\sqrt{E}} + 21\ \% \quad [E \text{ in GeV}]. \tag{4.8}$$

The Forward Electromagnetic Calorimeter

The Forward ElectroMagnetic Calorimeter (FEMC) is a conventional lead glass calorimeter and covers polar angles between $10^\circ < \theta < 36^\circ$ and $144^\circ < \theta < 170^\circ$ in the forward regions at $284 < |z| < 340$ cm. They are read out by vacuum photo-triodes. The FEMC energy resolution is determined to be:

$$\frac{\sigma_E}{E} = \sqrt{\left(\frac{5.0}{\sqrt{E}} + 0.35\right)^2 + \left(\frac{6.0}{E}\right)^2}\ \% \quad [E \text{ in GeV}], \tag{4.9}$$

with a spatial resolution of:

$$\sigma_{x,y} \approx \frac{8.2}{\sqrt{E}} \quad [\text{mm}]. \tag{4.10}$$

The Luminosity Monitoring

To measure the luminosity (using low Q^2 Bhabha events), two detectors are mounted around the beam-pipe. At 7.7 m away from the intersection point, there is the Very Small Angle Tagger (VSAT) and at 2.5 m the Small angle TIle Calorimeter (STIC) which replaces the Small Angle Tagger (SAT) since 1994. The VSAT covers polar angles between $0.29° < \theta < 0.4°$. It is a W-Si calorimeter of 24 radiation lengths giving a relative energy resolution of $\sim 5\%$ for 45.6 GeV/c particles. The STIC is a lead-scintillator sampling device, using wavelength shifting fibres and phototetrode tubes for readout. For 45.6 GeV/c particles the energy resolution is $\sigma_E/E = 2.7\%$.

4.3 Particle Identification

In this section a brief description will be given of the identification of the main particles which can be considered as 'stable' on the scale of the DELPHI experiment. As indicated by the acronym DELPHI, the particles concerned are leptons ($e^{\pm}$, $\mu^{\pm}$), photons (γ) and hadrons ($\pi^{\pm}$, π^0 , $K^{\pm}$, $K^0_{L,S}$, $\overline{K}^0_{L,S}$, p, $\overline{p}$, n and $\overline{n}$).

Muons are identified by the Muon Chambers (MUC) which are split into the Barrel Muon Chambers (MUB, 3 layers, $53° < \theta < 157°$), the Forward Muon Chambers (MUF, 2 layers, $20° < \theta < 42°$) and the Surrounding Muon Chambers (MUS, 1 layer), covering the gaps between MUB and MUF. The MUC are located behind the HCAL and consist of conventional drift chambers filled with admixtures of argon, CO_2 and isobuthane.

For *electron* identification, information of the HPC, FEMC and TPC can be used and to a lesser extent the VD and RICH.

Photon identification is performed by the HPC and FEMC. In case a photon converts in an earlier stage, before having reached the HPC (FEMC), the resulting e^+e^--pair can be detected by the TPC and partly by the RICH.

Neutral hadrons can be detected by the HPC (π^0) and the HCAL (K^0_L, $n\overline{n}$).

Charged hadrons ($\pi^{\pm}$, $K^{\pm}$, $p\overline{p}$) can be identified by using the information of different detectors. For particle momenta larger than ~ 0.25 GeV/c, the TPC provides a dE/dx-measurement. As mentioned before, the TPC-dE/dx measurement also provides electron identification, as can be seen in figure 4.8. For low momentum particles (30 MeV/$c < p <$ 1.5 GeV/c), the VD-dE/dx measurement can be used as illustrated in figure 4.9. However, the most powerful $\pi^{\pm}$, $K^{\pm}$, $p\overline{p}$ -identification is obtained from

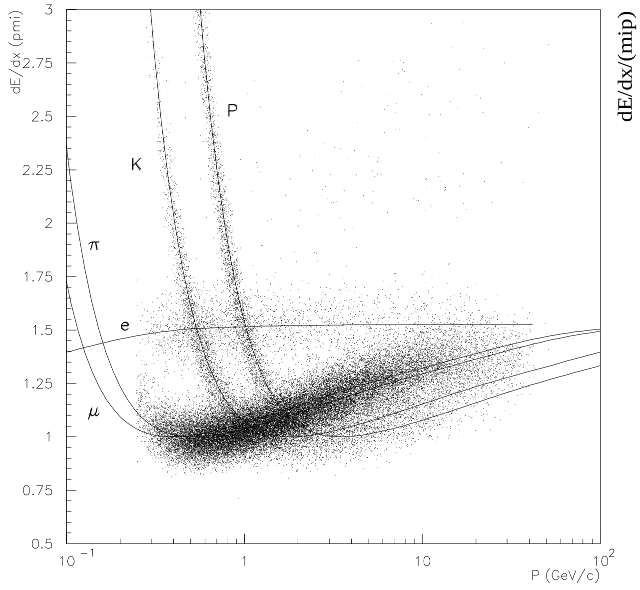

Figure 4.8: The TPC dE/dx measurement versus momentum.

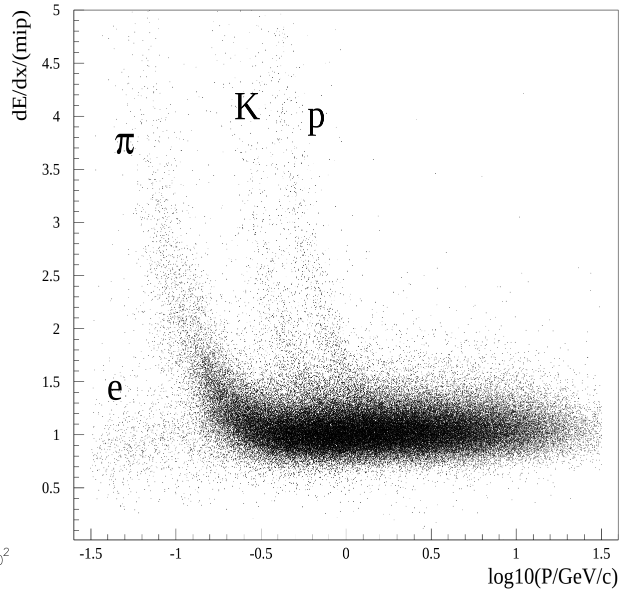

Figure 4.9: The VD dE/dx measurement versus momentum.

the RICH. This detector and its particle identification will be discussed in more detail in chapters 5 and 6.

For completeness it should be mentioned that both in the barrel and forward regions, Time-of-Flight (TOF) systems of scintillating counters have been installed ($15^\circ < \theta < 165^\circ$). These counters serve as a cosmic muon trigger but also give information on particles (mostly photons and muons) which happened to pass through small uncovered zones such as gaps for cabling and support structures or cracks between the different modules of a detector. In regions where no TOF information can be collected, lead-scintillator counters ('ϕ-taggers') have been installed.

4.4 Data Taking and Control Systems

The data taking and control systems are linked to the DELPHI detector via the DELPHI Online-Cluster which consists of a large group of inter-connected computer-stations (mainly VAX 4000-series). The online cluster is used to perform three basic tasks: the slow control (SC), the trigger and data acquisition (DAQ) and the data quality checking (QC). Under normal data-taking circumstances each of these tasks is executed by an operator, thus a three-person crew is needed to run the entire experiment. Each of these tasks, which are computerised to a large extent, will be shortly discussed below.

Slow Control System

The main task of the SC system is to monitor and control the detector hardware and its electronics to ensure optimal detector stability for data-taking but also to guarantee maximum safety conditions.

The SC system controls the switching of the low and high voltages of all detectors ('off', 'standby', 'ramping', 'ready' or 'error') as well as their gas systems, detector heating and cooling, pressure regulation systems and calibration systems. The hardware-connections are mostly provided by G64-micro-computers (about 70 in total) via Ethernet-links. The SC basically comprises four inter-locked sub-systems: a display system for the status of the (sub-)detectors, an error handling system, a gas control system and a separated safety system. Depending on the circumstances, both the safety and the error-handling system can take action without human intervention.

From the monitoring point of view, the SC system surveys a large series of (sub)-detector parameters which may vary in time (e.g. temperatures, pressures, low- and high-voltages, drift velocities etc.) and stores the information in the DELPHI-database. At a later stage this information is folded with the recorded physics data.

The Trigger System

The time window between two consecutive Beam Cross Overs (BCO) at LEP is 22 μs (11 μs in 8 bunch mode). The DELPHI trigger system is designed to handle high luminosities with a large back-ground event rate and consists of four levels (T1, T2, T3 and T4). The T1-decision is made after 3 μs, using ID and OD information and/or FCA and FCB information. In the barrel region the T1 is supported by the scintillating layer in the HPC (see fig. 4.7). Within 39 μs after a positive T1 outcome (the T1-rate is of the order of 400 Hz) the T2 will have verified the information from the slow drift detectors (e.g. charged tracks in the TPC and electromagnetic showers in the HPC) to confirm the T1-decision. The T2 rate is typically of the order of 4 Hz. This rate is diminished to about 2 Hz by the T3, which uses the full granularity and resolution to make its decision. The remaining background is further reduced by the T4 which flags events for physics analysis and simultaneously provides the information for the QC an the online event display. The trigger efficiency for multi-hadronic events is almost 100%.

The Data Acquisition System

The DAQ stores all events triggered at the T2-level as 'raw-data'. It uses the ZEBRA bank structure. ZEBRA is a memory management programme for handling dynamic data structures. The size of a multi-hadronic event is of the order of 50 Kbyte. Each event is labelled with an individual number, the LEP fill number and the DELPHI run number. A run is defined as a time-period in which the detector was in stable conditions. Each run is recorded in a separate data file. Finally, the data-files are stored on IBM-3480 cassettes. At a later stage, discussed below, these tapes are read by the DELPHI offline system which is used for data-processings and physics analyses.

Big Brother

The operating crew is supported by a computerised vocal system named 'Big Brother' (BB), which simultaneously monitors the status of the LEP accelerator (e.g beam and background level) as well as the status of the SC and the DAQ. BB can take action without human intervention. For example, if the SC status of one of the main detectors in DELPHI is 'in error' (e.g. high voltage trip), BB will automatically 'pause' the DAQ and broadcast an error message. After intervention of the SC-operator, the SC status will go back to normal ('ready') and BB will automatically restart the DAQ.

The Data Quality Checking

The DELPHI QC system has the task to give fast feedback on the quality of the data-output of each of the detectors. For this purpose a large series of histograms which give information on the basic signal-readout of the detectors have been defined. These histograms are filled online during data-taking and compared by eye with the histograms one normally would expect to obtain. Furthermore, the QC-operator disposes of an online event display programme (discussed below), which produces a 3-dimensional display of any event which passed the T4-trigger level.

4.5 The Data Analysis Chain

The recorded raw-data undergo a chain of treatments before they can be released for physics analyses. An overview of the chain is given in figure 4.10 in the form of a flow-chart. It basically consists of three software packages: an analysis package to prepare the data for physics, a graphics package for interactive event display, and a package for detector simulation to enable the comparison of the real data with Monte Carlo data.

The DELANA Package and DST Production

The principal reconstruction programme is the DELPHI ANAlysis is package DELANA [35]. The ZEBRA-structured data handling package used inside DELANA is called TANAGRA (Track ANAlysis and GRAphics package). For each sub-detector, DELANA contains a programme-module which performs the calibration and alignment of the raw-data and includes relevant information from the SC monitoring which has been stored

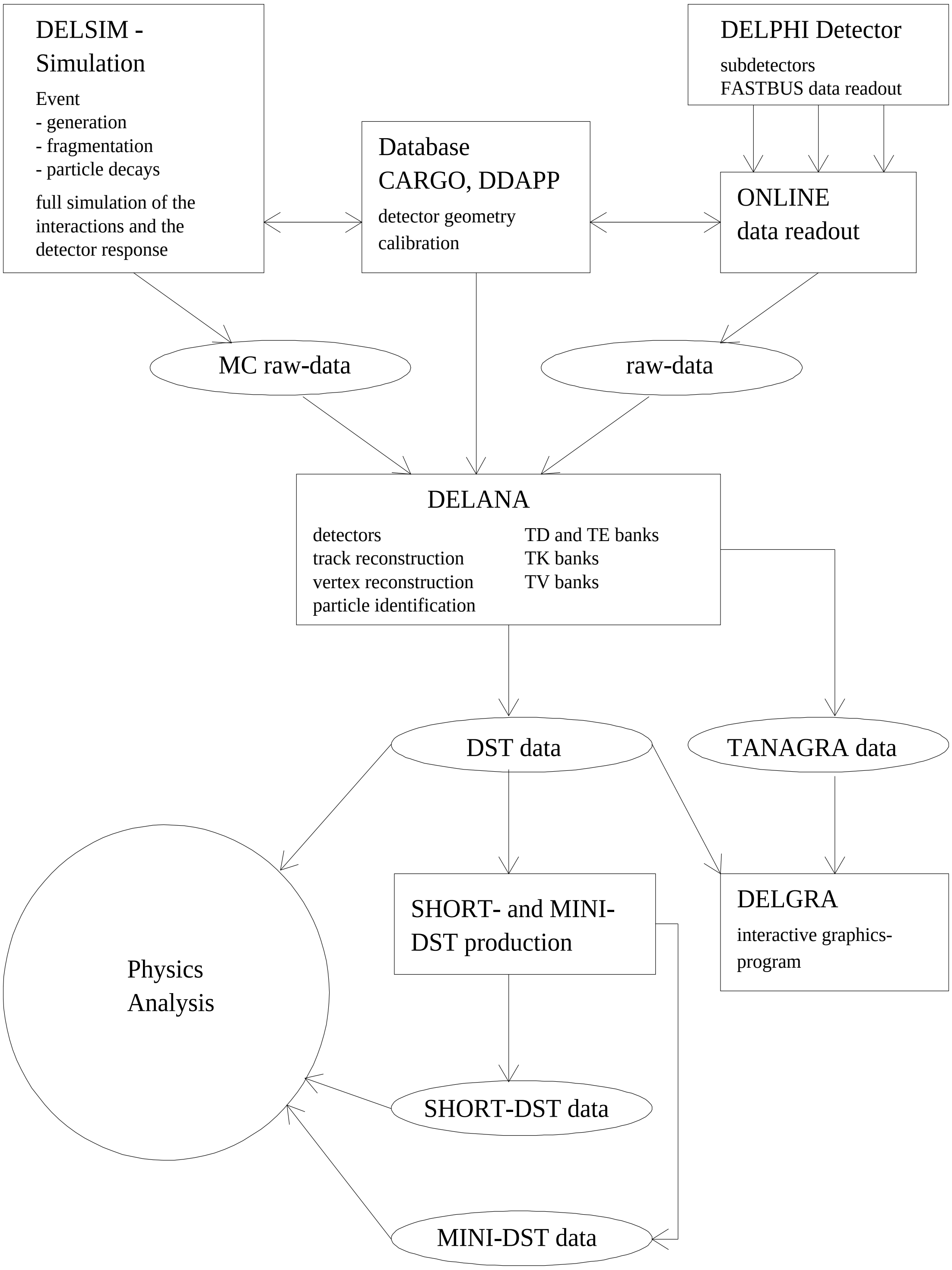

Figure 4.10: The Delphi offline analysis chain.

in the DELPHI-database. The event reconstruction proceeds according to the following six steps:

1. *First stage pattern recognition.* For each sub-detector, an independent local pattern recognition is performed which produces Track Elements (TE) e.g. space points and directions, energy deposition etc.

2. *Track fit.* The available TE's are combined into track candidates. For each candidates a track fit is performed.

3. *Track extrapolation.* After having resolved ambiguities, the fitted tracks are extrapolated through all the sub-detectors. In this way one can obtain an optimal estimation of the particles' trajectory through each sub-detector.

4. *Second stage pattern recognition.* The local pattern recognition is repeated, including the information of the sub-detectors obtained by the track extrapolation.

5. *Associating calorimeter information.* The charged track candidates are associated with the available energy clusters obtained from the calorimeters. From the remaining energy clusters, neutral tracks are created. At this stage, charged tracks are also linked to the RICH information for particle identification.

6. *Primary Vertex fit.* Finally, combining all reconstructed tracks, the primary event vertices are fitted.

The outcome of the event reconstruction procedure is stored on Data Summary Tapes (DST) in a tree structure of banks which contain all information needed for physics analyses. The size of an average multi-hadronic event on a DST is about 80 Kbyte.

From the DST a condensed version called Short DST (SDST) is produced. During the SDST production, additional processings are performed as well as a first stage analysis to obtain basic physics information:

- Second order corrections for calibration and alignment are applied on the TE-level and the track- and vertex-fits are repeated (DSTFIX)
- b-event tagging (AABTAG package)
- e, γ and π^0 identification (ELEPHANT package)
- μ identification (MUFLAG package)
- $\mathrm{K^0_S}$ and Λ^0 reconstruction (RECV0 package)
- Second stage RICH fixing (RICFIX package)
  $\pi^{\pm}$, $\mathrm{K}^{\pm}$, $\mathrm{p\overline{p}}$ identification (HADIDENT package)

The output obtained from the application of these packages makes a certain amount of DST-information more or less obsolete for standard physics analyses and allows a reduction in size of ~50% compared to the DST. For physics analyses in DELPHI, the SDST information is most commonly used. An option to reduce the volume of the SDST by a factor 3, can be obtained through the production of a Mini-DST (MDST). The MDST contains just the minimum information needed for physics analyses and does not allow re-evaluations (e.g. track re-fits etc.) of its content.

Different standardised software packages are available for obtaining the information stored on DST, SDST and MDST for physics analyses. Most commonly used are the SKEleton ANAlysis programme (SKELANA) and the PHDST input/output package [36].

The Event Display

The DELPHI GRAphics package (DELGRA) offers the possibility of a 3-dimensional colour display of an event, visualising the contributions obtained from the different sub-detectors. It is a practical tool to investigate both the performance of the detector (QC) and the performance of the event reconstruction programmes. Especially for the W-physics at LEP-2, the DELGRA package may turn out to be a powerful tool to visualise possible new physics. An example is given in figure 10.3 (page 145), which displays a semi-leptonic W-event.

The DELPHI Simulation Package

The Monte Carlo of the DELPHI-experiment is called DELPHI SIMulation (DELSIM) [37]. It basically consists of three different parts:

- an event generator
- the simulation of particle interactions with(in) detector components
- the signal response of each sub-detector

The event generator is chosen according to the process one is interested in. In DELSIM the JETSET 7.3 PS [17] event generator is used to simulate $Z^0 \to q\overline{q}$ events. The simulation of interactions with(in) detector components during a particles' passage contains the following effects:

- Compton scattering
- pair production
- bremsstrahlung

- positron annihilation
- δ-ray emission
- photon conversion
- nuclear interactions and absorptions
- multiple scattering
- decay of short-living particles ($\tau < 10^{-9}s$)

A complete description of the detector materials and their characteristics is obtained from a the DELPHI-database which contains the full blue-print geometry of DELPHI. The signal response is different for each sub-detector of which the basic parameters (temperatures, pressures, drift velocities etc.) are obtained from the SC monitoring information in the DELPHI-database.

The DELSIM output is of the same format as the raw data and undergoes the same treatment as discussed above. On the resulting DST (SDST, MDST) extra banks are included which contain information on the simulation origin of the generated event and its particles.

Chapter 5

DELPHI RICH Detectors

5.1 Introduction

In the mid 1930's the Russian physicist P. Cherenkov started investigating the source of the blue light radiated by substances which were being exposed to radioactive radiation. These investigations lead to the discovery of a new kind of radiation [38]. In 1938, I. Frank and I. Tamm published the theoretical explanation of what was later called the Cherenkov-effect i.e. Cherenkov radiation [39]. Cherenkov, Frank and Tamm shared the 1958 Nobel prize for their work. The Ring-Imaging Cherenkov technique, using gaseous UV-photon detectors was firstly proposed by Ypsilantis and Séguinot in 1977[40]. DELPHI is the only LEP-experiment using RICH counters for $\pi^{\pm}$, $K^{\pm}$, $p\overline{p}$ -identification from 0.7 up to 45.6 GeV/c.

The emission of Cherenkov radiation is a property of the gross structure of the medium through which a charged particle passes. The electric field of the charged particle produces a macroscopic polarisation due to displacement of bound electrons. If the particle velocity exceeds the velocity of light in the medium, coherence is possible between polarisations originating from different points along the path of the particle. The radiation is emitted in a forward cone of semi-angle $\theta_{\check{c}}$ ($\equiv$ Cherenkov angle) with respect to the direction of flight of the particle according to the equation 5.1, where n is the refractive index of the medium and β $(= v/c)$ is the relativistic velocity.

$$\cos\theta_{\check{c}} = \frac{1}{\beta n} \tag{5.1}$$

Thus by obtaining $\theta_{\check{c}}$, one can calculate the velocity of the particle. In order to obtain the mass m –and thus identify the particle– it is also necessary to know the momentum p of the particle. With $\beta = p/E = \sqrt{1 - 1/\gamma^2}$ equation 5.1 can be transformed into:

$$m = \frac{p}{\beta\gamma} = p\sqrt{n^2\cos^2\theta_{\check{c}} - 1} \qquad \wedge \qquad \gamma = 1/\sqrt{1-\beta^2} \tag{5.2}$$

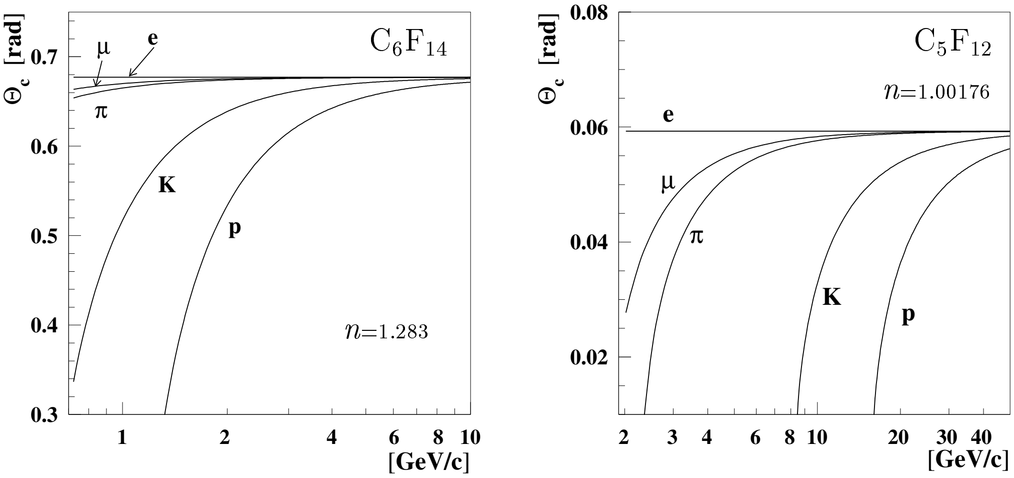

Figure 5.1: The expected Cherenkov angle versus momentum for two different materials, liquid C_6F_{14} ($n = 1.283$) and gaseous C_5F_{12} ($n = 1.00176$) at 1030 mbar pressure.

The theoretically expected values for $\theta_{\check{c}}$ as a function of p are illustrated in figure 5.1 for two Cherenkov media used in the DELPHI. Several features of Cherenkov radiation can be deduced from the above equations:

- for a given refractive index, there is a *threshold* velocity i.e. momentum below which no radiation can be emitted:

$$\beta_{th} = 1/n \qquad \text{i.e.} \qquad P_{thres.} = \frac{m}{\sqrt{n^2 - 1}} \tag{5.3}$$

- for a given refractive index, independent of the mass of the particle, there is a *maximum* Cherenkov angle $\theta_{\check{c}}^{max}$:

$$\cos\theta_{\check{c}}^{max} = \frac{1}{n} \qquad \text{for} \qquad \beta \approx 1 \tag{5.4}$$

- for a given momentum p, the angle of emission $\theta_{\check{c}}$ depends on the frequency (i.e. wavelength) of the Cherenkov radiation, since n is wavelength-dependent.

In classical dynamics, the power radiated in a given direction by an electric current depends only on the currents' component which is perpendicular to the direction of the observed radiation. Hence, for Cherenkov radiation, the component of the current which contributes to the radiation is proportional to $\sin\theta_{\check{c}}$. As the power is proportional to the current squared, the intensity of the Cherenkov radiation is proportional to $\sin^2\theta_{\check{c}}$. The full electro-dynamical expression for the number of emitted Cherenkov-photons per energy interval is [41]:

$$\Delta N_{emitted} = \frac{Q^2\alpha}{\hbar c} \cdot L \cdot \sin^2\theta_{\check{c}} \cdot \Delta E \tag{5.5}$$

where Q is the charge of the particle (in units of electron charge), α is the electromagnetic fine structure constant, h is Planck's constant, c is the velocity of light in vacuum, L is the length (in cm) of the particle path in the radiator medium and ΔE is the width of the energy band over which the photons can be detected. This equation also underlines the fact that Cherenkov radiation is evenly distributed in photon energy. Expressing the terms in equation 5.5 in convenient units, one can write the number of detected photons in a Cherenkov detector as:

$$N_{detected} = N_0 \cdot L \cdot \sin^2 \theta_{\check{c}}. \tag{5.6}$$

N_0 is commonly known as the *quality factor* of the detector which is defined as:

$$N_0 = \frac{Q^2 \alpha}{\hbar c} \cdot \int \epsilon_{coll}(E)\ \epsilon_{det}(E)\ \mathrm{d}E = 370\ (\mathrm{cm}^{-1}\mathrm{eV}^{-1}) \cdot \int \epsilon_{coll}\ \epsilon_{det}\ \mathrm{d}E \tag{5.7}$$

where ϵ_{coll} represents the collection efficiency for Cherenkov light and thus accounts for the characteristics of the materials used in the detector design and ϵ_{det} is the photon detection efficiency e.g. the quantum efficiency of the photon transducer (photo-multiplier or equivalent) [42]. For the DELPHI RICH detectors the efficiency ϵ_{coll} covers the reflectivity of the mirrors and the transmission of several detector components such as quartz windows, radiator gas, drift gas, etc. and ϵ_{det} contains the quantum efficiency for photon conversion and the electron detection efficiency.

The DELPHI RICH consist of two parts, a Forward RICH (FRICH) in each end-cap and a Barrel RICH (BRICH) in the barrel region. To enable a good Cherenkov angle reconstruction it is very important to have exact information on the particle trajectory through the RICH. This is especially important in an environment of potentially high track densities as they occur at LEP-energies. Therefore the BRICH is sandwiched between the tracking detectors OD and TPC, and the FRICH between FCA and FCB. The working principle and design of the DELPHI-RICH detectors will be shortly discussed below on the basis of the Barrel RICH.

5.2 The Barrel RICH

The Barrel RICH [43] covers polar angles between $45° < \theta < 135°$. The design principle as illustrated in figure 5.2, can be divided into two parts: photon *production* and photon *detection*.

Photon Production

In order to perform particle identification from $0.7 < p < 45.6$ GeV/c, the BRICH contains two different radiator media, both belonging to the same chemical family of per-

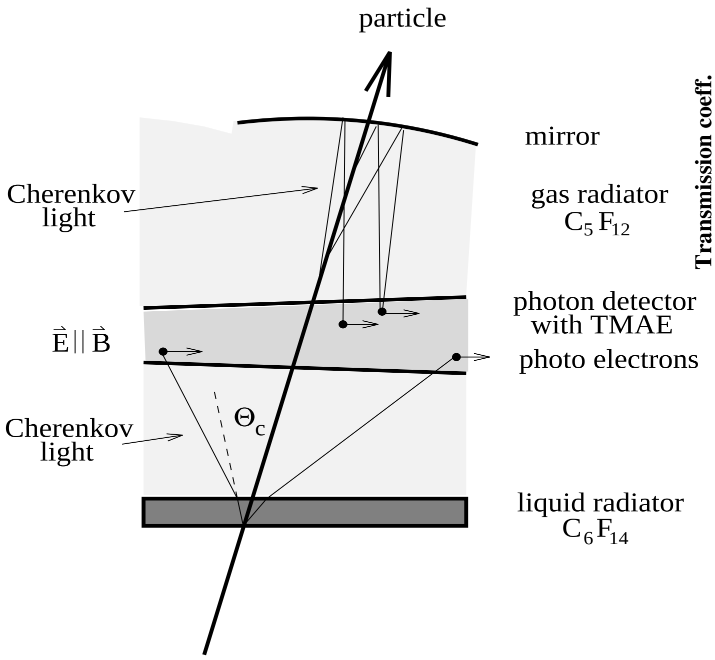

Figure 5.2: The working Principle of the Barrel RICH.

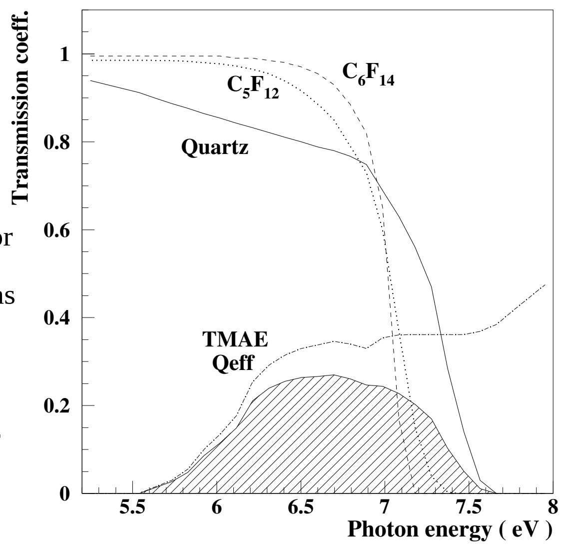

Figure 5.3: The transmission coefficients of for the BRICH.

fluorocarbons C_nF_{2n+2} (or simply CF). A liquid radiator (1 cm thick C_6F_{14}) to identify particles with momenta below ∼8 GeV/c and a gas radiator (∼42 cm C_5F_{12}) for identification above ∼2.7 GeV/c. The Cherenkov light from the thin liquid radiator is projected directly onto a UV-sensitive photon detector which converts UV-photons into photo-electrons. This kind of focusing is often referred to as 'proximity focusing'. The photo-electrons appear in a ring-like or parabolic configuration, depending on the angle of incidence of the particle. The Cherenkov light from the gas radiator is reflected by focusing mirrors onto the opposite side of the same photon detector.

An overview of the most relevant properties of the Cherenkov fluids used for the DELPHI RICH detectors is given in table 5.1. Perfluorocarbons have been chosen mainly because they combine a suitable refractive index with good UV-transmission and a low chromatic dispersion [44]. Moreover, they can support high electric fields and have the practical advantages of being thermally stable, non-flammable, non-toxic and under normal conditions chemically inert.

C_nF_{2n+2}	n refr.index at 7 eV, 1 bar	T boiling temp.(°C)	dn/dE (x10^{-6}) 6.5–7.5 eV	$\frac{\Delta n}{(n-1)}$	$P_{thres.}$ [GeV/c] $\pi^\pm$	$K^\pm$	$p\bar{p}$	$\theta_{\check{c}}^{max}$ [mrad]
C_4F_{10}	1.001530	−2	53	3.5%	2.5	8.9	17.0	55.3
C_5F_{12}	1.001720	28	51	3.0%	2.4	8.4	16.0	58.6
C_6F_{14}	1.283	57	9300	3.3%	0.17	0.6	1.2	677.1

Table 5.1: Some key properties of the Cherenkov fluids for DELPHI RICHes.

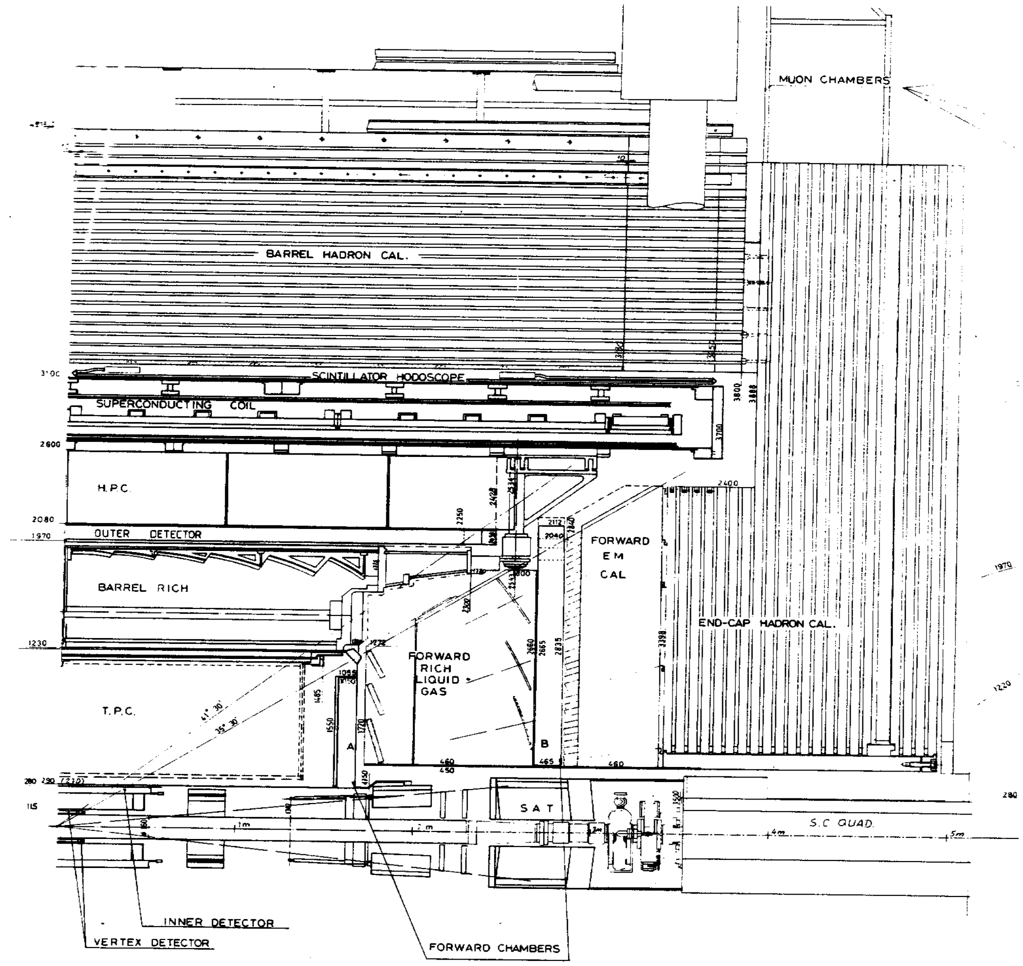

Figure 5.4: Schematic view of the position of the Barrel and Forward RICH in DELPHI.

Photon Detection

The UV-photon-detector is a TPC-like drift device entirely made of quartz to allow UV-photon transmission from both sides. Inside the drift volume[1], the Cherenkov UV-photons will liberate electrons by ionisation of the drift gas. The photo-sensitive agent in the drift gas, Tetrakis-diMethyl-Amino-Ethylene (TMAE), is sensitive for photons with energies higher than $\sim$5.5 eV. A homogeneous electric field ($\vec{E}||\vec{B}$) causes the electrons to drift towards the end of the photon detector, where they are detected by a Multi-Wire-Proportional-Chamber (MWPC, not indicated in figure 5.2). The UV-photon-detector delivers 3-dimensional information for each detected photon: the MWPC gives x and y-information whereas z-information is obtained from the drift time measurement. To reduce the loss of photo-electrons at the quartz entrance window (due to transversal diffusion), the drift tube is given a slight taper, which causes the electrons always to drift horizontally away from the quartz window towards the MWPC at the wider end of the tube.

[1]The drift volume is frequently called '(drift) tube' for BRICH and '(drift) box' for FRICH.

Since the fundamental principle of the DELPHI-RICH detectors relies on the production and detection of UV-photons, it is of utmost importance that the key detector elements are either UV-transparent or UV-sensitive. The principle parameters of the BRICH as a function of photon energy are shown in figure 5.3. The transmission coefficients indicated are for 8 mm quartz (solid line), 1 cm liquid C_6F_{14} (dashed line) and 15 cm gaseous C_5F_{12} (dotted line). The dash-dotted line indicates the TMAE quantum efficiency (Q_{eff}^{TMAE}). The hashed area represents the quartz UV-transmission folded with the Q_{eff}^{TMAE}, which can be taken as a measure of the photon conversion capacity of the drift tubes. The lower limit for photon detection is determined by the Q_{eff}^{TMAE} at ~5.6 eV (i.e. 221 nm) whereas the upper limit is determined by the quartz at ~7.7 eV (i.e. 160 nm). The average Cherenkov photon wavelength in the RICH is ~190 nm. The UV-properties of the different RICH-fluids will be discussed in more detail below, in section 5.5. A schematic overview of the position of BRICH and FRICH in the DELPHI assembly is shown in figure 5.4.

The BRICH Detector Components

The BRICH can be divided into 48 units of 15° in R_ϕ, 24 in each half of the barrel region. Three design components are centrally covered for all units:

- The BRICH is integrally heated to a constant temperature of 40°C to avoid condensation of the C_5F_{12} and the TMAE-loaded drift gas.
- The complete detector is kept at a constant pressure of 1030 mbar to keep the detector parameters constant and to reduce the identification gap between the liquid and the gas radiator.
- The Very High Voltage (VHV) which defines the electric drift field inside the drift tubes is set to a constant value. The VHV, which can produce at maximum an E-field of 1 kV/cm, is normally operated at ~360 V/cm.

A longitudinal cross-section of one unit is shown in figure 5.5. Each unit consists of seven parts:

- *A liquid radiator.* The liquid radiator is a tray (1 cm thick, 150 cm long) with a 4 mm thick quartz exit window. One liquid radiator tray can contain about 5 l of C_6F_{14}, thus all radiators together take a volume of 240 l. The outer quartz window is equipped with 130 μm wide metallic strips with a pitch of 6 mm along R_z. These strips are connected via a resistor chain to the VHV.
- *A gas radiator.* The gas radiator is a 42 cm thick layer of C_5F_{12}. All 48 units basically form one big volume, also surrounding the open spaces around the drift tubes and the liquid radiators. The total gas volume is ~24 m^3, which is equivalent to about 140 l of liquid C_5F_{12}. As mentioned above, the gas is kept at a constant temperature of 40°C and at a fixed pressure of 1030 mbar.

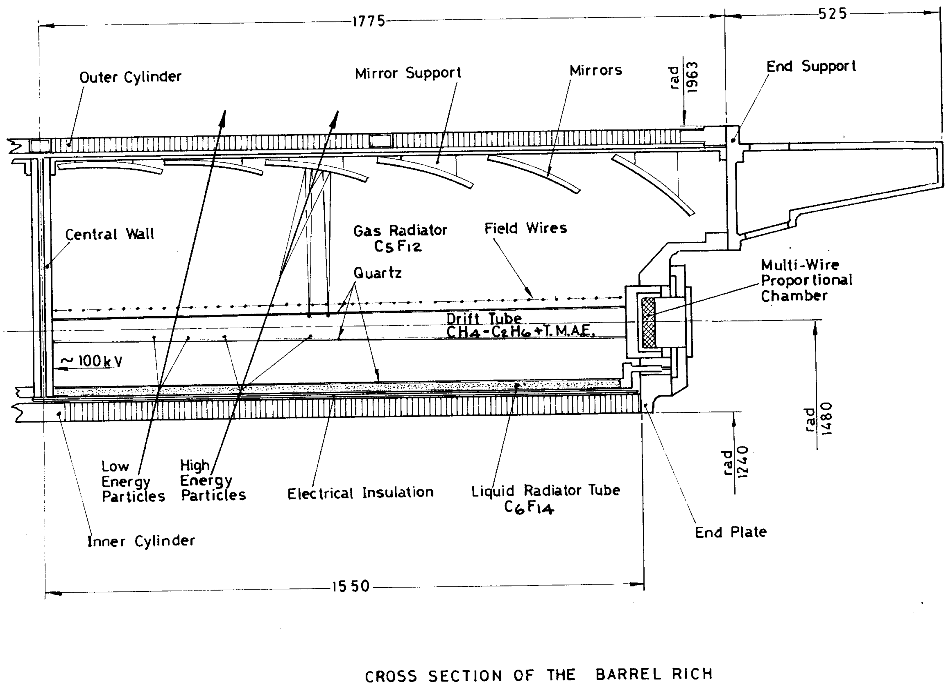

Figure 5.5: Schematic view of the Barrel Ring-Imaging Cherenkov Counter.

- *A row of six parabolic mirrors.* The mirrors are coated with 50 nm aluminium and 60 nm MgF_2 as a protective layer. This assures a very high reflectivity for UV-light (> 90%) [45]. In total the BRICH contains 288 mirrors.

- *A quartz drift tube.* Each drift tube is entirely made of 4 mm thick quartz[2], 155 cm long and 34.5 cm wide. It is 4.2 cm thick at the mid-wall side and 6.2 cm at the MWPC-side. The integrated volume of all drift tubes is 1280 l. The drift gas is an admixture of methane-ethane (75%-25%) with ~0.1% TMAE vapour. The TMAE is added by bubbling the main gas mixture through a TMAE bath of constant temperature of 28°C . The quartz windows are equipped (by vacuum deposition) on both sides with 100 μm metallic strips with a pitch of 3 mm along z. These strips are connected via a resistor chain to the VHV. The system of strips and degraders on the different sub-systems provides a very homogeneous electric drift field ($E_{\mathrm{trans.}}/E_{\mathrm{longit.}} < 10^{-4}$). Figure 5.6 shows a longitudinal view of the BRICH with the configuration of the equipotential lines of the electric drift field.

- *A MWPC.* Each drift tube is equipped with a MWPC [46] to measure the x and y-position of arriving electrons. The design of the MWPC is shown in figure 5.7. Each chamber consists of 128 anode wires with a pitch of 2.62 mm and 8 blocks of 16 cathode-strips (3.8 mm wide) perpendicular to the anode wires. The x-position of the photo-electron is obtained by means of avalanche multiplication. The multiplication factor is of the order of $2{\cdot}10^5$. The y-position is obtained from the induced cathode signal. Between the individual wires, UV-blinds are

[2]fused silica, Nippon Silica, Japan.

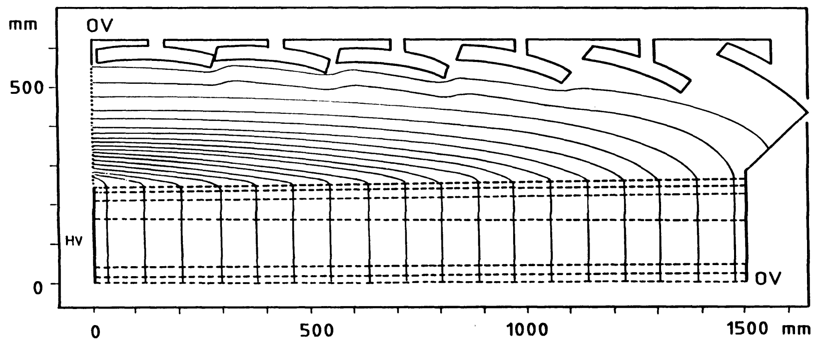

Figure 5.6: The equipotential lines of the BRICH electric drift field.

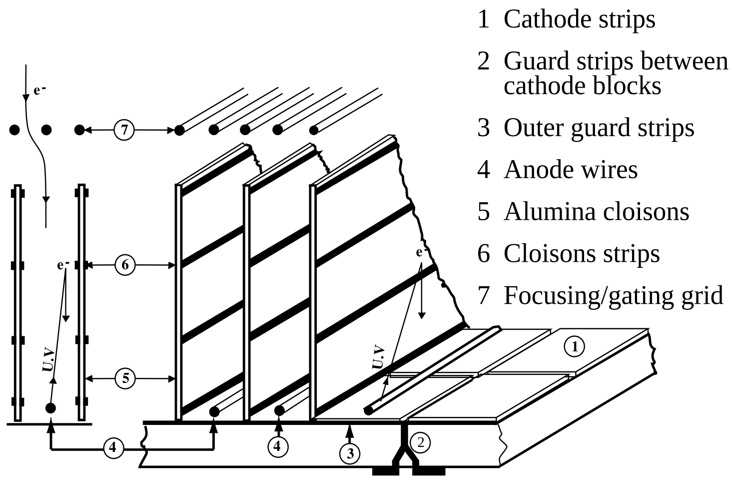

Figure 5.7: The Barrel RICH Multi Wire Proportional Chamber (MWPC)

installed to absorb UV-photons originating from the primary avalanche. This effect, called 'photon-feedback', causes secondary avalanches and increases the single point resolution. For the 48 MWPCs, a total number of 12 288 signal channels are read out by fastbus electronics: the signals are discriminated and recorded by time digitisers ($\sim$120 MHz clock frequency).

- *A mid-wall mirror.* Small mirrors are mounted on the mid-wall between the liquid radiator and the drift tube. The Cherenkov light of tracks passing the liquid radiator close to $\theta = 90°$, which would normally be absorbed, is reflected into the drift tube.

- *A UV-calibration-system.* A support structure holding 45 precisely located quartz fibres is mounted on the mirror side of most drift tubes to measure the drift velocity of electrons. Five rows of 9 fibres are positioned at different distances to the MWPC. The fibres guide light from a UV-lamp –focused by a small lens– onto the drift tube. The UV-lamp is pulsed when the DELPHI system triggered a forward-backward Bhabha scattering event and thus no tracks are expected in the barrel region. The support structure is also equipped with a system similar to the strips on the drift tubes, connected to the VHV (see fig. 5.6).

5.3 The Forward RICH

The Forward RICH [47] consists of two end-cap detectors, covering polar angles between $15° < \theta < 35°$ and $145° < \theta < 165°$. The FRICH and the BRICH are different in geometry (fig. 5.4), but employ the same principle. The main differences of the FRICH compared to the BRICH will be discussed in this section.

In each end-cap, the FRICH consists of 12 units each of which containing a drift box with 2 MWPCs and a calibration system, 3 liquid radiators and a gas radiator with 5 parabolic mirrors. Instead of C_5F_{12}, the FRICH uses C_4F_{10} as a radiator gas (4 m^3 per end-cap). A small disadvantage of C_4F_{10} with respect to C_5F_{12} is its lower refractive index (table 5.1) causing the threshold values for identification to be higher. However, using C_4F_{10}, with a boiling temperature of -2°C, the FRICH does not need to be heated but can be operated at ambient temperature (∼32°C) and atmospheric pressure. An important advantage for physics is the fact that the C_4F_{10} UV-transparency for photon-energies between 7 eV and 8 eV is approximately 100%. The drift gas is pure ethane which is bubbled through a 25°C TMAE bath. The MWPCs are equipped with a double layer of UV-blinds to reduce photon-feedback. The total number of readout channels per end-cap is 13 440. A fundamental difference with UV-photon detector of the BRICH is the fact that the electric drift field is not parallel to the DELPHI magnetic field. The photo-electrons drift with a Lorentz-angle of 52° and will always approach the MWPC under with angle unequal to 90°. The liquid radiator consists of three separated trays, each with an optimal position with respect to the interaction point. A total volume of 36 l C_6F_{14} is needed per end-cap.

5.4 Monitoring and Control

To achieve good data quality and adequate data processings, stable operation of the different sub-systems and monitoring of the relevant detector parameters is very important. Safety and stability during data taking is maintained by computerised control and monitoring features of the numerous RICH sub-systems. Rapid feedback is achieved by having the control systems interlinked via the DELPHI Online-Cluster which also gives access to the DELPHI database. The monitoring and control of the different RICH sub-systems is summarised in table 5.2.

On the BRICH an extended computerised heating system uses about 400 sensors to monitor and regulate the mean detector temperature of 40°C to ±0.3°C. No heating control is needed on the FRICH since it is operated at the ambient DELPHI temperature. However the temperature is monitored and stored on database. Special heating control maintains the TMAE bubbler temperature within ±0.1°C.
An elaborate system controls and monitors the drift gas of the photon detectors. Before the drift gases are saturated with TMAE, oxygen and water are removed. Water is a very strong UV-absorber and is monitored to be lower than 5 ppm. Oxidised TMAE

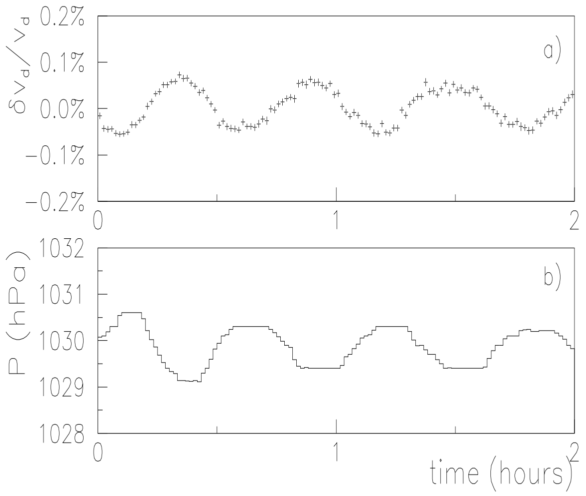

Figure 5.8: The BRICH relative change in drift velocity in time (a) compared to the pressure regulation (b) in time.

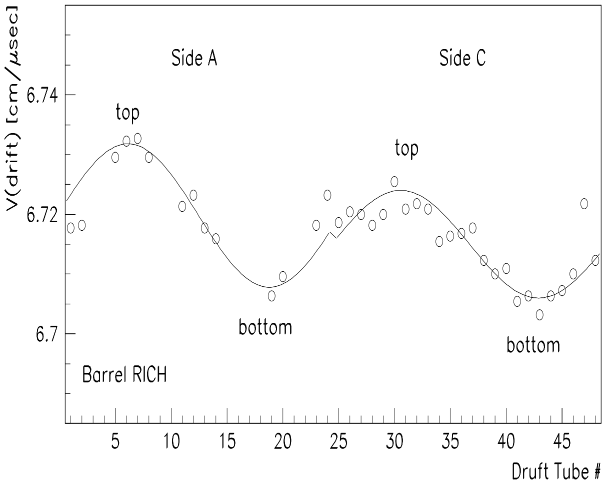

Figure 5.9: The BRICH drift velocity versus the drift tube number in each half of the BRICH. The top-bottom fluctuations can be explained by a temperature difference of about 1.5°C.

products are very electro-negative and will cause severe losses of photo-electrons. The oxygen content of the drift gas is kept well below 1 ppm.

The UV-calibration system monitors the single electron drift velocity. The maximum drift distance is 150 cm in the BRICH and 45 cm in the FRICH. In the BRICH the drift velocity is determined with an accuracy of ∼0.05% [48]. It is therefore possible to observe slight fluctuations of ∼0.06% in the drift velocity due to variations of ∼1.5 mbar in the pressure control as is illustrated in figure 5.8. Also the effect of ∼1.5°C temperature difference between the top and the bottom part of the BRICH can be observed by a change in the drift velocity as is shown in figure 5.9.

	Barrel RICH		*Forward* RICH	
	Computer Control	Online Monitoring	Computer Control	Online Monitoring
Gas radiator pressure	continuously	continuously	continuously	continuously
Liquid radiator pressure	continuously	continuously	continuously	continuously
Drift gas pressure	continuously	continuously	continuously	continuously
Temperature	continuously	continuously	ambient	continuously
Drift velocity (and $\theta^{\mathrm{Frich}}_{\mathrm{Lorentz}}$)		continuously		regularly
Electron life time		continuously		regularly
VHV status		continuously		continuously
MWPC HV (trips/status)	auto-recover	continuously	auto-recover	continuously
Refractive index CF-gas		optional		optional
UV transparency C_4F_{10}				weekly
UV transparency C_5F_{12}		weekly		
UV transparency C_6F_{14}		weekly		weekly

Table 5.2: The monitoring and control of the parameters of the DELPHI RICHes.

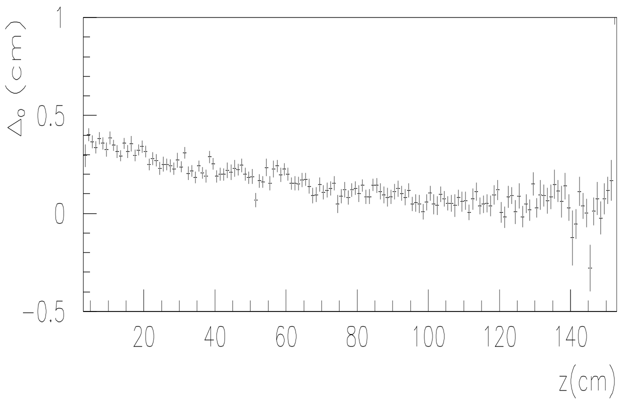

Figure 5.10: A typical distribution of the relative track position $\Delta_0 = Z_{\mathrm{RICH}} - Z_{\mathrm{TPC}}$.

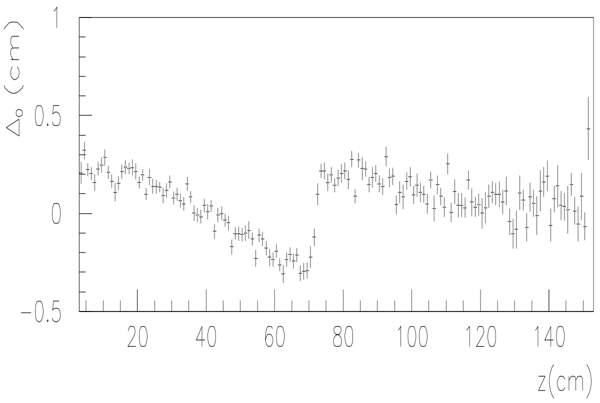

Figure 5.11: $\Delta_0 = Z_{\mathrm{RICH}} - Z_{\mathrm{TPC}}$ for a drift tube with a short circuit at $z = 72$ cm.

The FRICH UV-calibration is performed before or after a LEP-physics run. Lorentz angle and drift velocity are parametrised as a function of pressure and temperature. In this way a precision in the drift velocity of $\sim 0.1\%$ is achieved.

Sample lines from the gas radiator systems are connected to sonar-based devices which monitor the sound velocity in the radiator gases. A change in the composition of the gases will give a change in the sound velocity measurement.

The VHV for the drift field of the photon detectors and the HV of the MWPCs are constantly monitored. Occasionally a MWPC might draw too high a current and will trip. The MWPC is automatically ramped up to operational voltages again and the incident is recorded on the database.

The RICH monochromator systems and the surveillance of the UV-transmission of the RICH-fluids will be discussed below.

A Fabry-Pérot interferometer has been installed to perform measurements of the refractive indices of the gaseous radiator fluids [49].

Monitoring on the electronics readout chain is performed online by the DELPHI QC.

An example of offline monitoring is the measurement of the exact location of a short-circuit between two metallic strips on a drift tube, which disturbs the homogeneous electric drift field. Figure 5.10 shows a typical distribution for the relative difference Δ_0 versus the drift distance in the BRICH, where Δ_0 is defined as the relative difference between the z-coordinate of a passing track measured by the BRICH and the TPC ($\Delta_0 = Z_{\mathrm{RICH}} - Z_{\mathrm{TPC}}$). Figure 5.11 shows the same distribution for a drift tube which has developed a short circuit at $z = 72$ cm. This information is taken into account during data-processing.

5.5 The RICH UV-Monochromator Systems

The UV-transparency of the different RICH Cherenkov fluids is frequently monitored by online stand-alone monochromator systems.

The simultaneous determination of the UV-transparency of different samples is based on the measurement of UV-photon transmission rates by means of photo-multipliers and sample cells of variable depth. UV-light from a deuterium lamp is selected by a monochromator and sent via a beam splitter into sample cells of short depth d_S. The sample cells have two quartz windows. Photo-multipliers (PM) measure a UV-photon rate R_S which is equivalent to equation 5.8(a), where R_0 is the initial photon rate. A scan of up to 150 different wavelengths between 160 and 220 nm can be performed i.e. in minimum steps of 0.4 nm. Then, the cells are moved to a long depth d_L and the scan sequence is repeated (eq. 5.8(b)). Finally, the absorption constant k_λ can be obtained according to equation 5.9. Once k_λ is known, one can calculate the transmission $T(\lambda)$ for any desired depth d (i.e. thickness) according to $T_d(\lambda) = e^{-k_\lambda \cdot d}$ $(= R_d/R_0)$.

$$R_S(\lambda) = R_0(\lambda) \cdot e^{-k_\lambda \cdot d_S} \quad \text{(a)} \qquad , \qquad R_L(\lambda) = R_0(\lambda) \cdot e^{-k_\lambda \cdot d_L} \quad \text{(b)} \tag{5.8}$$

$$k_\lambda = \frac{1}{\Delta d} \cdot \ln \frac{R_S}{R_L}(\lambda) \qquad \wedge \qquad \Delta d = d_L - d_S \tag{5.9}$$

$$\text{Transmission Quality reference} \quad : \quad \mathrm{Q}^T \equiv \int_{1600}^{2200} T \; d\lambda \; [\text{Å}] \tag{5.10}$$

The transmission integrated over the measured wavelength range may be taken as a quality reference for the DELPHI RICH radiator fluids (eq. 5.10). Thus for the spectral range from 1600Å to 2200Å, a 100% transparent sample would lead to Q^T=600Å. For CF-liquids, integral values $\mathrm{Q}^T > 400$Å may be taken as an indication of good quality. High quality CF-gases should be measured to have values $\mathrm{Q}^T > 520$Å. The integrated transmission folded with the TMAE quantum efficiency ($\mathrm{Q}^T_{eff} \equiv \int_{1600}^{2200} T \cdot \mathrm{Q}^{\mathrm{TMAE}}_{eff} \; d\lambda$ [Å])[3] gives an indication of the photo-electron yield in the photon detector. Therefore, the larger the value Q^T_{eff} , the more photo-electrons one expects to detect, leading to a smaller Cherenkov angle resolution and thus a better particle separation.

The monochromator prototype-design (1989 [50]) for the BRICH consisted of three sample cells. In the beginning of 1991, the system was redesigned including a fourth cell. The prototype was accordingly upgraded and the production of two new systems for the FRICH was started. The schematic layout of a rack containing the FRICH monochromator system is shown in figure 5.12. The upgraded prototype system is connected to the BRICH (the main difference between the BRICH- and FRICH-monochromator systems is that the FRICH-system can be heated centrally whereas for the BRICH-system the cells are heated individually by heating tapes). Each monochromator system consists of four cells which are made of stainless steel bellows to allow changing the depth, two cells for Cherenkov fluids (liquid/gas) and two cells for the photon-detector gases (with/without

[3]The transmission quality values Q^T and Q^T_{eff} are often expressed without their units ([Å]).

TMAE). The transparency is measured for CF-liquid samples of $\Delta d = 1$ cm at 25°C, for CF-gas samples of $\Delta d = 15$ cm at 40°C (BRICH) or at ambient temperature (FRICH). Multiple sample lines (e.g. see fig. 5.19, page 51) allow to extract samples from different parts of the fluid-systems e.g. before/after filtering or at the input/output of the detector. Drift gases are only extracted from the BRICH. Drift gas samples without TMAE ($\Delta d = 15$ cm at 25°C) can be extracted before/after filtering and before it entering the liquid-TMAE bubblers. The TMAE loaded drift gas samples ($\Delta d = 1.5$ cm at 40°C) are mainly measured before entering in the BRICH and at each output of a pair of drift tubes.

The monochromator[4] uses a concave holographic grid as its single reflecting surface and is steered by a 24 V 5-phase stepping motor. The depth of the sample-cells is changed by synchro-motors[5]. The photo-multipliers[6] are treated with wavelength-shifter. The photon rates are counted in 1000 ms time intervals by a 100 MHz rate-meter[7].

The flow of gases or liquids through the cells (via passive flow-meters) is controlled by electro-valve switching. Four different flow-modes can be set i.e. 'Standby', 'Measure', 'Purge' and 'Automatic'. When the system is not in operation ('Standby') it is being flushed permanently with argon. The 'Standby'-mode is also used to verify the stability of the systems. Since argon does not absorb UV-light in the RICH photon detection range, an argon transmission measurement should result in a 100% UV-transparency. To start a sample flow the electro-valve switching is set to 'Measure'-mode. At the end of the measurement one can switch to 'Purge'-mode. The 'Automatic'-mode, giving the option to steer the switching via software, is not actively used.

Standard CF-transmission measurements are performed at atmospheric pressure, covering a photon detection range from 160 nm to 220 nm. A measurement typically takes about 50 minutes, of which 30 minutes are reserved to stabilise the deuterium lamp[8] (i.e. R_0 in eq.5.8). In the same time the cells are being flushed with samples to purge the argon, which is normally in the system if not in operation. Approximately 10 minutes is needed per scan. The complete measurement procedure is controlled by G-64 micro-processor logic.

The software consists of two programmes, one to start (or stop) a measurement and one for online analysis of the data. Both programmes run on the DELPHI Online-Cluster. The start programme consists of a menu which enables reading and writing information to G-64 by Ethernet-communication. From the menu one can select the starting point of the measurement (default at 160 nm), the end point (default at 220 nm) and the step-size (default 2.4 nm). Automatic book-keeping is performed at any time when information is either received or written to one of the G-64s. The start-menu offers an additional option to add extra information of the measurement to the log-files (kind of samples etc.). When a measurement is finished, the resulting data-file can be read

[4]Minuteman Model 302-VM.
[5]Berger: Stepping motor RDM-564/50, synchro-motor RSM-68/3-47/8.
[6]EMI 9884B.
[7]Lecroy, NIM Model 4604.
[8]Hamamatsu 30W L1626.

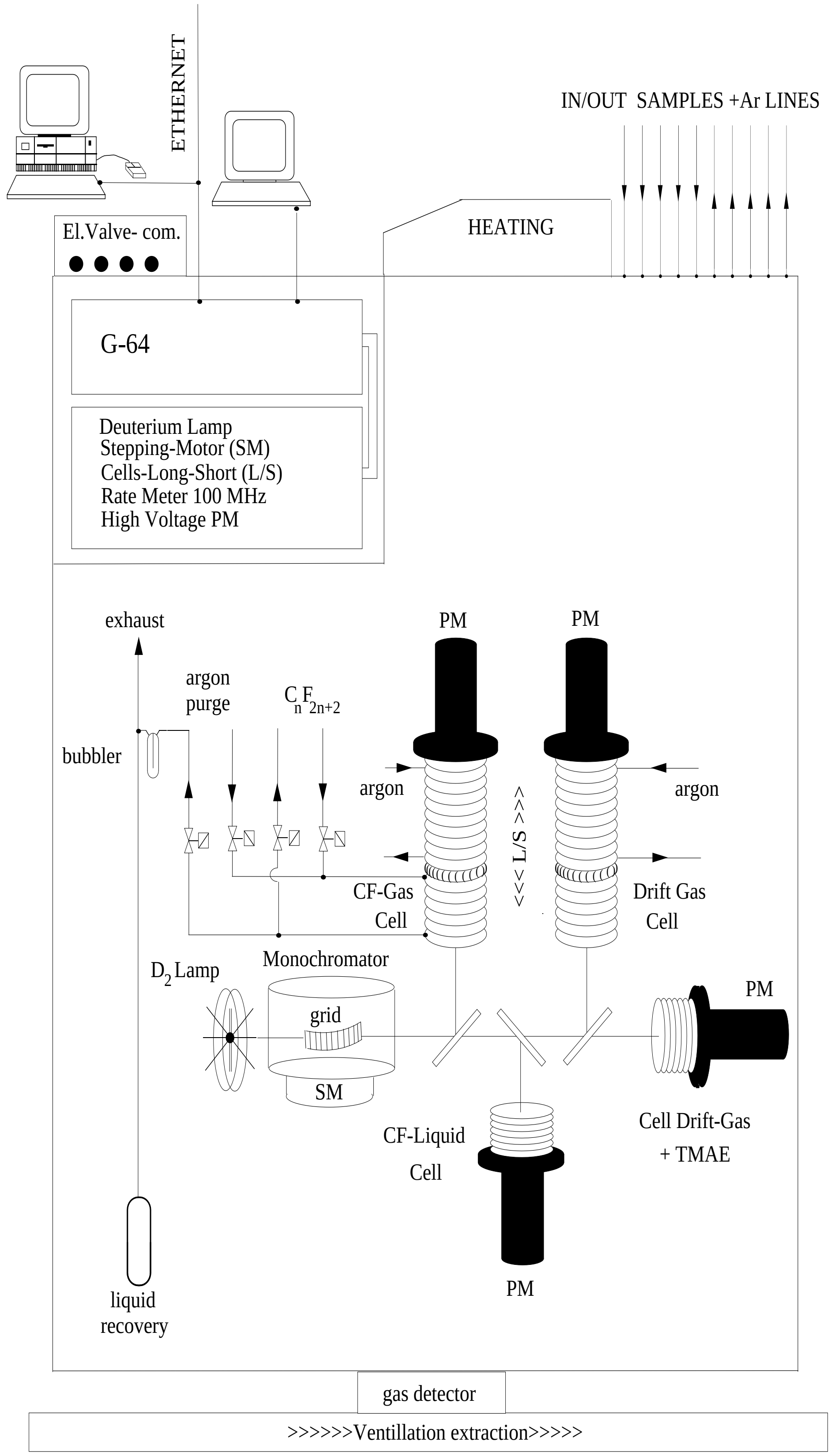

Figure 5.12: A schematic side-view of the FRICH UV-monochromator rack.

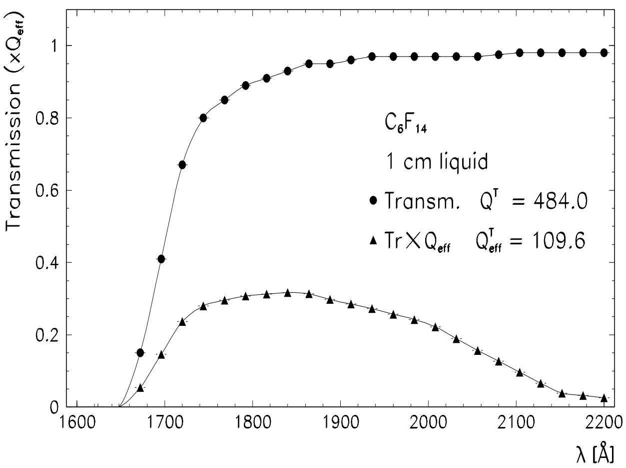

Figure 5.13:
The UV-transmission for liquid C_6F_{14}.

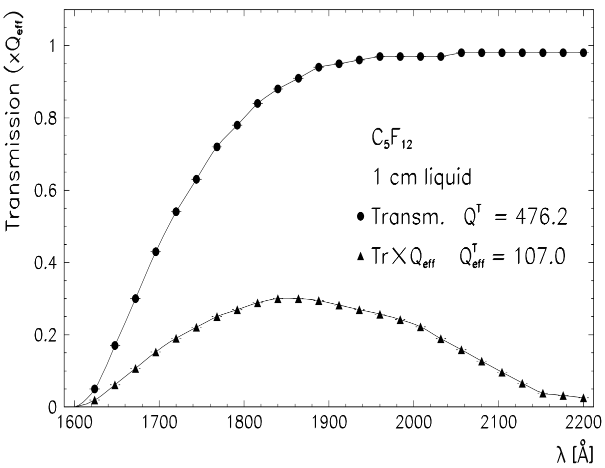

Figure 5.14:
The UV-transmission for liquid C_5F_{12}.

from the G-64 memory and is automatically stored on the DELPHI Online-Cluster for further analysis.

The analysis programme offers a wide range of options for online calculations (e.g. Q^T), graphics display of transmissions and absorptions, listing or printing results and for updating the RICH-data-base. The online calculation automatically accounts for the PM noise counts, electronics dead-time etc. and offers a menu with analysis requirements such as the ratio signal to background of the PM's and options to normalise a measurement on the results obtained from 100% transparent argon samples. Additional options are available to compare different measurements and to estimate the contamination of water and oxygen in the samples.

5.5.1 UV-Transparency of C_6F_{14}

A UV-transmission measurement of a high quality C_6F_{14} sample is shown in figure 5.13. The integral value is Q^T=484Å. High quality C_6F_{14} typically starts transmitting around 1650Å, showing a fairly steep rising slope ($T_{1800} \approx 85\%$) and reaching 100% transmission around 1950Å. Under normal operation the slope is slightly less steep for the BRICH liquid ($T_{1800} \approx 75\%$), which still leads to a good quality $Q^T \sim$430Å. This is mainly due to the fact that one has to maintain a rather large system of C_6F_{14} in the BRICH (240 l). For the same reason the FRICH values usually are slightly higher ($Q^T \approx$440Å).

For high quality C_6F_{14} samples, the value $Q^T_{eff} \approx 110$Å. For the bulk volume of the BRICH Q^T_{eff} is just below 100Å, which is equivalent to an average number of $\sim$13 detected photons for saturated Cherenkov rings. This makes C_6F_{14} an excellent radiator medium for RICH applications.

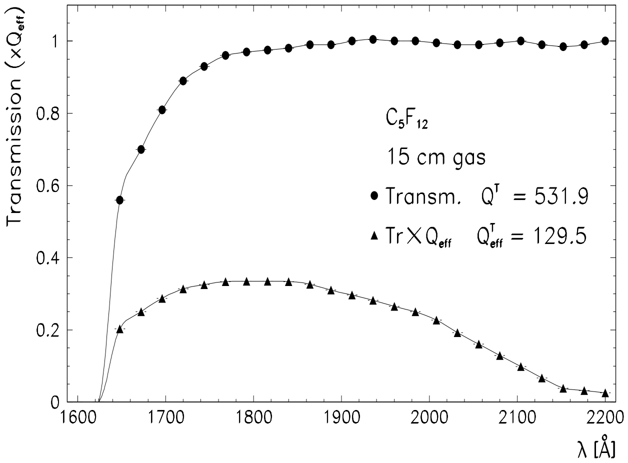

Figure 5.15:
The UV-transmission for gaseous C_5F_{12}.

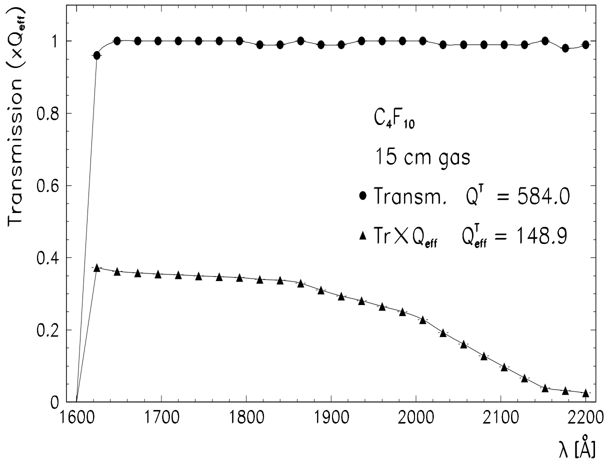

Figure 5.16: The UV-transmission for gaseous C_4F_{10} (Quartz window cut-off at 1600Å).

5.5.2 UV-Transparency of C_5F_{12}

Figure 5.14 shows a transmission measurement of C_5F_{12} in liquid form. C_5F_{12} clearly starts transmitting at shorter wavelength i.e. at 1610Å. Another characteristic difference between C_6F_{14} and liquid C_5F_{12} is the difference in the rising slope, which is lower for C_5F_{12} ($T_{1800} \approx 80\%$). From the quality value $Q^T_{eff} =$107Å one can conclude that one would expect more or less the same amount of detected photons if one were to use C_5F_{12} as liquid radiator medium instead of C_6F_{14} (assuming equal refractive indices).

A typical UV-transmission measurement of 15 cm C_5F_{12}-vapour (at 40°C) before it enters the gas radiator, is shown in figure 5.15. Gaseous C_5F_{12} becomes transparent at ∼1620Å and $T_{1800} = 100\%$. A quality value $Q^T_{eff} = 130$ corresponds to an average of about 8 detected photons for saturated Cherenkov rings in the Brich gas radiator.

5.5.3 UV-Transparency of C_4F_{10}

The UV-transmission of the C_4F_{10} radiator gas of the Frich is only measured in gas-phase. C_4F_{10} has a boiling point of −2°C (see table 5.1) and the monochromator systems are not designed to operate at such low temperatures. The excellent UV-transmission of gaseous C_4F_{10} with a $Q^T = 584$Å is shown in figure 5.16. The transmission measurement is limited at short wavelength by the cut-off of the quartz windows of the monochromator cell around 1600Å.

C_4F_{10} shows a better UV-transmission than C_5F_{12}, but it has a smaller refractive index. Compared to the 42 cm thick C_5F_{12} gas radiator of the Brich, the better UV-transmission of C_4F_{10} and the 58 cm thick gas radiator of the Frich compensate for the lower refractive index. Therefore, the number of photons to be detected in the Frich is of the same order as for the Brich gas radiator.

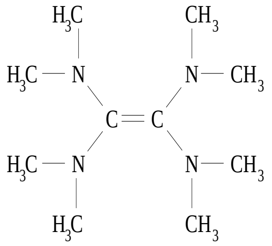

Figure 5.17: The chemical structure of TMAE ($C_2[N(CH_3)_2]_4$).

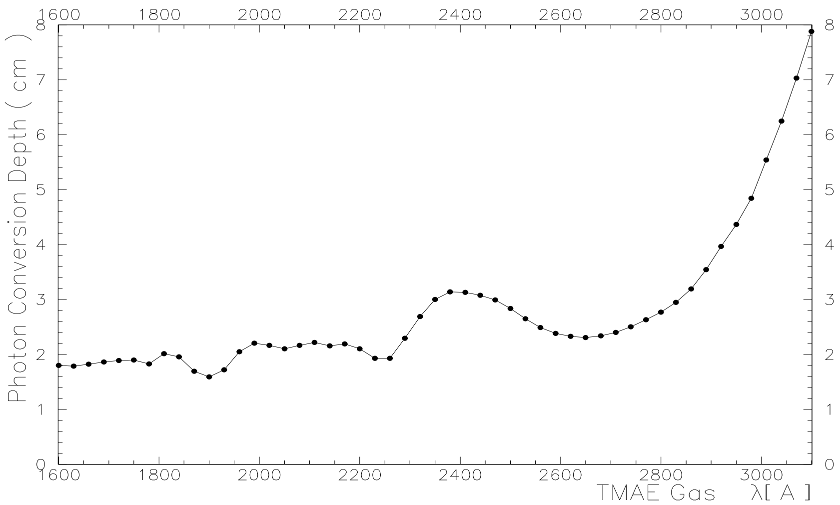

Figure 5.18: The UV-photon conversion depth of saturated TMAE-vapour at 28°C and atmospheric pressure.

5.5.4 Photon Conversion in TMAE-Loaded Drift Gas

The chemical structure of TMAE is shown in figure 5.17. TMAE is known for its low ionisation potential of ∼5.5 eV. TMAE has a freezing point of −4°C and a boiling point of 177°C, thus it is a liquid at room temperature. The maximum concentration of TMAE which can be obtained in the drift gas is equivalent to the ratio of the TMAE vapour pressure to the absolute pressure of the drift gas in the bubbler (at 28°C).

The monochromator systems offer the possibility to measure the photon conversion depth ($d_\lambda^{\rm conv.} = 1/k_\lambda$) of the TMAE-loaded drift gas at atmospheric pressure and enable monitoring of relative changes during the BRICH operation. Figure 5.18 shows the photon conversion depth in cm versus wavelength for the BRICH 28°C saturated TMAE-vapour in the methane-ethane drift gas mixture [51].

From the measurement at atmospheric pressure the mean photon conversion depth over the RICH photon detection range[9] from 1600Å to 2200Å is $\overline{d^{\rm conv.}} = 19.7$ mm. This is equivalent to $\overline{d^{\rm conv.}} \approx 18.5$ mm for the BRICH pressure of 1030 mbar. For the average Cherenkov photon wavelength in the BRICH (∼1900Å) the mean photon conversion depth is about 14.8 mm (at 1030 mbar).

With a relatively short photon conversion depth, photons originating from the liquid radiator will be detected mainly at one side of the drift tube, whereas photons from gas radiator mostly will be detected on the opposite side (see fig. 5.2). Test-measurements performed on samples obtained from different temperatures of the TMAE-bubbler (16°C, 20°C, 24°C and 28°C) have shown that $\overline{d^{\rm conv.}}$ changes by ∼8%°C^{-1} [52].

[9] The fact that Cherenkov photon production is proportional to $1/\lambda$ is not taken into account.

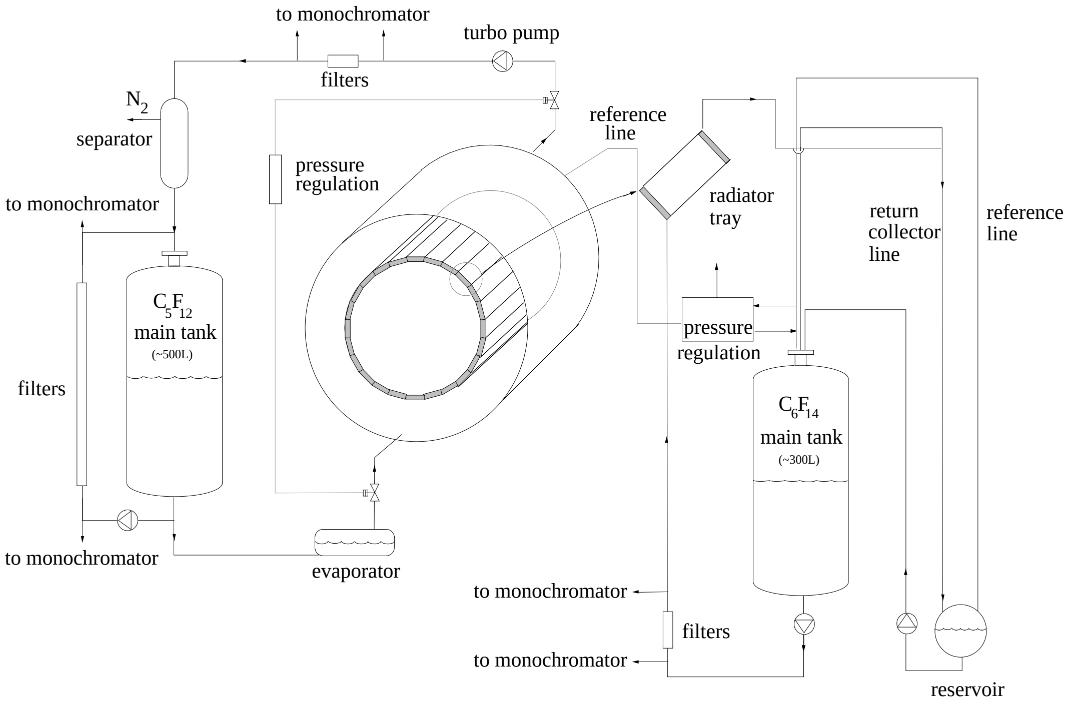

Figure 5.19: The BRICH Cherenkov radiator systems.

5.6 Operational Experiences

To enable an efficient and powerful particle identification for physics analyses, it is of vital importance to have the RICH detectors operational in stable conditions with Cherenkov fluids of optimal quality. As has been mentioned before, with the DELPHI RICH detectors one has to deal with fairly large quantities of these fluids. A schematic impression of the BRICH systems which handle these fluids is shown in figure 5.19. In this section some experiences with Cherenkov fluids and the BRICH commissioning procedures will be discussed.

5.6.1 Treatment of the RICH Cherenkov Fluids

The BRICH monochromator system is also connected to a small circulation system (i.e. filter-system) which allows tests on the UV-transparency of small samples (< 7 l) of CF-liquids. This test setup is used to examine the quality of samples of raw-products as they are delivered by the producers[10]. The raw products normally contain a large amount of oxygen and water, both of which strongly absorb UV-light below ∼190 nm. Figure 5.20 shows an example of the UV-transmission-curve for a raw C_6F_{14} sample. The rather poor quality is indicated by $Q^T = 203.8$Å. However, the quality improves considerably after oxygen and water have been filtered out by means of recirculation

[10] in recent years C_4F_{10}, C_5F_{12} and C_6F_{14} have been purchased from 3M, St.Paul, MN 55144, USA.

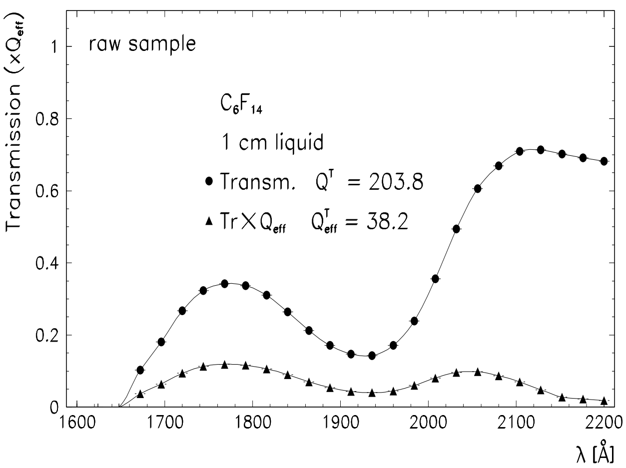

Figure 5.20: The UV-transmission for a raw sample C_6F_{14}.

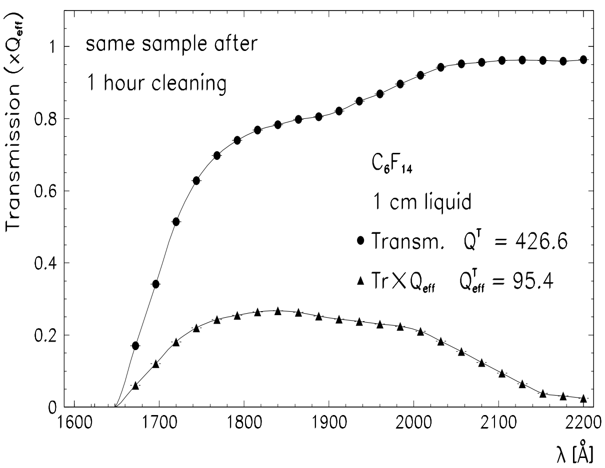

Figure 5.21: The UV-transmission for C_6F_{14} after 1 hour cleaning with OXISORB.

(∼1 hour) through a small OXISORB[11] filter. The UV-transmission curve after this cleaning procedure, shown in figure 5.21, yields an Q^Tvalue of 426.2Å. When a test-sample proves to be of good quality after cleaning, the total batch is inserted into the main tank and internally recirculated through Molecular Sieve[12] (MS) filters. The cleaning of a bulk volume of CF-liquids may take a few days up to a fortnight, depending on the initial quality and the recirculation flow rate. The improvement of the bulk quality is monitored by the monochromator system. When at a certain stage the transmission integral-value no longer increases, the MS-filter is exchanged. Hence, the monochromator systems are also a useful tool to verify the cleaning efficiency of the filters.

MS-filters are not as efficient as OXISORB-filters because they primarily clean out water (by adhesion) and to a lesser extent oxygen. However, a MS-cartridge is low in price and can be regenerated whereas an OXISORB cartridge (cleaning water *and* oxygen) is quite expensive for bulk applications and can be used only once. Regeneration is performed by inserting up to four cartridges in parallel in an oven in which they are heated to ∼200°C whilst being purged with nitrogen. The water content in the exhaust gas is constantly monitored by a water-meter. To account for the oxygen cleaning, one has the availability of oxygen filters in the form of dispersed copper[13] (DC) which can also be regenerated. Activated copper can chemically bind oxygen ($2Cu + O_2 \rightarrow 2CuO$). Its regeneration can be achieved by flushing an admixture of argon and hydrogen (7%) at ∼200°C ($CuO + H_2 \rightarrow Cu + H_2O$) through the cartridge, again monitoring the water content in the exit gas [53]. In chemistry, dispersed copper is known as a catalyst. Up to 1992 DC-filters were used in series with MS-filters to clean the RICH Cherenkov fluids.

In 1992 severe losses in the UV-transmission of the C_6F_{14} were observed in the monochromator transmission measurements for liquids which had been recirculated through the MS/DC-filters. The measured liquids seemed completely degraded and the Q^T-value appeared to be far below acceptance level of 400Å. The comparison in

[11]Messer Griesheim Co., D-400 Düsseldorf, Germany.
[12]Chemische Fabrik Uetikon, Switzerland.
[13]Catalyst and Chemicals, Brussels, Belgium.

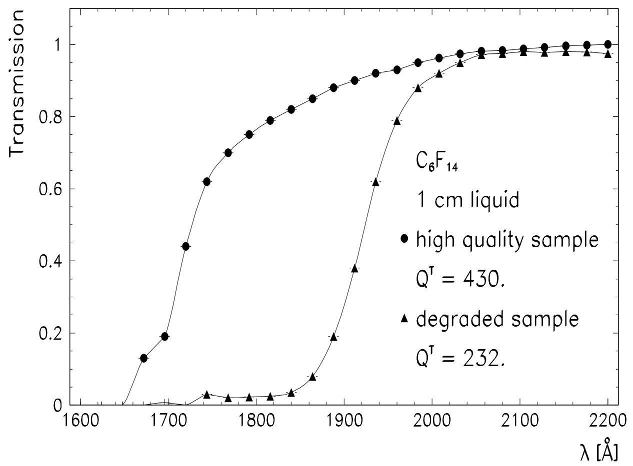

Figure 5.22: The UV-transmission curves for a high quality sample and for a degraded sample C_6F_{14}.

UV-transmission between a batch of good quality and a degraded batch is shown in figure 5.22. It was only by classical distillation of different samples that it became clear from the boiling temperatures and distillation ranges that the chemical composition of the raw samples was seriously different compared to the producers indications. The samples contained several C_nF_{2n+2}-compounds other than C_6F_{14}. Additionally, by UV-visible and infrared spectrometry, it could be shown that samples from some batches were contaminated with incompletely fluorinated molecules $(C_nH_xF_{2n+2-x})$ which can chemically react in the presence of a DC-catalyst and oxygen in the following way [53]:

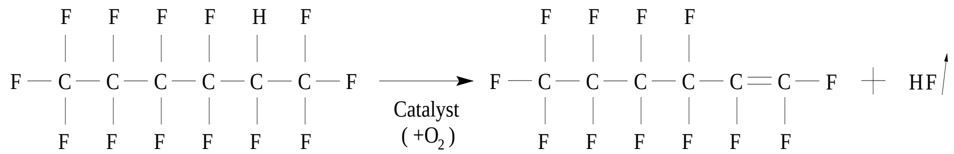

If a sample contains a large amount of oxygen, a freshly installed DC-cartridge may reach a very high temperature which favours the above reaction. The resulting double bonds between the carbon atoms absorb UV-light, causing the loss in UV-transmission. Furthermore, depending on the concentration of $C_nH_xF_{2n+2-x}$, by polymerisations 'oil-like' C_nF_{2n} (n may become large) can be produced:

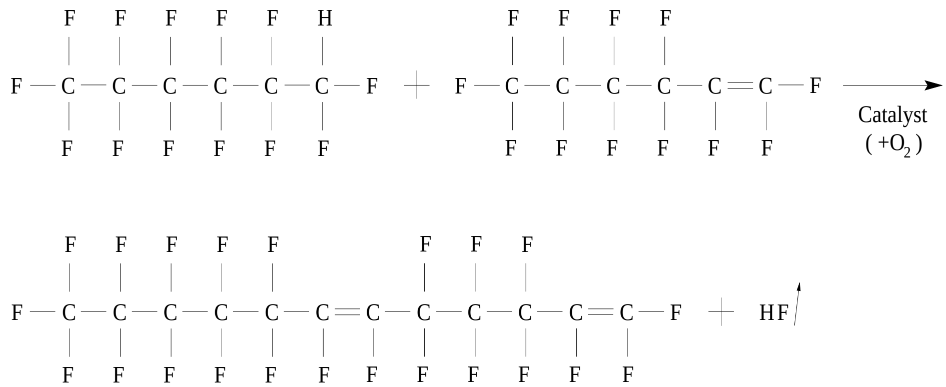

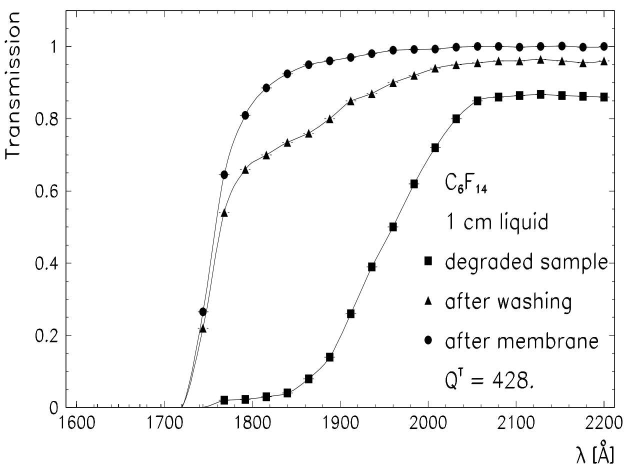

Figure 5.23: The UV-transmission curves for a degraded C_6F_{14} sample, after washing treatment and after membrane filtering.

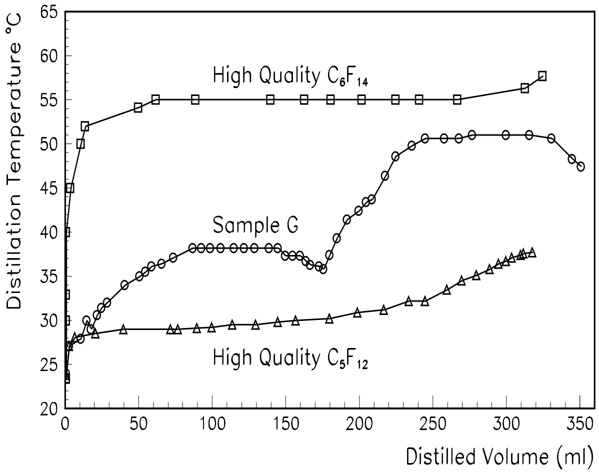

Figure 5.24: The fractional distillation curves for high quality C_5F_{12} and C_6F_{14} samples and for a CF-sample of unknown composition.

The degraded liquids were removed and the DC-filters were taken out of all the RICH fluid systems to safeguard the optimal operation of the detector and to avoid degrading the fluid quality. Although the HF-molecule which is produced during the catalyst reaction is known to be an aggressive gas, no evidence of damage was found on the performance of the detector. Other methods to clean oxygen from samples proved successful: applying capillary membranes [54], saturating CF-liquids with argon or nitrogen and ultrasonic degassing [55].

To confirm the catalyst reaction mechanism, a procedure to recover the degraded liquids was achieved by applying an ionic process, washing with manganese-oxide and using capillary membranes [53]. The results are illustrated in figure 5.23. The recovered liquid has an acceptable quality of $Q^T \approx 428$Å.

The results obtained from the distillations mentioned above not only proved a difference in the composition of liquid samples but also demonstrated the possibility to separate liquid mixtures (e.g. C_5F_{12}/C_6F_{14}). Figure 5.24 shows the fractional distillation curves for high quality C_5F_{12} and C_6F_{14} samples and for a sample of unknown composition. Fractional distillation can be applied only if the mixture is not azeotrope[14] and if it contains ingredients which have discrete boiling temperatures. An online C_5F_{12}/C_6F_{14}-separation plant was installed for the BRICH during the 1995 winter shut-down [56] to overcome instabilities in the refractive indices of both the BRICH liquid and gas radiators due to leaks between the systems inside the detector [57]. Small leaks in the liquid radiator system, which had developed throughout the years, reached a too high leak rate, endangering the safety and the stable operation of the detector. The online separation plant contains a 7.5 m high distillation column with a maximum capacity of 200 kg/h ($\approx$ 125 l/h). It can separate any C_5F_{12}/C_6F_{14}-mixture. The distilled CF-liquids have purities over 95%.

[14] azeotrope mixtures are characterised by a constant minimum or maximum boiling point which is lower or higher than that of any of the components.

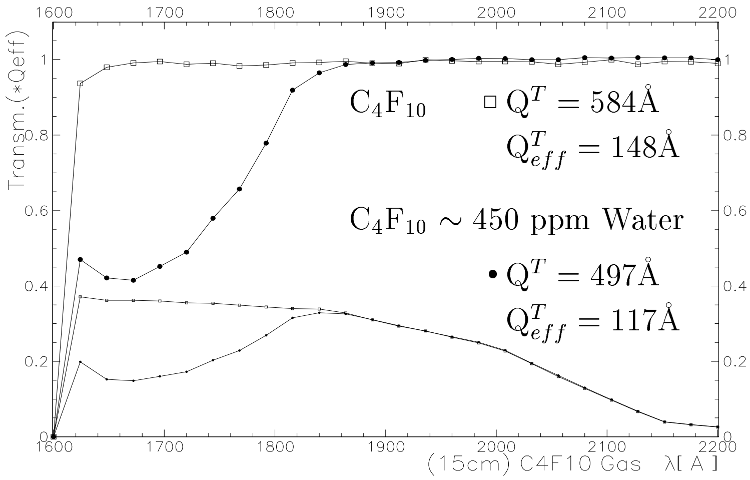

Figure 5.25: The UV-transmission for C_4F_{10} before start of 1994 physics run and after cleaning in gas-phase with MS-filters. The difference in transmission could be explained by a 450 ppm water contamination, estimated by the online monochromator analysis programme.

The treatment of C_4F_{10} for the FRICH gas radiator systems is illustrated by figure 5.25. Just before the start of the 1994 LEP-run the monochromator transmission measurements indicated a $\sim$20% loss in the quality Q^T_{eff} (thus $\sim$20% loss in the number of detected photo-electrons). Assuming only the presence of water –which has its maximum absorption at 1670Å– a contamination of $\sim$450 ppm water could be estimated with the online monochromator analysis programme. The expected high quality was retrieved after the gas was passed through MS-filters.

5.6.2 Barrel RICH Commissioning Procedures

During winter times, when the available power to operate the LEP collider is very expensive, the physics data-taking is stopped for about 4 months. These so called 'shut-down' periods are used for maintenance and operations on both the accelerators and the detectors of the different experiments.

The RICH detectors of the type used in DELPHI are fairly complex systems and can not simply be switched off in one action. Since one is dealing with large volumes in a quartz environment at temperatures and pressures above nominal, it is necessary to allow a long purge for the different fluid systems and a slow ramp-down of temperatures and pressures. Before one can obtain free access to the BRICH detector, the different subsystems and the interlock- and safety-systems between them have to be de-activated according to a specific procedure.

Ramp-down and start-up phases of the BRICH are potentially critical because most subsystems (e.g. heating, pressure, liquid and gas radiator, drift gas, VHV, etc.) –and thus the detector parameters– are changing to a large extent. For instance, one should not (de-) pressurise the gas radiator if the drift gas pressure control is not actively linked, risking to damage the quartz tubes; one should avoid testing the VHV to nominal voltages if the gas radiator is filled with nitrogen; the temperatures should be ramped slowly to avoid rapid increase of mechanical stress on the different detector elements.

```
--------------+-------------------+---------------------+--------------------+------------------------+------------------------+---
START_UP SCHEDULE DELPHI BARREL RICH                                                                        E.Schyns   31-Mar-95
--------------+-------------------+---------------------+--------------------+------------------------+------------------------+---
BRICH START_95 3/4   WEEK 14       10/4   WEEK 15        17/4   WEEK 16      24/4    WEEK 17           1/5    WEEK 18           8/5
--------------+-------------------+---------------------+--------------------+------------------------+------------------------+---
              +3   4   5   6  7   +10  11  12  13  14   +17  18  19  20  21  +24   25   26   27   28  +1    2    3    4    5   +8
Pit-Meetings  +        PM         +PM       PM      --  +--       PM      PM  +PM        PM        PM  +PM        PM        PM  +PM
              +                   +                     +                    +                        +                        +
              + side...C.....A    +                     +                    +                        +                        +
LEP/DELPHI    +DELPHI +  GSS  +---+          LEP   +---+--+ FLAMABLE         +                        +             ::::-------+---
              +closed ! alarm !NBI+         closed !EASTER! Gases            +    DELPHI-SOFT-WEEK    +             ::: PHYSICS
              +       + tests +---+                +---+--+ START SC-shifts  +                        +             ::::-------+---
              +                   +                     +                    +                        +                        +
Barrel        +TEST before +  OFF +START---->@40' READY +  READY     READY   + READY   READY   READY  + READY   READY   READY  +
HEATING       +closing A/C !      +                     +                    +                        +                        +
              +            +      +                     +                    +                        +                        +
RADIATOR      +Commissioning/ UV  +        C6F14 (300L) +   C5F12 (300L)     + READY   READY   READY  + READY   READY   READY  +
FLUIDS        +C5F12-C6F14 /Transm+         READY       +    READY           +                        +                        +
              +                   +                     +                    +                        +                        +
Rack HEATING  +   OFF         OFF +  OFF         OFF    +    START--->@40'   + READY   READY   READY  + READY   READY   READY  +
Polytubes     +                   +                     +                    +                        +                        +
              +                   +                     +                    +                        +                        +
GAS RADIATOR  + Barrel on N2 (system runs on testvolume)+        N2          +      pressure + P=1030+ READY   READY   READY  +
              +                   +                     +     @STANDBY       +        test   ! FILL  +                        +
              +                   +                     +                    +      dP=10mBar+ C5F12 +                        +
LIQ RADIATOR  +       N2          +  N2      START LEAK +        N2          +                        + FILL    READY   READY  +
              +                   +         TESTS @40'  +     @STANDBY       +      Follow dP         + C6F14                  +
              +                   +                     +                    +                        +                        +
DRIFT GAS     + N2/He (leak-tests)+        N2/He        +    N2  TESTS       +      Follow dP  START + START   READY   READY  +
SYSTEM        +                   +                     +        AUTOMAT.    +               gas MIX+ TMAE                   +
              +                   +                     +                    +                        +                        +
+-------------+                   +HEATING  LIQ.  DELPHI+                    +PRESSURES DRIFT/ GAS    + INTERLOCKS   +  ALL    +
INTERLOCKS/SC +      OFF          +         RAD.  WATER +                    +  (?)    GAS / RADIATOR+ ACTIVE       +  ON     +
+-------------+                   +         (SC)  COOL. +                    +                        +                        +
- - - - - - - + - - - - - - - - - +- - - - - - - - - - -+- - - - - - - - - - -+- - - - - - - - - - - - + - - - - - - - - - - - - -+- -
ONLINE         3/4                 10/4                  17/4                 24/4                     1/5
- - - - - - - + - - - - - - - - - +- - - - - - - - - - -+- - - - - - - - - - -+- - - - - - - - - - - - + - - - - - - - - - - - - -+- -
MWPC HIGH     + G64-CAEN-MWPC     +                     +      TESTS         +        @STANDBY        +    READY       READY  +
VOLTAGE       + control TESTS     +                     +                    +   (Cooling Preamps ON) +                        +
              +                   +                     +                    +                        +                        +
VHV           + TEST-RAMPup  OFF  +        OFF          +       OFF          +        @STANDBY        +    READY       READY  +
              + (few kV)          +                     +                    +                        +                        +
FASTBUS       +  ON  OFF  ON      +    TESTS (in LOCAL) + TESTS (in GLOBAL)  +        @STANDBY        +    READY       READY  +
              +                   +                     +       (partition)  +                        +                        +
CALIBRATION   +      OFF          +        OFF          +       OFF          +        @STANDBY        +    TEST        READY  +
              +                   +                     +                    +                        +                        +
WSDEBR et al. +(MORE MEMORY)      +                     +                    +                        +                        +
DAS           +(INSTALLED)        +    TESTS (in LOCAL) + TESTS (in GLOBAL)  +        @STANDBY        +                READY  +
              +                   +                     +                    +                        +                        +
Slow Control  +      OFF          +START    checks      +  double-checks.... +      re-checks         +  X-checks      READY  +
              +                   +HEATING              +                    +                        +                        +
Quality Check +      OFF          +        OFF          +      TESTS         +        @STANDBY        +                READY  +
              +                   +                     +                    +                        +                        +
ON CALL SHIFT +       NO          +         NO          +     @STANDBY       +        YES             +    YES         YES    +
--------------+-------------------+---------------------+--------------------+------------------------+------------------------+---
```

Figure 5.26: The BRICH 1995 start-up schedule.

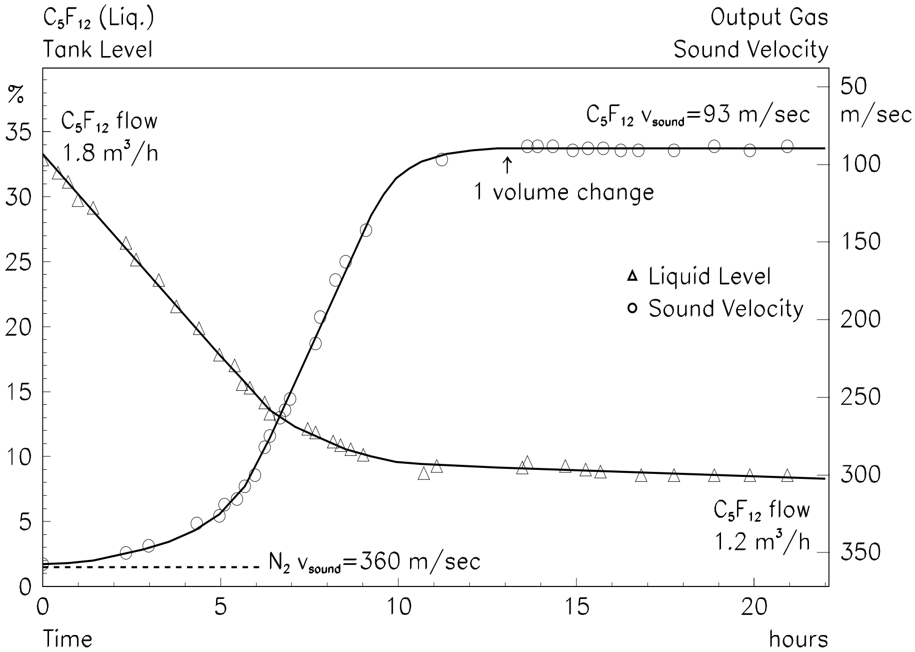

Figure 5.27: The monitoring of the filling of the BRICH gas radiator.

In the case of a detector start-up one first needs testing of the sub-systems, especially those which have undergone an intervention during the shut-down. As an example figure 5.26 shows the time-schedule and sequential procedures for the 1995 BRICH start-up. The tests mainly concern the detector leak tightness, the preparation of the Cherenkov fluids and the computer communication i.e. readout and safety interlocks, especially for sub-systems which happened to be (partly) dismantled or uncabled.

After having recorded ∼1.4 million Z^0 events during the 1994 LEP run, early December of the same year the BRICH was successfully ramped down for the winter shut-down and was according to schedule (figure 5.26) ready again on day one for the 1995 LEP physics data taking. The commissioning of the BRICH after a winter shut-down typically takes 4-5 weeks (preparation, tests and execution) of which about 3 weeks are reserved for preparations and tests. In terms of manpower, about 10 detector and computer experts need in total 20 to 25 man-weeks time.

An important point during the BRICH ramp-down and start-up periods is the monitoring of the changes caused by the (de-) activation of the sub-systems. The monitoring provides fast feedback during the process. Figure 5.27 for example illustrates the online surveillance of the filling of the BRICH gas radiator by a sonar-based device [50]. The instrument measures the sound-velocity in the exit gas of the radiator, which at the start is filled with nitrogen (right-hand axis, $V_{\mathrm{sound}} = 360$ m/s). The gaseous C_5F_{12} is introduced into the detector at the bottom, slowly pushing out the lighter nitrogen at the top. The left-hand axis of the figure shows the level of liquid C_5F_{12} in the main tank which is injected into the evaporator (see fig. 5.19, page 51). The filling of the BRICH gas radiator takes about 13 hours and can be completed during one volume exchange (24 m^3) [44].

Chapter 6

Particle Identification with the Barrel RICH

The RICH raw data undergo several processings (as indicated in section 4.5) and are evaluated by various algorithms before they can be properly used for physics with identified particles. In this section the offline handling of the RICH-data for particle identification and some aspects concerning the tuning of the RICH detector simulation will be discussed. Finally, a short overview will be given on the various ring-finding algorithms for RICH particle identification.

6.1 Raw Data Handling and Alignment

The monitoring and control information (see table 5.2) is read from the database during the data-processing. The database also contains the overall detector geometry as well as fixed detector survey information such as the reflectivity of the mirrors and the quartz UV transmission. In an early stage the raw data are calibrated and some corrections are applied (e.g. short-circuits, fig. 5.11). Furthermore, the data are treated (i.e. 'cleaned') by algorithms to reduce background, followed by an alignment procedure.

The RICH photon-detectors are designed to detect single photo-electrons and as such they are very sensitive to background. Cherenkov rings from the liquid radiator can cover up to 3 drift tubes and thus are much more affected by background than rings from the gas radiator which have a maximum diameter of $\sim$5 cm. Various sources of background are evaluated such as electronic noise, cross-talk, after-pulses, δ-rays, photon-feedback and ionisation electrons ($\mathrm{d}E/\mathrm{d}x$) caused by the tracks passing through the drift tubes. Most background appears in the form of clusters. Figure 6.1 illustrates a background-cluster in local R_ϕ. By removing these R_ϕ-clusters, which mainly occur for liquid rings, more than 50% of the background is rejected. Although the background in the RICHes is complicated, it has been successfully simulated in the Monte Carlo. The comparison between BRICH data and detector simulation for saturated liquid rings ($p > 6$ GeV/c) is shown in figure 6.2. The cleaning algorithms increase the signal to background ratio around the peak from S/Bg= 0.34 to S/Bg=1.5, rejecting only 15% of the true signal [58].

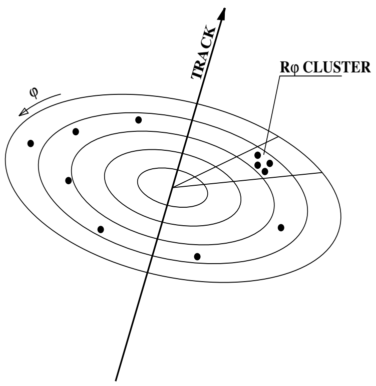

Figure 6.1: An illustration of a background R_ϕ-cluster.

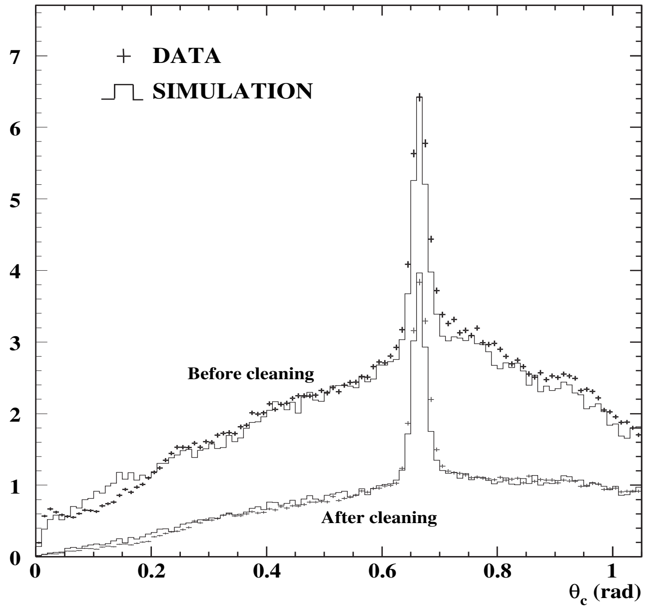

Figure 6.2: Comparison of BRICH data with Monte Carlo before and after cleaning of $\theta_{\check{c}}$ in the liquid radiator.

The RICH offline alignment is based on the adjustment of the refractive indices and the geometrical positions of the different components inside the detector. A software package called ERA [59] [60] has been developed to handle the position of the 456 mirrors, 120 radiator trays and 172 photon-detectors and which can simultaneously update the RICH geometry database. The spread of $\theta_{\check{c}}$-distributions is minimised using the 45.6 GeV/c tracks from $Z^0 \to \mu^+\mu^-$ events. These well isolated tracks are accompanied by a very low background and always produce saturated Cherenkov rings (eq. 5.4, page 35). The expected Cherenkov angle depends only on the refractive index whereas the measured angle also depends on the position of the elements. The significance of a good alignment is illustrated by figure 6.3, where in terms of $\theta_{\check{c}}$ a comparison is made between the aligned FRICH gas rings (i.e. aligned drift box and mirrors) and a forced 1 mm shift of the aligned drift box [61].

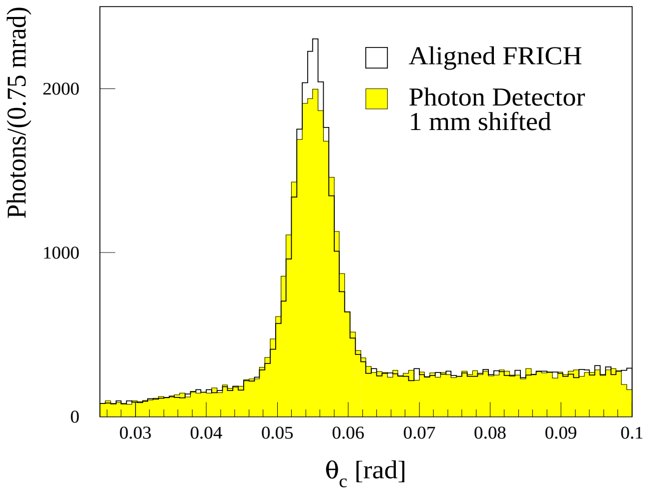

Figure 6.3: The FRICH Cherenkov angle distribution for $Z^0 \to \mu^+\mu^-$ in the gas radiator after alignment and after a forced shift of the drift box 1 mm away from the aligned position. A 1 mm shift is equivalent with a decrease of $\sim$10% in resolution.

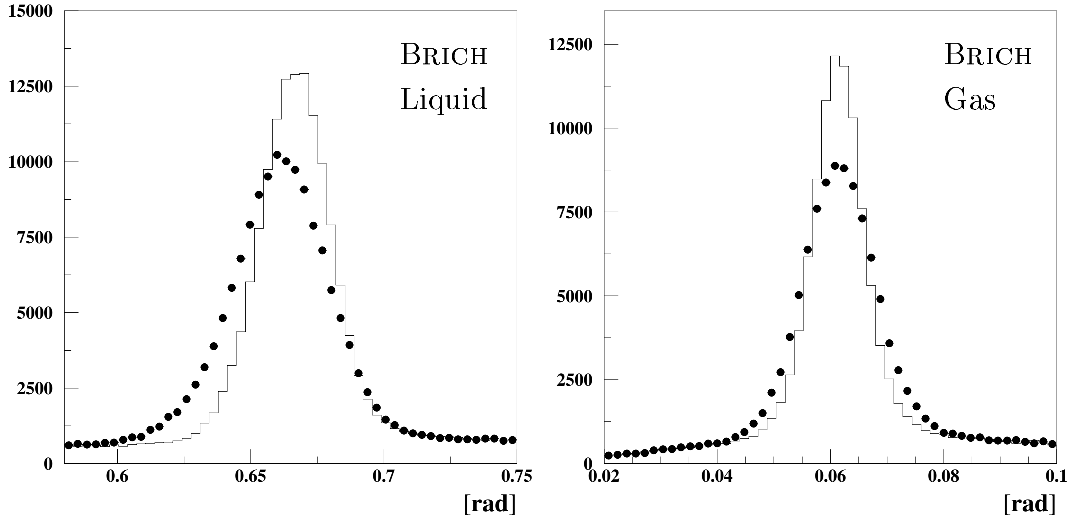

Figure 6.4: The BRICH Cherenkov angle for liquid and gas radiator, *before* (dots) and *after* (histogram) alignment.

Table 6.1: The resolutions for 1994 data and Monte Carlo after alignment obtained from $\sim 50\,000$ $Z^0 \rightarrow \mu^+\mu^-$ events [32][61].

(mrad)	*Barrel* RICH		*Forward* RICH	
	Liquid	Gas	Liquid	Gas
Data $\sigma_{\text{p.e.}}$	13.3	4.3	11.4	2.5
Simulation $\sigma_{\text{p.e.}}$	10.6	4.3	7.6	2.4
Data σ_{ring}	5.2	1.5	5.0	1.2

The improvements achieved by the BRICH alignment can clearly be seen in figure 6.4 for Cherenkov angle distributions of single photo-electrons measured from $Z^0 \rightarrow \mu^+\mu^-$. For the 1994 data and Monte Carlo the single photo-electron resolutions are enlisted in table 6.1. A standard test to verify whether the alignment has been successful is shown in figure 6.5 where the single photo-electron resolution is shown as a function of the 12 mirror sectors along R_z. The slope in the resolution which remains after the alignment is purely determined by the diffusion of the electrons depending on their long drift distance towards the MWPC.

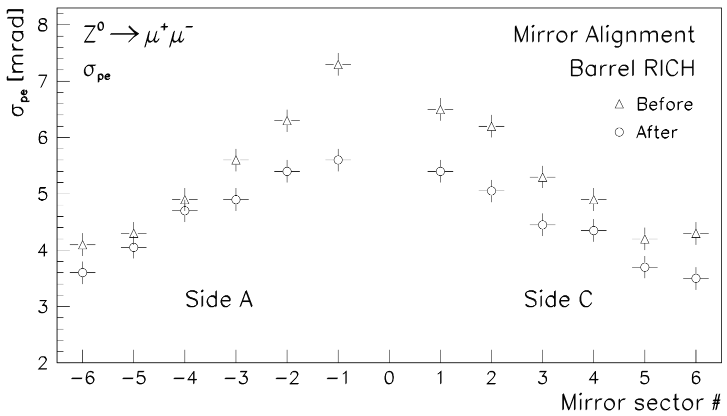

Figure 6.5: Single p.e. resolution versus mirror sector, before (triangles) and after (circles) the alignment. Mirror sectors ± 6 are closest to the MWPCs and mirror sector ± 1 are closest to the mid-wall.

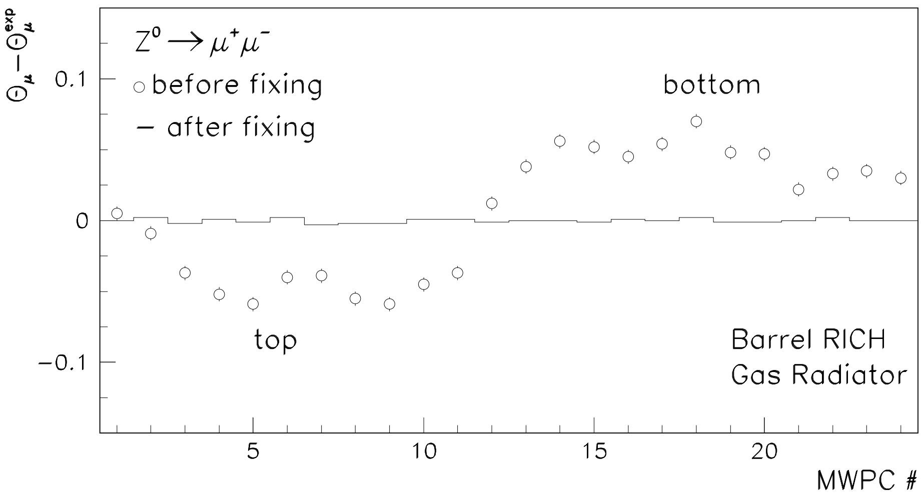

Figure 6.6: Due to the presence of C_6F_{14} vapour in the C_5F_{12} gas, the refractive index is larger at the bottom and smaller at the top in the BRICH gas radiator.

6.2 RICH Fixing

The results of the main processing are stored on DST (see fig. 4.10). For the production of the Short DST the RICH data undergo a second evaluation –commonly called 'RICH fixing'– which is performed by the RICFIX-package [62] (see section 4.5). The RICFIX package does the fine-tuning of the parameters which are important for the detector simulation. Additionally, several detector variations which have not been taken into account during the DST-production are included, both for data and Monte Carlo.

The corrections mostly depend on the polar angles of the tracks and mainly concern the detector acceptance, the refractive index (gas only), the expected Cherenkov angle resolution, the expected number of photo-electrons and photon-feedback caused by the $\mathrm{d}E/\mathrm{d}x$ of the tracks (discussed below). For the Monte Carlo fine-tuning, RICFIX performs random operations on the single photo-electrons (smearing, removing etc.) and includes photon-feedback for single photo-electrons (discussed below). Time dependent effects are simulated by systematic smearing of the rings.

The RICFIX-package obtains most of its information from $Z^0 \rightarrow \mu^+\mu^-$ events but applies corrections on all Z^0-data. For example, due to leaks (in 1994) between the BRICH liquid and the gas radiator systems (page 54), the gas radiator is not filled with pure C_5F_{12} but contains a certain amount of C_6F_{14} vapour, which has an influence on the refractive index of the gas. Since C_6F_{14} vapour is about 15% heavier than C_5F_{12} vapour, one can expect different refractive indices at the top and the bottom of the detector. This is illustrated in figure 6.6, which shows the distribution of $\theta_{\check{c}}^{\mathrm{meas.}} - \theta_{\mu}^{\mathrm{exp.}}$ for muons from $Z^0 \rightarrow \mu^+\mu^-$ versus the MWPC-chamber-number. This effect only occurs in the data and is corrected (i.e. the refractive index is fixed to a constant value) by RICFIX.

The di-muon events were also used to study the influence of photon-feedback. The

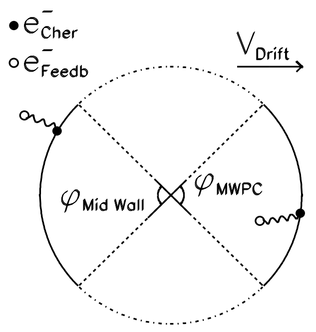

Figure 6.7: The feedback photons created during the avalanche multiplication in the MWPC, have a larger $\theta_{\check{c}}$ on one side and a smaller $\theta_{\check{c}}$ on the other side of the ring.

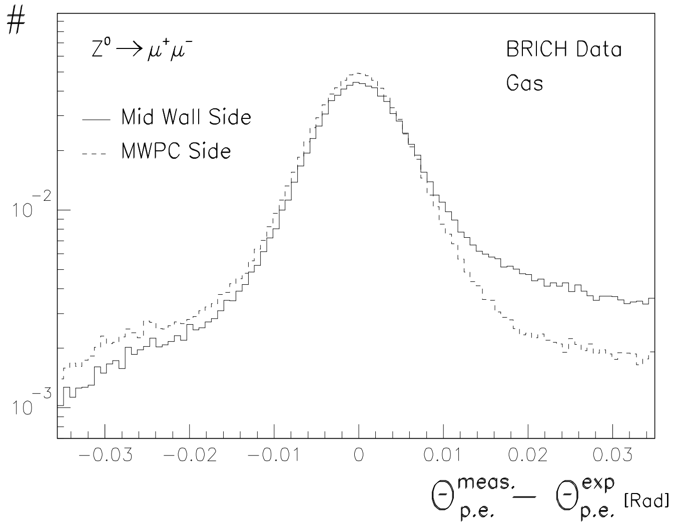

Figure 6.8: The $\theta_{\check{c}}$ distribution for single photo-electrons in saturated gas rings ($Z^0 \rightarrow \mu^+\mu^-$) for two opposite sectors in local φ of the ring.

approach, illustrated in figure 6.7, is based on the fact that the signal caused by photon-feedback shall always appear delayed in time (i.e. in z) after the detection of the original photo-electron. The effect can be seen in the data only by splitting clean saturated gas rings into two equal and opposite sectors (in local φ) and comparing the single photo-electron Cherenkov angle distributions. The reconstructed $\theta_{\check{c}}$ for the feedback signal from the MWPC-side of the ring is always smaller and the angle for feedback signal from the mid-wall side is always bigger than the $\theta_{\check{c}}$ measured for the original photo-electron. The comparison between $\theta^{\text{meas.}}_{\check{c}} - \theta^{\text{exp.}}_{\mu}$ of the two opposite sectors is shown in figure 6.8, where the effect becomes clearly visible in the tails of the distributions. From the above exercise the photon-feedback (including electronics dead-time) was estimated to have an 11% probability, producing a secondary electron with a mean distance of $\sim$15.2 mm behind the original photo-electron.

The effect has not been taken into account in the detector simulation. If one would not split the ring in two sectors, the distribution would simply be wider (i.e. the sum of the two distributions is wider), thus the resolution would be worse in the data compared to the Monte Carlo. Therefore photon feedback is added for both liquid and gas rings in the Monte Carlo by the RICFIX package (as of 94-B3 data-processing), using the above parameters estimated from gas rings.

For rings originating from the liquid radiator, photon-feedback can also come from another source i.e. from the cloud of ~ 600 ionisation electrons ($\mathrm{d}E/\mathrm{d}x$) of the track passing through the drift tube. In contrast with a gas ring, the track will always pass inside a liquid ring. The 11% feedback probability (at 15.2 mm distance) can produce a long tail of feedback electrons behind the track. This tail may cross with the Cherenkov ring, depending on the polar angle of the track, and thus can decrease the resolution. On average one can still expect $\sim$1 feedback electron at $\sim$5 cm behind the track ionisation. The influence of the feedback caused by the ionisation electrons is illustrated in figure 6.9, which shows the position in local φ on the ring of the detected

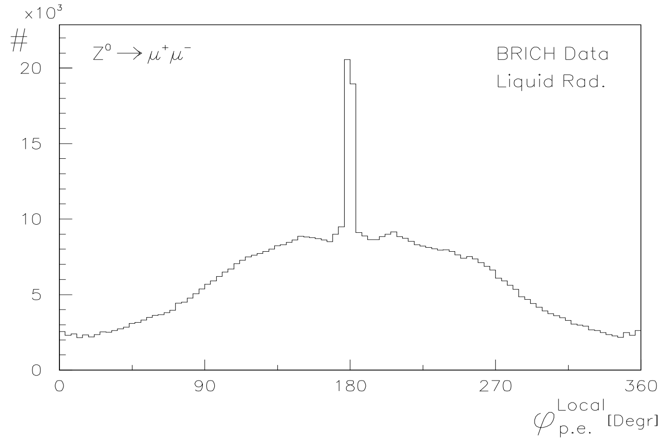

Figure 6.9: The $\varphi^{\mathrm{local}}_{\mathrm{p.e.}}$ distributions for single photo-electrons in saturated liquid rings ($\mathrm{Z}^0 \to \mu^+\mu^-$), showing a large peak behind the track.

electrons. The large peak around 180° contains more than 50% feedback electrons. This effect is not included in the RICH simulation and the two bins are removed from the data by the RICFIX programme. Although this removal causes an average loss of ~ 1 photo-electron per ring, it can improve the resolution for $\mathrm{Z}^0 \to \mu^+\mu^-$ up to $\sim 5\%$, depending on the polar angle of the track (as of 94-B3 data-processing).
The shape of the distribution in figure 6.9 actually reflects the dependence on the polar angle of the track. Only full liquid rings are produced by tracks with polar angles $73° < \theta < 107°$. Outside this window the 'rings' will have a parabolic shape due to internal reflection of the Cherenkov light inside the liquid radiator.

The comparison between data and Monte Carlo *before* and *after* the treatment by the RICFIX package for the BRICH is shown in figure 6.10 for single photo-electrons and in figure 6.11 for the result on gas rings from $\mathrm{Z}^0 \to \mu^+\mu^-$. The results of standard tests performed on $\mathrm{Z}^0 \to q\bar{q}$ events will be presented in section 6.4.

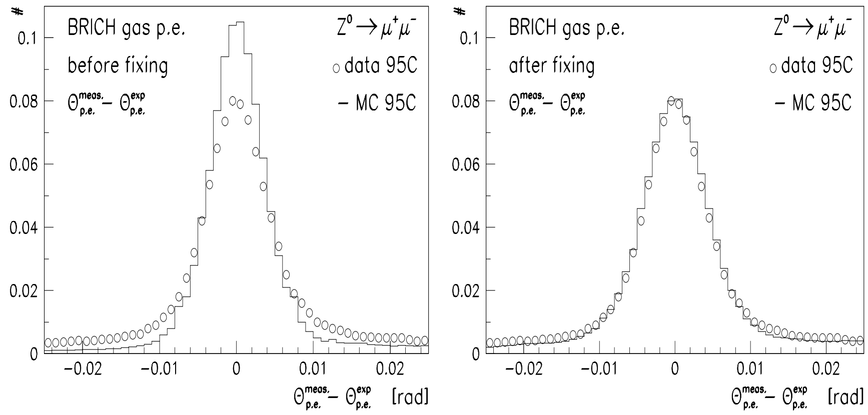

Figure 6.10:
The comparison between data and Monte Carlo for single photo-electrons *before* and *after* treatment by RICFIX.

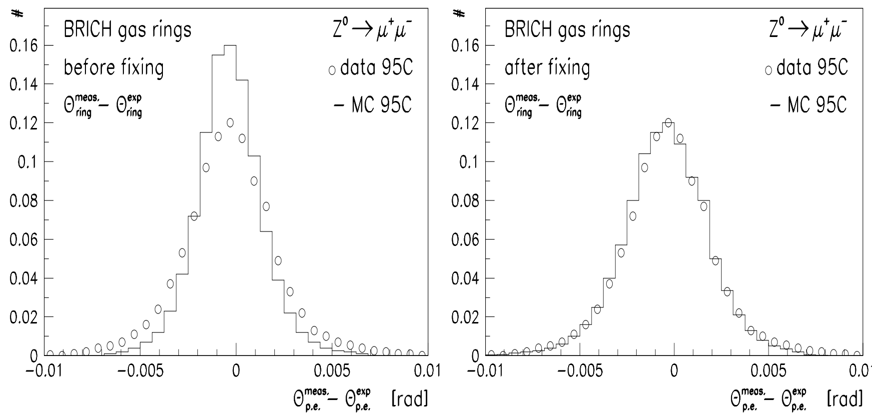

Figure 6.11:
The comparison between data and Monte Carlo for Cherenkov rings (by RIBMEAN §6.4) *before* and *after* treatment by RICFIX.

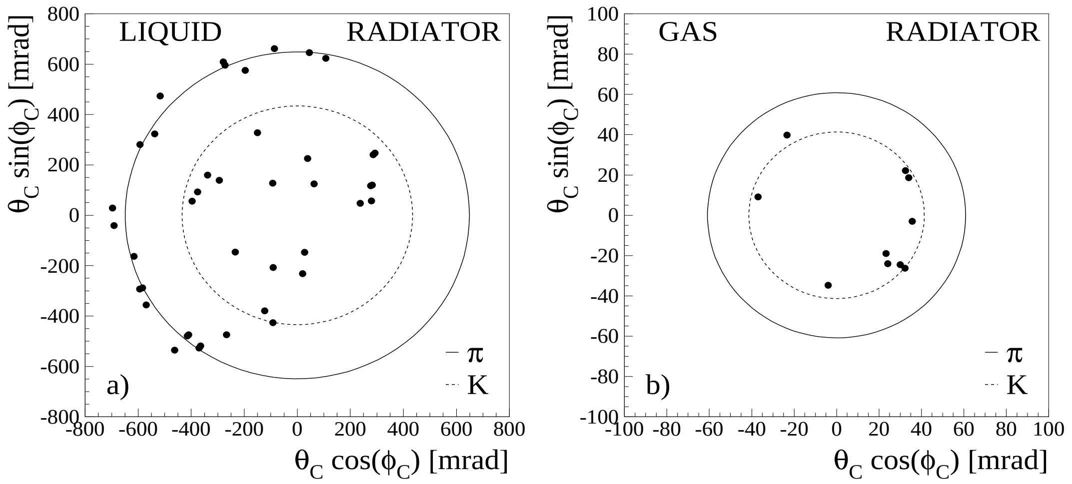

Figure 6.12: The 2-dimensional representation of photo-electrons associated to a track producing a liquid ring (a) and a track producing gas ring (b). The superimposed circles represent the expected rings for the $K^{\pm}$ and $\pi^{\pm}$ hypothesis.

6.3 Ring-Finding Algorithms for RICH Data

Throughout the years several algorithms have been developed to reconstruct Cherenkov rings for RICH particle identification [32][63]. At LEP energies these algorithms mostly have to handle high track densities (i.e. overlapping rings) and various sorts of background. The topologies of the different physics channels which can be studied at LEP set different requirements (e.g. efficiency, purity) which may be satisfied best by a certain algorithm compared to others. For the BRICH liquid and gas radiator, figure 6.12 shows the 2-dimensional representation of photo-electrons which have been associated to two different tracks. The circles indicate the expected Cherenkov angles for the pion and kaon hypothesis (in both cases the particle momenta are below the proton threshold).

Five different algorithms have been applied for DELPHI RICH physics analyses. Two algorithms, called HADSIGN [64] and RINGSCAN [65], apply a maximum likelihood technique. The fundamental difference between the two is that HADSIGN assigns a probability to the $e^{\pm}$, $\mu^{\pm}$, $\pi^{\pm}$, $K^{\pm}$ and $p\overline{p}$ hypothesis whereas RINGSCAN does not apply a constraint on the particle masses. A third algorithm (NN-method) applies a triangular method using a non-adaptable network, also without a constraint on the particle mass [60][66]. The disadvantage of the NN-method is that at least 3 photo-electrons are required to reconstruct a ring, thus one can expect a low efficiency for particles with momenta just above threshold. The most recent algorithm applies a taxonomic clustering technique which was firstly developed to solve the biological taxonomy problem of the ring-like growth of bacteria [67][68]. The above methods treat background by including it in the model. The fifth algorithm, called RIBMEAN, is used for the different topics and analyses presented in chapters 7, 8 and 8.1. This algorithm will be discussed in the next section where more details will be shown on its performance.

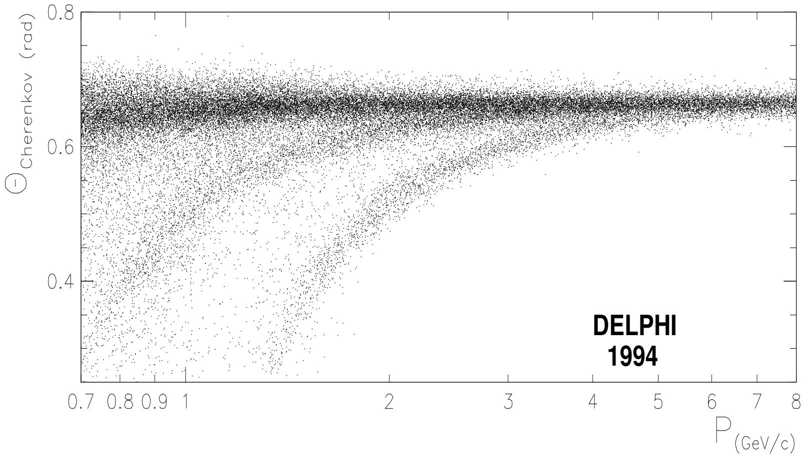

Figure 6.13: The BRICH liquid radiator Cherenkov angle versus momentum obtained from 50 000 events $Z^0 \to q\overline{q}$. Only those tracks were selected which had at least 80 wire hits in the TPC and for which the OD information was used for the track reconstruction.

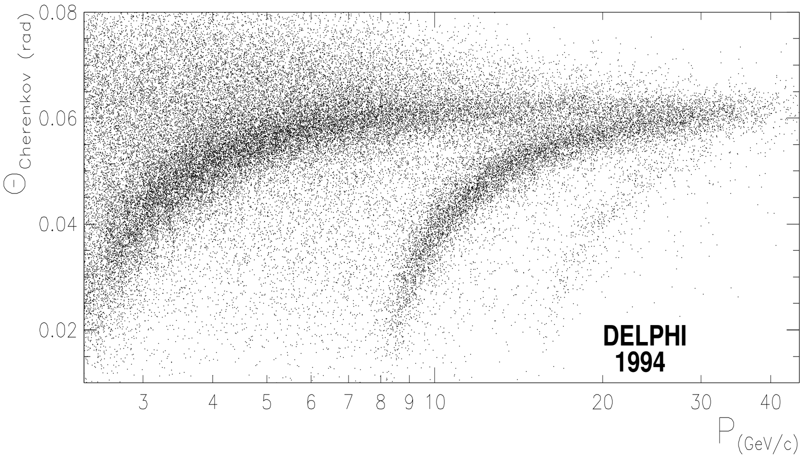

Figure 6.14: The BRICH gas radiator Cherenkov angle measurement versus momentum obtained from 450 000 events $Z^0 \to q\overline{q}$. Only those tracks were selected for which TPC and OD information was used for the track reconstruction.

6.4 The RIBMEAN Algorithm

The starting point of the RIBMEAN clustering and weighting method [69] is a set of measured photo-electrons which are associated to a track. The mean Cherenkov angle is determined in three steps. First, the photo-electrons are weighted and clustered with respect to each hypothesis ($e^{\pm}$, $\mu^{\pm}$, $\pi^{\pm}$, $K^{\pm}$ and $p\overline{p}$). Different weights are given depending on the background environment, e.g. on the (non)-ambiguity[1], the photon conversion depth and the geometrical position in the ring[2]. The cluster with the largest sum of weights is selected. Then, the liquid-liquid-, gas-gas- and liquid-gas-ambiguities are resolved. Finally, the clustering procedure is repeated and the average Cherenkov angle, the mean photo-electron uncertainty and the integer number of photo-electrons are calculated and quality bits (discussed below) are set.

Figure 6.13 shows RIBMEAN the Cherenkov angle distribution for the liquid rings versus momentum. The three bands correspond to pions (uppermost), kaons (middle) and protons (lowest). The equivalent distribution for the gas radiator is shown in figure 6.14. The distributions are derived from 1994 data after RICH alignment and RICH-fixing has been applied. The novelty in the 94-B3 processed data was the clear band at high momentum (i.e. $p > 16$ GeV/c) giving significant proof of the presence of high momentum protons.

[1] ambiguous photo-electrons are associated to different tracks or to liquid/gas of the same track.

[2] for the BRICH liquid, the background is larger for photo-electrons near the open end of the parabola.

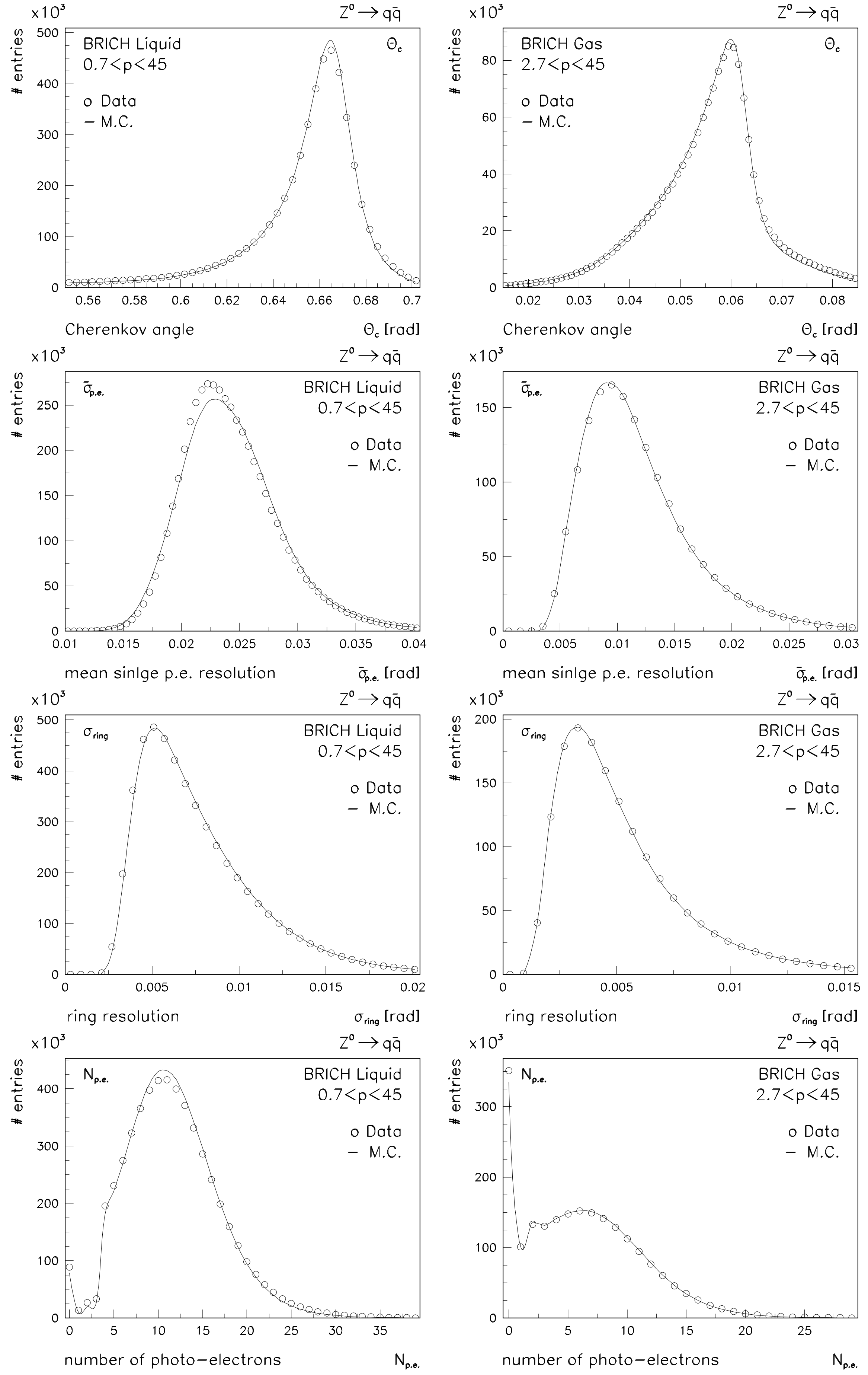

Figure 6.15: The RIBMEAN data and Monte Carlo distributions of the key RICH parameters for physics.

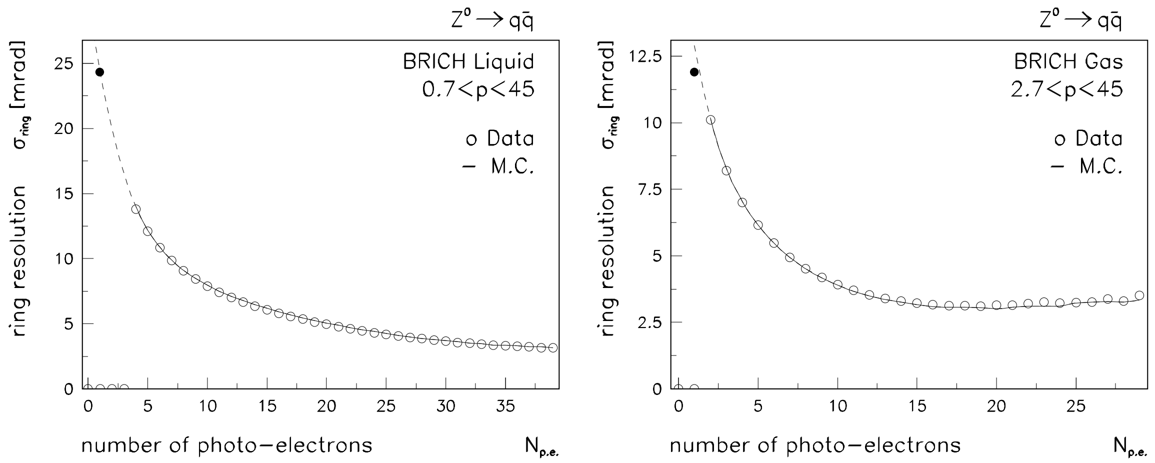

Figure 6.16: The RIBMEAN data and Monte Carlo comparison for the number of photo-electrons versus the ring resolution. The black points indicate the mean value of the distributions for the single photo-electron resolutions in the 2nd row in figure 6.15. The dashed lines represent the extrapolation of the Monte Carlo.

The RIBMEAN package offers a few benefits compared to other algorithms. A quality value is appointed to each reconstructed ring, which allows the selection of very clean samples. The quality depends on the RICH detector status, the track reconstruction quality, the fraction of the total number of photo-electrons used for the calculation of the mean Cherenkov angle and the total number of clusters associated to the track.

Furthermore, an important advantage of the RIBMEAN algorithm is the fact that its performance can be simulated rather well by the Monte Carlo. For the BRICH, figure 6.15 shows the RIBMEAN comparison between data and Monte Carlo for the key parameters for physics. The results are obtained from ∼1 000 000 events data and ∼2 000 000 events $Z^0 \rightarrow q\overline{q}$ Monte Carlo (94-B3),with only minimal requirements on the RIBMEAN quality value (i.e. the first 3 quality bits, see chapter 7 and appendix A).

A standard test, after the complete processing (i.e. background cleaning, RICH alignment, RICH fixing) has been finished and a ring reconstruction (e.g. RIBMEAN) has been applied, is to verify whether one has had good control over the detector parameters and systematic uncertainties during the different procedures. For this one can look at the mean Cherenkov ring resolution as a function of the number of photo-electrons per ring, $N_{\text{p.e.}}$. If the data quality is good and the systematic errors are small compared to the statistical errors, the Cherenkov ring resolution is expected to decrease proportional to $1/\sqrt{N_{\text{p.e.}}}$. This is illustrated in figure 6.16 for the BRICH liquid radiator ($N_{\text{p.e.}} > 3$ and $\theta_{\check{c}} > 0.25$ rad) and gas radiator ($N_{\text{p.e.}} > 1$ and $\theta_{\check{c}} > 0.015$ rad).

An additional test can be performed by extrapolating the distributions to $N_{\text{p.e.}} = 1$, which should come near to the mean single photo-electron resolution. The mean values of the distributions for the single photo-electron resolutions of figure 6.15 (2nd row) are indicated as black points in figure 6.16. The Monte Carlo distributions and the extrapolations show a good agreement with the distribution obtained for the data.

The final step is the translation of the acquired RICH information into useful observables which can be applied for physics analyses. The most commonly used observable

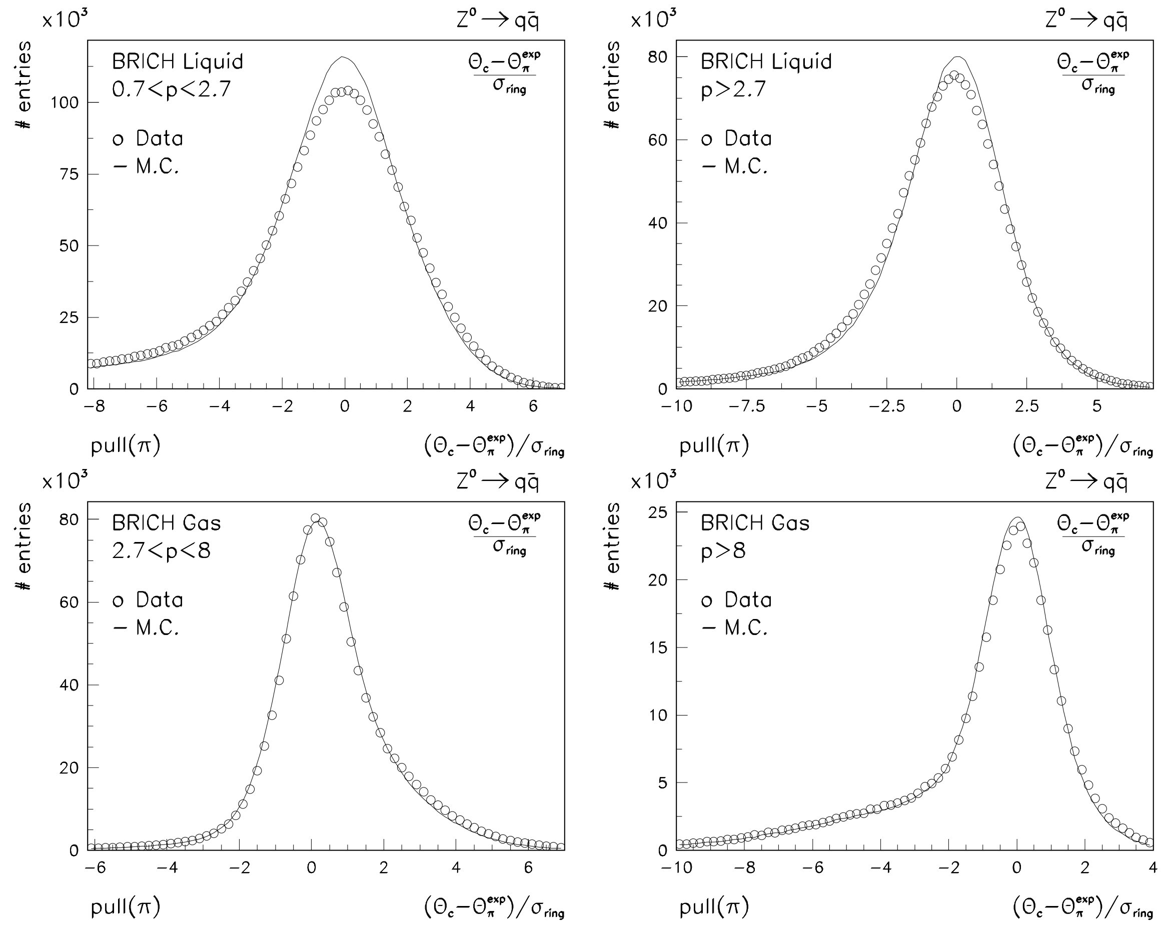

Figure 6.17: The RIBMEAN data and Monte Carlo comparison for $(\theta_{\check{c}} - \theta_\pi^{\text{exp.}})/\sigma_{\text{ring}}$ in two different momentum windows in the BRICH liquid and gas radiator.

is expressed as: $(\theta_{\check{c}} - \theta_i^{\text{exp.}})/\sigma_{\text{ring}}$, where i stands for the particle which is taken into consideration[3]. This observable is often referred to as 'pull'. Figure 6.17 shows the comparison between data and Monte Carlo for the pull distributions calculated for the pion hypothesis i.e. $(\theta_{\check{c}} - \theta_\pi^{\text{exp.}})/\sigma_{\text{ring}}$, integrated over different momentum windows for the liquid and the gas radiator of the BRICH. The bottom-left figure is the most significant since in the momentum area between 2.7 and 8 GeV/c mainly pions are expected to radiate in the gas radiator.

The pull-distributions for discrete momenta are expected to have a Gaussian-like shape with a linear background. These distributions basically reflect the particle separating power of the RICHes. Figures 6.18 and 6.19 show the expected Cherenkov distributions including the 2.5 standard deviation bands for $\pi^\pm$, $K^\pm$ and $p\bar{p}$ in the BRICH liquid and the gas radiators, derived from the 94-B3 Monte Carlo. Figures 6.20 and 6.21 show a magnification of the crossing areas where separation is becoming more difficult.

The particle separation for reconstructed Cherenkov rings, expressed in standard deviations, is shown in figure 6.22 for $\pi^\pm/K^\pm$, $K^\pm/p\bar{p}$ and $\pi^\pm/p\bar{p}$. However, these distribution do not reflect the total separating power of the BRICH, since there is always a none-zero (Poissonian) probability for a particle with momentum *above* threshold not to

[3] An alternative observable could be based on $m^2 = p^2(n^2\cos^2\theta_{\check{c}} - 1)$ (see eq. 5.2, page 34).

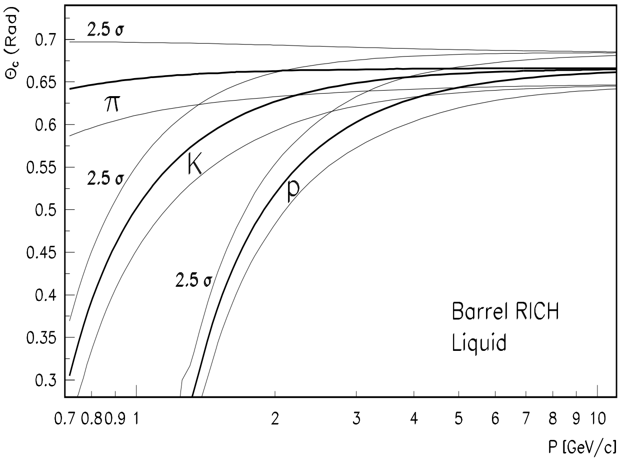

Figure 6.18: The BRICH liquid radiator RIBMEAN $\theta_{\check{c}}$ and the 2.5 sigma bands.

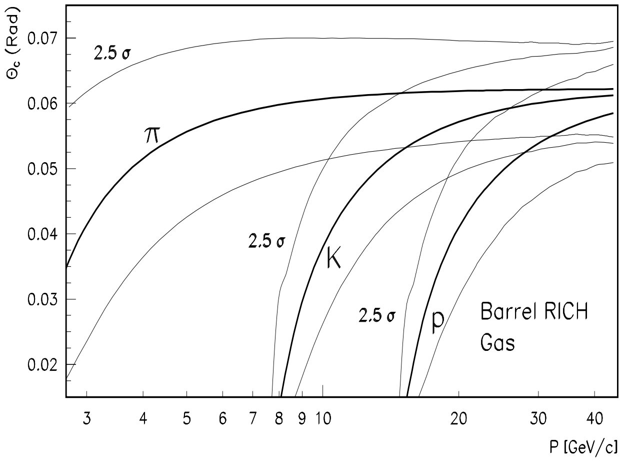

Figure 6.19: The BRICH gas radiator RIBMEAN $\theta_{\check{c}}$ and the 2.5 sigma bands.

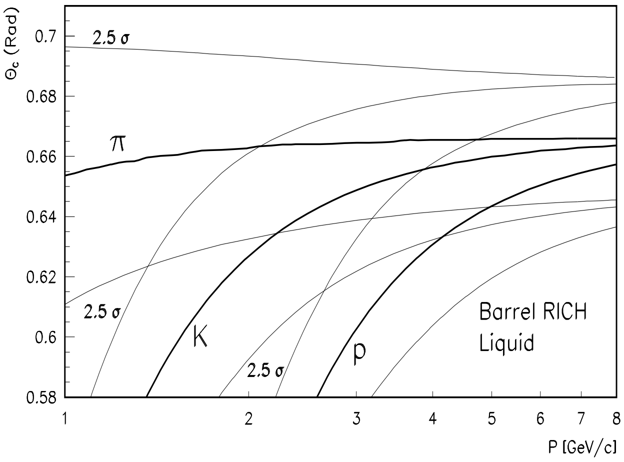

Figure 6.20: The crossing area's of the RIBMEAN $\theta_{\check{c}}$ and the 2.5 sigma bands for the BRICH liquid radiator.

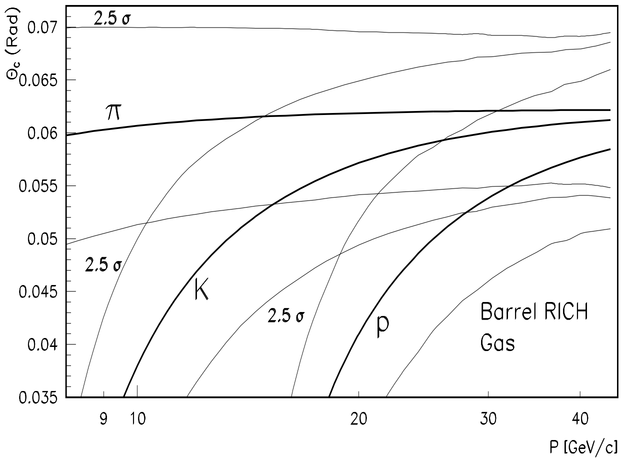

Figure 6.21: The crossing area's of the RIBMEAN $\theta_{\check{c}}$ and the 2.5 sigma bands for the BRICH gas radiator.

radiate Cherenkov light. The reverse can also occur: a particle with momentum *below* threshold is not expected to radiate but can be allocated a ring reconstructed from the background. In other words, the distributions in figure 6.22 are slightly overestimated if one accounts only for the reconstructed rings. The degree of over estimation can be obtained from figure 6.23 which shows the probability distributions for zero Cherenkov angle reconstruction for the BRICH liquid and gas radiator for $\pi^{\pm}$, $K^{\pm}$ and $p\overline{p}$. To obtain the total $\pi^{\pm}/K^{\pm}$, $K^{\pm}/p\overline{p}$ and $\pi^{\pm}/p\overline{p}$ separation the distributions of figure 6.23 should be convoluted with the distributions for the reconstructed Cherenkov rings of figure 6.22.

The pull distributions play a key role in the NEWTAG package for RICH $\pi^{\pm}$, $K^{\pm}$ and $p\overline{p}$ tagging which will be discussed in the next chapter.

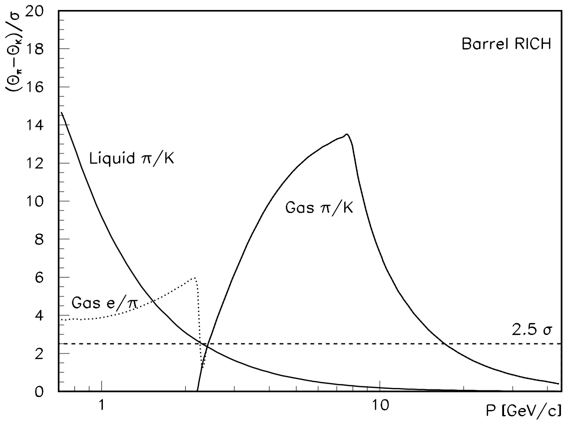

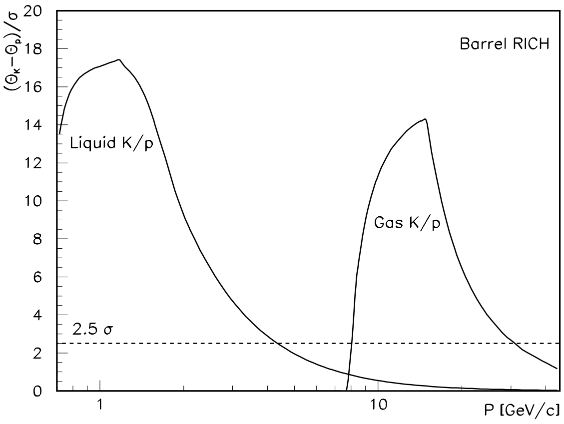

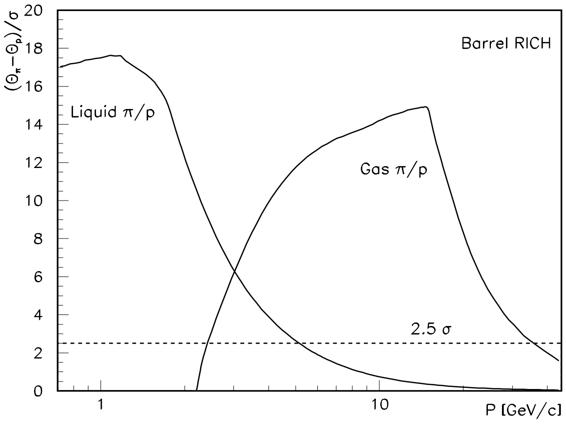

Figure 6.22: The $\pi^\pm/\mathrm{K}^\pm$, $\mathrm{K}^\pm/\mathrm{p}\overline{\mathrm{p}}$ and $\pi^\pm/\mathrm{p}\overline{\mathrm{p}}$ separation for reconstructed rings in the BRICH liquid and gas radiator. The dashed lines indicate the 2.5 standard deviations limit. The dotted line in the top-left plot shows the $e^\pm/\pi^\pm$ separation for momenta below the theoretical pion threshold in the gas radiator.

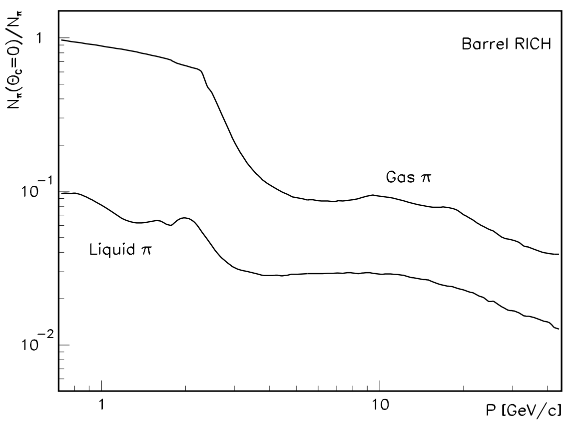

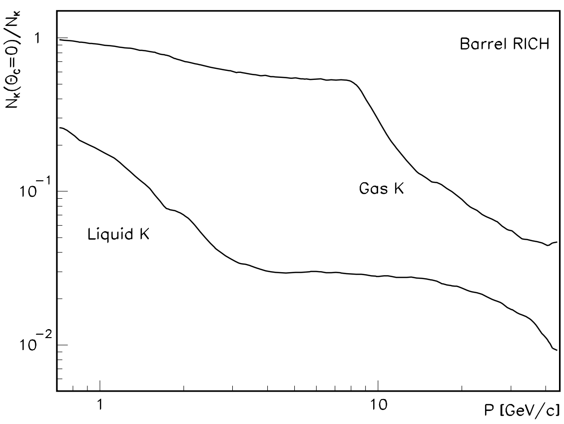

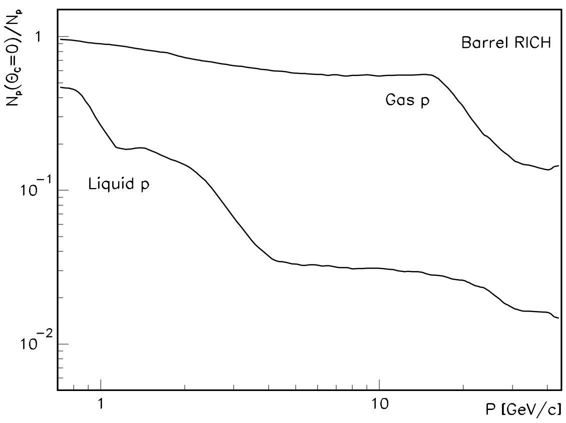

Figure 6.23: The BRICH liquid and gas probability distribution for $\pi^\pm$, $\mathrm{K}^\pm$, $\mathrm{p}\overline{\mathrm{p}}$ for zero Cherenkov angle reconstruction (i.e. $\theta_{\check{c}} = 0$, $N_{\mathrm{p.e.}} = 0$). To obtain the total $\pi^\pm/\mathrm{K}^\pm$, $\mathrm{K}^\pm/\mathrm{p}\overline{\mathrm{p}}$ and $\pi^\pm/\mathrm{p}\overline{\mathrm{p}}$ separation these distributions should be convoluted with the distributions of figure 6.22.

Chapter 7

The NEWTAG Package

The NEWTAG package [70] is a set of routines for particle identification which use the information from the Barrel and Forward RICH detectors as reconstructed by the RIBMEAN clustering algorithm [69]. It is based on the experience and performance of the RIBMEAN tagging routines which have been available up to now. It basically contains four parts: a pion[1]-, kaon-, proton-tag and a heavy-tag[2]. The main motivations to develop this package were:

- the need for a 'stand-alone' package which is easy to use for looping over Ntuples and simultaneously is easy to include in code to run over DSTs of different formats, independent of the DST unpacking-software applied (SKELANA, PHDST, PXDST, etc.).
- the urgent desire for a practical tool for testing the RICH fixing code (RICFIX) to compare detector simulated $Z^0 \to q\bar{q}$ with real data.
- the non-existence of a tag for high momentum protons ($p > 10$ GeV/c). Due to better understanding of the detector, supplementary improvements in the RICH software enabled the signal of high momentum protons in the gas radiator to be seen for the first time in the 94-B3 processed data.
- the non-existence of a pion-tag for RIBMEAN output.
- the determination of optimal acceptance- and momentum-windows for combined usage of RICH liquid and gas radiators information for the different hypotheses and different acceptance and separation requirements, i.e. π, K, p - σ_{acc}, σ_{sep}- liquid, gas - signal, veto.
- to facilitate access to the RICH data for physics analyses.

[1]Since the RICHes can hardly separate pions from electrons and muons, in this chapter, electrons and muons are taken as pions, unless stated otherwise.

[2]heavy (HV) refers to a heavy particle with mass bigger than the pion mass, i.e. kaon or proton.

Because NEWTAG only needs physical input parameters, it can be applied independent of any DELPHI DST format (full, long, short, mini) and independent of DST unpacking-software. It also can be included easily in a function to loop over Ntuples. The only requirement is that it needs output from the RIBMEAN package as input.

Since the NEWTAG package is based on the output of the RIBMEAN clustering algorithm, it has been included in the RIBMEAN pam-file. It consists of 4 routines:

```
REMIGU ( PMO, ALI, AGA, SILI, SIGA, IFLI, IFGA, NLI, NGA, RFXL, RFXG,
         IBF, IPI, IKA, IPR,  IHV,  JPI,  JKA,  JPR, JHV )

REMINI ( R1, I1, I2, I3, I4, I5, I6, I7 )

XNEWTAG ( IDTAN, IPI, IKA, IPR, IHV, JPI, JKA, JPR, JHV )

RNEWTAG ( IDTAN, IPI, IKA, IPR, IHV, JPI, JKA, JPR, JHV )
```

REMIGU is the actual 'stand alone' track by track tagging routine. Apart from the track momentum PMO and an indicator IBF for Barrel RICH (IBF=1) or Forward RICH (IBF=2), it needs the standard RIBMEAN output from both liquid (`LI`) and gas (`GA`) radiator as input (Cherenkov `A`ngle, `SI`gma angle, quality `F`lag, `N`umber of photo-electrons and `R`e`F`ractive inde`X`). REMIGU gives per hypotheses one integer value for the tag i.e. IPI, IKA, IPR, IHV and one integer value for the (combined liq-gas) RIBMEAN quality bits JPI, JKA, JPR, and JHV. A more detailed description of REMIGU is given in section 7.1.

REMINI is the initialisation routine called from inside the REMIGU tagging routine.

XNEWTAG is an interface routine between REMIGU and RIBMEAN. By calling this routine once per track, the default NEWTAG will be performed fully automatically (no matter what year the data were produced). The only input value is the track identifier, either the VECSUB pointer from SKELANA or TANAGRA id. It calls REMIGU and thus their output is identical if the same track selection requirements are applied. Concerning the track quality XNEWTAG checks if at least the TPC information was used in the track reconstruction for tracks in the barrel region only.

RNEWTAG is similar to XNEWTAG, but it performs an explicit track selection for the RICH. In case a track is passing through the barrel region, RNEWTAG verifies if at least the TPC and the OD information was used in the track reconstruction. For tracks in the forward direction at least FCB is required. Calling RNEWTAG is most probably the safest way to start using RICH tagging, since all default track selection checks are done explicitly inside this routine.

7.1 The REMIGU Tagging Routine

Since REMIGU has been developed firstly focusing on the Barrel RICH, its description given here below will be for the Barrel RICH tagging, as will be the presented figures and tables. The small adaptations for tagging using Forward RICH are explained in section 7.7.
Both liquid and gas radiators are operational for particles with momenta from 0.7 up to 45 GeV/c. For each radiator the information can be separated in 2 different classes:

1. Liquid/gas *signal* applies to particle momentum windows where sufficient Cherenkov photons are measured and a ring is reconstructed (see figs 6.13 and 6.14, page 65), i.e. the RIBMEAN clustering finds at least a minimum number of photo electrons ($N_{\mathrm{p.e.}}$) with a minimum $\theta_{\check{c}}$. For liquid signal $\theta_{\check{c}} > 0.25$ rad. and $N_{\mathrm{p.e.}} > 3$. Gas signal is defined as $\theta_{\check{c}} > 0.015$ rad. and $N_{\mathrm{p.e.}} > 1$. Identification of this kind is often referred to as 'ring identification'.

2. Liquid/gas *veto* applies to momentum windows where for one - or more - hypotheses no signal is expected, i.e. the velocity of the particle is below threshold. This kind of identification is often referred to as 'veto identification' and the tracks as 'veto tracks'. Liquid veto is defined as $N_{\mathrm{p.e.}} < 4$ and gas veto as $N_{\mathrm{p.e.}} < 2$.

One can distinguish between 4 different veto identification areas, one in the liquid and three in the gas radiator, which are defined as follows:

1. *proton liquid veto* (under the kaon band up to the proton threshold at 1.3 GeV/c). Since a signal for both the pion and kaon hypothesis is expected, this should lead to a positive proton identification.

2. *π-K-p gas veto* (below the pion threshold at 2.7 GeV/c in the gas radiator). Electrons will still produce a signal. This can be used to improve the electron rejection for kaon and proton tagging on the liquid signal.

3. *K-p gas veto* (under the pion band up to the kaon threshold at 8.5 GeV/c). The pion hypothesis is cancelled out and one can use the liquid signal for tagging between the remaining two, especially in momentum areas where separation between all three hypotheses is merely impossible.

4. *proton gas veto* (under the kaon band up to the proton threshold at $\sim$ 17.5 GeV/c). Similar to the proton liquid veto.

REMIGU value	Tag Output IXX	Quality Output JXX	(combined) liquid/gas Quality bits (*)
−1	not tagged	not selected	(lack Qbits 1,2 and/or 3 in liquid and/or gas)
0	very loose	very loose	(Qbits 1,2 and 3 in liquid and/or gas)
1	loose	loose	(Qbits 1,2,3 and 4 in liquid and/or gas)
2	standard	standard	(Qbits 1,2,3,4 and 5 in liquid and/or gas)
3	tight	tight	(Qbits 1,2,3,4,5 and 6 in liquid and/or gas)
			XX = PI, KA, PR, HV

Table 7.1: REMIGU output values for IXX and JXX.
(*) Up to now the liquid veto tracks have not been included in RICFIX. Therefore, apart from the proton veto tag, $\theta_{\check{c}} > 0.25$ rad and $N_{\text{p.e.}} > 3$ have been added as extra quality selection criteria for JXX in the liquid. An abstract of the RIBMEAN quality bits can be found in appendix A.

As mentioned before, the tag routine REMIGU gives two integer output values per hypothesis, a tag value IXX and a tag/track quality JXX, where XX[3] stands for PI, KA, PR or HV. The values which can be assigned to IXX and JXX are listed in table 7.1.
The basic philosophy behind the tag values of IXX is twofold:

1. inside 2.5 standard deviations of the hypothesis ($\sigma_{\text{acc}} < 2.5$),
2. more than 0, 1, 2 or 3 standard deviations separation from the nearest neighbour hypothesis ($\sigma_{\text{sep}} > 0$, 1, 2 or 3),

where σ_{acc} and σ_{sep} – depending on the measured and expected Cherenkov angle and the uncertainty – are defined as follows:

$$\sigma_{\text{acc}} = \frac{\mid \theta_{\check{c}}^{\text{meas.}} - \theta_{\check{c}}^{\text{exp.(i)}} \mid}{\sigma_{\text{ring}}^{\text{exp.}}} \qquad i = \text{pion}, \text{kaon}, \text{proton} \tag{7.1}$$

$$\sigma_{\text{sep}} = \frac{\theta_{\check{c}}^{\text{meas.}} - \theta_{\check{c}}^{\text{exp.(j)}}}{\sigma_{\text{ring}}^{\text{exp.}}} \qquad j = \text{pion}, \text{kaon}, \text{proton}, \;\; j \neq i \tag{7.2}$$

However, the tag value IXX can have different (optimised) acceptance and separation definitions for the different hypotheses. This depends on the momentum of the particle i.e. on the use of signal and/or veto as well as the feasibility of acceptable π/K or K/p separation. For example, the 2.5 σ_{acc} can be increased by 20% in those areas where one can expect a signal with a large separation w.r.t. the nearest neighbour hypothesis.

[3] everywhere throughout this chapter, XX refers to PI, KA, PR or HV.

The tag/track quality values JXX contain the RIBMEAN track quality output. They can also implicitly contain track reconstruction information which is checked in XNEWTAG and RNEWTAG. More details on this will be discussed in section 7.6.

7.2 Pion Tag

The pion tag is defined fairly straight forward since one expects a signal over the whole momentum window between 0.7 and 45 GeV/c. Two optimal momentum areas have been determined for different tagging.

1. 0.7< p <2.7 GeV/c tag based on liquid signal.
   IPI =0,1,2 or 3 is defined as more than 0,1,2 or 3 standard deviations above the kaon hypothesis. The nominal σ_{acc} is increased by 20% for p <1.1 GeV/c.

2. p >2.7 GeV/c tag based on gas signal.
   Apart from the K-p gas veto area, one can easily define IPI the same as above: IPI=0,1,2 or 3 for σ_{sep} more than 0,1,2 or 3 away from the kaon-hypothesis. Below the kaon threshold in the gas (at 8.5 GeV/c), it is somehow unphysical to follow the same strategy since the separation w.r.t a none signal is infinite. Therefore below 8.5 GeV/c, IPI is defined as combination of σ_{acc} and the number of measured photo electrons as follows: IPI=0,1,2 or 3 for σ_{acc} less than 4,3,2 or 1 and(!) $N_{\text{p.e.}}$ bigger than 2,3,4 or 5. In this way one can achieve slightly higher rejections. The nominal σ_{acc} is increased by 20% for p <15 GeV/c.

7.3 Kaon Tag

Tagging a kaon is rather difficult, because often one has to achieve separation from both pions and protons. Three optimal momentum windows have been determined:

1. 0.7< p <2.7 GeV/c tag based on liquid signal.
   For p <1.3 GeV/c IKA =0,1,2 or 3 is defined as more than 0,1,2 or 3 standard deviations away from the pion hypothesis (the proton is still below threshold in the liquid). Above 1.3 GeV/c the kaon hypothesis is sandwiched between the pion and proton hypotheses, thus IKA is defined as the most conservative separation from the two. For p <1.8 GeV/c the nominal σ_{acc} is increased by 12%.

2. 2.7< p <8.5 GeV/c tag based on combined liquid signal and gas K-p veto.
   A gas veto track (0 or 1 $N_{\text{p.e.}}$ detected in the gas) cancels out the pion hypothesis and tagging is reduced to the kaon and proton hypothesis in the liquid, where K/p separation goes from $\sim 6\ \sigma_{\text{sep}}$ at 2.7 GeV/c down to $\sim 0.8\ \sigma_{\text{sep}}$ at 8.5 GeV/c. For p <3.5 GeV/c the nominal σ_{acc} is increased by 12% and IKA =0,1,2 or 3 is defined as σ_{sep} >0,1,2 or 3 with respect to the proton-hypothesis. For higher

momenta $\sigma_{\rm sep}$ is always smaller than 3 and IKA has been defined less rigid. For $3.5 < p < 5.5$ IKA =0,1,2 or 3 is defined as $\sigma_{\rm sep}$ >0,1,1.5,2 and for $5.5 < p < 8.5$ as $\sigma_{\rm sep}$ >0,0.5,1,1.5 w.r.t. the proton-hypothesis.

3. $p > 8.5$ GeV/c tag on gas signal.
For $p < 17.5$ GeV/c IKA =0,1,2 or 3 is defined as more than 0,1,2 or 3 standard deviations away from the pion hypothesis (the proton is still below threshold in the gas). Above 17.5 GeV/c IKA is similarly as in the liquid, defined as $\sigma_{\rm sep}$ >0,1,2,3 w.r.t. the most conservative hypothesis. Below 15 GeV/c the nominal $\sigma_{\rm acc}$ is increased by 20%.

7.4 Proton Tag

For proton tagging five optimal momentum windows have been determined:

1. $0.7 < p < 1.3$ GeV/c tag based on proton liquid veto.
As mentioned in the introduction the proton liquid veto should lead to a positive proton identification. In practice however this is rather complicated and very much depending on the track selection, because low momentum protons have a strong curvature in the magnetic field, do not necessarily reach the OD and are more sensitive to multiple scattering. Also low momentum tracks are accompanied by a difficult background, so one should not expect too high an efficiency (a combined tag with $\mathrm{d}E/\mathrm{d}x$ information of TPC might be more appropriate in this momentum area). Since a liquid veto track is defined as $N_{\rm p.e.} < 4$, IPR is set equal 0,1,2 or 3 if $N_{\rm p.e.}$ equals 3,2,1 or 0 respectively.

2. $1.3 < p < 2.7$ GeV/c tag based on liquid signal.
IPR =0,1,2 or 3 is defined as $\sigma_{\rm sep}$ more than 0,1,2 or 3 standard deviations away from the kaon hypothesis. Up to 1.5 GeV/c the nominal $\sigma_{\rm acc}$ is increased by 20%.

3. $0.7 < p < 9$ GeV/c tag based on combined liquid signal and gas K-p veto.
Again, the gas veto (0 or 1 $N_{\rm p.e.}$ detected in the gas) cancels out the pion hypothesis and tagging is reduced to kaon-proton separation in the liquid. With slightly different momentum intervals a similar strategy as for the kaon is applied for the proton. Below 4 GeV/c the nominal $\sigma_{\rm acc}$ is increased by 12% and IPR =0,1,2 or 3 is defined as $\sigma_{\rm sep}$ >0,1,2 or 3 w.r.t. the kaon-hypothesis. For higher momenta $\sigma_{\rm sep}$ is always smaller than 3. Therefore, like IKA, also IPR has been defined less rigid. For $4 < p < 6.5$ GeV/c IPR =0,1,2 or 3 is defined as $\sigma_{\rm sep}$ >0,1,1.5 or 2 and for $6.5 < p < 9$ GeV/c as $\sigma_{\rm sep}$ >0,0.5,1 or 1.5 w.r.t. the kaon-hypothesis.

4. $9 < p < 17.5$ GeV/c tag based on proton gas veto.
Similar to the proton liquid veto but because of the high particle momentum also quite feasible in reality. Since the gas veto requirement is $N_{\rm p.e.} < 2$, IPR is set to 2 or 3 if $N_{\rm p.e.}$ equals 1 or 0 respectively (this implies that in this case IPR will never be equal 1 or 2!).

5. $17.5 < p < 45$ GeV/c tag based on gas signal.
   IPR =0,1,2 or 3 is defined as $\sigma_{\text{sep}} >$0,1,2 or 3 w.r.t. the kaon hypothesis. Below 24.5 GeV/c the nominal σ_{acc} is increased by 20%.

7.5 Heavy Tag

The aim of the heavy particle tag is to produce a strongly enriched sample of kaons and protons with a high efficiency. Its main power lays in the fact that it does not need to combine liquid signal with gas veto information below the kaon threshold in the gas. In other words, compared to the sum of the kaon and proton tag, the extra gain in the heavy particle tag mainly comes from the gas radiator veto tracks. Four optimal momentum windows have been determined:

1. $0.7 < p < 2.7$ GeV/c tag based on liquid signal.
   This is the logical combination of the kaon- and proton-tag (logical .or.) as described in section 7.3-1 and section 7.4-1 above.

2. $2.7 < p < 8.5$ GeV/c tag based on gas veto.
   All veto tracks will be tagged as heavy particles. Since the track veto requirement for the gas is $N_{\text{p.e.}} < 2$, IHV is set to 2 or 3 if $N_{\text{p.e.}}$ equals 1 or 0 respectively (this implies that IHV will never be equal 1 or 2!).

3. $8.5 < p < 17.5$ GeV/c tag based on gas veto or gas signal.
   Kaons will yield a gas signal whilst the protons are still in the veto-identification mode. Therefore the tag value IHV contains the logical combination of the kaon tag (section 7.3-3) and the proton tag (section 7.4-4).

4. $17.5 < p < 45$ GeV/c tag based on gas signal.
   In this momentum window a gas signal is expected for both kaons and protons. Here IHV =0,1,2 or 3 is defined as $\sigma_{\text{sep}} >$0,1,2 or 3 w.r.t. the pion hypothesis and σ_{acc} as the logical combination of the σ_{acc} for the kaon tag (section 7.3-3) and the proton tag (section 7.4-5).

7.6 Tag/Track Quality

The tag/track quality values JXX can be assigned at different places: firstly in the interface routines RNEWTAG and XNEWTAG and secondly in the tagging routine REMIGU.

1. In RNEWTAG an explicit RICH-independent track selection is applied. If either TPC or OD information has not been used in the track reconstruction (for forward tracks FCB) no tagging is performed and the return values for both IXX and JXX are set equal to -1. Similar in XNEWTAG, for tracks in the barrel region, no

tagging is performed if the TPC was not used and the return values for IXX and JXX are set equal to −1.
Thus the RNEWTAG or XNEWTAG output JXX =−1 does not(!) necessarily mean that the RICHes where off, because the track - for various reasons - also can have missed the TPC, OD or FCB.

2. In the tag routine REMIGU JXX can be set as listed in table 7.1. Here, the first three RIBMEAN quality bits (extrapolation, acceptance, run selection) for liquid and/or gas are required, depending on the tag hypothesis and on the particle's momentum.
   The liquid veto tracks have not been included in RICFIX. Therefore, apart from the proton veto tag, a measured signal ($\theta_{\check{c}} > 0.25$ rad and $N_{\mathrm{p.e.}} > 3$) has been added as extra quality selection criterion for JXX in the liquid.
   If the first 3 (out of 6) quality bits of RIBMEAN are set, the values for JXX are set equal to zero in REMIGU. Although the tag/track quality output values JXX =0 commonly are called 'very loose', this nevertheless means that the track is of quite good quality already. For every additional RIBMEAN quality bit which has been set, the values for JXX are increased by 1 (see table 7.1). Thus JXX can at maximum be equal to 3 if all 6 RIBMEAN liquid and/or gas quality bits have been set.

In the RIBMEAN algorithm the quality bits[4] 4 and 5 are differently defined for the two classes of RICH information (signal/veto). To achieve good tagging, the liquid and gas radiator information has to be combined and thus also the RIBMEAN quality bits for liquid and gas. In any case of combined usage of liquid and gas information for tagging, the REMIGU quality output JXX simply is the most conservative of two.

The JXX values are not always equal for each hypothesis (i.e. PI, KA, PR or HV). It depends on what combination is made for what momentum bin. One should therefore realise that one might happen to select different track samples for different hypotheses (see figure 7.1), especially for low momentum particles.

7.7 Adaptations for Forward RICH Tagging

To apply tagging in the Forward RICH region, the same routine REMIGU can be used indicating Forward RICH input (IBF=2). The main differences w.r.t. the Barrel RICH come from the fact that Forward RICH uses a different radiator gas (C_4F_{10} instead of C_5F_{12}) and from the fact that there is more particle induced background in the Forward RICH. The smaller refractive index of C_4F_{10} results in higher momentum thresholds for Cherenkov light production for each hypothesis. Therefore the different limits for the momentum windows as defined for tagging in the Barrel RICH are increased by 11%. Due to the higher background the gas signal is defined as $\theta_{\check{c}} > 0.015$ rad. and $N_{\mathrm{p.e.}} > 3$

[4] An abstract of the RIBMEAN quality bits can be found in appendix A.

thus gas veto is defined as $N_{\text{p.e.}} < 4$.
The tag/track quality output for tracks in the forward region might differ from the barrel because the ionisation of the track in the photon detector is not available.

7.8 Appropriate Tagging and Alternatives

For appropriate tagging the track selection criteria should contain a contribution from the track reconstruction, a momentum acceptance and a geometry acceptance in the following way:

Barrel RICH standard track selection criteria

- At least OD and TPC information should be used in the track reconstruction
- Momentum window $0.7 < p < 45$ GeV/c
- $\mid \cos(\Theta_{track}) \mid < 0.68$ (IBF=1)

Forward RICH standard track selection criteria

- At least FCB information should be used in the track reconstruction
- Momentum window $0.7 < p < 45$ GeV/c
- $0.82 <\mid \cos(\Theta_{track}) \mid < 0.97$ (IBF= 2)

On average about 35% of the tracks in the barrel region have no OD information (multiple scattering, hadronic interactions etc.). Likewise in the forward region about 55% of the tracks have no FCB information. These tracks will especially affect the veto identification performance, since the OD (FCB) information provides a guarantee for a good track in the RICH. Depending on the physics subject one is dealing with, this might cause a serious impact on the results of the analysis. Therefore one might have good reasons to apply a less conservative track selection. At the cost of some decrease in purity, the following alternatives can be applied for tracks which do not pass the standard selection criteria:

- Tracks without OD information ($\sim$ 35%).
  To overcome a too large drop in statistics, one can include an extra requirement for those tracks which do not have this information. This extra requirement would be JXX =3 i.e. a 'tight' ring has been found by RIBMEAN and the RICH drift tube sector in question being operational has undergone an extra check (see appendix A, bits 5, 6). Mainly depending on the momentum of the particle, an

average drop in the purity of about 10 to 15% can be expected in both the K-p-gas veto area and the proton veto area. However, the overall increase in statistics is about 25% (for 94-B3 data), which might be very useful for certain types of analyses.
Another alternative might be to require a higher number of wire hits in the TPC (one or two factors more than the nominal 30).

- Tracks without FCB information ($\sim$ 55%).
  On top of requiring JXX =3, other options could be to require FCA, TPC and/or Inner Detector.

- Tracks without TPC information.
  ($\sim$2% of the tracks in the barrel region p >0.7 GeV/c). In this case one could require Inner Detector plus OD and/or Inner Detector information instead. However, one should keep in mind that for these tracks the determination of θ_{track} might be mediocre.

For certain physics cases a more conservative track selection can be required to obtain a higher purity. For example a geometry cut around the mid wall ($|\cos\theta_{\check{c}}| > 0.017$) might be useful especially when veto tracks play a dominating role.

To simplify the study of tagging effects for special user demands and to ease possible future changes of the REMIGU routine for different physics (LEP2) or different detector circumstances, 4 parameters are centrally set at the start of the routine. ACL=2.5 and ACG=2.5 are the nominal values σ_{acc} (equation 7.1) are set at for the liquid and gas signal. IVTL=4 and IVTG=2 are the nominal values for the maximum number of photo-electrons required to define a veto track in the liquid and the gas radiator.

One special logical (LGVETO) is defined to suppress electrons in the tagging below 2.7 GeV. Electrons are the only particles which will emit light in the gas radiator between 0.7 and 2.7 GeV (π-K-p *gas veto* see section 7.1). Its default value however is .false. because -as expected- in the gas radiator these low momentum tracks tend to have rather big resolution and high background. It is very difficult to treat this correctly in the detector simulation and therefore one may expect discrepancies in comparing data with Monte Carlo.

Also a group of 20 logical variables are set centrally at the beginning of the routine, mostly defining the different tag momentum windows, signal and veto tracks as well as the expectations per hypothesis.

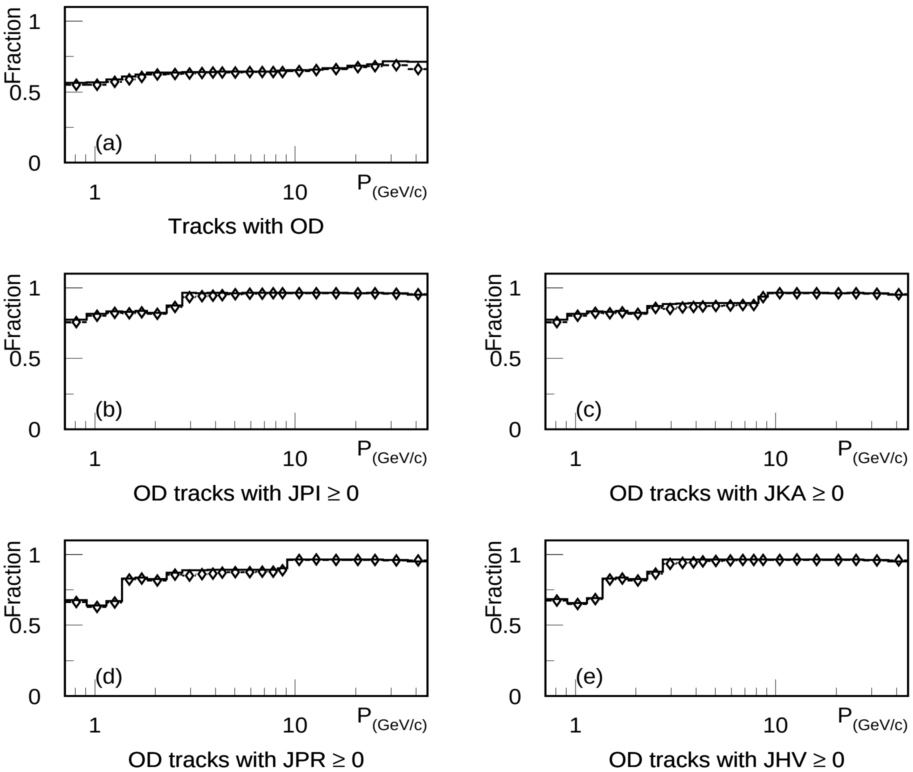

Figure 7.1: Track selection efficiency versus momentum. (a) Fraction of tracks in the barrel region for which at least OD information was used in the track reconstruction versus momentum.
(b,c,d,e) Fraction of tracks of fig.(a) versus momentum for PI(b), KA(c), PR(d), HV(d) tag for which the primary quality bits are set. The differences between b, c, d and e are due to mixed combination of the RICH information for different tags (diamonds=data, line=simulation).

7.9 Efficiency, Purity, Rejection

The RICH detectors in DELPHI are by no means 'stand-alone' systems for particle identification. The performance very much depends on a good track reconstruction. In other words: if a track is not very well reconstructed, one *can not* expect an optimal particle identification, even if the RICH were to be perfectly in operation. Therefore one should make a clear distinction between the DELPHI *track reconstruction efficiency* and the RICH *particle identification efficiency*. The results for the Barrel RICH, presented in this and the next section are based on $\sim$1 000 000 selected events $Z^0 \to q\overline{q}$ data and $\sim$2 000 000 events detector simulation (both 94-B3 short DST). To determine the NEWTAG particle identification efficiencies ($\mathcal{E}^{\rm YY}_{\rm XX}$), as well as purities ($\mathcal{P}^{\rm YY}_{\rm XX}$) and rejections ($\mathcal{R}^{\rm YY}_{\rm XX}$), a two-step track selection is performed.
The first step could be called a pre-selection. This takes place in the interface routines RNEWTAG, XNEWTAG. Here, independent of the RICH, a sample of well reconstructed tracks is selected. For RNEWTAG, figure 7.1(a) shows as a function of momentum the fraction of tracks in the barrel region ($47° < \theta_{\rm track} < 133°$) for which at least OD information has been used for the track reconstruction. Giving equal weight to each bin, the mean fraction between 0.7$< p <$45 GeV/c is 63.2% for data and 64.4% for simulation. The presence of TPC information is virtually 100%.

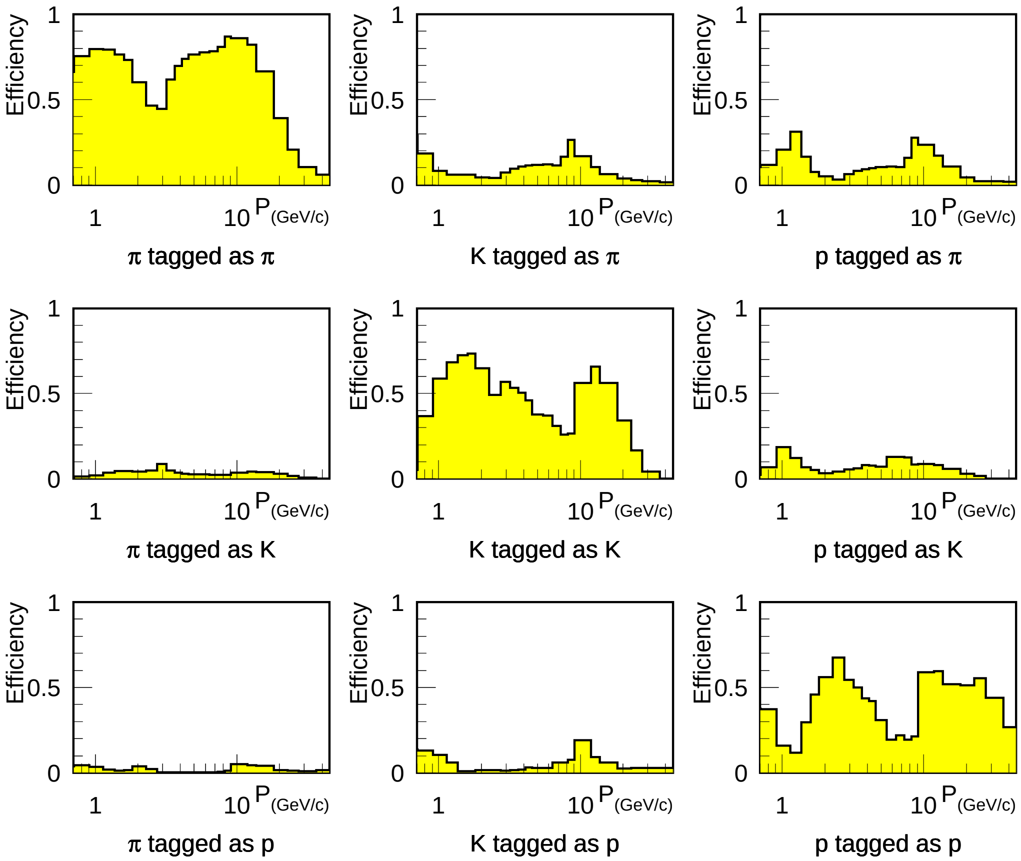

Figure 7.2: Efficiency matrix for the PI, KA, PR RNEWTAG 'standard' output (IXX $\geq$2) and 'very loose' selected tracks (JXX $\geq$0) versus momentum (Barrel RICH).

The second selection step takes place in REMIGU. It applies an extra RICH track selection based on the primary quality bits from RIBMEAN i.e. JXX ≥ 0 (bits 1,2 and 3 from either the liquid and/or gas radiator i.e. extrapolation, acceptance and run selection). These primary quality bits are merely determined by the detector status and the detector geometry, thus they are set independent of the RIBMEAN clustering algorithm (see appendix A). This can lead to slightly different subsamples for PI, KA, PR or HV since each tag applies a different combination of liquid/gas radiator information (thus also quality bits) for different momenta. Figures 7.1(b,c,d,e) show - out of the first selection - the RNEWTAG-fraction of tracks selected for the four different tags i.e. JXX $\geq$ 0. The mean fraction for data (M.C.) between 0.7$< p <$45 GeV/c for JPI, JKA, JPR and JHV is respectively 91.3 (92.2)%, 88.4 (89.6)%, 86.3 (87.5)% and 89.7 (90.5)%.

After the track selection one can apply 'very loose', 'loose', 'standard' or 'tight' tagging for the different hypotheses on the selected subsample. The results on the efficiency, purity and rejection refer to a track sample selected from the barrel region for which TPC and OD have been used in the track reconstruction i.e. the sample of fig 7.1(a), thus independent of RIBMEAN and NEWTAG. As an example, figure 7.2 shows the efficiency matrix for the standard RNEWTAG output (IXX $\geq$ 2) for a 'very loose' selected track sample (JXX $\geq$ 0). The diagonal elements clearly carry the biggest populations.

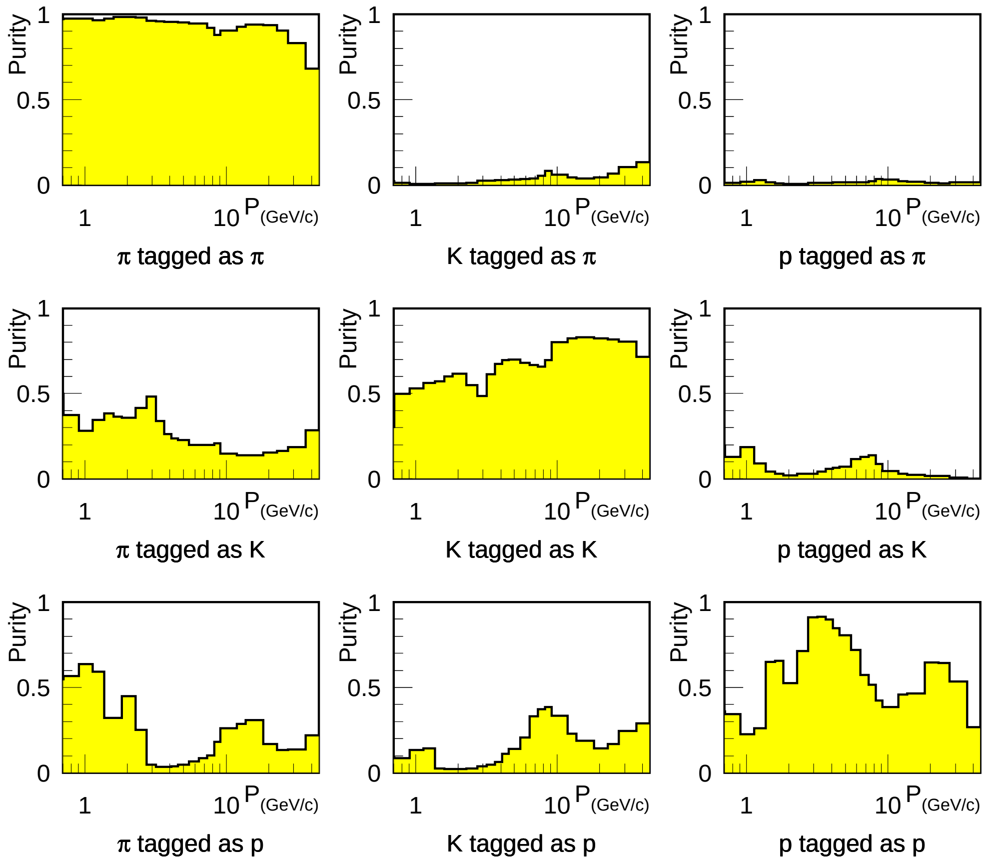

Figure 7.3: Purity matrix for the PI, KA, PR RNEWTAG 'standard' output (IXX ≥2) and 'very loose' selected tracks (JXX ≥0) versus momentum (Barrel RICH).

The corresponding purity and rejection matrices are given in figures 7.3 and 7.4. The efficiency, purity and rejection matrices are determined from the detector simulation. The matrix elements $\mathcal{E}_{\rm XX}^{\rm YY}$, $\mathcal{P}_{\rm XX}^{\rm YY}$ and $\mathcal{R}_{\rm XX}^{\rm YY}$ are defined as follows:

$$\mathcal{E}_{\rm XX}^{\rm YY} = \frac{\sum \text{XX selected.and.tagged as YY}}{\sum \text{XX}} \tag{7.3}$$

$$\mathcal{P}_{\rm XX}^{\rm YY} = \frac{\sum \text{XX selected.and.tagged as YY}}{\sum \text{all selected.and.tagged as YY}} \tag{7.4}$$

$$\mathcal{R}_{\rm XX}^{\rm YY} = \mathcal{E}_{\rm YY}^{\rm YY}/\mathcal{E}_{\rm XX}^{\rm YY} \quad \text{XX} \neq \text{YY} \qquad \text{XX}, \text{YY} = \text{PI, KA, PR or HV} \tag{7.5}$$

For the same 'standard' tag, figure 7.5 shows the efficiency, purity and rejection matrix elements for the heavy-tag. In the top right hand plot the sum of the equivalent kaon and proton tag are superimposed mainly to illustrated the gain in efficiency for gas veto tracks. The improvement in efficiency of the heavy particle tag compared to the sum of the kaon and proton tag goes from ∼10% at 3 GeV/c up to ∼50% at 9 GeV/c. Figure 7.6 shows the comparison in efficiency and purity between the 'very loose', 'loose', 'standard' and 'tight' tagging for JXX ≥0 quality output tracks. For the total momentum window ($0.7 < p < 45$ GeV/c), giving equal weight to each bin, the mean $\mathcal{E}_{\rm XX}^{\rm YY}$, $\mathcal{P}_{\rm XX}^{\rm YY}$ and $\mathcal{R}_{\rm XX}^{\rm YY}$ for the different values of IXX and JXX are given in table 7.2.

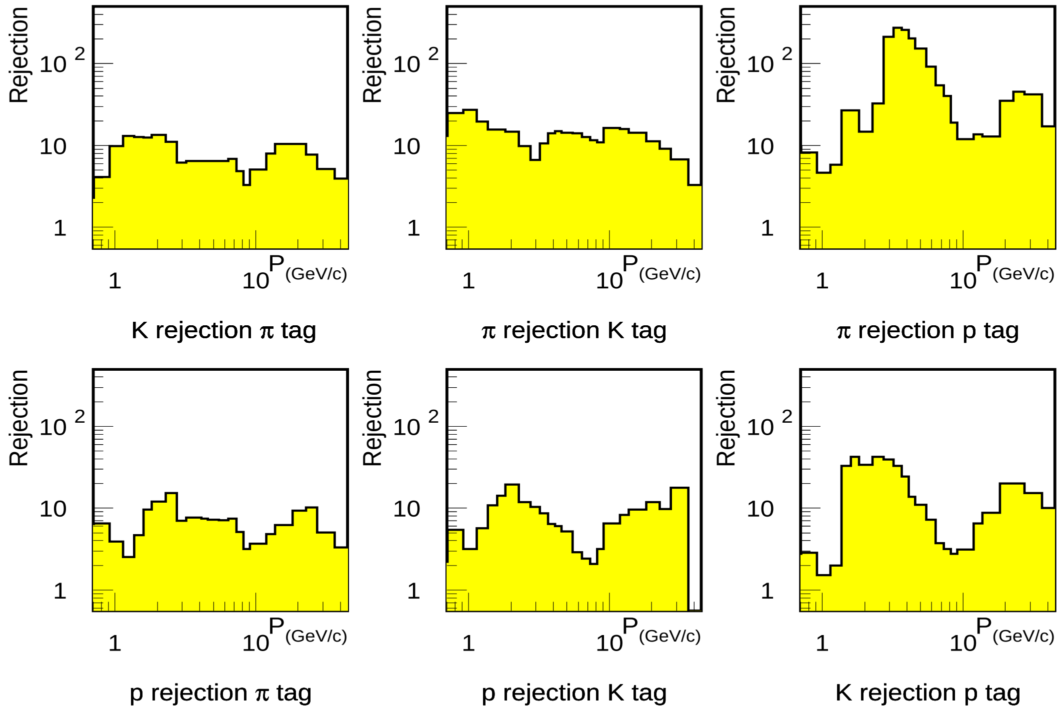

Figure 7.4: Rejection matrix for the PI, KA, PR RNEWTAG 'standard' output (IXX ≥ 2) and 'very loose' selected tracks (JXX ≥ 0) versus momentum (Barrel RICH).

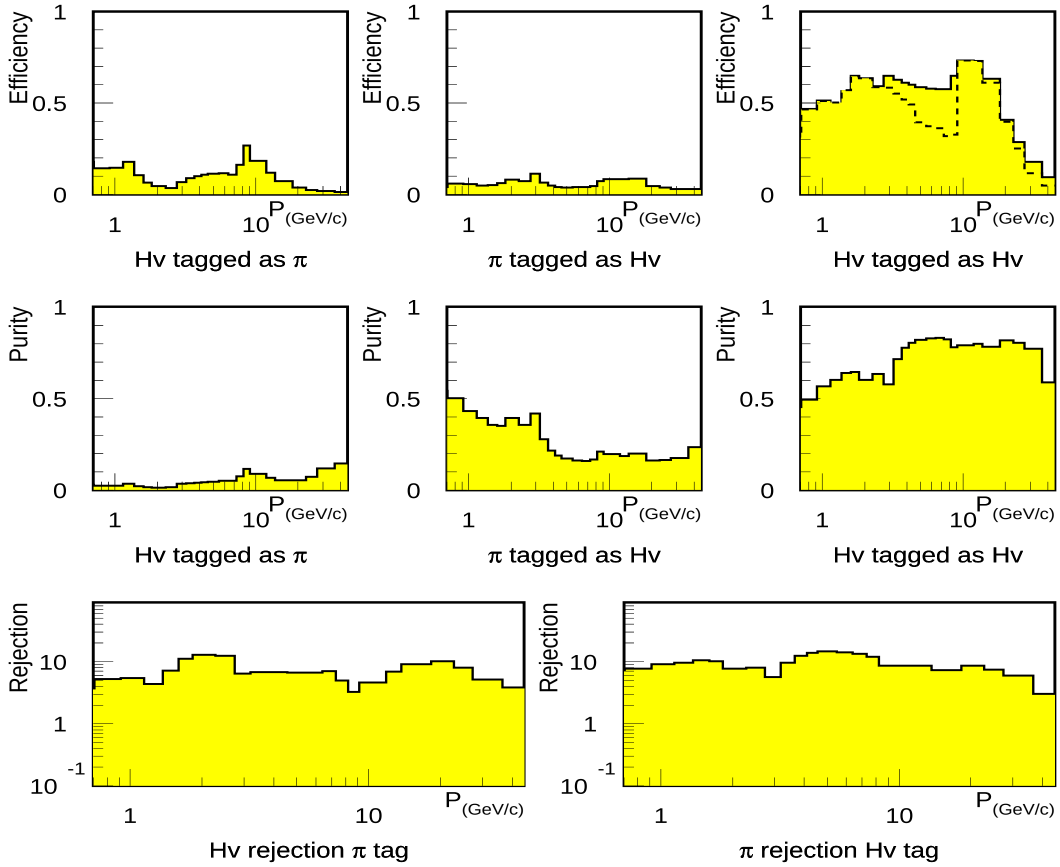

Figure 7.5: Heavy particle RNEWTAG 'standard' output (IXX ≥ 2) $\mathcal{E}^{\rm YY}_{\rm XX}$, $\mathcal{P}^{\rm YY}_{\rm XX}$ and $\mathcal{R}^{\rm YY}_{\rm XX}$ for XX, YY = PI, HV for 'very loose' selected tracks (JXX ≥ 0) versus momentum (Barrel RICH). The first element $\mathcal{E}^{\rm PI}_{\rm PI}$ is omitted since it is equal to $\mathcal{E}^{\rm PI}_{\rm PI}$ in figure 7.2. The dashed line gives the result of the sum of the 'standard' KA, PR output from figure 7.2.

JPI	≥ 0		≥ 1		≥ 2		≥ 3		≥ 0		≥ 3	
[%]	$\mathcal{E}^{\mathrm{PI}}_{\mathrm{PI}}$	$\mathcal{P}^{\mathrm{PI}}_{\mathrm{PI}}$	$\mathcal{E}^{\mathrm{PI}}_{\mathrm{PI}}$	$\mathcal{P}^{\mathrm{PI}}_{\mathrm{PI}}$	$\mathcal{E}^{\mathrm{PI}}_{\mathrm{PI}}$	$\mathcal{P}^{\mathrm{PI}}_{\mathrm{PI}}$	$\mathcal{E}^{\mathrm{PI}}_{\mathrm{PI}}$	$\mathcal{P}^{\mathrm{PI}}_{\mathrm{PI}}$	$\mathcal{R}^{\mathrm{PI}}_{\mathrm{KA}}$	$\mathcal{R}^{\mathrm{PI}}_{\mathrm{PR}}$	$\mathcal{R}^{\mathrm{PI}}_{\mathrm{KA}}$	$\mathcal{R}^{\mathrm{PI}}_{\mathrm{PR}}$
IPI												
≥ 0	70.7	79.0	65.7	80.4	55.5	81.7	52.1	81.7	3.7	5.1	10.6	7.5
≥ 1	64.3	81.5	60.2	82.8	51.4	84.0	48.2	84.0	5.7	9.1	14.2	11.9
≥ 2	56.2	83.0	52.8	84.2	45.7	85.4	42.8	85.4	7.0	13.5	18.0	14.5
≥ 3	47.7	84.5	45.0	85.3	39.2	86.3	36.8	86.3	7.1	13.5	18.0	14.4
JKA	≥ 0		≥ 1		≥ 2		≥ 3		≥ 0		≥ 3	
[%]	$\mathcal{E}^{\mathrm{KA}}_{\mathrm{KA}}$	$\mathcal{P}^{\mathrm{KA}}_{\mathrm{KA}}$	$\mathcal{E}^{\mathrm{KA}}_{\mathrm{KA}}$	$\mathcal{P}^{\mathrm{KA}}_{\mathrm{KA}}$	$\mathcal{E}^{\mathrm{KA}}_{\mathrm{KA}}$	$\mathcal{P}^{\mathrm{KA}}_{\mathrm{KA}}$	$\mathcal{E}^{\mathrm{KA}}_{\mathrm{KA}}$	$\mathcal{P}^{\mathrm{KA}}_{\mathrm{KA}}$	$\mathcal{R}^{\mathrm{KA}}_{\mathrm{PI}}$	$\mathcal{R}^{\mathrm{KA}}_{\mathrm{PR}}$	$\mathcal{R}^{\mathrm{KA}}_{\mathrm{PI}}$	$\mathcal{R}^{\mathrm{KA}}_{\mathrm{PR}}$
IKA												
≥ 0	53.2	45.3	46.7	51.4	42.2	52.0	39.7	52.0	9.0	3.8	19.3	8.9
≥ 1	46.1	51.7	40.3	58.1	36.8	59.0	34.6	58.9	9.8	5.1	20.2	10.6
≥ 2	38.0	58.2	33.1	65.2	30.6	66.1	28.7	66.1	12.1	6.8	24.0	13.1
≥ 3	29.9	59.2	25.8	66.7	24.0	67.7	22.5	67.7	17.1	8.2	32.3	16.5
JPR	≥ 0		≥ 1		≥ 2		≥ 3		≥ 0		≥ 3	
[%]	$\mathcal{E}^{\mathrm{PR}}_{\mathrm{PR}}$	$\mathcal{P}^{\mathrm{PR}}_{\mathrm{PR}}$	$\mathcal{E}^{\mathrm{PR}}_{\mathrm{PR}}$	$\mathcal{P}^{\mathrm{PR}}_{\mathrm{PR}}$	$\mathcal{E}^{\mathrm{PR}}_{\mathrm{PR}}$	$\mathcal{P}^{\mathrm{PR}}_{\mathrm{PR}}$	$\mathcal{E}^{\mathrm{PR}}_{\mathrm{PR}}$	$\mathcal{P}^{\mathrm{PR}}_{\mathrm{PR}}$	$\mathcal{R}^{\mathrm{PR}}_{\mathrm{PI}}$	$\mathcal{R}^{\mathrm{PR}}_{\mathrm{KA}}$	$\mathcal{R}^{\mathrm{PR}}_{\mathrm{PI}}$	$\mathcal{R}^{\mathrm{PR}}_{\mathrm{PI}}$
IPR												
≥ 0	47.4	39.6	40.8	46.1	38.6	46.6	37.0	46.6	28.6	8.3	66.2	20.1
≥ 1	42.2	45.7	36.3	52.5	34.4	53.3	32.9	53.2	42.9	9.7	95.7	21.6
≥ 2	35.3	50.9	30.3	57.8	28.8	59.3	27.5	59.2	60.0	14.2	135.7	27.5
≥ 3	25.9	56.6	22.3	62.3	21.3	64.2	20.2	64.2	76.7	23.9	187.0	43.7
JHV	≥ 0		≥ 1		≥ 2		≥ 3		≥ 0		≥ 3	
[%]	$\mathcal{E}^{\mathrm{HV}}_{\mathrm{HV}}$	$\mathcal{P}^{\mathrm{HV}}_{\mathrm{HV}}$	$\mathcal{E}^{\mathrm{HV}}_{\mathrm{HV}}$	$\mathcal{P}^{\mathrm{HV}}_{\mathrm{HV}}$	$\mathcal{E}^{\mathrm{HV}}_{\mathrm{HV}}$	$\mathcal{P}^{\mathrm{HV}}_{\mathrm{HV}}$	$\mathcal{E}^{\mathrm{HV}}_{\mathrm{HV}}$	$\mathcal{P}^{\mathrm{HV}}_{\mathrm{HV}}$	$\mathcal{R}^{\mathrm{HV}}_{\mathrm{PI}}$	$\mathcal{R}^{\mathrm{PI}}_{\mathrm{HV}}$	$\mathcal{R}^{\mathrm{HV}}_{\mathrm{PI}}$	$\mathcal{R}^{\mathrm{PI}}_{\mathrm{HV}}$
IHV												
≥ 0	60.7	53.7	52.2	57.4	48.0	57.8	45.6	57.8	6.2	3.4	11.0	6.3
≥ 1	54.7	58.4	46.9	62.5	43.4	63.2	41.3	63.2	6.9	4.3	11.9	7.5
≥ 2	47.2	62.8	40.3	67.8	37.8	68.9	35.9	68.9	8.3	6.1	14.6	10.6
≥ 3	35.9	68.7	31.1	73.3	29.3	74.9	27.7	74.9	13.0	8.7	23.1	15.8

Table 7.2: RNEWTAG mean Barrel RICH efficiency and purity giving each bin ($0.7 < p < 45$ GeV) equal weight, for 'very loose', 'loose', 'standard' and 'tight' pion, kaon, proton and heavy particle tag values (IXX) and tag/track quality (JXX). The numbers are derived from ~2.000.000 Monte Carlo events. Of the mean rejection only the 'very loose' and 'tight' values are listed.

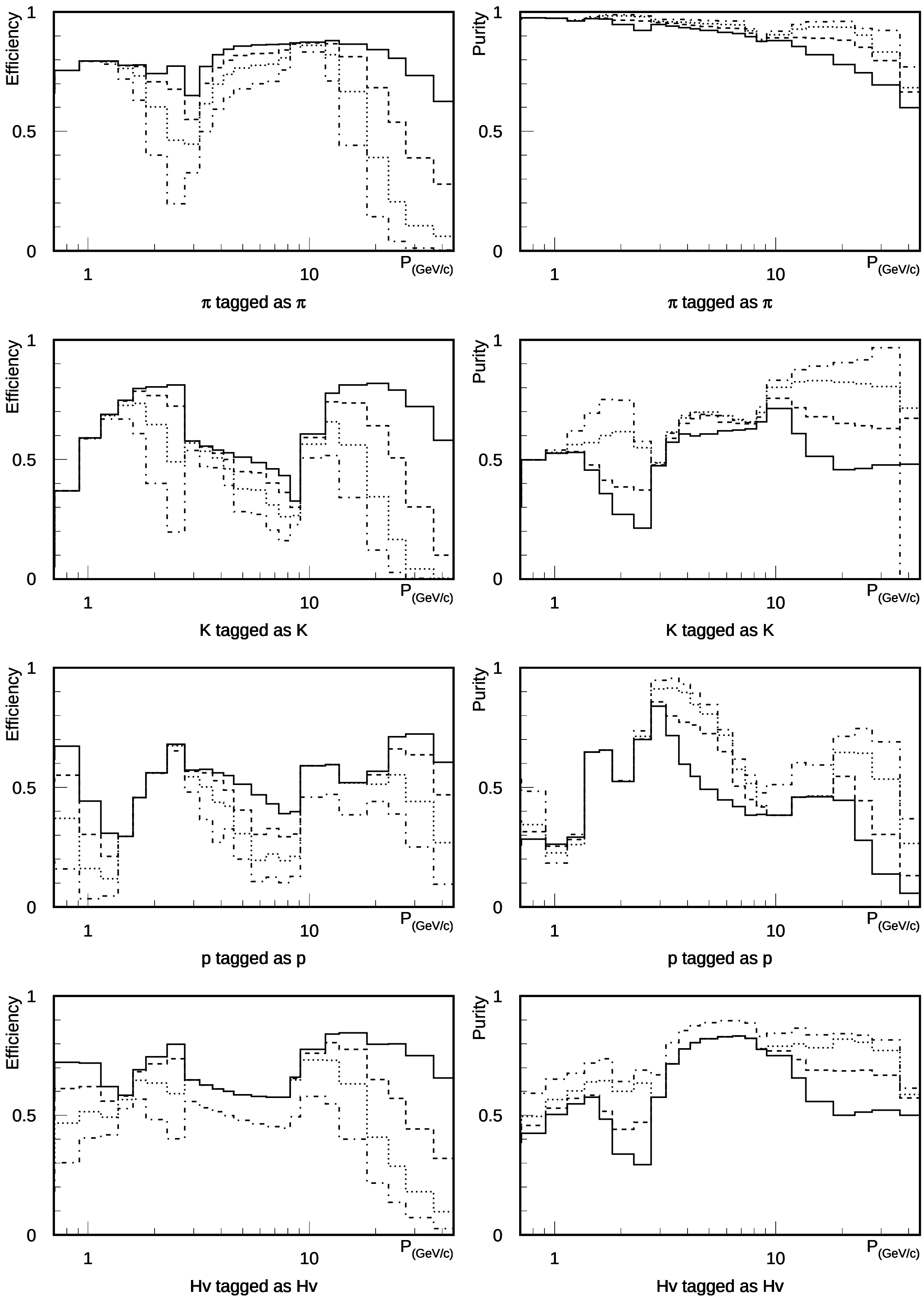

Figure 7.6: Efficiency $\mathcal{E}^{\mathrm{YY}}_{\mathrm{XX}}$ and purity $\mathcal{P}^{\mathrm{YY}}_{\mathrm{XX}}$, XX=PI, KA, PR, HV for 'very loose' (line), 'loose' (dash), 'standard' (dot) and 'tight' (dash-dot) tagging (94-B3 Monte Carlo) and tag quality output JXX $\geq$0 versus momentum (Barrel RICH).

Chapter 8

NEWTAG Performance on Data and Monte Carlo

8.1 Data versus Detector Simulation

The understanding of the tagging and its performance can be tested by comparing what is seen on real data with the result obtained from detector simulation where the identity of a particle a priori is known. There are different ways to make this comparison.

A straight forward test is to use pions from $K^0_S \rightarrow \pi^+\pi^-$-decays and protons from $\Lambda^0 \rightarrow p\pi^-$-decays obtained from the V^0 reconstruction [32]. In this way one can select highly enriched samples of identified particles without using RICH information. By requiring only very well reconstructed K^0_S's (V^0-flag=22) one can obtain a sample of about 151 000 (94-B3 data) and 336 000 (94-B3 Monte Carlo) pions with a momentum between 0.7 and 45 GeV/c for which the OD was used in the track reconstruction. The pion purity of the sample is 94.3%, giving equal weight to each bin.

The left hand column of figure 8.1 shows the result on data and Monte Carlo for the pion, kaon, proton and heavy 'standard' RNEWTAG output. The right hand column shows the equivalent result on data and Monte Carlo for protons from well reconstructed Λ^0's (V^0-flag=$\pm$33). A sample of 35 300 (94-B3 data) and 71 600 (94-B3 Monte Carlo) protons was selected. Giving equal weight to each momentum bin, the proton purity between 0.7 and 25 GeV/c is 75.3%,

The shape of the distributions in both columns in figure 8.1 can be directly understood from the way the RICH particle identification works. For example, the top left efficiency plot (π tagged as π) can be divided into three momentum windows. Between 0.7 and 2.7 GeV/c, only liquid radiator information is used. The efficiency slowly drops from 80% down to a local minimum of $\sim$ 45% at 2.7 GeV/c, simply because the $\pi^\pm/K^\pm$ separation slowly decreases with rising momentum (see fig. 6.13, page 65). Above 2.7 GeV/c, only gas radiator information is used and the efficiency rises again up to $\sim$85% at 9 GeV/c. Basically, only pions produce light in this window. The gas ring

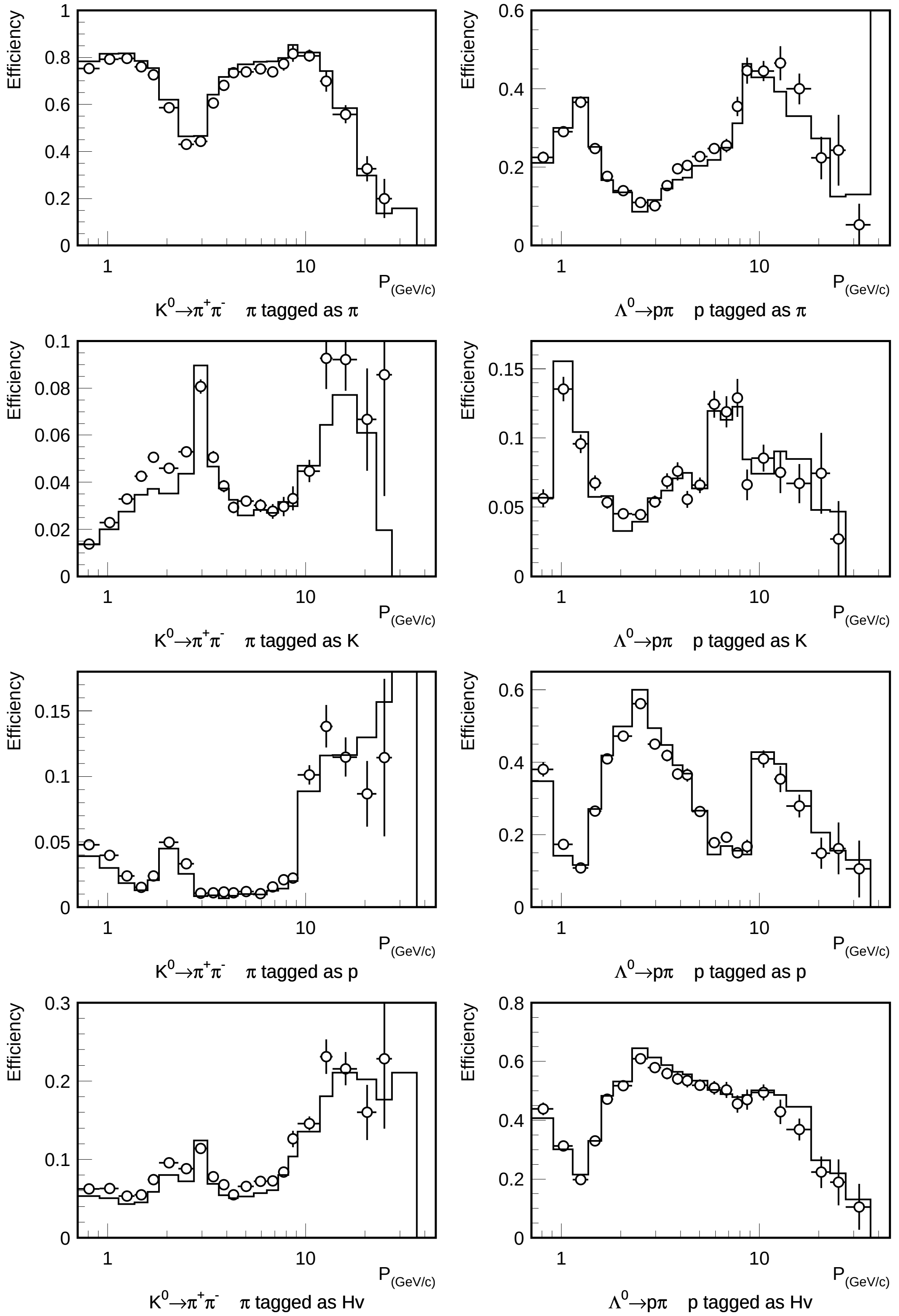

Figure 8.1: Efficiencies data (points) vs Monte Carlo (lines) for pions from K^0_S decay and protons from Λ^0 decay for 'standard' RNEWTAG output (IXX $\geq$2) and 'very loose' selected tracks (JXX $\geq$0) versus momentum (Barrel RICH).

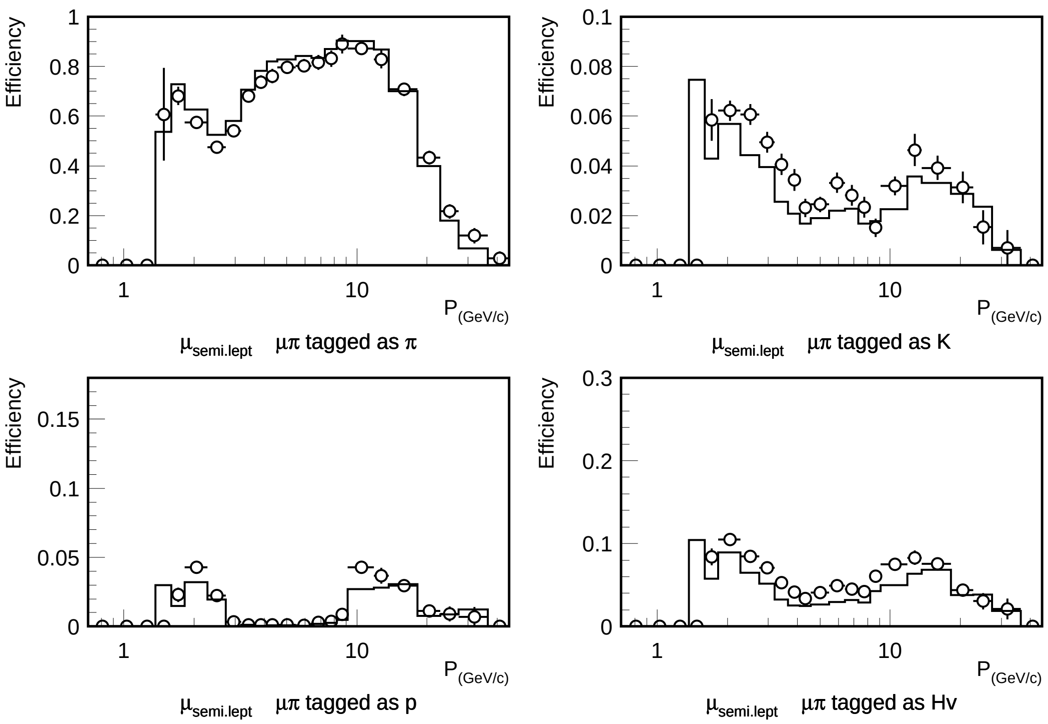

Figure 8.2: Efficiencies for data (points) and Monte Carlo (lines) derived with muons from semi-leptonic decays, for 'standard' RNEWTAG output (IXX $\geq$2) and 'very loose' selected tracks (JXX $\geq$0) versus momentum (Barrel RICH).

resolution improves because with increasing momentum more photons are produced and the curvature of the tracks gets smaller. For momenta above 9 GeV/c the same explanation is valid as for the window in the liquid radiator.

To test especially the momentum area above 10 GeV/c with higher statistics, one can use muons from semi-leptonic decays identified in the Muon Chambers (RICH can not distinguish between pions, muons and electrons). Accepting 'loose', 'standard' and 'tight' MUID-tag output, 32 800 (data) and 49 600 (Monte Carlo) muons were found. Apart from requiring OD, an additional selection cut to reject kaons in the sample was to require the TPC dE/dx measurement to be between zero and 2.5 standard deviations of the pion hypothesis and at least 30 wire hits. This yields a muon (+pion) purity between 1.4 and 45 GeV/c of 97.5%. Figure 8.2 shows the comparison between data and Monte Carlo for the different tags. In the momentum windows where enough statistics is available, the ratios of data over Monte Carlo in figures 8.1 and 8.2 eventually can be used as an efficiency correction factor in physics analyses.

Another way to compare data with Monte Carlo is simply to plot the fraction of tagged particles ($N_{\text{tagged}}/N_{\text{tot}}$) out of the total sample of selected tracks. Figure 8.3 shows this fraction for 'standard' RNEWTAG (IXX $\geq$ 2) for 'very loose' selected tracks (JXX $\geq$ 0) versus momentum.

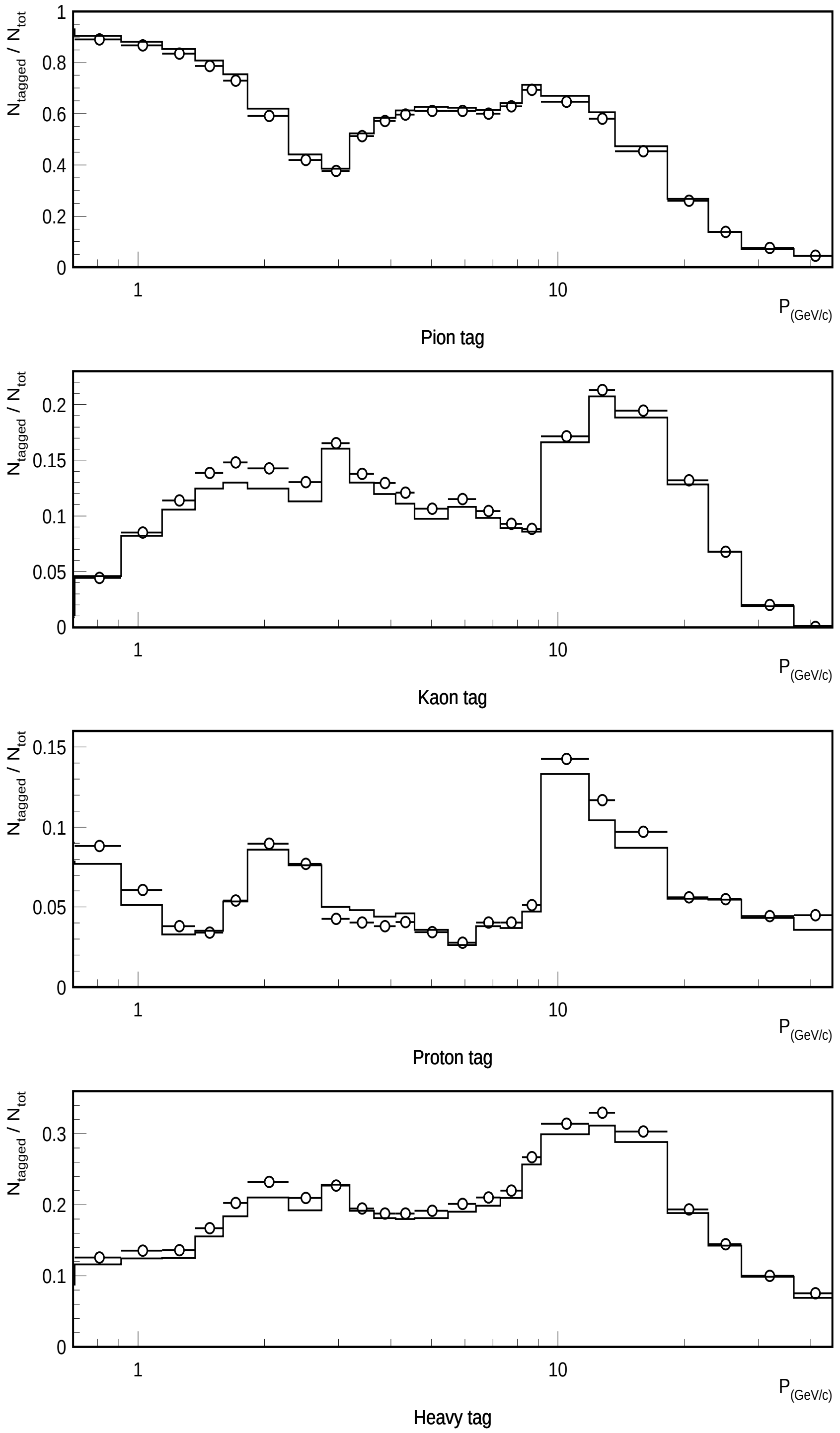

Figure 8.3: Fraction of tagged hadrons in data (points) and Monte Carlo (lines) for 'standard' RNEWTAG output (IXX $\geq$2) and 'very loose' selected tracks (JXX $\geq$0) versus momentum (Barrel RICH).

8.2 Reconstruction of Some Resonances in $Z^0 \to q\overline{q}$

In this section the performance of RICH $\pi^{\pm}$, $K^{\pm}$ and $p\overline{p}$ -identification and it's relevance for physics analyses will be illustrated on the basis of the reconstruction of some resonances[1] in $Z^0 \to q\overline{q}$. Both for data and Monte Carlo, $\sim$1 000 000 selected hadronic events (94-B3 production) were used. The event selection criteria will be discussed in more detail in section 9.1. To obtain optimal statistics for particle identification, the NEWTAG package was applied without requiring the Outer Detector (OD) information to be used in the track reconstruction (i.e. XNEWTAG). In all selected events, tracks were only accepted in the barrel region and with momenta between 0.7 and 45 GeV/c for which the TPC information was used in the track reconstruction. Additionally, the opening angle between two tracks was required to be less than 53° ($\cos\theta > 0.6$). If not stated otherwise, this holds for all cases discussed below.

8.2.1 Reconstruction of $\phi(1020) \to K^+K^-$

For the reconstruction of $\phi(1020) \to K^+K^-$ extra track selection requirements were included on the impact parameter[2]. Only those tracks were selected which had an impact parameter less than 1 cm transverse to the beam axis (R_ϕ) and less than 2 cm along the beam axis (R_z).

Figure 8.4 shows the development of the K^+K^- invariant mass distribution for different XNEWTAG requirements. From left to right, the track selection increases from 'very loose', 'loose', and 'standard' to 'tight' (i.e. JKA $\geq 0, 1, 2, 3$). From top to bottom, first the distributions without RICH particle identification, followed in descending order by 'very loose', 'loose', 'standard' and 'tight' kaon tagging (i.e. IKA $\geq 0, 1, 2, 3$) applied for *both* particles. For data (Monte Carlo) the circles (solid lines) indicate the signal $M(K^+K^-)$ and the triangles (dashed lines) the like-sign background $M(K^{\pm}K^{\pm})$. *Without* particle identification, only a small signal of $\phi(1020)$ is visible whereas increasingly clear signals appear *with* particle identification.

To illustrate the performance of the different XNEWTAG output values, the ratio signal to like-sign background (S/Bg) for each combination of tag and track quality selection (IJKA) is indicated in each plot. The ratios S/Bg are derived simply by integrating over the bins under the peak of the distributions obtained from the data, subtracting the content of the same bins derived from the like-sign background, thus not accounting for reflections.

From this fairly modest approach on the $\phi(1020)$ reconstruction one may draw two conclusions. Firstly, using RICH particle identification, one can easily obtain a ratio of S/Bg ~ 1.6. By applying different tag and track selection requirements, this ratio can be increased up to S/Bg ~ 4.8, thus improving by a factor ~ 3. Secondly, the results on

[1] anti-particles are implicitly included, unless stated otherwise.

[2] the impact parameter is defined as the distance of closest approach of the track to the primary vertex.

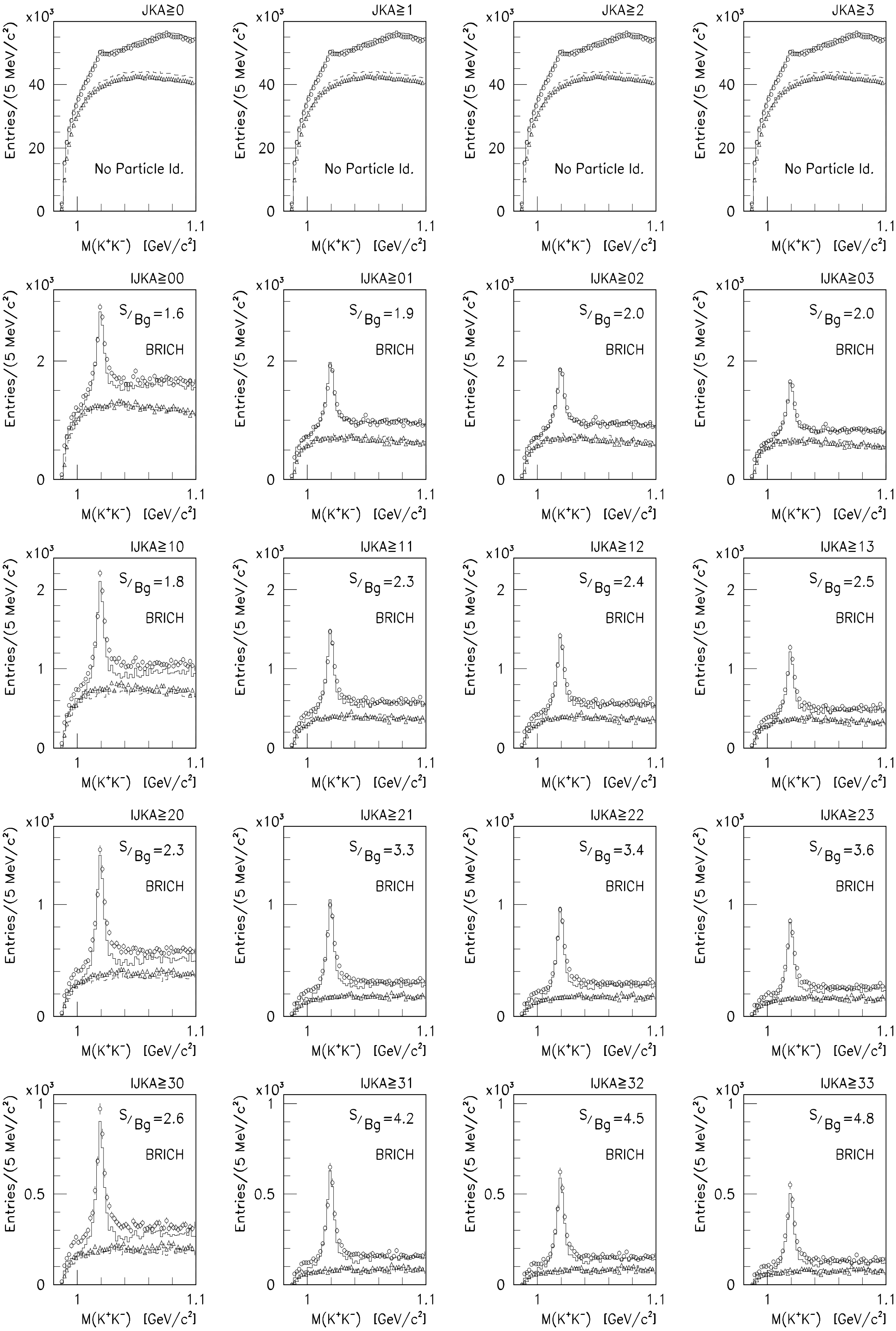

Figure 8.4: XNEWTAG reconstruction of $\phi(1020) \to K^+K^-$ for 'very loose', 'loose', 'standard' and 'tight' tagging and track selection for *both* particles, compared to the same track selections without particle identification. The circles (solid lines) indicate the signal $M(K^+K^-)$ for data (Monte Carlo). The triangles (dashed lines) indicate the like-sign background. IJKA $\geq$ IJ $\equiv$ (IKA $\geq$ I, JKA $\geq$ J), I,J =0,1,2,3.

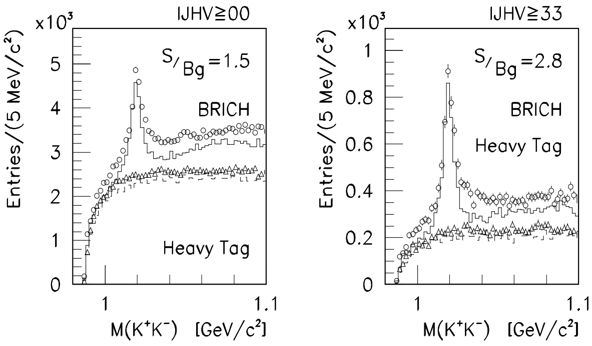

Figure 8.5: XNEWTAG reconstruction of $\phi(1020)\rightarrow K^+K^-$ for 'very loose' and 'tight' heavy tag and track selection for both particles. The circles (solid lines) indicate the signal $M(K^+K^-)$ for data (Monte Carlo). The triangles (dashed lines) indicate the like-sign background.

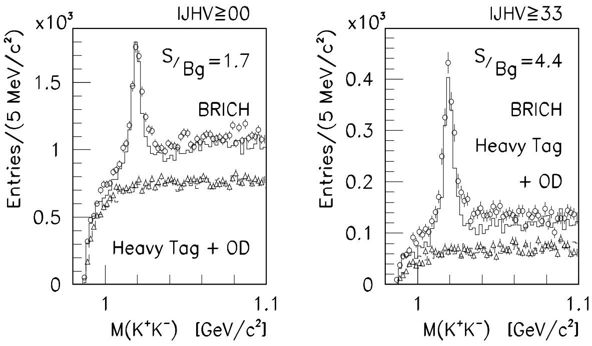

Figure 8.6: RNEWTAG reconstruction of $\phi(1020)\rightarrow K^+K^-$ for 'very loose' and 'tight' heavy tag and track selection for both particles. The circles (solid lines) indicate the signal $M(K^+K^-)$ for data (Monte Carlo). The triangles (dashed lines) indicate the like-sign background.

data and Monte Carlo are in good agreement. This points out that both the detector simulation [37] and the hadronic generator tuning [21] for kaons are performing very well.

An alternative way to select an enriched kaon sample with RICH is to apply the heavy particle tag instead of explicitly tagging kaons. The heavy particle tag puts emphasis on a high $\pi^\pm$ rejection and does not distinguish between $K^\pm$ and $p\overline{p}$ identification (see section 7.5). Figure 8.5 shows the result obtained from the most loose and the most tight heavy tag (XNEWTAG). The circles (solid lines) indicate the signal $M(K^+K^-)$ for data (Monte Carlo) and the triangles (dashed lines) the like-sign background $M(K^\pm K^\pm)$. Again, clear signals of $\phi(1020)$ appear. The results on data and Monte Carlo are in less good agreement, which can partly be understood from the working principle of the heavy tag. Particles with momentum $2.7 < p < 8.5$ GeV$/c$ are tagged as a heavy particle if no Cherenkov angle is measured in the gas radiator. However, if for example, a track is not well reconstructed, or a MWPC's has tripped, *also* no Cherenkov angle will be measured. For the data, this may cause a higher number of combinations per event to calculate M(KK).

To assure that a track is well reconstructed, one can require that the OD information has been used in the track reconstruction (RNEWTAG). This is illustrated in figure 8.6. By including the OD, a better agreement between data and Monte Carlo is obtained and the ratio S/Bg can be increased to ~ 4.4. However, the $\phi(1020)$ reconstruction efficiency drops by a factor ~ 2.

Regarding figure 8.5, one can make a direct comparison with the equivalent plots in figure 8.4 i.e. the first plot of the second row (IJKA $\geq$ 00) and the fourth plot of the bottom row (IJKA $\geq$ 33). By applying the heavy tag (without the OD requirement), one can achieve an increase in the $\phi(1020)$ reconstruction efficiency up to a factor ~ 2 at

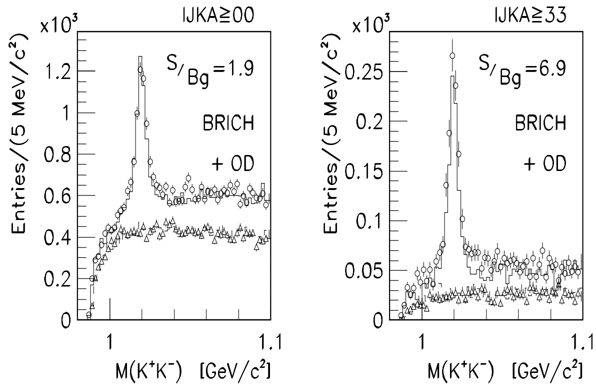

Figure 8.7: RNEWTAG reconstruction of $\phi(1020) \to K^+K^-$ for 'very loose' and 'tight' kaon tag and track selection for both particles. The circles (solid lines) indicate the signal $M(K^+K^-)$ for data (Monte Carlo). The triangles (dashed lines) indicate the like-sign background.

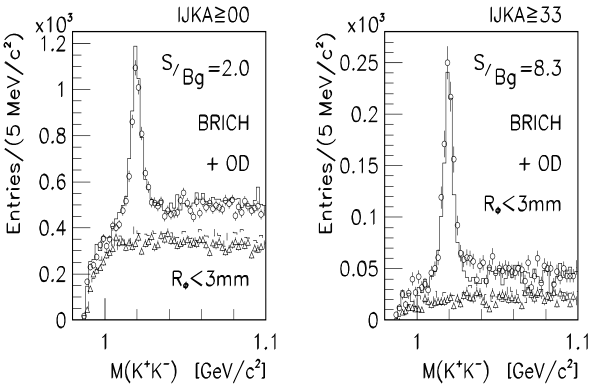

Figure 8.8: RNEWTAG reconstruction of $\phi(1020) \to K^+K^-$ like figure 8.7 reducing the selection criteria on the track impact parameter from $R_\phi < 1$ cm to $R_\phi < 3$ mm.

the cost of a decrease of up to $\sim 50\%$ in the ratio S/Bg relative to the kaon tag. There are several options to increase the purity in the reconstruction of $\phi(1020) \to K^+K^-$ even further:

1. By requiring the OD information to be used in the track reconstruction, one can increase the ratio S/Bg up to ~ 6.9, as is shown in figure 8.7. The loss in reconstruction efficiency is about a factor 2.

2. The requirements on the particle impact parameters can be set more tight (e.g. $R_\phi < 3$ mm). Combined with the previous option, this can increase the ratio S/Bg up to ~ 8.3. This is shown in figure 8.8.

3. At low momenta ($\sim 0.2 < p < 0.7$ GeV/c), the RICH kaon identification can be complemented by the measurement of the specific energy loss $\mathrm{d}E/\mathrm{d}x$ in the TPC.

For the DELPHI measurement of inclusive $\phi(1020)$ production [71], these three options have been successfully applied.

The availability of different methods to obtain -in this case- an enriched kaon sample with different degrees of tagging and track-quality selections helps to ease the study of systematic effects due to the RICH particle identification (an equivalent study will be discussed in more detail in section 9.4.3).

8.2.2 Reconstruction of $\mathrm{K_S^0}$, ρ^0, $\mathrm{f_0(980)} \to \pi^+\pi^-$

For the measurement of the $\pi^+\pi^-$ invariant mass distributions the requirements on the track impact parameters were set rather loose, less than 10 cm for R_ϕ and less then 20 cm for R_z. Figure 8.9 shows the results from the data and Monte Carlo for 'very loose' track selection *without* particle identification (left) and *with* 'very loose' particle identification (middle). The lower combinatorics for the data distribution may be understood from the same explanation as discussed before for the heavy particle tag (section 8.1, page 93). On the right hand side the like-sign subtracted distributions *with* particle identification are shown. Clear signals from $\mathrm{K_S^0} \to \pi^+\pi^-$, $\rho^0 \to \pi^+\pi^-$ and $\mathrm{f_0(980)} \to \pi^+\pi^-$ are visible. However, due to the high $\pi^\pm$ multiplicity in $\mathrm{Z^0}$ decays, no obvious enrichment of the different signals can be achieved. The shape of the distributions for low $\mathrm{M}(\pi^+\pi^-)$ is due to reflections which also cause the ρ^0-peak to be shifted.

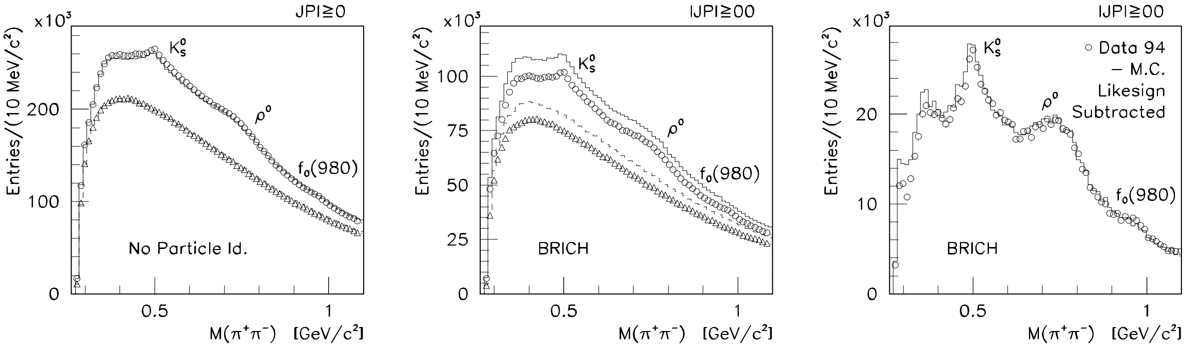

Figure 8.9: XNEWTAG invariant mass distributions for $\mathrm{M}(\pi^+\pi^-)$ without particle identification (left), with 'very loose' $\pi^\pm$ tag and track selection for both particles (middle) and the same distributions after subtraction the like-sign background (right). The circles (solid lines) indicate $\mathrm{M}(\pi^+\pi^-)$ for data (Monte Carlo). The triangles (dashed lines) indicate the like-sign background.

As for the $\phi(1020)$, an improvement in the reconstruction of ρ^0 and $\mathrm{f_0(980)}$ (fig. 8.10) can be obtained by requiring the OD and setting tighter impact parameter cuts ($R_\phi < 3$ mm). The latter not only suppresses contributions from $\mathrm{K_S^0} \to \pi^+\pi^-$ but also suppresses reflections, especially at low $\mathrm{M}(\pi^+\pi^-)$.

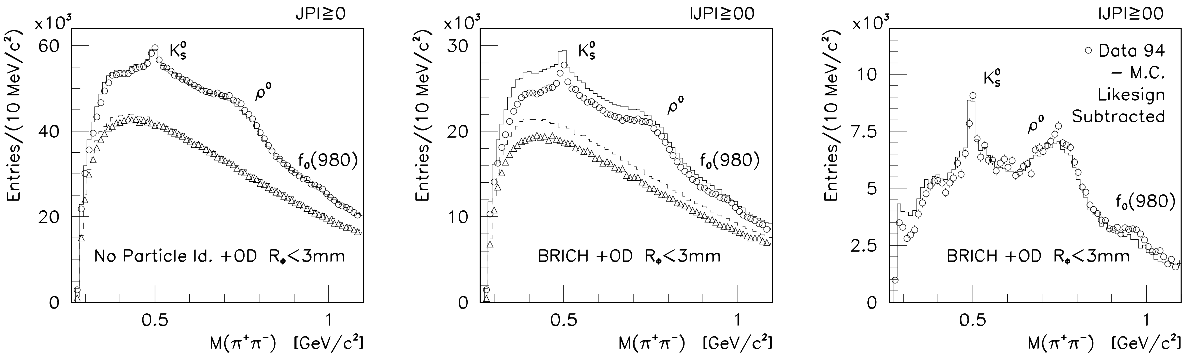

Figure 8.10: The invariant mass distributions for $\mathrm{M}(\pi^+\pi^-)$ like figure 8.9 but now RNEWTAG combined with $R_\phi < 3$mm.

8.2.3 Reconstruction of $K^*(892)^0 \to K^+\pi^-$

To obtain the $K^+\pi^-$ invariant mass distributions, the track impact parameters were required to be less than 1 cm in R_ϕ and less than 2 cm in R_z. Additionally, a particle was rejected if it was simultaneously tagged as a kaon and a pion. If no particle identification is applied (left fig. 8.11), hardly any signal of the $K^*(892)^0 \to K^+\pi^-$ is observable, whereas a clear mass peak appears using 'very loose' XNEWTAG (middle fig. 8.11). The data are well reproduced by the Monte Carlo.

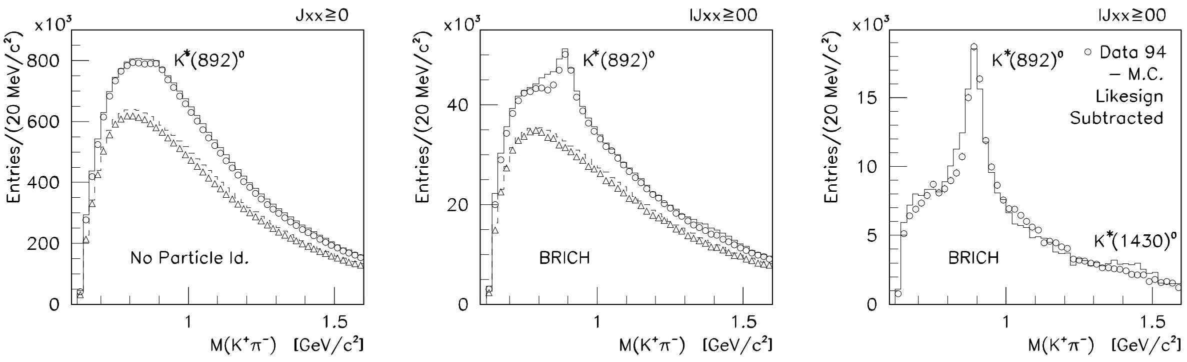

Figure 8.11: XNEWTAG invariant mass distributions for $M(K^+\pi^-)$ without particle identification (left), with 'very loose' tag and track selection for both particles (middle) and the same distributions after subtraction of the like-sign background (right). The circles (solid lines) indicate $M(K^+\pi^-)$ for data (Monte Carlo). The triangles (dashed lines) indicate the like-sign background.

Subtracting the like-sign background (right fig. 8.11), also a signal of $K^*(1430)^0$ becomes visible, but only in the Monte Carlo and not in the data distribution. The $K^*(1430)^0$ production rate has been measured by the OPAL Collaboration [72] using 1990–1992 LEP data. This measurement has been included in the 1994 tuning of the DELPHI hadronic event generator [21]. However, this $K^*(1430)^0$ production rate seems to be a factor 2.4 higher than a more recent DELPHI measurement [71] using 94-B3 RICH data.

8.2.4 Reconstruction of $\Lambda^0 \rightarrow p\pi^-$

For the measurement of the $p\pi^-$ invariant mass distributions, the track impact parameters were required to be less than 10 cm for R_ϕ and less then 20 cm for R_z. A particle was rejected if it was simultaneously tagged as a proton and a pion. Additionally, the leading particle had to be tagged as a proton[3], or, in the case without particle identification, the leading particle was given the proton mass. Without particle identification, no signal of $\Lambda^0 \rightarrow p\pi^-$ can be seen (left fig. 8.12). After application of the 'very loose' tag and track selection (middle, right fig. 8.12), the Λ^0 signal becomes clearly visible.

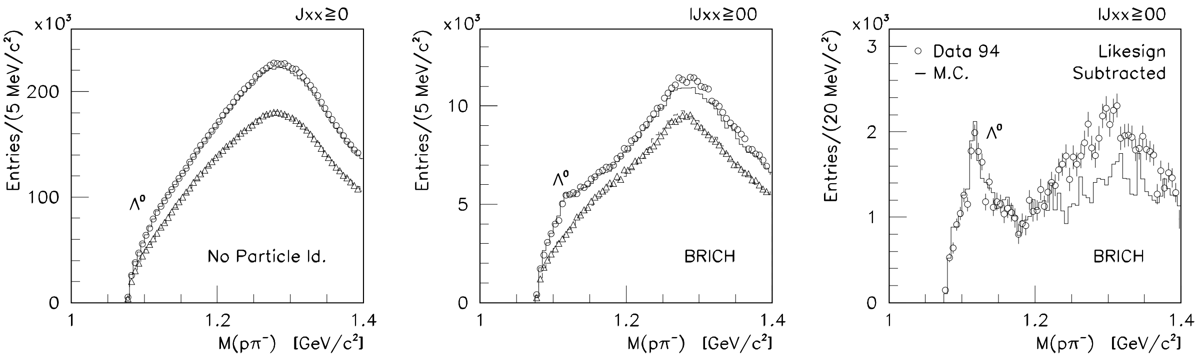

Figure 8.12: XNEWTAG invariant mass distributions for $M(p\pi^-)$ without particle identification (left), with 'very loose' tag and track selection (middle) and the same distributions after subtraction of the like-sign background (right). The circles (solid lines) indicate $M(p\pi^-)$ for data (Monte Carlo). The triangles (dashed lines) indicate the like-sign background.

The RICH particle identification can complement the DELPHI V^0 reconstruction [32] in the barrel region. Here, the background can be suppressed by rejecting the V^0 candidate if the leading outgoing particle is identified as a pion by the RICH. In this way, the Λ^0 purity of an optimised V^0 sample can be increased from $\sim$90% up to $\sim$97% [73][74].

[3] in $\Lambda^0 \rightarrow p\pi^-$, of the two outgoing particles, the proton obtains the largest fraction of the Λ^0 energy.

8.2.5 Reconstruction of $\Lambda^0(1520) \rightarrow pK^-$

To obtain the pK^- invariant mass distributions, the track impact parameters were required to be less than 1 cm in R_ϕ and less than 2 cm in R_z and a particle was rejected if it was simultaneously tagged as a proton and a kaon. Applying no particle identification (obviously) does not yield any $\Lambda^0(1520)$ signal (left fig. 8.13). However, by using the loosest RICH particle identification, also no obvious signal of $\Lambda^0(1520)$ can be observed (middle, right fig. 8.13).

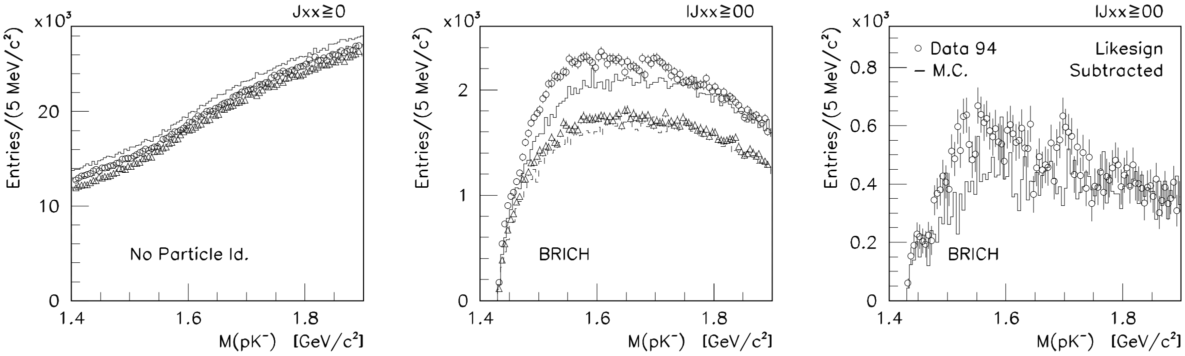

Figure 8.13: XNEWTAG invariant mass distributions for $M(pK^-)$ without particle identification (left), with particle identification (middle) and the distributions after having subtracted the like-sign background (right). The circles (solid lines) indicate $M(pK^-)$ for data (Monte Carlo). The triangles (dashed lines) indicate the like-sign background.

Only after including the TPC particle identification below 0.7 GeV/c and applying tight tagging, the $\Lambda^0(1520)$ mass peak appears, as is shown in figure 8.14. Only data are shown since $\Lambda^0(1520)$ production is not included in the Monte Carlo. Additionally, extra selection criteria were applied. The impact parameters were required to be less than 2.5 mm in R_ϕ and R_z and the $\cos\theta_h$ was required to be larger than -0.8, where θ_h is the helicity angle of the proton i.e. the angle of the proton in the pK^- rest frame with respect to pK^- line of flight.

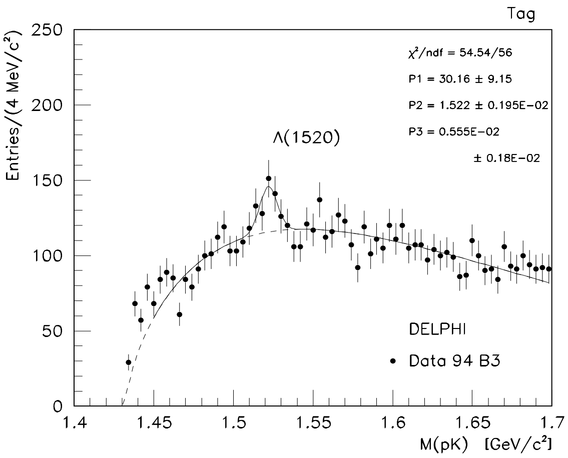

Figure 8.14: The invariant mass distributions for $M(pK^-)$ applying XNEWTAG complemented by the TPC particle identification for $0.3 < p < 0.7$ GeV/c, ('tight' tagging and 'loose' track selection). The area above the dashed line contains about 120 signal events. The ratio signal to like-sign background in the peak is about 1.26.

8.3 Reconstruction of Some Resonances in $Z^0 \to b\bar{b}$

The aim of this section is to illustrate how the RICH particle identification performs under different circumstances compared to the previous section (e.g. different event topology) and having $\sim$ 80% less statistics available. A subsample of b-flavour enriched[4] events was selected. For reasons of simplicity, only the most relevant distributions are shown. Also here, anti-particles are implicitly included, the opening angle between two tracks was required to be less then $\sim 53°$ and the OD information was *not* required in the track reconstruction.

8.3.1 Reconstruction of $\phi(1020) \to K^+K^-$

For the most loose and the most tight tagging and track selection, the invariant mass distributions for K^+K^- are shown in figure 8.15. The tagging and track selection requirements were taken identical to the equivalent entries (IJKA $\geq 00, 33$) in figure 8.4.

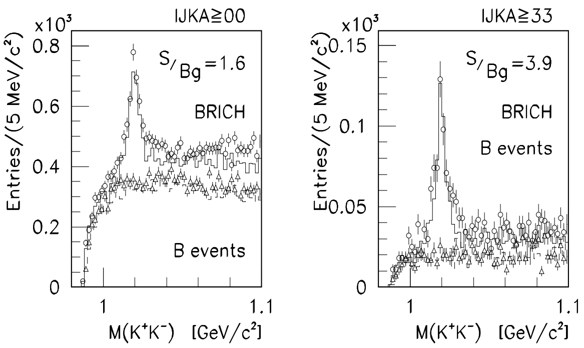

Figure 8.15: XNEWTAG reconstruction of $\phi(1020) \to K^+K^-$ in b-events for 'very loose' and 'tight' tag and track selection for both particles. The circles (solid lines) indicate the signal $M(K^+K^-)$ for data (Monte Carlo). The triangles (dashed lines) indicate the like-sign background.

Keeping in mind that the $\pi^\pm$, $K^\pm$ and $p\bar{p}$ production rates in the DELPHI tuning of the hadronic event generator [21] is performed for inclusive particle production only, the agreement of the data with Monte Carlo prediction for b-events is very good.

By enhancing the tagging requirements, the ratio signal to background can be increased by a factor ~ 2.4 from S/Bg ~ 1.6 up to S/Bg ~ 3.9.

[4]The method of selecting b-events will be discussed in detail in section 9.1. The most relevant point in the frame of this section is that the b-event probability ($\mathcal{P}_E^+$) was required to be less than 0.01, producing a sample of $\sim$198 000 b-enriched events with a $\sim$ 78% b-purity.

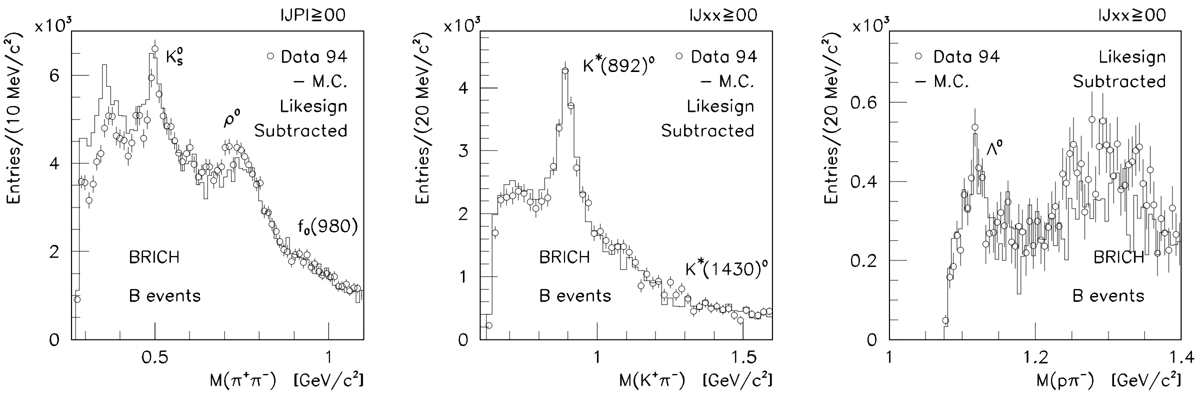

Figure 8.16: XNEWTAG like-sign subtracted invariant mass distributions in b-events for $M(\pi^+\pi^-)$ (left), $M(K^+\pi^-)$ (middle) and $M(p\pi^-)$ (right). Both particles have been tagged 'very loose'. The open points indicate the data, the histograms represent the Monte Carlo.

8.3.2 Reconstruction of K^0_S, ρ^0, $f_0(980)$, $K^*(892)^0$ and Λ^0

The like-sign subtracted invariant mass distributions for $M(\pi^+\pi^-)$, $M(K^+\pi^-)$ and $M(p\pi^-)$ in the sample of b-enriched events are shown in figure 8.16. The tag and track selection requirements were taken identical to the equivalent figures from the previous section (figs 8.9, 8.11, 8.12). The mass peaks of K^0_S, ρ^0, $K^*(892)^0$ and Λ^0 are clearly visible. Apart from the ρ^0, the Monte Carlo predictions for b-events are in rather good agreement with the data, especially in the peak-regions.

Chapter 9

$\pi^{\pm}$, $\mathrm{K}^{\pm}$ and $\mathrm{p\overline{p}}$ Production in $\mathrm{Z}^0 \rightarrow q\overline{q}$, $\mathrm{Z}^0 \rightarrow b\overline{b}$, $\mathrm{Z}^0 \rightarrow u\overline{u}, d\overline{d}, s\overline{s}$

During the 1994 LEP run DELPHI collected ~1 400 000 hadronic Z^0 events. Throughout the year, the RICH detectors were operational in optimal and stable conditions. Due to an improved understanding of the RICH-detector (as indicated in chapter 6) and supplementary implementations in the RICH software, a significant signal of high momentum protons was observed for the first time in the barrel gas RICH after the 94-B3 data processing.
Using the barrel RICH detector which offers the possibility of a complete $\pi^{\pm}$, $\mathrm{K}^{\pm}$ and $\mathrm{p\overline{p}}$ identification, DELPHI is the only LEP-experiment able to perform precision measurements on $\pi^{\pm}$, $\mathrm{K}^{\pm}$ and $\mathrm{p\overline{p}}$ spectra in hadronic Z^0 decays, covering the full momentum range from 0.7 up to 45 GeV/c. Below 0.7 GeV/c, the RICH particle identification can be complemented by the measurement of the specific energy loss $\mathrm{d}E/\mathrm{d}x$ in the TPC, down to 0.3 GeV/c.
The analysis on $\pi^{\pm}$, $\mathrm{K}^{\pm}$ and $\mathrm{p\overline{p}}$ production, presented in this chapter, is based on the barrel RICH and the NEWTAG package described in chapter 7.

Three event samples were considered for this analysis, a sample containing all quark flavours i.e. *udscb* (mostly referred to as the inclusive sample or '$q\overline{q}$-sample'), a subsample of b-flavour enriched events (mostly referred to as 'b-sample') and a uds-flavour enriched subsample ('uds-sample'). The selection criteria for these events will be discussed in the next section.

9.1 Event and Charged Particle Selection Criteria

The availability of a large data set allows measurements on identified particles with high precision and a selection of hadronic events with minimal detector distortions. The hadronic selection was performed in three steps. A track selection for the global event selection, then the hadronic event selection and finally an extra track selection

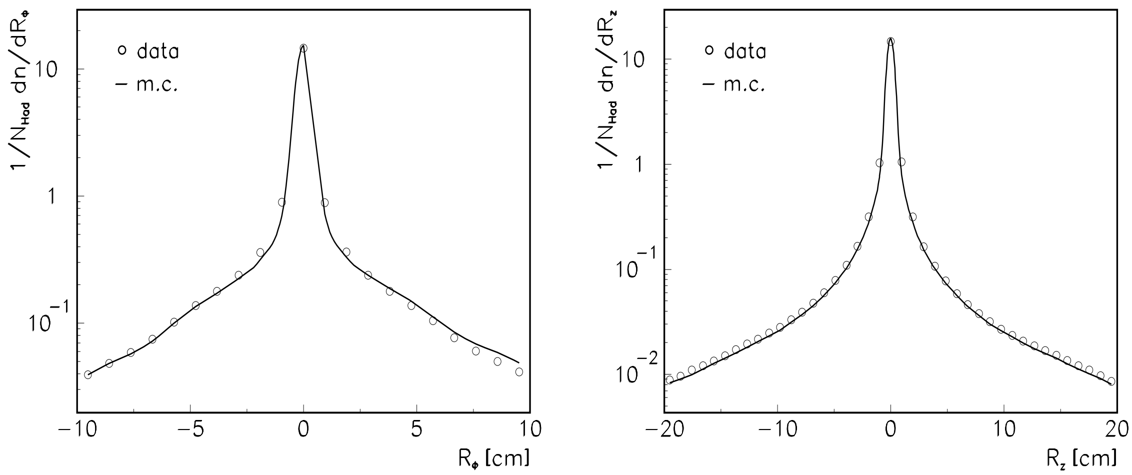

Figure 9.1: The impact parameter distributions in R_ϕ and R_z after the hadronic event selection for data and Monte Carlo.

for the barrel RICH. For the first step, tracks were selected according to the following criteria:

a. The particle momentum p had to be greater than 0.3 GeV/c and lower than 70 GeV/c. The lower limit is necessary because low momentum particles follow a strongly curved path in the 1.2 T magnetic field, reducing the detection (i.e. reconstruction) efficiency. The upper limit reduces the selection of tracks with a large uncertainty.

b. The measured track length was required to be larger than 30 cm, mainly to assure a reasonable momentum resolution.

c. The relative uncertainty on the measured momentum had to be smaller than 50% and the absolute uncertainty had to be less than 5 GeV/c.

d. The impact parameter had to be less than 10 cm in radius transverse to the beam axis (R_ϕ) and less than 20 cm along the beam axis (R_z). This requirement reduces beam gas events, cosmic events as well as tracks originating from interactions with detector materials.

e. The track had to have a polar angle between 15° and 165° .

All charged particles which passed the above criteria were taken into consideration for the second selection step, selecting hadronic events, based on the following requirements:

α. The candidate event had to contain at least 5 charged tracks with $p > 0.3$ GeV/c. This requirement totally suppresses Bhabha events and substantially reduces lepton decays of the Z^0 as well as two-photon events.

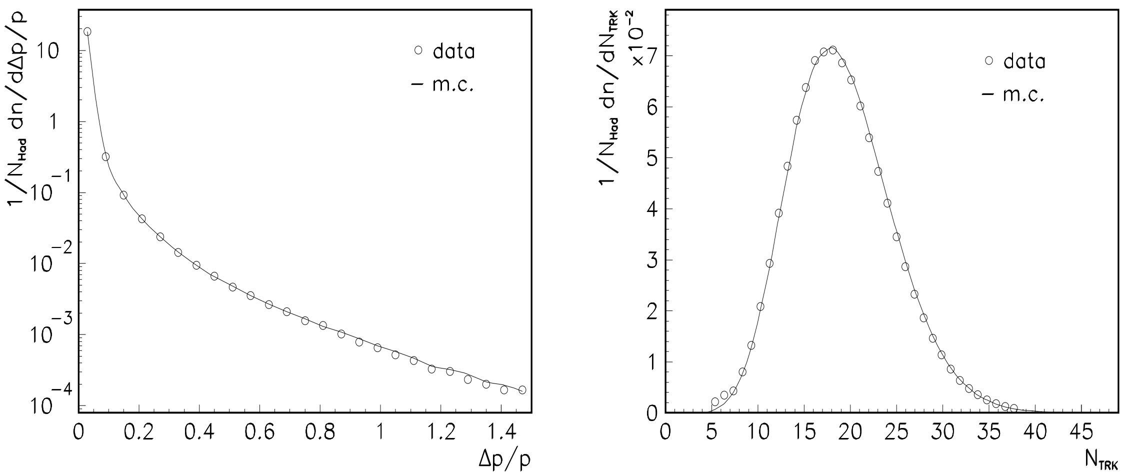

Figure 9.2: The distributions for $\Delta p/p$ and the number of selected tracks per event after the hadronic event selection for data and Monte Carlo.

β. The total energy of the charged particles in the event had to be larger than 15 GeV (i.e. larger than 16% of the centre of mass energy).

γ. At least one charged track per event was required to have a polar angle inside the DELPHI barrel region, i.e. between 47° and 133° , where the barrel RICH is operational.

Since this analysis is based on data measured by the barrel RICH detector, as a third selection step, only those tracks from the selected hadronic events were accepted if they met the following additional criteria:

i. The track polar angle had to be between 47° and 133° .

ii. The particle momentum had to be larger than 0.7 GeV/c.

iii. TPC information was used for the track reconstruction.

iv. Particles with $p < 2.7$ GeV/c had to have negative charge. By this requirement particles coming from interactions with detector materials (i.e. secondary interactions) are strongly suppressed.

A fifth track selection option for the barrel region could be:

v. The Outer Detector (OD) information was used for the track reconstruction.

This option obviously helps to select a sample of better reconstructed tracks and thus helps to achieve a higher $\pi^{\pm}$, $K^{\pm}$ and $p\overline{p}$ purity after particle identification. Unfortunately, the loss in statistics (see fig. 7.1, page 81) due to this requirement does not justify the relatively small gain in the final purity, especially in the case of the b-sample.

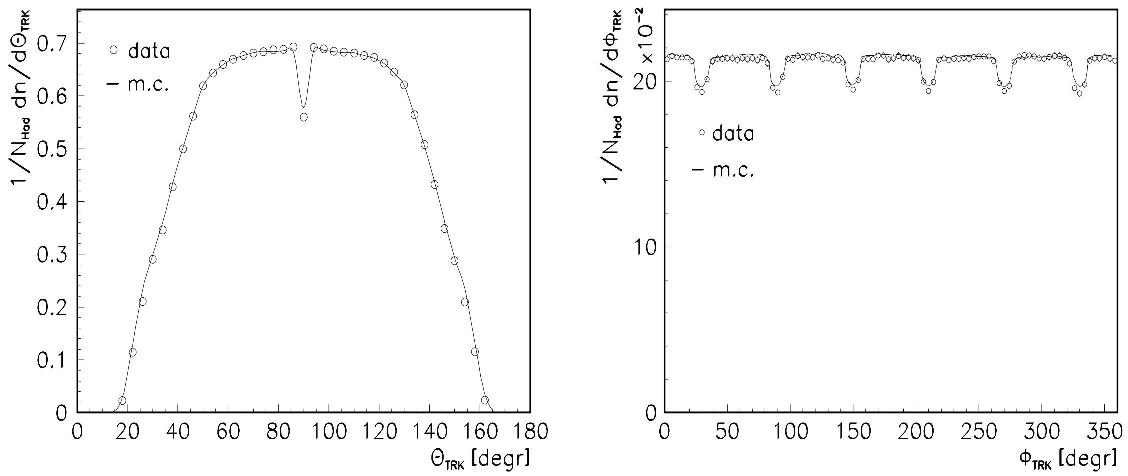

Figure 9.3: The distributions of θ_{track} and ϕ_{track} after the hadronic event selection for data and Monte Carlo.

Therefore it has not been applied for the nominal track selection. However, for the study of systematic effects, it turns out to be very useful, as will be discussed in section 9.4.3.

Finally, a run-selection was performed, removing small data taking periods which were potentially unstable[1].

Comparing data with Monte Carlo (DELSIM), figure 9.1 shows the normalised distributions of the impact parameters in R_ϕ and in R_z, for those tracks which passed the hadronic event selection. Likewise, figure 9.2 shows the agreement between data and Monte Carlo for $\Delta p/p$ and the number of particles per selected event. For the latter, one can observe a small discrepancy between data and Monte Carlo for events with a low particle multiplicity. These background events are caused by $e^+e^- \rightarrow \gamma\gamma \rightarrow$ hadrons and $Z^0 \rightarrow \tau^+\tau^- \rightarrow$ hadrons. Finally, figure 9.3 shows the same comparison for the normalised distributions in θ_{track} and ϕ_{track}. Clearly visible are the effects of the edges between the 60° segments and the mid-wall of the TPC (as described in chapter 4), which slightly reduce the track reconstruction efficiency. However, these effects are well reproduced by the detector simulation.

Of the in total ~1 400 000 events collected by DELPHI in 1994, ~1 068 000 hadronic events were selected after all the selection criteria. Out of ~2 380 000 generated full detector simulated Monte Carlo events, ~2 027 000 hadronic events passed the same selection criteria.

[1]The run periods concerned, mostly refer to detector start-up periods, power interruptions, large pressure drops during thunderstorms etc.

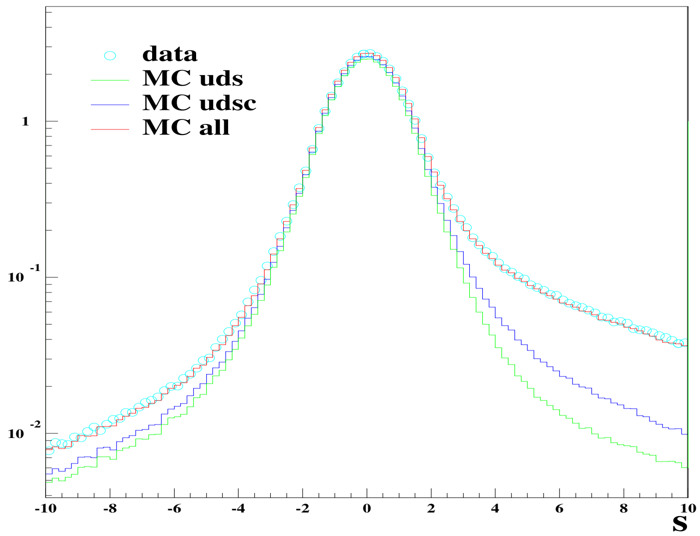

Figure 9.4: The data and Monte Carlo significance distributions for different event-samples.

9.2 Tagging $b\overline{b}$ and $u\overline{u}, d\overline{d}, s\overline{s}$ Events

To separate b- and uds-flavour enriched subsamples from the $q\overline{q}$-sample, the method of topological life-time b-tagging [32][75] was applied. The method, which will be discussed below, is based on the application of an algorithm calculating an event probability $\mathcal{P}_E$.

Hadrons from Z^0 decay which contain a b-quark, enjoy a long life (typically $\sim 1.6\ 10^{-12}$ sec) and have large mass and energy ($m_b \approx 5.3$ GeV$/c^2$, $\langle E_b \rangle \approx 0.7 \cdot E_{beam}$). Their average flight distance $d = \beta\gamma c\tau$ is of the order of 3 mm, which causes many b-hadron decay products to have large impact parameters.
The impact parameter is defined as the minimum distance between the reconstructed track trajectory and the reconstructed primary interaction point (primary vertex). However, the sign of the impact parameter is defined with respect to the jet direction, which implies the sign to be positive if the vector joining the primary vertex and the point of nearest approach of the track has a positive projection onto the jet-axis of the jet in which it belongs.
The uncertainty on the impact parameter is determined by the accuracy on the point of nearest approach and the accuracy on the measurement of the primary vertex. In this respect the significance S_0 of a given track is defined as the ratio of the impact parameter to its uncertainty. The significance S_0 is the only tagging variable used in the probability method which originally was proposed by the ALEPH collaboration [76]. As an example figure 9.4 shows the significance for tracks of different event flavour samples. The negative significance distribution mainly reflects the detector resolution and is used to build the track probability function $\mathcal{P}(S_0)$, which - by definition - is the probability for a track from the primary interaction to have a significance with absolute value S_0 or greater.
For any group of N tracks one can define the N-track probability according to equa-

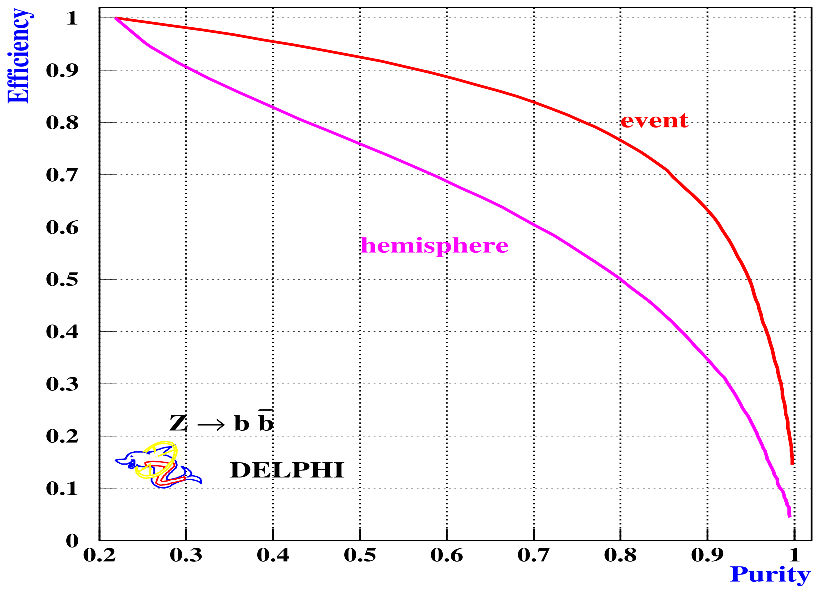

Figure 9.5: The b-tagging efficiency vs purity for the event probability $\mathcal{P}_E^+$ and for the hemisphere probability $\mathcal{P}_H^+$.

tion 9.1. $\mathcal{P}_N$ gives the probability for a group of N tracks to originate from the primary vertex. Provided that the significances of these tracks are uncorrelated, a flat distribution of $\mathcal{P}_N$ is expected for a group of tracks from the primary vertex, while tracks from b-hadron decays should have a sharp peak at zero.

$$\mathcal{P}_N \equiv \Pi \cdot \sum_{j=0}^{N-1} (-\ln \Pi)^j / j! \ , \quad \text{where} \quad \Pi \equiv \prod_{i=1}^{N} \mathcal{P}(S_i) \tag{9.1}$$

The event probability $\mathcal{P}_E^+$ is the computed probability, using all the reconstructed N-tracks of an event which have positive impact parameters. Likewise, the hemisphere probability $\mathcal{P}_H^+$ is the probability computed from the reconstructed tracks with a positive impact parameter belonging to that hemisphere. Figure 9.5 shows the relation between efficiency and purity for the event probability $\mathcal{P}_E^+$ and the hemisphere probability $\mathcal{P}_H^+$, calculated from simulated events.

For this analysis, the event probability $\mathcal{P}_E^+$ was used to select (or suppress) b-events. The comparison between data and Monte Carlo for the distribution of $\mathcal{P}_E^+$ is shown in figure 9.6. Requiring $\mathcal{P}_E^+$ to be less than 0.01 resulted in a subsample of $\sim$198 000 b-enriched events from the data. From the Monte Carlo simulation $\sim$424 000 events were selected, giving a subsample of 78.5% b-purity. The contamination of u-d-s-c flavour was respectively 2.4%,1.8%,2.6% and 14.7%.

A uds-flavour enriched event sample was obtained by using the b-tagging information to suppress b-events (i.e. anti-b-tagging). By requiring $\mathcal{P}_E^+$ to be bigger than 0.15, 668 000 events were selected from the data and 1 243 000 from the Monte Carlo, with a uds-purity of 81.7%. The contamination of b- and c-flavour was respectively 3.8% and 14.5%.

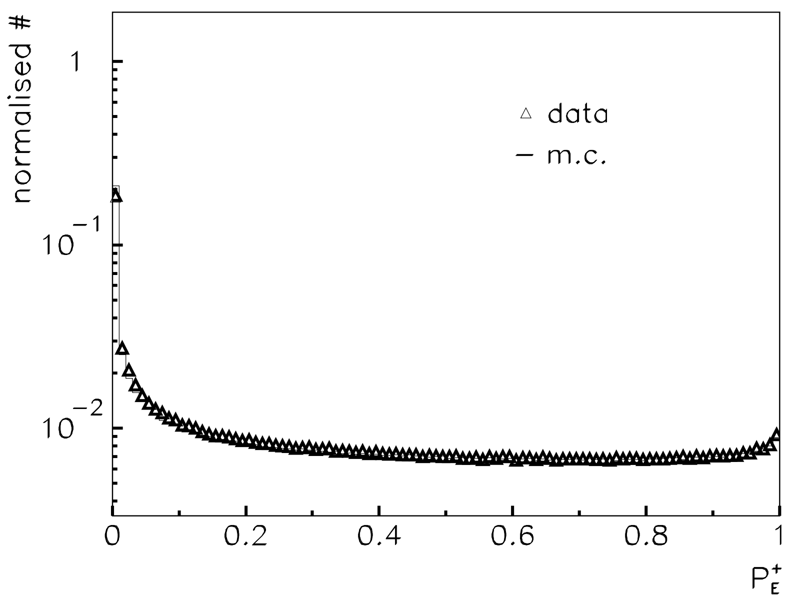

Figure 9.6: The b-tag probability distribution $\mathcal{P}_E^+$ for data and Monte Carlo.

To enable a reasonable study of the systematic effects, two more b-samples and two more uds-samples were selected. A sample of higher b-purity (82.3%) for which $\mathcal{P}_E^+ <$ 0.005 and a less pure sample (73.3%) for which $\mathcal{P}_E^+ < 0.02$. For the anti-b-tagging a uds-sample of higher purity (82.5%) was selected for which $\mathcal{P}_E^+ > 0.2$ and of lower purity (80.3%) for which $\mathcal{P}_E^+ > 0.1$. This will be discussed in more detail in section 9.4.

Alternative methods exist to tag events containing b-hadrons. Firstly, they can be reconstructed in an exclusive way from their decay products. Secondly, they can be tagged by the measurement of a high p_t lepton from the semi-leptonic decay of the b-quark. However, both methods suffer from rather low efficiencies and small branching ratios in the observable decay channels (e.g. Br($B^0 \to e^+\nu_e X$) $\approx$ 10%). The method of life-time b-tagging, on the contrary, offers a quite high efficiency and allows the combined study of $\pi^{\pm}$, K$^{\pm}$ and p$\overline{\rm p}$ production in b- and uds-events as will be discussed in the next sections.

9.3 The Analysis Method

In this analysis the NEWTAG-package is used for RICH particle identification. The real particle content of a sample is obtained from the measured particle content by efficiency matrix inversion. The efficiency matrix is derived from Monte Carlo. The computation of the real $\pi^{\pm}$, $\mathrm{K}^{\pm}$, $\mathrm{p\overline{p}}$ content[2] is expressed in equation 9.2. For $i, j = \pi^{\pm}$, $\mathrm{K}^{\pm}$ or $\mathrm{p\overline{p}}$, the vector element N_i stands for the (normalised) number of particles of kind i and matrix element $\mathcal{E}_i^j$ represents the efficiency to tag a particle of true identity i as a particle of type j. In principle, any observable can be taken for x, e.g. momentum p, $X_p = p/p_{beam}$, $\xi_p = \ln(1/X_p)$, rapidity y etc.

$$\begin{pmatrix} N_\pi \\ N_\mathrm{K} \\ N_\mathrm{p} \end{pmatrix}^{\mathrm{Real}} (x) = \begin{pmatrix} \mathcal{E}_\pi^\pi & \mathcal{E}_\mathrm{K}^\pi & \mathcal{E}_\mathrm{p}^\pi \\ \mathcal{E}_\pi^\mathrm{K} & \mathcal{E}_\mathrm{K}^\mathrm{K} & \mathcal{E}_\mathrm{p}^\mathrm{K} \\ \mathcal{E}_\pi^\mathrm{p} & \mathcal{E}_\mathrm{K}^\mathrm{p} & \mathcal{E}_\mathrm{p}^\mathrm{p} \end{pmatrix}^{-1} \cdot \begin{pmatrix} N_\pi \\ N_\mathrm{K} \\ N_\mathrm{p} \end{pmatrix}^{\mathrm{Meas.}} (x) \tag{9.2}$$

The method implicitly accounts for particle miss-identification. In other words, the (bin-by-bin) multiplication of the measured distributions $N_i^{\mathrm{Meas.}}$ by the inverted efficiency matrix $\mathcal{E}^{-1}$ corrects in one step for any miss-identification of the $\pi^{\pm}$, $\mathrm{K}^{\pm}$ and $\mathrm{p\overline{p}}$ tagging. The only condition is that the full detector simulation describes the data well, because it is used to determine the matrix elements $\mathcal{E}_i^j$. An example of the efficiency matrix for the $q\overline{q}$-sample has been discussed in greater detail for the case $x = p$ in section 7.9 and has been illustrated in figure 7.2 of the same section.

The $\pi^{\pm}$, $\mathrm{K}^{\pm}$ and $\mathrm{p\overline{p}}$ production in $q\overline{q}$-, b- and uds-events is measured in the working area of the barrel RICH particle identification, accepting particle momenta from 0.7 up to 45 GeV/c. By applying NEWTAG, one can benefit maximally from the RICH particle identification.

Firstly, for each hypothesis, NEWTAG performs different degrees of tagging (i.e. 'very loose', 'loose', 'standard' or 'tight') and in a same way it simultaneously produces different degrees of track-quality flags as listed before in table 7.1 (section 7.1). Thus one can easily select various $\pi^{\pm}$, $\mathrm{K}^{\pm}$, $\mathrm{p\overline{p}}$ samples of different purity and efficiency. This allows to estimate the systematic effects of the method and the measurements, as will be discussed in more detail in the next section.

Secondly, mainly in the momentum window between 2.7 and 8.5 GeV/c, NEWTAG offers two options for tagging heavy particles[3] (i.e. kaons, protons). Either one can choose positive identification for both $\mathrm{K}^{\pm}$ and $\mathrm{p\overline{p}}$ through the combined use of liquid and gas radiator information or one can choose not to distinguish $\mathrm{K}^{\pm}$ from $\mathrm{p\overline{p}}$ by using only the gas radiator information (see 'veto-identification', section 7.1 and heavy-tag, section 7.5). Including the heavy particle tag in this analysis offers four advantages:

[2]Since the RICH particle identification in most cases can not differentiate between $\pi^{\pm}$, $e^{\pm}$ and $\mu^{\pm}$, in this section and the next section $\pi^{\pm}$ refers to $\pi^{\pm} + e^{\pm} + \mu^{\pm}$ unless explicitly indicated.

[3]Heavy particles are -as before- defined as particles which have masses larger than the pion-mass.

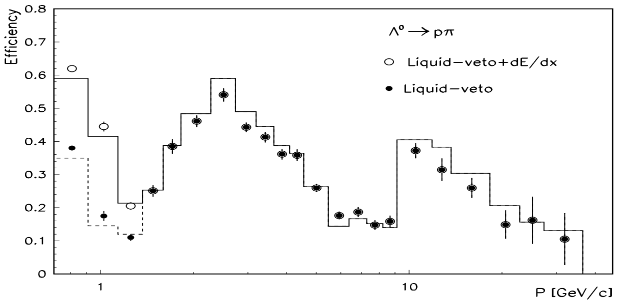

Figure 9.7: The gain in proton tagging efficiency due to the combination of RICH with the dE/dx measurement of the TPC at low momenta, tested on data and Monte Carlo with protons from Λ^0-decay.

1. It has a significantly higher efficiency compared to the sum of K$^{\pm}$ and p$\overline{\text{p}}$ (see figure 7.5, page 84).
2. By comparing the heavy-tag result with the sum of K$^{\pm}$ and p$\overline{\text{p}}$ one can verify systematic effects caused by the identification based on the liquid radiator (since it is used for K$^{\pm}$, p$\overline{\text{p}}$ but omitted in the heavy-tag).
3. One has the opportunity to perform a consistency check. The results on heavy-tag should be in agreement with the sum of the results obtained on K$^{\pm}$ and p$\overline{\text{p}}$.
4. It simplifies the method of matrix inversion. The 3x3 matrix equation 9.2 is reduced to the 2x2 matrix equation as expressed in equation 9.3.

$$\begin{pmatrix} N_\pi \\ N_{\mathrm{Hv}} \end{pmatrix}^{\mathrm{Real}} (x) = \begin{pmatrix} \mathcal{E}_\pi^\pi & \mathcal{E}_{\mathrm{Hv}}^\pi \\ \mathcal{E}_\pi^{\mathrm{Hv}} & \mathcal{E}_{\mathrm{Hv}}^{\mathrm{Hv}} \end{pmatrix}^{-1} \cdot \begin{pmatrix} N_\pi \\ N_{\mathrm{Hv}} \end{pmatrix}^{\mathrm{Meas.}} (x) \tag{9.3}$$

Note: from here onwards, the 3x3 matrix inversion method will be referred to as the '3x3-method' and the 2x2 matrix inversion method will be referred to as the '2x2-method'.

As already indicated in section 7.4, the low momentum proton tag ($p < 1.3$ GeV/c) based on the liquid veto-information has a low efficiency. This efficiency can be increased through the combination of the TPC dE/dx-measurement with the NEWTAG for protons, defining similar degrees of tagging and track quality flags. The dE/dx-proton tag for particle momenta between 0.7 and 1.3 GeV/c has been based on σ_{acc} – depending on the measured and expected dE/dx value and the uncertainty – according to equation 9.4.

$$\sigma_{\mathrm{acc}} = \frac{|\,(\mathrm{d}E/\mathrm{d}x)^{\mathrm{meas.}} - (\mathrm{d}E/\mathrm{d}x)^{\mathrm{exp.(p)}}\,|}{\sigma_{\mathrm{d}E/\mathrm{d}x}} \tag{9.4}$$

Tag values are set to 0,1,2 or 3 if the dE/dx measurement respectively is inside 3 ('very loose'), 2.5 ('loose'), 2 ('standard') or 1.5 ('tight') standard deviations of the proton

hypothesis, i.e. $\sigma_{\mathrm{acc}} < 3, 2.5, 2, 1.5$ (the tag value is set to -1 if σ_{acc} is larger than 3 standard deviations). Likewise, the track quality flag has been set to 0,1,2 or 3 if the number of wire hits in the TPC was larger than 30, 50, 70 or 90. The quality flag has been set to -1 if the number of wire hits in the TPC was below 30.
Figure 9.7 illustrates the gain in efficiency in contrast with the RICH-only proton tag of figure 8.1 for data and Monte Carlo 'standard' tag and 'very loose' track selection. However, the efficiency will drop rapidly if one chooses to apply a more tight track selection, both for the RICH-only tag and the combination with TPC.

Aiming for optimal statistics for the measurement of $\pi^{\pm}$, $\mathrm{K}^{\pm}$, $\mathrm{p\overline{p}}$ production in b-events, the 'loose' tag option was chosen. The b-sample obviously contains the lowest number of events compared to the $q\overline{q}$- and the uds-sample. For the same reason also 'loose' track quality criteria were applied besides the general requirements i-iv listed in section 9.1. For consistency, also for the $q\overline{q}$- and the uds-events the 'loose' tag and 'loose' track quality selection were applied. Additionally the 'loose' tag and track quality requirement allows high statistics for the selection of pions from $\mathrm{K^0_S} \to \pi^+\pi^-$ and protons from $\Lambda^0 \to \mathrm{p}\pi^-$. Thus one can obtain an optimal precision in the comparison between data and Monte Carlo from particle samples of known identity.

To avoid biases due to the different compositions of the event samples, the efficiency matrix was computed separately for each sample. The agreement between data and Monte Carlo for 'loose' tagging and a 'loose' track selection has been studied with pions from $\mathrm{K^0_S} \to \pi^+\pi^-$ and protons from $\Lambda^0 \to \mathrm{p}\pi^-$ decays and is shown in figure 9.8. The selection criteria for the $\mathrm{K^0_S}$ and Λ^0 candidates has been discussed in section 8.1. The pion purity from the $\mathrm{K^0_S}$-sample was estimated to be $\sim 94\%$ and the proton purity from the Λ^0-sample was estimated to be $\sim 75\%$ (section 8.1). On the right-hand side of the figure one can observe that the chance to misidentify a proton as a pion is clearly higher than the chance to misidentify it as a kaon. This can be explained by the low purity of the proton-sample. The dashed lines in the right-hand side column represent the correctly tagged part of the Monte Carlo, e.g. the dashed line in the top right plot ('p tagged as π') represents real pions of which the Λ^0 reconstruction indicates that they are a proton. However, the important point is that the detector simulation describes the data well.

The final stage is how to handle the primary quark flavour impurities in the b- and uds-sub-samples. With a purity of 78.5% for the b-sample and 81.7% for the uds-sample (see page 106), one must correct for the 21.5% $udsc$ and 18.3% bc flavour impurity respectively (see also table 9.1, page 116). This was achieved by purity matrix inversion as expressed in the equations 9.5(a) and 9.5(b).

$$
\begin{aligned}
\begin{pmatrix} N_i^b \\ N_i^{udsc} \end{pmatrix}^{\mathrm{Real}}\!(x) &= \begin{pmatrix} \mathcal{P}_b & 1-\mathcal{P}_{udsc} \\ 1-\mathcal{P}_b & \mathcal{P}_{udsc} \end{pmatrix}^{-1} \cdot \begin{pmatrix} N_i^b \\ N_i^{udsc} \end{pmatrix}^{\mathrm{Meas.}}\!(x) \qquad &\text{(a)} \\
&&(9.5) \\
\begin{pmatrix} N_i^{bc} \\ N_i^{uds} \end{pmatrix}^{\mathrm{Real}}\!(x) &= \begin{pmatrix} \mathcal{P}_{bc} & 1-\mathcal{P}_{uds} \\ 1-\mathcal{P}_{bc} & \mathcal{P}_{uds} \end{pmatrix}^{-1} \cdot \begin{pmatrix} N_i^{bc} \\ N_i^{uds} \end{pmatrix}^{\mathrm{Meas.}}\!(x) \qquad &\text{(b)}
\end{aligned}
$$

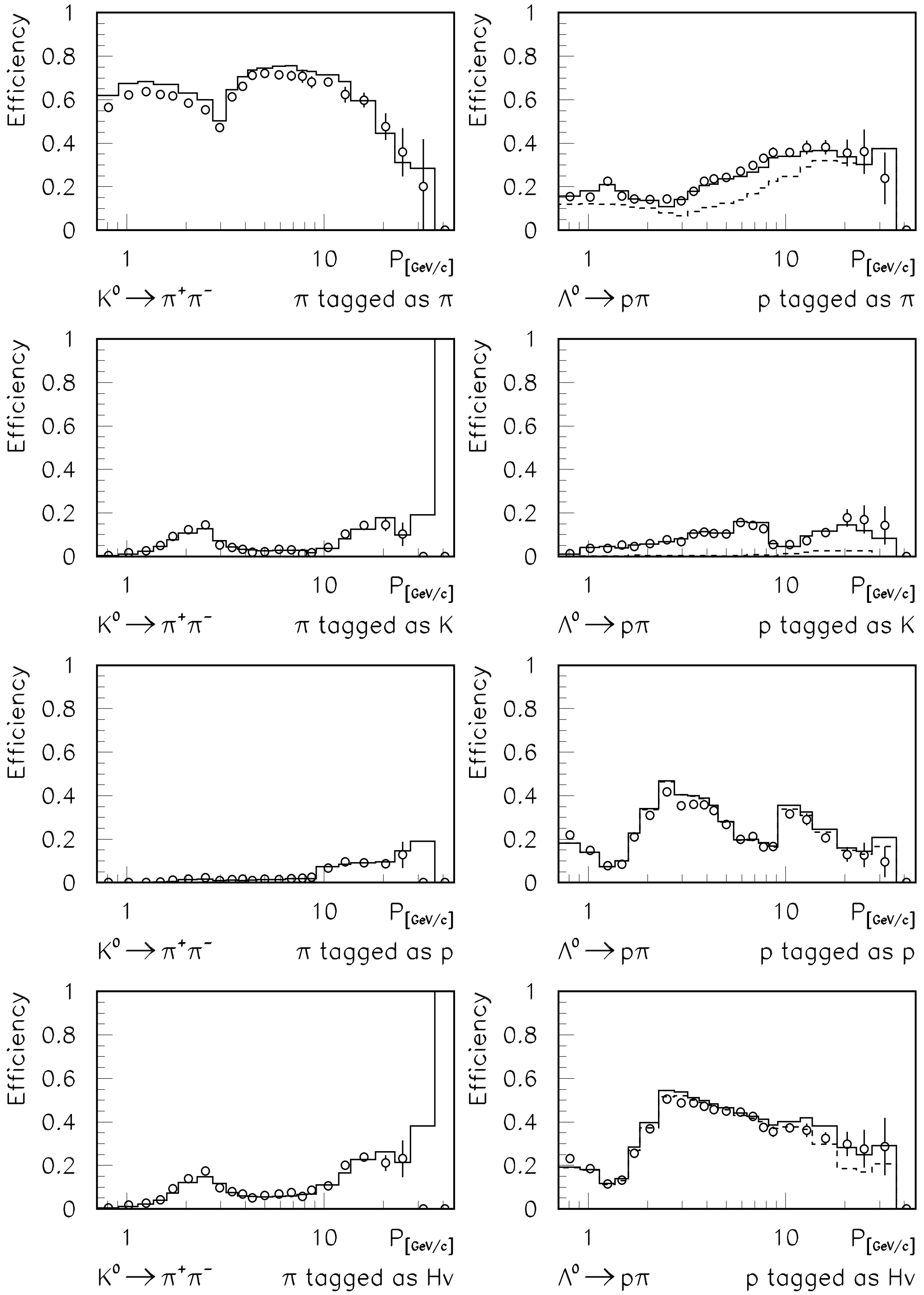

Figure 9.8: The XNEWTAG data-Monte Carlo comparison for 'loose' tagging and 'loose' track-selection with pions from K^0_S decay and protons from Λ^0 decay in $Z^0 \to q\overline{q}$.

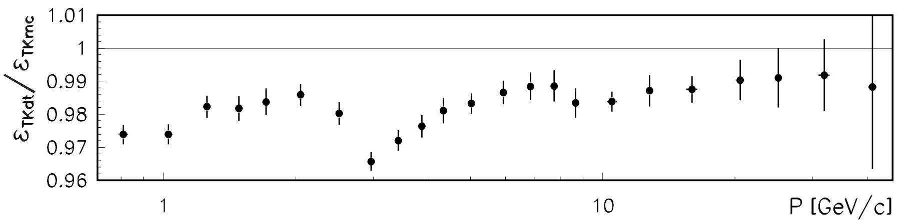

Figure 9.9: The data-Monte Carlo ratio of the 'loose' track selection efficiency $\mathcal{E}_{\rm sel}^{\rm data}/\mathcal{E}_{\rm sel}^{\rm m.c.}$.

For $i = \pi^{\pm}$, $K^{\pm}$, $p\overline{p}$ or $Hv^{\pm}$, the vector element N_i^b stands for the real (normalised) number of particles of kind i (eq. 9.2) from the b-tagged sample and N_i^{udsc} represents the equivalent for none-b-tagged events. Likewise, N_i^{uds} stands for the real (normalised) number of particles of kind i from the anti-b-tagged sample and N_i^{bc} for the equivalent for none-anti-b-tagged events. The elements of the purity matrix $\mathcal{P}_{b(c)}$ and $\mathcal{P}_{uds(c)}$ were determined from full detector simulation. The difference between the two equations lies in the treatment of the c-flavour contribution, which is the main impurity in both the b-sample and the uds-sample.

9.4 Corrections and Uncertainties

In this section an overview of the corrections which have been applied to obtain the final distributions will be treated first, followed by a discussion on the statistical and systematic uncertainties.

Corrections, other than those performed implicitly by the matrix inversion methods from the previous section, can basically be classified in two groups. One group could be called 'local corrections' and the other group could be called 'global corrections'. Both groups however, rely on the Monte Carlo simulation.

9.4.1 Local Corrections

Local corrections are specifically linked to the TPC and RICH detectors and their particle identification. Two local correction factors were applied, one on the track selection efficiency based on the track quality (as defined in table 7.1 and on page 110) and one on the tagging efficiency.
The track (quality) selection efficiency can be expressed according to equation 9.6.

$$\mathcal{E}_{\rm sel} = \frac{\text{the number of tracks of a certain quality in the barrel region}}{\text{the total number of tracks in the barrel region}} \qquad (9.6)$$

For the 'loose' track selection, the ratio of data and Monte Carlo for $\mathcal{E}_{\rm sel}$ versus momentum is illustrated in figure 9.9. The correction factor is applied bin-by-bin on the measured distributions and is for most bins of the order of 1–2%.

An example of the Monte Carlo efficiency matrix elements versus momentum are given in figure 7.2(page 82) and figure 7.6 (page 86). The only means to verify whether one might have to apply corrections on the efficiency matrix is to make the comparison between data and Monte Carlo using pions from K^0_S and protons from Λ^0 as is shown in figure 9.8. Unfortunately, not all bins of the individual elements of the efficiency matrix (eqs 9.2, 9.3) can be verified. Since no equivalent kaon sample is available, one can only consider the columns of the efficiency matrix for pion and proton tagging. Moreover, especially for the K^0_S, one can only compare the particles with momenta less than $\sim$ 10 GeV/c. Mainly because at higher momenta the statistics is too low but also to avoid a bias due to the topology of the K^0_S decay. At high momenta, the opening angle between the two outgoing tracks will be very small and the Cherenkov ring reconstruction may be more complicated due to overlapping rings.

With one exception (discussed below), the correction factors were derived only from the positive identification distributions (i.e. 'π tagged as π', 'p tagged as p' and 'p tagged as Hv' in figure 9.8), i.e. from only those distributions, equivalent to diagonal elements of the efficiency matrix. This strategy is based on the following reasons:

1. The diagonal elements are the most important.
2. To overcome biases due to the impurity of the samples. This is especially the case with the Λ^0 sample.
3. To avoid an 'over-correction'. To maintain the unitarity of the efficiency matrix, a correction applied on a diagonal element has to be propagated to the off-diagonal elements of the same column. For example, regarding the simplified 2x2 matrix for pion-heavy tagging of equation 9.3, if the positive pion identification efficiency $\mathcal{E}^{\pi}_{\pi}$ is *de*creased, than the efficiency to misidentify a pion as a heavy-particle ($\mathcal{E}^{\mathrm{Hv}}_{\pi}$) has to *in*crease. Repeating the same exercise with a correction factor derived (less accurately) from an off-diagonal element, propagation to the diagonal element might cause an 'over-correction'.

One exception was made concerning the discrepancy between data and Monte Carlo in five momentum bins around 2 GeV/c for the $\pi^{\pm}$ misidentification. Of all off-diagonal matrix elements, the elements $\mathcal{E}^{\mathrm{K}}_{\pi}$ in the 3x3-method and $\mathcal{E}^{\mathrm{Hv}}_{\pi}$ in the 2x2-method have the most significant influence on the matrix inversion method, especially around 2 GeV/c. In the left-hand column of figure 8.1 it can be seen that the relative difference between data and Monte Carlo for $\mathcal{E}^{\mathrm{K}}_{\pi}$ and $\mathcal{E}^{\mathrm{Hv}}_{\pi}$ around 2 GeV/c is of the order of 20-30%. This is caused by badly reconstructed tracks.

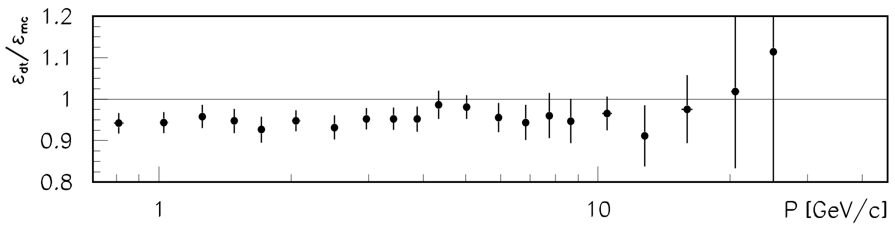

Figure 9.10: The data-Monte Carlo ratio of $\mathcal{E}_{\pi}^{\text{data}}/\mathcal{E}_{\pi}^{\text{m.c.}}$ for 'loose' track selection and 'loose' pion tagging for $\pi^{\pm}$ from $\mathrm{K}_{\mathrm{S}}^{0} \to \pi^{+}\pi^{-}$.

As an example, figure 9.10 shows the ratio of the pion tagging efficiency for data and Monte Carlo for the top-left distributions 'π tagged as π' in figure 9.8. From this ratio, a constant correction factor, performing a straight line fit over different bins, was computed for three momentum areas. One area between 0.7 and 2.7 GeV/c, where only liquid radiator information is used for pion tagging and two areas above 2.7 GeV/c. Although for $p > 2.7$ GeV/c only gas information is used for tagging pions, nevertheless, two areas were chosen, below and above 5.5 GeV/c, mainly to make an approximative distinction due to difference in curvature of the tracks and its influence on the Cherenkov angle resolution, even if the effects are fairly small.
For the proton and heavy particle tagging an equivalent procedure was followed. The correction factors for the liquid radiator areas were typically of the order of $\sim 5\%$. For the gas radiator areas the correction factors were typically of the order of $\sim 3\%$.

9.4.2 Global Corrections

Global corrections refer to overall detector effects and general selection cuts. They are derived from Monte Carlo by comparing the distributions at the hadronic level *before* detector simulation (generator level) with the distributions *after* the detailed detector simulation. The correction factors ($c^{(f,i)}$) can be obtained from the ratio as expressed in equation 9.7 where $i = \pi^{\pm}$, $\mathrm{K}^{\pm}$, $\mathrm{p\overline{p}}$ or $\mathrm{Hv}^{\pm}$ and f represents the event sample i.e. the $q\overline{q}$-, b- or uds-sample.

$$c^{(f,i)} = \frac{N_{gen}^{(f,i)}}{N_{sim}^{(f,i)}} \tag{9.7}$$

$N_{gen}^{(f,i)}$ stands for the distributions at the hadronic level *before* detector simulation whereas $N_{sim}^{(f,i)}$ stands for the distributions *after* the detailed simulation of the DELPHI detector, including all steps of the analysis. The factor $c^{(f,i)}$ basically corrects for effects such as:

1. Event and track selection
2. Track losses

3. Resolution effects
4. Secondary interactions
5. Detector geometry

For example, the effect of lost tracks due to the detector geometry or moreover due to track reconstruction inefficiency, can lead to an odd number of charged particles. This occurs in about 50% of all events.
$N_{sim}^{(f,i)}$ also includes initial state radiation. Although the effect is very small on the Z^0 resonance, $c^{(f,i)}$ covers this effect too. In the case of $i = \pi^{\pm}$ (being $\pi^{\pm} + e^{\pm} + \mu^{\pm}$, see footnote 2 page 108), an additional correction factor which takes care of the lepton contribution can be acquired from the ratio $N_{gen}^{(f,\pi^{\pm})}/N_{gen}^{(f,\pi^{\pm}+e^{\pm}+\mu^{\pm})}$. Concerning the track selection, it should be mentioned that correction for the selection cut, to suppress particles coming from secondary interactions i.e. accepting only negative charged particles below 2.7 GeV/c (item *iv*, page 103) is also included in $c^{(f,i)}$.
The simulation of hadronic Z^0 decays *before* detector simulation is performed by the JETSET 7.3 Parton Shower (PS) Monte Carlo programme [17]. To obtain the values for $N_{gen}^{(f,i)}$ 2.5 million $Z^0 \to q\overline{q}$ events were used. In the case of the b-events for particle momenta above 10 GeV/c, an additional 2.5 million $Z^0 \to b\overline{b}$ events were produced.

Finally, the corrected data distributions are obtained according to equation 9.8.

$$N_{cor}^{(f,i)} = c^{(f,i)} \cdot N_{data}^{(f,i)} \tag{9.8}$$

The correction factor $c^{(f,i)}$ contains all items mentioned before, except for the phenomenon of ghost particles. Ghost particles are particles in $N_{sim}^{(f,i)}$ which have no link to the simulation history. They appear, increasing with momentum, only above $\sim$ 20 GeV/c. The correction factor on the measured distributions was $\sim$ 0.3% at 20 GeV/c, slowly rising to $\sim$ 5% at 45 GeV/c.

Note: at the generator level (N_{gen}) all particles with a lifetime less than 10^{-9} s are included and are considered as unstable. Particles with longer lifetimes are all taken as stable particles. This means for instance that Λ^0 and K_S^0 decay and that K_L^0 is stable. This is not the case for N_{sim} (eq. 9.7), where lifetimes are properly taken into account.

9.4.3 Systematic Uncertainties

Due to the large data set, the accuracy on the measured distributions in most cases will be dominated by systematic uncertainties. The result of a detailed study of the uncertainties for the final $\pi^{\pm}$, $K^{\pm}$, $p\overline{p}$, $Hv^{\pm}$ normalised production rates is shown in figure 9.11 (page 119) and will be discussed in more detail at the end of this section. Uncertainties, other than those treated in this section have not been explicitly considered.

$\mathcal{P}_E^+$	b - purity	c - purity	$\mathcal{P}_E$	uds - purity	c - purity
< 0.005	82.3%	12.8%	> 0.20	82.5%	14.0%
< 0.010	78.5%	14.7%	> 0.15	81.7%	14.5%
< 0.020	73.3%	16.7%	> 0.10	80.3%	15.3%

Table 9.1: (anti)-b - tag event probability versus b - purity and versus the c - (im)purity.

For each event sample, the systematic uncertainty of each of the distributions can be divided into four different sources. These sources are: the analysis method, the event selection, the tagging and track selection and the correction factors.

Uncertainties due to the Analysis Method

The contribution to the systematic uncertainty due to the analysis method can be estimated by comparing the result for $\pi^\pm$ from the 3x3-method (eq. 9.2) with the result for $\pi^\pm$ from the simplified 2x2-method (eq. 9.3). Likewise one can compare the sum of results on $\mathrm{K}^\pm$ and $\mathrm{p\overline{p}}$ with the resulting $\mathrm{Hv}^\pm$ distribution. In this case however one should note that for a large part of the momentum window, one is also looking at effects due to different application of RICH information for particle identification.

Uncertainties due to the Event Selection

To study systematic effects caused by the event-tagging and the purity matrix inversion method (eq. 9.5), two additional b - samples and uds - samples of different purity were selected (see section 9.1, page 107). The applied event probability cuts and the resulting purities for these samples are listed in table 9.1. The middle row represents the values used for the measurement. Thus the b - purity was varying by $\sim 5\%$ and the uds - purity by $\sim 1\%$. The analysis was repeated for every event sample, including the corrections described above. The uncertainty due to the general hadronic event selection is very small. This will be treated below, when the estimation from the contribution of the correction factors is discussed.

Uncertainties due to Tagging and Track Selection

The NEWTAG package offers the opportunity to perform different degrees of tagging and different degrees of track-quality selections. This implies that one allows the measured Cherenkov angle $\theta_{\check{c}}^{\mathrm{meas.}}$ and its uncertainty $\sigma_{\mathrm{ring}}^{\mathrm{exp.}}$ (see eq. 7.2, page 74) to vary within different windows for different track samples. For reasons discussed before (see page 110) 'loose' tagging and 'loose' track selection criteria were chosen as the central values of the measurements in this analysis. To study systematic effects due to the tagging, the 'very loose' and 'standard' tagging were also selected. This basically means that one allows the $\pi^\pm$, $\mathrm{K}^\pm$, $\mathrm{p\overline{p}}$ separation to wander within an extra window of plus-minus one standard deviation. Thus three tag-samples ('very loose', 'loose', 'standard') per identification hypothesis ($\pi^\pm$, $\mathrm{K}^\pm$, $\mathrm{p\overline{p}}$, $\mathrm{Hv}^\pm$) were selected for each event sample.

Likewise for the track quality, the 'very loose' and 'standard' track selection were included to study systematic effects on the particle identification from the detector point of view. This was done for each of the three tag-samples and again for each hypothesis and each event sample.

The requirement of the Outer Detector being used in the track reconstruction helps to achieve higher purities after particle identification, since OD contributes with information of the track after it has passed the RICH. Although the loss in statistics is significant, one nevertheless can apply the OD requirement to select an extra subsample of higher quality and repeat the above exercise to study systematic effects.

All in all, for each hypothesis ($\pi^{\pm}$, $\mathrm{K}^{\pm}$, $\mathrm{p\overline{p}}$, $\mathrm{Hv}^{\pm}$) and for each of the three event samples ($q\overline{q}$-, b- and uds-sample), the whole procedure leads to 18 different subsamples (2x3x3 i.e. with or without the OD requirement, 'very loose', 'loose', 'standard' tag and 'very loose', 'loose', 'standard' track selection). It should be noted here that the 'tight' options were not applied mainly to avoid the introduction of fake systematic effects due to statistical fluctuations, especially for higher momenta.

The systematic uncertainty was computed for each bin by taking out of the 18 entries, half of the maximum deviation from the central value.

Uncertainties due to Corrections

Local and global corrections – defined in the previous section – take on average an equal share in the contribution to the systematic uncertainty. Since they operate mainly on the track quality and reconstruction efficiency, they approximately also cover the uncertainty caused by the general hadronic event selection.

For the uncertainty from the local correction factors, the largest part is claimed by the corrections on the efficiency matrix. By increasing the corrections by 10% an average relative contribution of the order of 15% for the $q\overline{q}$- and uds-sample and 20% for the b-sample was estimated. Assuming an uncertainty of 5% on the track selection efficiency correction (derived from $\mathcal{E}_{\mathrm{sel}}^{\mathrm{data}}/\mathcal{E}_{\mathrm{sel}}^{\mathrm{m.c.}}$), gave a relative contribution to the total systematic uncertainty of $\sim 2\%$.

The global factors $c^{(f,i)}$ contain corrections for several effects. The average relative contribution to the total uncertainty was estimated to be 15% for the $q\overline{q}$-sample and 20% for the b- and uds-sample. Some effects could be considered to be very small. For example, assuming an uncertainty of 5% on the effect of secondary interactions indicated the relative contributions to be $\ll 1\%$. An extra uncertainty of 5% was introduced to account for the uncertainty of the requirement to accept only negative charged particles below 2.7 GeV/c.

Ghost particles only occur at high momenta. Assuming a 10% uncertainty, the relative contribution of this effect was estimated to be $\ll 1\%$ at 20 GeV/c slowly rising to $\sim 10\%$ at 45 GeV/c.

The Uncertainty Distributions

For the normalised production rates in $Z^0 \to q\overline{q}$, $Z^0 \to b\overline{b}$ and $Z^0 \to u\overline{u}, d\overline{d}, s\overline{s}$, figure 9.11 shows the final result of the total uncertainty distributions ($\epsilon_{\rm tot}$) versus momentum for the $\pi^{\pm}$, $K^{\pm}$, $p\overline{p}$, $Hv^{\pm}$ normalised production rates for $q\overline{q}$-, b- and uds-events. The absolute value of the total uncertainty is unfolded in a systematic part ($\epsilon_{\rm syst}$) and a statistical part ($\epsilon_{\rm stat}$). From this figure one can see that in most cases the systematic uncertainties (triangles) play a dominating role. The shape of the distributions reflects the characteristics of the RICH particle identification.
For example, the $K^{\pm}$ distributions show successively three rising slopes. This can be understood from the fact that – with increasing momentum – the kaon-identification bands get more and more sandwiched between the pion and proton bands. Thus, the $\pi^{\pm}-K^{\pm}$ ($K^{\pm}-p\overline{p}$) separation slowly decreases. In other words, *if* the reconstructed Cherenkov angle were to be slightly *over*-estimated (or the angle resolution slightly underestimated), then a certain number of kaons would systematically be miss-identified as a pion (the opposite case will be discussed below). The first rising slope is determined by the $\pi^{\pm}-K^{\pm}$ separation in the region where liquid radiator information is used for identification ($0.7 < p < 2.7$ GeV/c). The second slope, for $2.7 < p < 8.5$ GeV/c, is determined by the $K^{\pm}-p\overline{p}$ separation in the liquid radiator. Here the pion hypothesis has been ruled out by the gas veto-identification (see section 7.1) and identification is reduced to the liquid radiator to separate $K^{\pm}$ from $p\overline{p}$. If the $\pi^{\pm}$ hypothesis would not have been ruled out, $K^{\pm}$ identification using liquid information would be merely impossible, (especially for $4 < p < 8.5$ GeV/c) and the second slope would have been steeper, rising to significantly higher values. The third slope ($\sim 10 < p < 45$ GeV/c) can be explained in the same way as the first one, but now for the gas radiator instead of the liquid radiator. The opposite effect i.e. *if* the reconstructed Cherenkov angle were to be slightly *under*-estimated (or the angle resolution slightly overestimated), is suppressed, simply because for a particle of momentum p, the separation with respect to a heavier mass hypothesis is always larger than the separation with respect to a lighter mass hypothesis. This explains the less steep first slope in the case of the $\pi^{\pm}$ distributions.

Another point of interest is that the first slope is missing for the $p\overline{p}$ distributions i.e. there is no visible systematic effect of the kind discussed above. This actually finds its reason in the fact that for low momenta, the protons are either in liquid veto-mode (below the proton threshold), or the $K^{\pm}-p\overline{p}$ separation is always larger than five standard deviations. Making a column-by-column comparison between the distributions in figure 9.11, one can verify the consistency of the statistical uncertainty. Keeping in mind that the vertical scales are logarithmic, the statistical uncertainty distributions have the same pattern, as one would expect. The same however, does not necessarily hold for the systematic uncertainty. Variations between the patterns can be understood by considering a change in the background for particle identification due to differences in the overall event topology (e.g. track density, particle multiplicity) for the three samples. This may become more plausible in the next sections, where the final results will be presented.

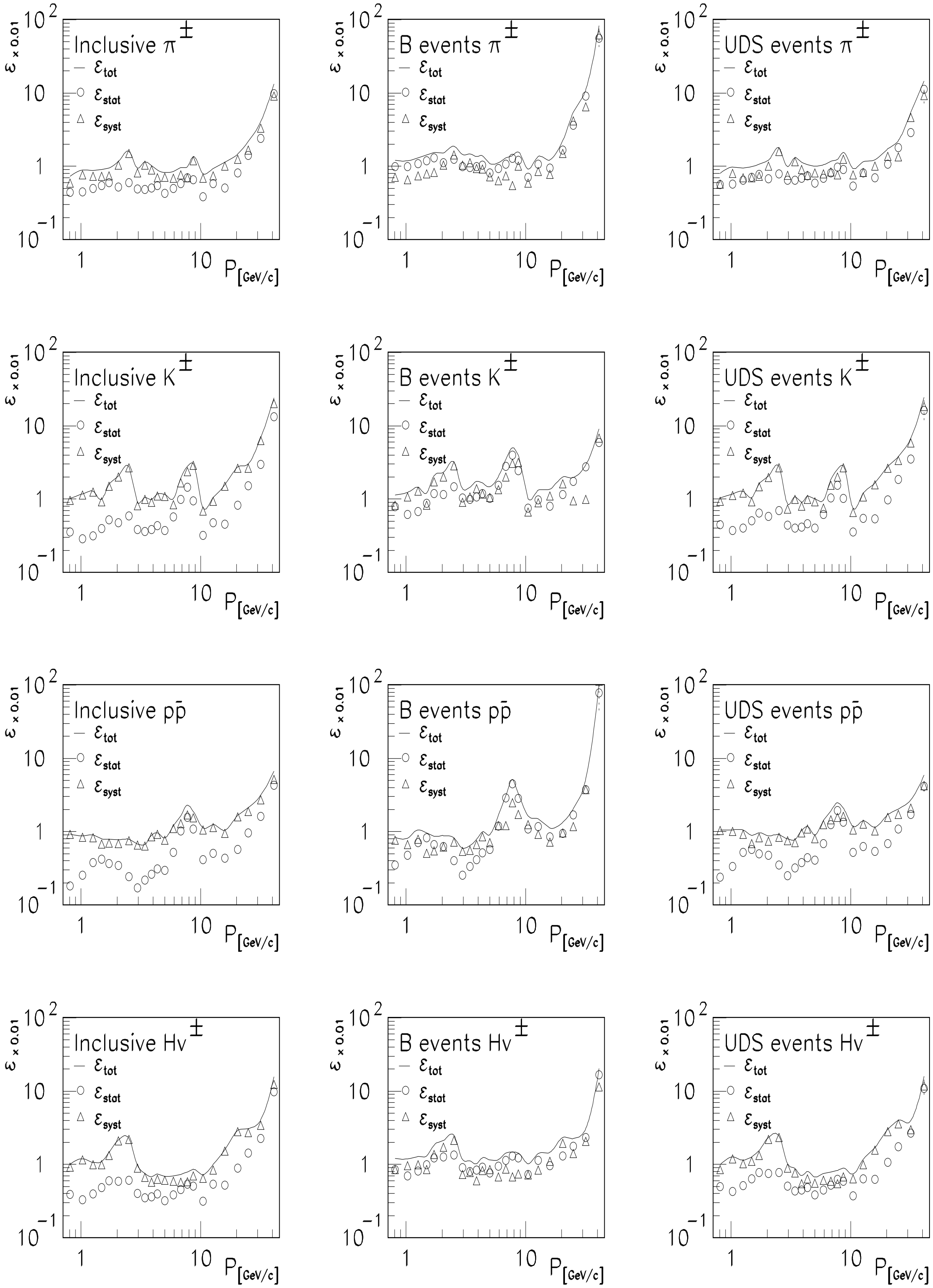

Figure 9.11: Statistical and systematic uncertainties versus momentum for the normalised $\pi^{\pm}$, K$^{\pm}$, p$\overline{\rm p}$ rates for $Z^0 \to q\overline{q}$, $Z^0 \to b\overline{b}$ and $Z^0 \to u\overline{u}, d\overline{d}, s\overline{s}$.

source of systematic uncertainty	$Z^0 \to q\overline{q}$ $\overline{\epsilon_{\text{source}}/\epsilon_{\text{syst.}}}$	$Z^0 \to b\overline{b}$ $\overline{\epsilon_{\text{source}}/\epsilon_{\text{syst.}}}$	$Z^0 \to u\overline{u}, d\overline{d}, s\overline{s}$ $\overline{\epsilon_{\text{source}}/\epsilon_{\text{syst.}}}$
analysis method	4 %	2 %	3 %
event selection	2 %	9 %	5 %
tagging and track selection	63 %	49 %	57 %
correction factors	31 %	40 %	35 %

Table 9.2: The sources of systematic uncertainty and their average relative contribution to the total uncertainty for $Z^0 \to q\overline{q}$, $Z^0 \to b\overline{b}$ and $Z^0 \to u\overline{u}, d\overline{d}, s\overline{s}$.

For the normalised production rates in $Z^0 \to q\overline{q}$, $Z^0 \to b\overline{b}$ and $Z^0 \to u\overline{u}, d\overline{d}, s\overline{s}$, table 9.2 shows the average relative contribution to the systematic uncertainty of the four sources.

9.5 Normalised Production Rates

There are two ways to obtain the normalised production rates of $\pi^{\pm}$, $\mathrm{K}^{\pm}$, $\mathrm{p\overline{p}}$ versus momentum from the matrix inversion in equation 9.9.

$$\begin{pmatrix} N_\pi \\ N_\mathrm{K} \\ N_\mathrm{p} \end{pmatrix}^{\mathrm{Real}} (x) = \begin{pmatrix} \mathcal{E}_\pi^\pi & \mathcal{E}_\mathrm{K}^\pi & \mathcal{E}_\mathrm{p}^\pi \\ \mathcal{E}_\pi^\mathrm{K} & \mathcal{E}_\mathrm{K}^\mathrm{K} & \mathcal{E}_\mathrm{p}^\mathrm{K} \\ \mathcal{E}_\pi^\mathrm{p} & \mathcal{E}_\mathrm{K}^\mathrm{p} & \mathcal{E}_\mathrm{p}^\mathrm{p} \end{pmatrix}^{-1} \cdot \begin{pmatrix} N_\pi \\ N_\mathrm{K} \\ N_\mathrm{p} \end{pmatrix}^{\mathrm{Meas.}} (x) \tag{9.9}$$

The normalised rates f_i (fractions) can be calculated either according to equation 9.10a or according to equation 9.10b.

$$f'_i = \frac{N_i^{\mathrm{Real}}}{N_{\pi e\mu}^{\mathrm{Real}} + N_\mathrm{K}^{\mathrm{Real}} + N_\mathrm{p}^{\mathrm{Real}}} \qquad \Rightarrow \qquad \textstyle\sum_i f'_i \equiv 1 \qquad \text{(a)}$$

$$\text{where} \quad N_i^{\mathrm{Real}} = \textstyle\sum_j \left((\mathcal{E}_j^i)^{-1} \cdot N_j^{\mathrm{Meas.}} \right) \qquad ; \qquad i,j = \pi e\mu, \mathrm{K}, \mathrm{p} \tag{9.10}$$

$$f_i = \textstyle\sum_j \left((\mathcal{E}_j^i)^{-1} \cdot \dfrac{N_j^{\mathrm{Meas.}}}{N_{\mathrm{total}}^{\mathrm{Meas.}}} \right) \qquad \Rightarrow \qquad \textstyle\sum_i f_i \stackrel{?}{=} 1 \qquad \text{(b)}$$

From equation 9.10a it is clear that the sum of the fractions f'_i shall always be unity. However, this does not obviously hold for equation 9.10b, but is only true if the efficiency matrix is correct. For example, if a certain number of particles were to be tagged both as a pion and a kaon, the sum of the fractions f_i would not be unity if the efficiency matrix was determined wrongly. In this way one has an extra opportunity to test the consistency of the method and the particle identification. Like for the 3x3-method, the same is valid for the 2x2-method, as is expressed in equations 9.11 and 9.12. In order to allow these consistency tests, the procedure of equations 9.10b and 9.12b was chosen to compute the normalised production rates in $\mathrm{Z}^0 \to q\overline{q}$, $\mathrm{Z}^0 \to b\overline{b}$ and $\mathrm{Z}^0 \to u\overline{u}, d\overline{d}, s\overline{s}$.

$$\begin{pmatrix} N_\pi \\ N_\mathrm{Hv} \end{pmatrix}^{\mathrm{Real}} (x) = \begin{pmatrix} \mathcal{E}_\pi^\pi & \mathcal{E}_\mathrm{Hv}^\pi \\ \mathcal{E}_\pi^\mathrm{Hv} & \mathcal{E}_\mathrm{Hv}^\mathrm{Hv} \end{pmatrix}^{-1} \cdot \begin{pmatrix} N_\pi \\ N_\mathrm{Hv} \end{pmatrix}^{\mathrm{Meas.}} (x) \tag{9.11}$$

$$f'_i = \frac{N_i^{\mathrm{Real}}}{N_{\pi e\mu}^{\mathrm{Real}} + N_\mathrm{Hv}^{\mathrm{Real}}} \qquad \Rightarrow \qquad \textstyle\sum_i f'_i \equiv 1 \qquad \text{(a)}$$

$$\text{where} \quad N_i^{\mathrm{Real}} = \textstyle\sum_j \left((\mathcal{E}_j^i)^{-1} \cdot N_j^{\mathrm{Meas.}} \right) \qquad ; \qquad i,j = \pi e\mu, \mathrm{Hv} \tag{9.12}$$

$$f_i = \textstyle\sum_j \left((\mathcal{E}_j^i)^{-1} \cdot \dfrac{N_j^{\mathrm{Meas.}}}{N_{\mathrm{total}}^{\mathrm{Meas.}}} \right) \qquad \Rightarrow \qquad \textstyle\sum_i f_i \stackrel{?}{=} 1 \qquad \text{(b)}$$

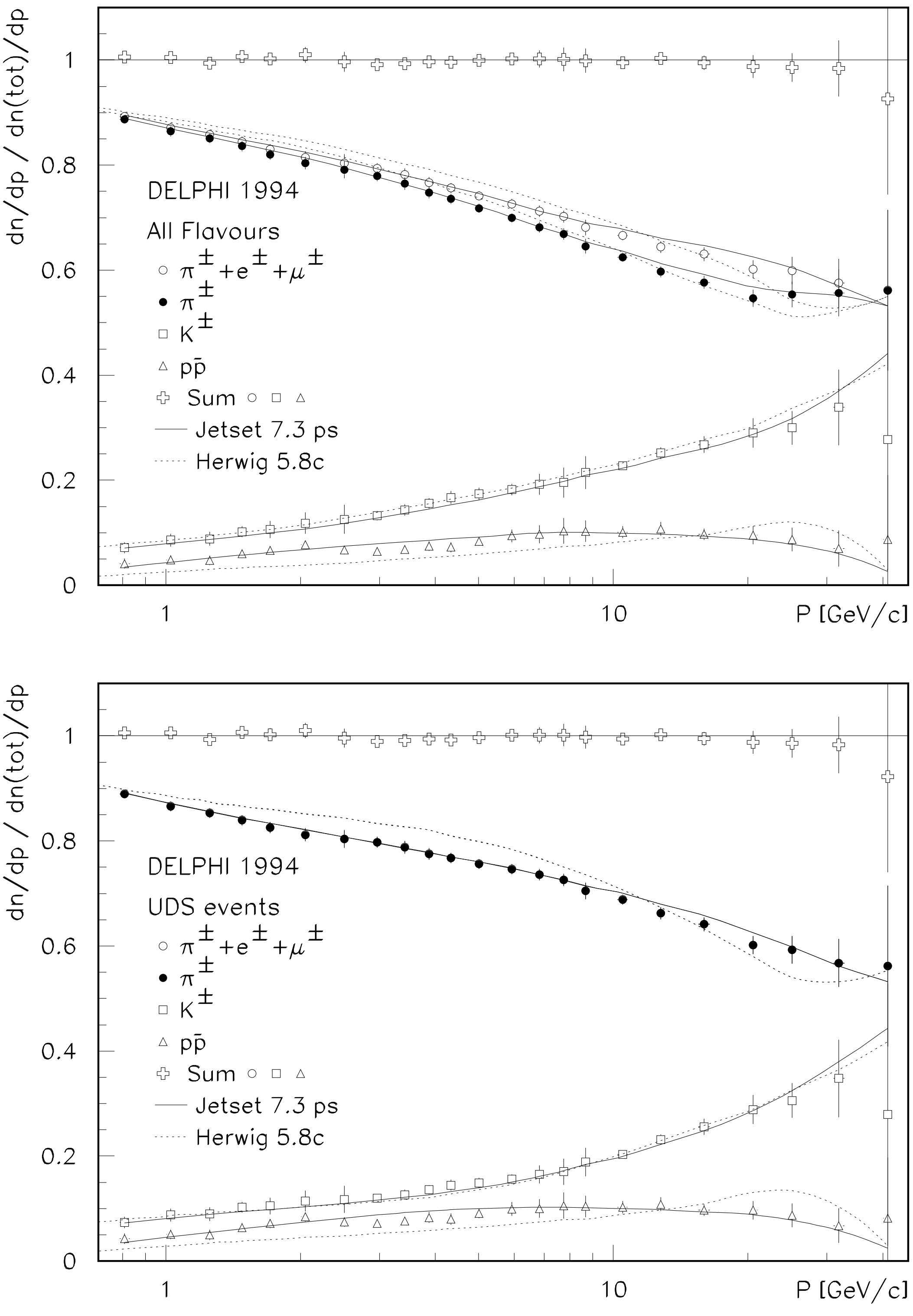

Figure 9.12: Normalised production rates of $\pi^{\pm}$, $K^{\pm}$, $p\overline{p}$ in $Z^0 \to q\overline{q}$, $Z^0 \to u\overline{u}, d\overline{d}, s\overline{s}$.

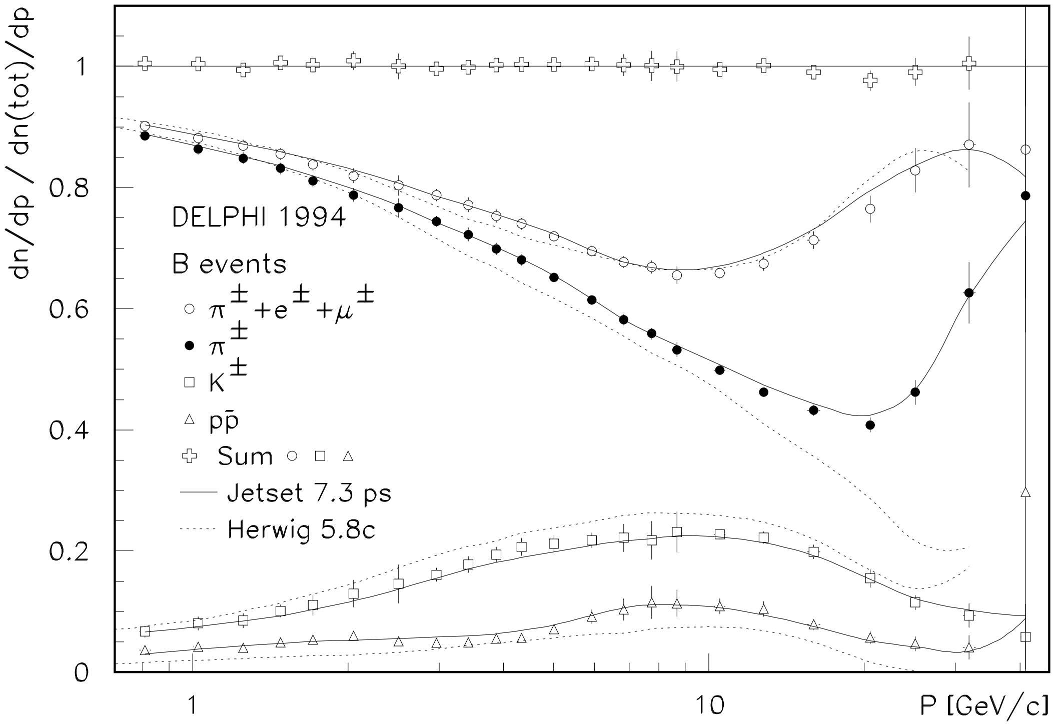

Figure 9.13: Normalised production rates of $\pi^{\pm}$, $K^{\pm}$, $p\overline{p}$ in $Z^0 \to b\overline{b}$.

Figure 9.12 shows the normalised $\pi^{\pm}$, $K^{\pm}$, $p\overline{p}$ production rates as derived by the 3x3-method from the $q\overline{q}$- and uds-sample. The open circles represent the pion distribution before having corrected for the lepton contribution, to enable the consistency test as discussed above. The closed circles depict the pions after the lepton correction. In the case of the uds-events, the open and closed circles merely coincide, indicating a very low lepton production. The equivalent normalised $\pi^{\pm}$, $K^{\pm}$, $p\overline{p}$ rates obtained from the b-sample are shown in figure 9.13. Also included are the predictions from JETSET 7.3 PS (full lines) and HERWIG 5.8C (dotted lines) [77].

For all three event samples, JETSET turns out to give a good description of the data. For $\pi^{\pm}$ and $K^{\pm}$ in $q\overline{q}$-events and for $K^{\pm}$ in uds-events also the HERWIG prediction is good. In all other cases however, HERWIG seems to fail, especially for protons.

Comparing the b-sample with the uds-sample, the distributions show approximately the same behaviour in the momentum region below ~ 3 GeV/c. However, clear differences occur for very high momenta ($p > 20$ GeV/c). In b-events, high momentum $K^{\pm}$ production seems to be suppressed whereas high momentum $\pi^{\pm}$ production prevails. On the other hand, the $K^{\pm}$ production in the intermediate momentum window ($3 < p < 20$ GeV/c) is clearly higher in b-events compared to uds-events. For high momenta ($p > 20$ GeV/c) the $K^{\pm}$ production rate is about a factor three higher in uds-events, which may be an indication for those kaons to contain a primary $u(\overline{u})$-quark or $s(\overline{s})$-quark. This will be illustrated in section 9.9.

The $\pi^{\pm}$ and $Hv^{\pm}$ distributions acquired from the 2x2-method are shown in figure 9.14. To illustrate the consistency of the matrix inversion method, an overlay of the sum of $K^{\pm}$ and $p\overline{p}$ from the 3x3-method (triangles) is included.

The values and uncertainties corresponding to the distributions are enlisted in the summary tables 9.3-9.6, including the JETSET 7.3 PS predictions.

Summary Table of Normalised Production Rates in $Z^0 \to q\overline{q}$

Momentum GeV/c	DELPHI f_π %	$\epsilon_{\rm tot}$	$\epsilon_{\rm stat}$	$\epsilon_{\rm syst}$	JS73PS f_π %
0.70 - 0.91	88.72	± 0.73	± 0.44	± 0.58	89.49
0.91 - 1.14	86.41	± 0.89	± 0.44	± 0.77	87.58
1.14 - 1.37	85.08	± 0.88	± 0.50	± 0.73	86.09
1.37 - 1.60	83.60	± 0.90	± 0.54	± 0.72	84.84
1.60 - 1.82	82.04	± 0.95	± 0.60	± 0.74	83.81
1.82 - 2.28	80.37	± 1.16	± 0.52	± 1.04	82.46
2.28 - 2.74	79.11	± 1.60	± 0.60	± 1.48	80.79
2.74 - 3.19	77.89	± 0.94	± 0.49	± 0.80	79.28
3.19 - 3.65	76.45	± 1.14	± 0.48	± 1.04	78.02
3.65 - 4.10	74.74	± 1.02	± 0.50	± 0.89	76.94
4.10 - 4.56	73.56	± 0.88	± 0.54	± 0.70	75.83
4.56 - 5.47	71.82	± 0.82	± 0.43	± 0.70	74.55
5.47 - 6.38	69.92	± 0.85	± 0.50	± 0.69	72.78
6.38 - 7.29	68.19	± 0.96	± 0.58	± 0.76	71.26
7.29 - 8.21	66.89	± 0.99	± 0.70	± 0.70	70.15
8.21 - 9.12	64.57	± 1.35	± 0.65	± 1.18	69.03
9.12 - 11.85	62.47	± 0.79	± 0.38	± 0.69	67.83
11.85 - 13.68	59.71	± 0.94	± 0.58	± 0.73	66.10
13.68 - 18.24	57.67	± 1.13	± 0.51	± 1.01	64.67
18.24 - 22.80	54.66	± 1.48	± 0.81	± 1.24	62.52
22.80 - 27.36	55.36	± 2.18	± 1.41	± 1.66	60.46
27.36 - 36.47	55.69	± 4.10	± 2.41	± 3.31	57.01
36.47 - 45.00	56.11	± 13.30	± 9.72	± 9.09	53.23

Table 9.3: The normalised production rates for $\pi^\pm$ in $Z^0 \to q\overline{q}$.

Momentum GeV/c	DELPHI f_K %	$\epsilon_{\rm tot}$	$\epsilon_{\rm stat}$	$\epsilon_{\rm syst}$	JS73PS f_K %
0.70 - 0.91	7.17	± 1.02	± 0.35	± 0.95	7.06
0.91 - 1.14	8.58	± 1.18	± 0.29	± 1.14	8.03
1.14 - 1.37	8.84	± 1.28	± 0.31	± 1.24	8.76
1.37 - 1.60	10.21	± 0.99	± 0.39	± 0.91	9.39
1.60 - 1.82	10.63	± 1.58	± 0.52	± 1.49	9.94
1.82 - 2.28	11.84	± 2.06	± 0.47	± 2.01	10.73
2.28 - 2.74	12.55	± 2.75	± 0.59	± 2.69	11.80
2.74 - 3.19	13.25	± 0.89	± 0.39	± 0.80	12.81
3.19 - 3.65	14.32	± 1.05	± 0.36	± 0.99	13.72
3.65 - 4.10	15.59	± 0.98	± 0.38	± 0.91	14.52
4.10 - 4.56	16.72	± 1.17	± 0.43	± 1.09	15.31
4.56 - 5.47	17.39	± 1.15	± 0.37	± 1.09	16.26
5.47 - 6.38	18.23	± 1.02	± 0.57	± 0.84	17.57
6.38 - 7.29	19.25	± 1.94	± 0.99	± 1.67	18.77
7.29 - 8.21	19.55	± 2.78	± 1.44	± 2.37	19.81
8.21 - 9.12	21.47	± 3.04	± 0.94	± 2.89	20.92
9.12 - 11.85	22.73	± 0.76	± 0.32	± 0.69	22.27
11.85 - 13.68	25.17	± 1.04	± 0.48	± 0.93	24.19
13.68 - 18.24	26.77	± 1.56	± 0.45	± 1.49	25.98
18.24 - 22.80	29.04	± 2.75	± 0.82	± 2.63	28.78
22.80 - 27.36	29.97	± 3.03	± 1.52	± 2.62	31.77
27.36 - 36.47	33.86	± 6.91	± 2.97	± 6.24	36.99
36.47 - 45.00	27.78	± 24.12	± 13.30	± 20.12	44.15

Table 9.4: The normalised production rates for $K^\pm$ in $Z^0 \to q\overline{q}$.

Momentum GeV/c	DELPHI f_p %	$\epsilon_{\rm tot}$	$\epsilon_{\rm stat}$	$\epsilon_{\rm syst}$	JS73PS f_p %
0.70 - 0.91	4.11	± 0.93	± 0.18	± 0.92	3.45
0.91 - 1.14	4.85	± 0.87	± 0.25	± 0.84	4.39
1.14 - 1.37	4.71	± 0.90	± 0.38	± 0.82	5.15
1.37 - 1.60	5.97	± 0.79	± 0.42	± 0.67	5.77
1.60 - 1.82	6.61	± 0.79	± 0.36	± 0.70	6.25
1.82 - 2.28	7.68	± 0.77	± 0.34	± 0.69	6.80
2.28 - 2.74	6.73	± 0.79	± 0.24	± 0.75	7.41
2.74 - 3.19	6.46	± 0.68	± 0.17	± 0.66	7.90
3.19 - 3.65	6.83	± 0.67	± 0.22	± 0.63	8.26
3.65 - 4.10	7.46	± 0.89	± 0.26	± 0.85	8.54
4.10 - 4.56	7.23	± 0.96	± 0.31	± 0.91	8.86
4.56 - 5.47	8.37	± 0.82	± 0.29	± 0.77	9.19
5.47 - 6.38	9.40	± 1.21	± 0.52	± 1.09	9.64
6.38 - 7.29	9.70	± 1.64	± 1.02	± 1.29	9.97
7.29 - 8.21	10.37	± 2.29	± 1.56	± 1.67	10.04
8.21 - 9.12	10.30	± 1.88	± 1.08	± 1.54	10.05
9.12 - 11.85	10.12	± 1.12	± 0.41	± 1.04	9.91
11.85 - 13.68	10.75	± 1.24	± 0.50	± 1.14	9.71
13.68 - 18.24	9.71	± 1.04	± 0.43	± 0.95	9.35
18.24 - 22.80	9.54	± 1.68	± 0.57	± 1.58	8.69
22.80 - 27.36	8.72	± 2.11	± 0.95	± 1.88	7.77
27.36 - 36.47	7.00	± 3.16	± 1.61	± 2.72	5.99
36.47 - 45.00	8.68	± 6.69	± 4.26	± 5.16	2.62

Table 9.5: The normalised production rates for $p\overline{p}$ in $Z^0 \to q\overline{q}$.

Momentum GeV/c	DELPHI f_{Hv} %	$\epsilon_{\rm tot}$	$\epsilon_{\rm stat}$	$\epsilon_{\rm syst}$	JS73PS f_{Hv} %
0.70 - 0.91	11.40	± 0.99	± 0.39	± 0.91	10.51
0.91 - 1.14	13.08	± 1.19	± 0.33	± 1.14	12.42
1.14 - 1.37	14.99	± 1.07	± 0.39	± 0.99	13.91
1.37 - 1.60	15.87	± 1.09	± 0.48	± 0.98	15.16
1.60 - 1.82	17.11	± 1.46	± 0.59	± 1.33	16.19
1.82 - 2.28	19.23	± 2.16	± 0.58	± 2.08	17.54
2.28 - 2.74	19.87	± 2.27	± 0.61	± 2.19	19.21
2.74 - 3.19	20.89	± 0.97	± 0.40	± 0.88	20.72
3.19 - 3.65	21.02	± 0.75	± 0.35	± 0.66	21.98
3.65 - 4.10	22.77	± 0.68	± 0.36	± 0.57	23.06
4.10 - 4.56	24.14	± 0.74	± 0.40	± 0.63	24.17
4.56 - 5.47	25.74	± 0.68	± 0.32	± 0.60	25.45
5.47 - 6.38	27.65	± 0.70	± 0.38	± 0.58	27.22
6.38 - 7.29	29.22	± 0.73	± 0.45	± 0.57	28.74
7.29 - 8.21	29.89	± 0.78	± 0.53	± 0.57	29.85
8.21 - 9.12	31.77	± 0.85	± 0.50	± 0.69	30.97
9.12 - 11.85	33.04	± 0.72	± 0.32	± 0.65	32.17
11.85 - 13.68	35.24	± 1.00	± 0.54	± 0.84	33.90
13.68 - 18.24	36.09	± 1.59	± 0.52	± 1.51	35.33
18.24 - 22.80	37.71	± 2.92	± 0.89	± 2.78	37.48
22.80 - 27.36	37.92	± 3.08	± 1.43	± 2.72	39.54
27.36 - 36.47	41.24	± 4.07	± 2.26	± 3.39	42.99
36.47 - 45.00	46.00	± 15.65	± 9.72	± 12.27	46.77

Table 9.6: normalised production rates for $Hv^\pm$ particles ($K^\pm/p\overline{p}$) in $Z^0 \to q\overline{q}$.

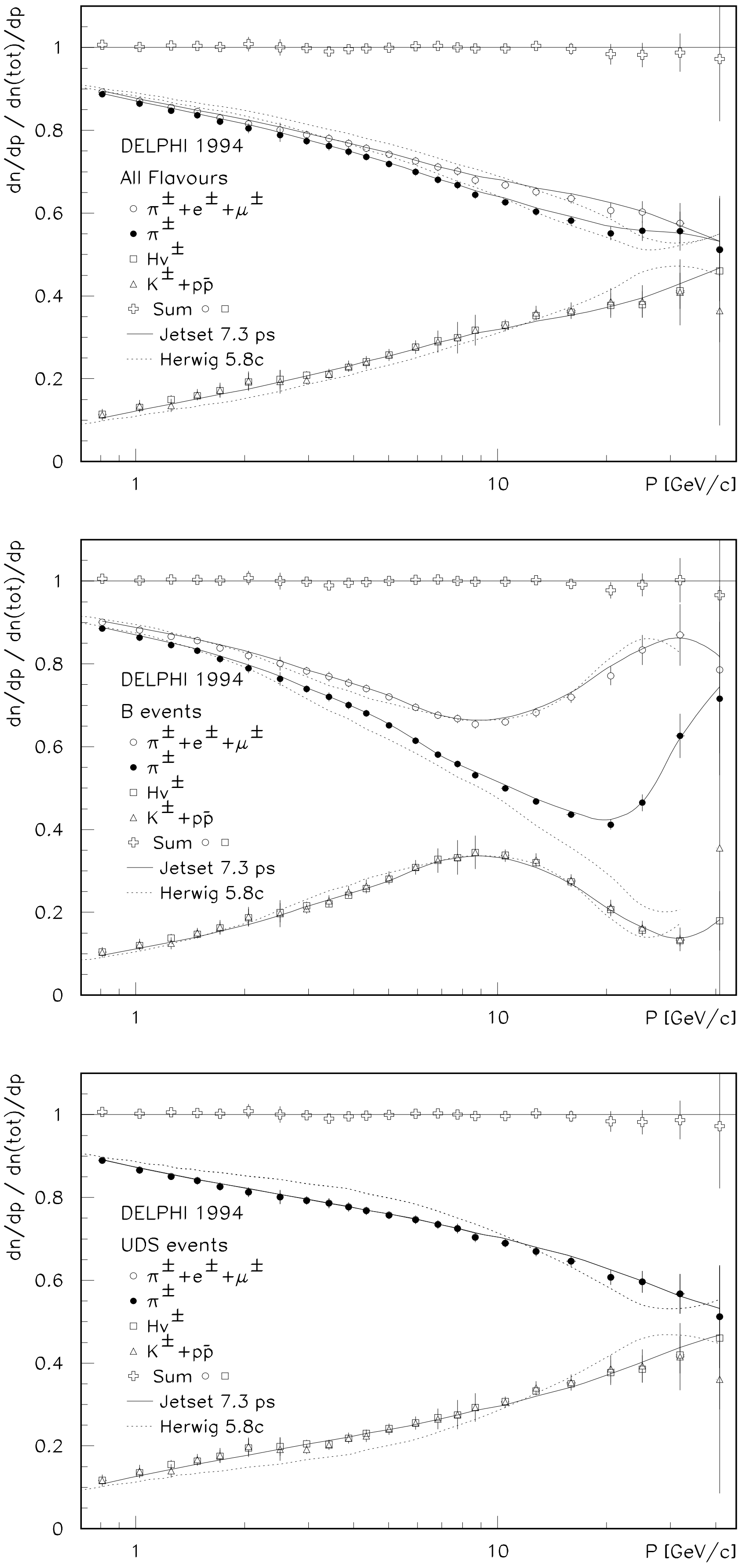

Figure 9.14: The normalised production rates of $\pi^{\pm}$ and heavy particles in $Z^0 \to q\bar{q}$, $Z^0 \to b\bar{b}$ and $Z^0 \to u\bar{u}, d\bar{d}, s\bar{s}$.

Summary Table of Normalised Production Rates in $Z^0 \to b\bar{b}$

Momentum GeV/c	DELPHI f_π %	ϵ_{tot}	ϵ_{stat}	ϵ_{syst}	JS73PS f_π %
0.70 - 0.91	88.57	± 1.21	± 0.99	± 0.71	88.77
0.91 - 1.14	86.34	± 1.18	± 0.99	± 0.68	86.85
1.14 - 1.37	84.86	± 1.31	± 1.08	± 0.76	85.12
1.37 - 1.60	83.15	± 1.42	± 1.18	± 0.81	83.53
1.60 - 1.82	81.12	± 1.54	± 1.30	± 0.84	81.92
1.82 - 2.28	78.79	± 1.52	± 1.11	± 1.02	79.75
2.28 - 2.74	76.66	± 1.89	± 1.25	± 1.43	77.01
2.74 - 3.19	74.39	± 1.44	± 0.99	± 1.03	74.25
3.19 - 3.65	72.25	± 1.46	± 0.95	± 1.12	72.09
3.65 - 4.10	69.87	± 1.36	± 0.99	± 0.95	70.12
4.10 - 4.56	68.07	± 1.39	± 1.04	± 0.94	68.23
4.56 - 5.47	65.13	± 1.08	± 0.81	± 0.74	65.46
5.47 - 6.38	61.46	± 1.12	± 0.92	± 0.66	61.60
6.38 - 7.29	58.17	± 1.30	± 1.07	± 0.73	58.19
7.29 - 8.21	55.87	± 1.40	± 1.29	± 0.57	55.83
8.21 - 9.12	53.23	± 1.57	± 1.20	± 1.01	53.94
9.12 - 11.85	49.84	± 0.92	± 0.71	± 0.62	50.73
11.85 - 13.68	46.23	± 1.36	± 1.06	± 0.86	47.45
13.68 - 18.24	43.25	± 1.22	± 0.95	± 0.75	44.36
18.24 - 22.80	40.83	± 2.24	± 1.67	± 1.47	42.43
22.80 - 27.36	46.20	± 5.51	± 3.62	± 3.70	46.61
27.36 - 36.47	62.64	± 11.18	± 9.12	± 5.98	62.07
36.47 - 45.00	78.62	± 83.44	± 55.48	± 62.05	74.48

Table 9.7: The normalised production rates for $\pi^\pm$ in $Z^0 \to b\bar{b}$.

Momentum GeV/c	DELPHI f_K %	ϵ_{tot}	ϵ_{stat}	ϵ_{syst}	JS73PS f_K %
0.70 - 0.91	6.70	± 1.14	± 0.79	± 0.81	6.60
0.91 - 1.14	8.05	± 1.23	± 0.61	± 1.09	7.53
1.14 - 1.37	8.51	± 1.45	± 0.68	± 1.30	8.43
1.37 - 1.60	10.11	± 1.21	± 0.88	± 0.85	9.31
1.60 - 1.82	11.03	± 2.08	± 1.18	± 1.71	10.32
1.82 - 2.28	12.98	± 2.32	± 1.16	± 2.00	11.77
2.28 - 2.74	14.59	± 3.20	± 1.48	± 2.85	13.71
2.74 - 3.19	16.08	± 1.38	± 1.04	± 0.91	15.55
3.19 - 3.65	17.76	± 1.45	± 0.99	± 1.08	17.01
3.65 - 4.10	19.43	± 1.74	± 1.06	± 1.40	18.10
4.10 - 4.56	20.67	± 1.66	± 1.19	± 1.15	18.93
4.56 - 5.47	21.23	± 1.47	± 1.02	± 1.03	19.85
5.47 - 6.38	21.73	± 2.03	± 1.53	± 1.34	20.94
6.38 - 7.29	22.19	± 3.45	± 2.81	± 1.88	21.64
7.29 - 8.21	21.76	± 5.01	± 3.96	± 3.04	22.04
8.21 - 9.12	23.09	± 3.98	± 2.43	± 3.12	22.50
9.12 - 11.85	22.77	± 1.00	± 0.75	± 0.69	22.31
11.85 - 13.68	22.24	± 1.32	± 0.98	± 0.86	21.37
13.68 - 18.24	19.85	± 1.36	± 0.80	± 1.03	19.26
18.24 - 22.80	15.47	± 1.99	± 1.16	± 1.59	15.33
22.80 - 27.36	11.50	± 1.97	± 1.73	± 0.72	12.18
27.36 - 36.47	9.38	± 2.93	± 2.76	± 0.83	10.25
36.47 - 45.00	5.86	± 9.04	± 5.95	± 6.71	9.31

Table 9.8: Normalised production rates for $K^\pm$ in $Z^0 \to b\bar{b}$.

Momentum GeV/c	DELPHI f_p %	ϵ_{tot}	ϵ_{stat}	ϵ_{syst}	JS73PS f_p %
0.70 - 0.91	3.65	± 0.84	± 0.35	± 0.78	3.05
0.91 - 1.14	4.20	± 0.81	± 0.48	± 0.68	3.81
1.14 - 1.37	3.99	± 1.06	± 0.70	± 0.82	4.36
1.37 - 1.60	4.94	± 0.96	± 0.82	± 0.54	4.77
1.60 - 1.82	5.36	± 0.86	± 0.67	± 0.58	5.07
1.82 - 2.28	6.00	± 0.88	± 0.63	± 0.65	5.31
2.28 - 2.74	5.06	± 0.82	± 0.40	± 0.74	5.57
2.74 - 3.19	4.78	± 0.59	± 0.25	± 0.57	5.84
3.19 - 3.65	4.96	± 0.65	± 0.33	± 0.59	6.00
3.65 - 4.10	5.54	± 0.78	± 0.41	± 0.68	6.34
4.10 - 4.56	5.60	± 0.99	± 0.51	± 0.87	6.87
4.56 - 5.47	7.11	± 0.91	± 0.57	± 0.68	7.81
5.47 - 6.38	9.16	± 1.69	± 1.18	± 1.21	9.39
6.38 - 7.29	10.34	± 3.10	± 2.86	± 1.20	10.62
7.29 - 8.21	11.50	± 5.13	± 4.50	± 2.42	11.14
8.21 - 9.12	11.38	± 3.32	± 2.84	± 1.72	11.11
9.12 - 11.85	10.88	± 1.64	± 1.08	± 1.25	10.65
11.85 - 13.68	10.43	± 1.49	± 1.18	± 0.94	9.42
13.68 - 18.24	7.87	± 1.11	± 0.85	± 0.71	7.57
18.24 - 22.80	5.71	± 1.34	± 0.95	± 0.91	5.20
22.80 - 27.36	4.72	± 2.05	± 1.68	± 1.15	4.21
27.36 - 36.47	4.08	± 5.28	± 3.74	± 3.70	3.49
36.47 - 45.00	29.72	± 137.3	± 77.8	± 113.0	8.97

Table 9.9: The normalised production rates for $p\bar{p}$ in $Z^0 \to b\bar{b}$.

Momentum GeV/c	DELPHI f_{Hv} %	ϵ_{tot}	ϵ_{stat}	ϵ_{syst}	JS73PS f_{Hv} %
0.70 - 0.91	10.47	± 1.20	± 0.84	± 0.80	9.66
0.91 - 1.14	11.95	± 1.18	± 0.69	± 0.98	11.34
1.14 - 1.37	13.79	± 1.27	± 0.80	± 1.01	12.79
1.37 - 1.60	14.73	± 1.30	± 0.98	± 0.87	14.08
1.60 - 1.82	16.26	± 1.83	± 1.23	± 1.37	15.39
1.82 - 2.28	18.73	± 2.12	± 1.26	± 1.69	17.08
2.28 - 2.74	19.94	± 2.50	± 1.34	± 2.12	19.28
2.74 - 3.19	21.57	± 1.16	± 0.90	± 0.73	21.40
3.19 - 3.65	22.01	± 1.11	± 0.80	± 0.80	23.01
3.65 - 4.10	24.13	± 1.02	± 0.83	± 0.62	24.44
4.10 - 4.56	25.76	± 1.23	± 0.91	± 0.83	25.79
4.56 - 5.47	27.97	± 1.15	± 0.77	± 0.87	27.66
5.47 - 6.38	30.82	± 1.16	± 0.95	± 0.70	30.34
6.38 - 7.29	32.80	± 1.43	± 1.14	± 0.72	32.26
7.29 - 8.21	33.22	± 1.47	± 1.31	± 0.69	33.19
8.21 - 9.12	34.47	± 1.43	± 1.23	± 0.74	33.61
9.12 - 11.85	33.85	± 1.02	± 0.73	± 0.74	32.96
11.85 - 13.68	32.01	± 1.41	± 1.13	± 0.80	30.79
13.68 - 18.24	27.42	± 1.46	± 0.96	± 1.08	26.84
18.24 - 22.80	20.66	± 2.33	± 1.30	± 1.94	20.53
22.80 - 27.36	15.72	± 2.25	± 1.75	± 1.17	16.39
27.36 - 36.47	13.18	± 3.12	± 2.34	± 1.94	13.74
36.47 - 45.00	17.98	± 20.28	± 16.79	± 11.29	18.28

Table 9.10: The normalised production rates for $Hv^\pm$ particles ($K^\pm/p\bar{p}$) in $Z^0 \to b\bar{b}$.

Summary Table of Normalised Production Rates in $Z^0 \to u\overline{u}, d\overline{d}, s\overline{s}$

Momentum GeV/c	DELPHI f_π %	ϵ_{tot}	ϵ_{stat}	ϵ_{syst}	JS73PS f_π %
0.70 - 0.91	88.87	± 0.80	± 0.56	± 0.60	88.77
0.91 - 1.14	86.56	± 0.98	± 0.57	± 0.81	86.85
1.14 - 1.37	85.28	± 0.95	± 0.64	± 0.73	85.12
1.37 - 1.60	83.90	± 0.99	± 0.70	± 0.72	83.53
1.60 - 1.82	82.51	± 1.07	± 0.78	± 0.76	81.92
1.82 - 2.28	81.13	± 1.21	± 0.67	± 1.03	79.75
2.28 - 2.74	80.34	± 1.78	± 0.78	± 1.60	77.01
2.74 - 3.19	79.71	± 0.99	± 0.65	± 0.77	74.25
3.19 - 3.65	78.77	± 1.31	± 0.64	± 1.16	72.09
3.65 - 4.10	77.50	± 1.13	± 0.68	± 0.92	70.12
4.10 - 4.56	76.73	± 1.06	± 0.74	± 0.78	68.23
4.56 - 5.47	75.61	± 1.00	± 0.59	± 0.83	65.46
5.47 - 6.38	74.60	± 1.04	± 0.69	± 0.80	61.60
6.38 - 7.29	73.55	± 1.16	± 0.81	± 0.85	58.19
7.29 - 8.21	72.56	± 1.24	± 0.98	± 0.78	55.83
8.21 - 9.12	70.47	± 1.54	± 0.90	± 1.27	53.94
9.12 - 11.85	68.81	± 0.93	± 0.53	± 0.79	50.73
11.85 - 13.68	66.22	± 1.15	± 0.80	± 0.84	47.45
13.68 - 18.24	64.12	± 1.22	± 0.69	± 1.03	44.36
18.24 - 22.80	60.17	± 1.73	± 1.07	± 1.37	42.43
22.80 - 27.36	59.25	± 2.25	± 1.80	± 1.32	46.61
27.36 - 36.47	56.75	± 5.45	± 2.86	± 4.61	62.07
36.47 - 45.00	56.19	± 14.56	± 11.31	± 9.00	74.48

Table 9.11: Normalised production rates for $\pi^{\pm}$ in $Z^0 \to u\overline{u}, d\overline{d}, s\overline{s}$.

Momentum GeV/c	DELPHI f_K %	ϵ_{tot}	ϵ_{stat}	ϵ_{syst}	JS73PS f_K %
0.70 - 0.91	7.34	± 1.03	± 0.45	± 0.95	7.24
0.91 - 1.14	8.78	± 1.18	± 0.37	± 1.13	8.21
1.14 - 1.37	8.98	± 1.27	± 0.40	± 1.22	8.89
1.37 - 1.60	10.27	± 1.05	± 0.51	± 0.93	9.45
1.60 - 1.82	10.52	± 1.61	± 0.65	± 1.48	9.84
1.82 - 2.28	11.43	± 2.06	± 0.58	± 1.98	10.37
2.28 - 2.74	11.72	± 2.77	± 0.70	± 2.69	11.02
2.74 - 3.19	11.99	± 0.86	± 0.44	± 0.76	11.60
3.19 - 3.65	12.65	± 1.07	± 0.40	± 1.01	12.12
3.65 - 4.10	13.57	± 0.90	± 0.42	± 0.82	12.64
4.10 - 4.56	14.45	± 1.09	± 0.46	± 1.00	13.23
4.56 - 5.47	14.91	± 1.00	± 0.40	± 0.92	13.94
5.47 - 6.38	15.59	± 0.97	± 0.62	± 0.76	15.02
6.38 - 7.29	16.52	± 1.86	± 1.03	± 1.53	16.11
7.29 - 8.21	17.01	± 2.53	± 1.55	± 2.00	17.23
8.21 - 9.12	18.86	± 2.84	± 1.02	± 2.65	18.38
9.12 - 11.85	20.33	± 0.75	± 0.36	± 0.68	19.92
11.85 - 13.68	23.14	± 1.21	± 0.55	± 1.09	22.23
13.68 - 18.24	25.60	± 1.66	± 0.53	± 1.58	24.84
18.24 - 22.80	28.87	± 2.79	± 0.98	± 2.62	28.62
22.80 - 27.36	30.59	± 3.82	± 1.84	± 3.34	32.43
27.36 - 36.47	34.77	± 6.80	± 3.53	± 5.79	37.98
36.47 - 45.00	27.88	± 24.47	± 16.19	± 18.19	44.30

Table 9.12: Normalised production rates for $K^{\pm}$ in $Z^0 \to u\overline{u}, d\overline{d}, s\overline{s}$.

Momentum GeV/c	DELPHI f_p %	ϵ_{tot}	ϵ_{stat}	ϵ_{syst}	JS73PS f_p %
0.70 - 0.91	4.30	± 1.06	± 0.24	± 1.04	3.60
0.91 - 1.14	5.10	± 1.06	± 0.34	± 1.00	4.62
1.14 - 1.37	5.02	± 1.05	± 0.52	± 0.93	5.48
1.37 - 1.60	6.40	± 0.89	± 0.57	± 0.71	6.19
1.60 - 1.82	7.13	± 0.96	± 0.50	± 0.85	6.75
1.82 - 2.28	8.40	± 0.88	± 0.47	± 0.76	7.44
2.28 - 2.74	7.45	± 0.91	± 0.35	± 0.86	8.19
2.74 - 3.19	7.17	± 0.79	± 0.25	± 0.78	8.77
3.19 - 3.65	7.62	± 0.78	± 0.32	± 0.73	9.22
3.65 - 4.10	8.31	± 1.03	± 0.38	± 0.98	9.51
4.10 - 4.56	7.99	± 1.17	± 0.44	± 1.10	9.79
4.56 - 5.47	9.11	± 0.90	± 0.41	± 0.81	10.01
5.47 - 6.38	9.91	± 1.42	± 0.69	± 1.25	10.16
6.38 - 7.29	10.00	± 1.92	± 1.25	± 1.47	10.27
7.29 - 8.21	10.55	± 2.48	± 1.92	± 1.57	10.21
8.21 - 9.12	10.41	± 2.09	± 1.34	± 1.61	10.16
9.12 - 11.85	10.22	± 1.18	± 0.52	± 1.07	10.00
11.85 - 13.68	10.84	± 1.40	± 0.62	± 1.27	9.79
13.68 - 18.24	9.74	± 1.15	± 0.53	± 1.03	9.37
18.24 - 22.80	9.70	± 1.71	± 0.69	± 1.57	8.84
22.80 - 27.36	8.74	± 2.03	± 1.09	± 1.71	7.79
27.36 - 36.47	6.76	± 2.71	± 1.72	± 2.09	5.79
36.47 - 45.00	8.17	± 5.93	± 4.19	± 4.20	2.46

Table 9.13: Normalised production rates for $p\overline{p}$ in $Z^0 \to u\overline{u}, d\overline{d}, s\overline{s}$.

Momentum GeV/c	DELPHI f_{Hv} %	ϵ_{tot}	ϵ_{stat}	ϵ_{syst}	JS73PS f_{Hv} %
0.70 - 0.91	11.75	± 0.98	± 0.50	± 0.86	10.84
0.91 - 1.14	13.52	± 1.26	± 0.43	± 1.20	12.84
1.14 - 1.37	15.50	± 1.14	± 0.51	± 1.04	14.38
1.37 - 1.60	16.36	± 1.27	± 0.63	± 1.11	15.63
1.60 - 1.82	17.53	± 1.53	± 0.78	± 1.34	16.59
1.82 - 2.28	19.52	± 2.33	± 0.75	± 2.21	17.81
2.28 - 2.74	19.87	± 2.44	± 0.78	± 2.32	19.22
2.74 - 3.19	20.53	± 1.02	± 0.50	± 0.91	20.36
3.19 - 3.65	20.41	± 0.87	± 0.44	± 0.78	21.34
3.65 - 4.10	21.87	± 0.70	± 0.45	± 0.57	22.16
4.10 - 4.56	22.99	± 0.80	± 0.48	± 0.66	23.03
4.56 - 5.47	24.21	± 0.67	± 0.38	± 0.58	23.95
5.47 - 6.38	25.59	± 0.75	± 0.45	± 0.61	25.18
6.38 - 7.29	26.82	± 0.79	± 0.52	± 0.58	26.37
7.29 - 8.21	27.48	± 0.83	± 0.62	± 0.56	27.45
8.21 - 9.12	29.28	± 0.89	± 0.59	± 0.70	28.54
9.12 - 11.85	30.72	± 0.74	± 0.37	± 0.67	29.92
11.85 - 13.68	33.29	± 1.17	± 0.64	± 1.00	32.02
13.68 - 18.24	34.96	± 1.69	± 0.63	± 1.58	34.22
18.24 - 22.80	37.69	± 3.00	± 1.07	± 2.81	37.46
22.80 - 27.36	38.56	± 3.99	± 1.73	± 3.59	40.21
27.36 - 36.47	41.99	± 3.98	± 2.66	± 2.95	43.77
36.47 - 45.00	46.00	± 15.98	± 10.83	± 11.70	46.77

Table 9.14: Normalised production rates for $Hv^{\pm}$ particles ($K^{\pm}/p\overline{p}$) in $Z^0 \to u\overline{u}, d\overline{d}, s\overline{s}$.

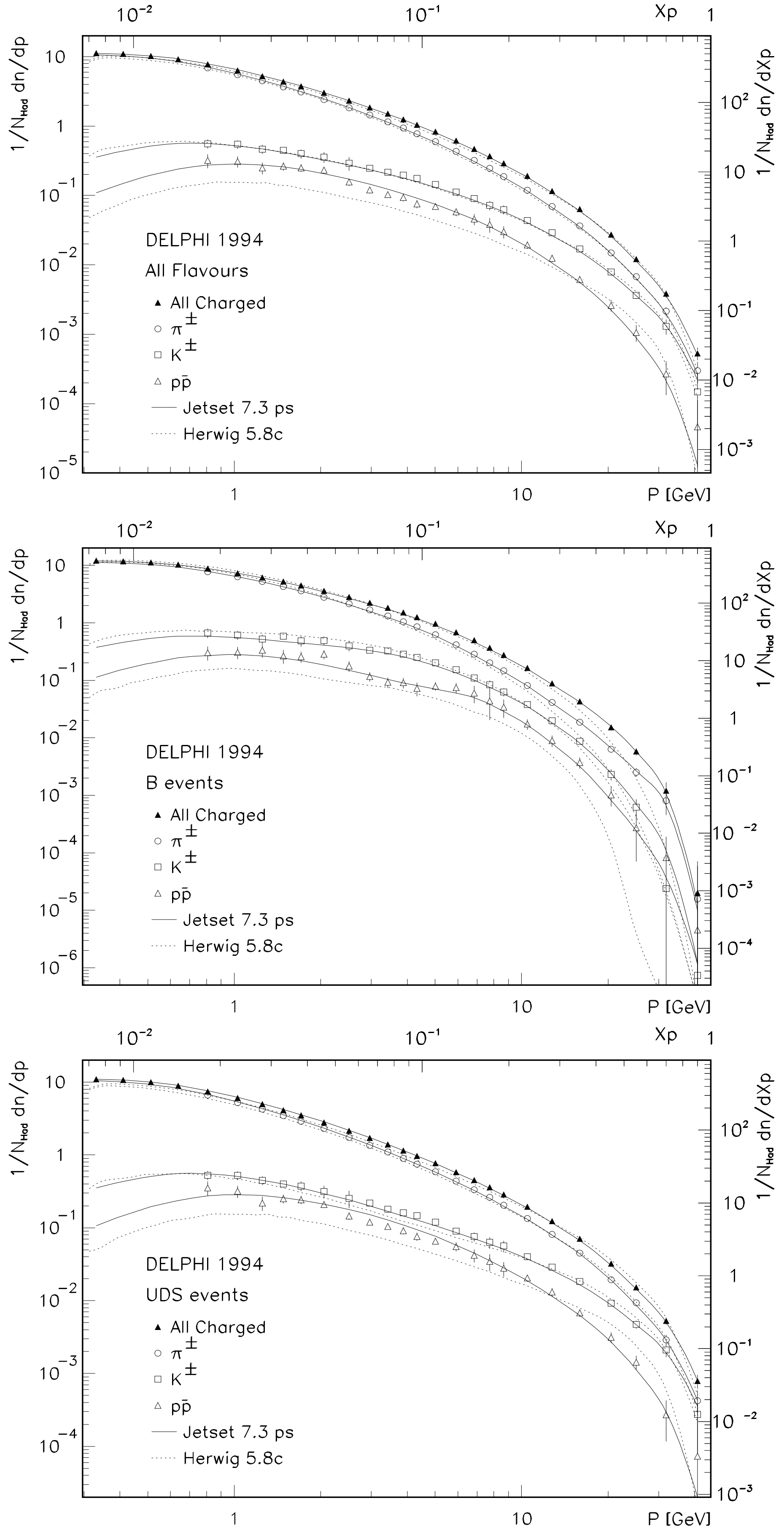

Figure 9.15: The differential cross-sections for $\pi^{\pm}$, $K^{\pm}$, $p\overline{p}$ in $Z^0 \rightarrow q\overline{q}$, $Z^0 \rightarrow b\overline{b}$ and $Z^0 \rightarrow u\overline{u}, d\overline{d}, s\overline{s}$.

9.6 Differential Cross-sections

Having obtained the normalised production rates, the distributions of the $\pi^\pm$, $K^\pm$, $p\overline{p}$ differential cross-sections versus momentum, the scaled momentum[4] X_p and versus ξ_p ($= \ln(1/X_p)$, for conversion see page 167) can be extracted rather easily. To enable an extra consistency test, the distributions for all charged particles have been included as well. Similar to the consistency test for the sum of the fractions f_i being equal to unity in the previous section, here the sum of the identified distributions should be equal to the distribution for all charged particles. This actually reflects the difference between the normalised production rates and differential cross-sections which basically is the factor $1/N_{\rm had}({\rm dn_{tot}}/{\rm d}p)$ i.e. the total charged particle differential cross-section. Figure 9.15 shows the $\pi^\pm$, $K^\pm$, $p\overline{p}$ differential cross-sections versus momentum (bottom and left hand axes) and versus the scaled momentum X_p (top and right hand axes), for $Z^0 \to q\overline{q}$, $Z^0 \to b\overline{b}$ and $Z^0 \to u\overline{u}, d\overline{d}, s\overline{s}$ as obtained from the 3x3-method. Since the LEP beam energy during the 1994 data taking was kept at the peak of Z^0 resonance (i.e. no scan), the difference between the top and bottom axes simply is a constant factor E_{beam}. The systematic uncertainties for the total charged particle distributions versus X_p and ξ_p were adopted from the inclusive DELPHI measurement performed on 1991, 1992 and 1993 DELPHI data. The inclusive total charged particle distributions are in good agreement with these previous DELPHI measurements [21].

The open circles in figure 9.15 represent the pions *after* the lepton correction (for reasons of simplicity, the curves for pions before correction and the curves of the sum have been omitted in these figures). The full lines are the predictions from JETSET 7.3 PS and the dotted lines represent HERWIG 5.8C. The $\pi^\pm$ and $Hv^\pm$ distributions based on the 2x2-method are shown in figure 9.16. Also here, to illustrate the consistency of the matrix inversion method, an overlay of the sum of $K^\pm$ and $p\overline{p}$ from the 3x3-method (triangles) is included for each event sample.

The differential cross-sections as a function of ξ_p are illustrated separately for each distribution in figure 9.17 (page 132), together with the predictions of JETSET and HERWIG. Here, the discrepancy between the data and especially HERWIG becomes very clear. For all three event samples, JETSET gives a better prediction of the measured spectra than HERWIG. The latter clearly fails to describe the proton spectra and generally overestimates the spectra for b-events and underestimates them for uds-events. The overall JETSET forecast is rather good. The only striking discrepancy can be found in the proton distributions. The proton distribution in b-events clearly shows two distinct local maxima. This subject will be discussed in more detail in section 9.9.

The values and uncertainties corresponding to the differential cross-sections dependence on momentum p and on the scaled momentum X_p are enlisted in appendices A, C and D (page 147), including the JETSET 7.3 PS predictions.

[4]The scaled momentum X_p is the momentum of the particle scaled to the beam energy, i.e. $X_p = p/E_{beam}$.

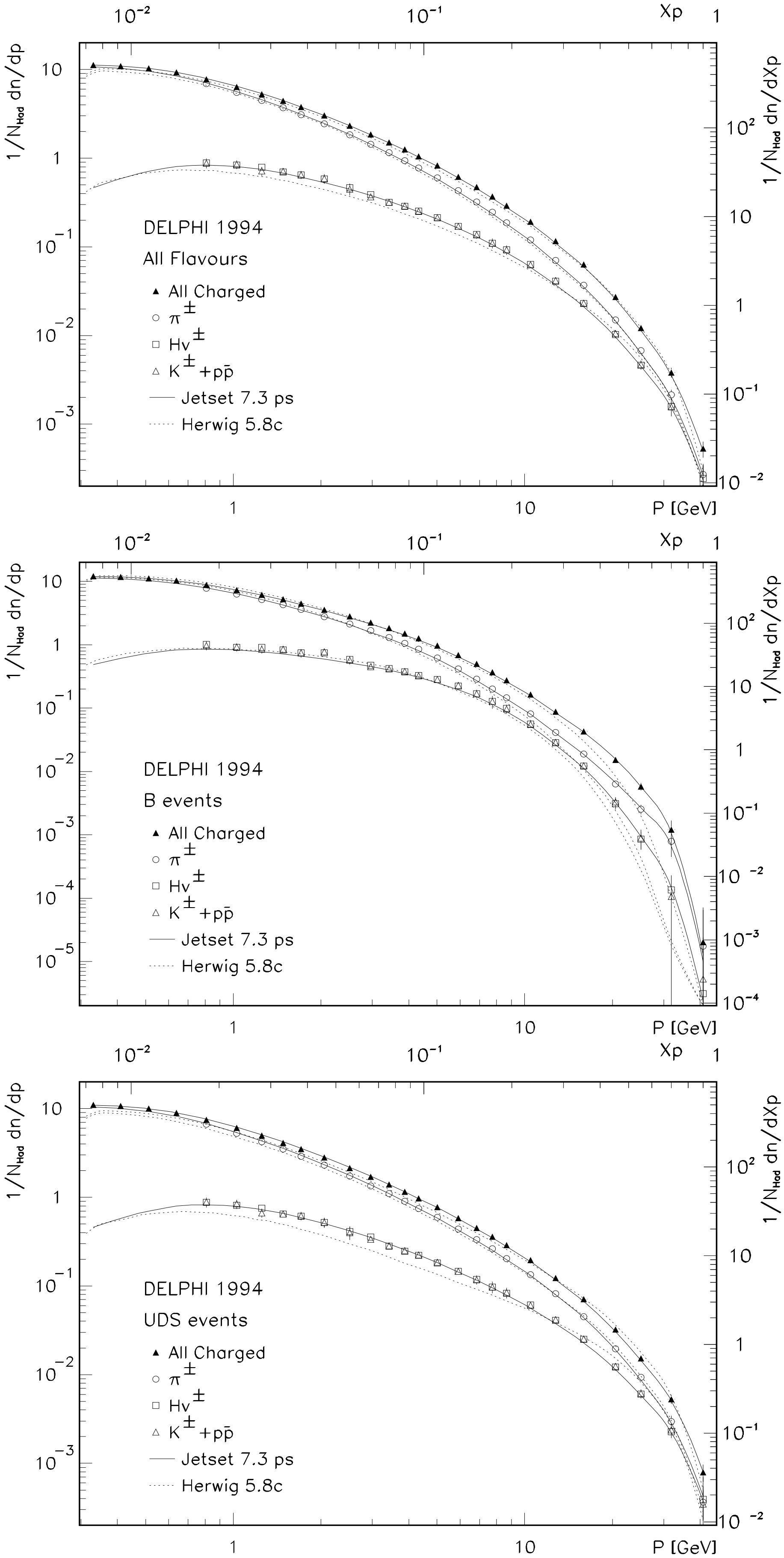

Figure 9.16: The differential cross-sections for $\pi^{\pm}$ and heavy particles in $Z^0 \to q\bar{q}$, $Z^0 \to b\bar{b}$ and $Z^0 \to u\bar{u}, d\bar{d}, s\bar{s}$.

9.7 Particle Multiplicities

The particle multiplicity can be obtained by integrating any differential cross-section distribution, no matter what observable has been measured e.g. p, X_p or ξ_p. The advantage of the observable ξ_p lays in the Gaussian like shape of the resulting distributions. As has been discussed in more detail in section 2.2 (page 12), based on the MLLA while assuming LPHD, an approximation of this Gaussian like shape can be given by the following equation [23,24][5]:

$$\mathcal{G}(\delta,\sigma,s,\kappa,N) = \frac{N}{\sigma\sqrt{2\pi}} \cdot \exp(\frac{1}{8}\kappa - \frac{1}{2}s\delta - \frac{1}{4}(2+\kappa)\delta^2 + \frac{1}{6}s\delta^3 + \frac{1}{24}\kappa\delta^4) \quad (9.13)$$

where

$$\begin{aligned}
\delta &:= \frac{\xi_p - \overline{\xi}_p}{\sigma} \\
\overline{\xi}_p &:= \text{mean of the distribution} \\
\sigma &:= \text{width of the distribution} \\
s &:= \text{skewness of the distribution} \\
\kappa &:= \text{kurtosis of the distribution} \\
N &:= \text{normalisation factor}
\end{aligned}$$

This five parameter expression can be used to perform a so called 'distorted Gaussian fit' on each of the acquired ξ_p distributions. Then, to obtain the particle multiplicity from the distributions, the result of the fit can be used to integrate over the total ξ_p range. Figure 9.18 gives an overview of the distorted Gaussian fits, performed on the data for each ξ_p-distribution. In most cases equation 9.13 gives a good description of the measurement.

The fit result on the distributions for all charged particles approaches zero value at $\xi_p \simeq 6.5$. One can use this information as a constraint at high ξ_p values for the fit-procedure on the identified particle distributions. For the $\pi^{\pm}$ distributions, the data cover slightly more than half of the ξ_p distribution. Only in this case, the option of the constraint for the fit procedure was applied, including a fairly large uncertainty (for $\xi_p = 6.7,\ 1/N_{\text{had}} \cdot \mathrm{d}n/\mathrm{d}\xi_p = 0.0 \pm 0.05$).

The final multiplicities, resulting from the integral of the distorted Gaussian fits, are listed in table 9.15, including the predictions from HERWIG 5.8C and JETSET 7.4 PS [21]. The statistical uncertainty was estimated by repeating the fit procedure five times, reducing equation 9.13 to a four parameter expression by freezing one of the five parameters and adding one standard deviation (derived from the five parameter fit) to the frozen parameter. The systematic uncertainty was estimated by repeating the five parameter fit for different ξ_p windows. The uncertainty caused by the extrapolation area, where no points have been measured, is included in the systematic uncertainty.

[5] Equation 9.13 very often is used to estimate the maximum position ξ_p^* of measured ξ_p distributions. It is believed that the value of ξ_p^* is depending on the mass of the identified particle. This subject will not be discussed in this analysis.

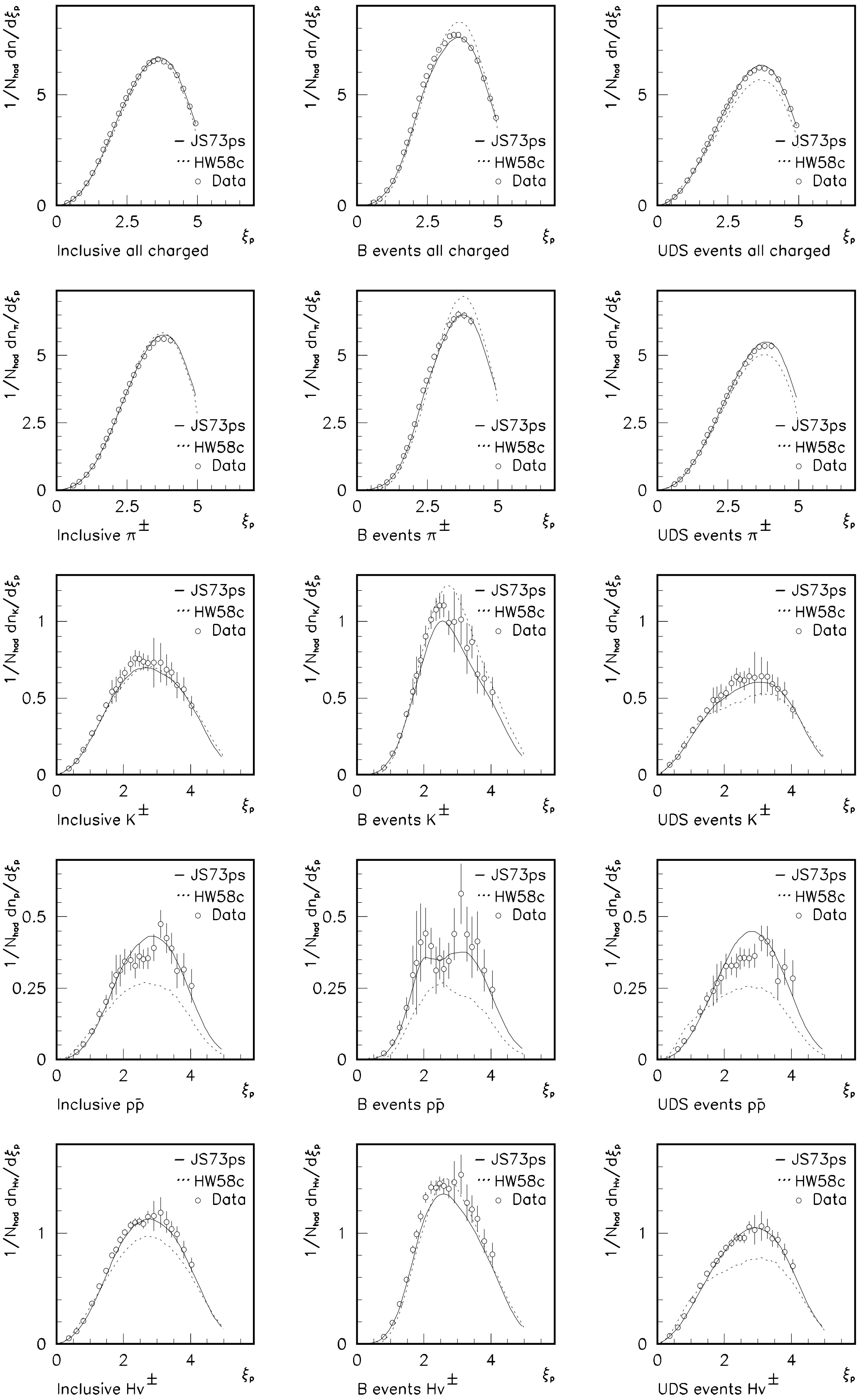

Figure 9.17: The ξ_p distributions vs JETSET 7.3 PS and HERWIG 5.8C in $Z^0 \to q\overline{q}$,$Z^0 \to b\overline{b}$ and $Z^0 \to u\overline{u}, d\overline{d}, s\overline{s}$.

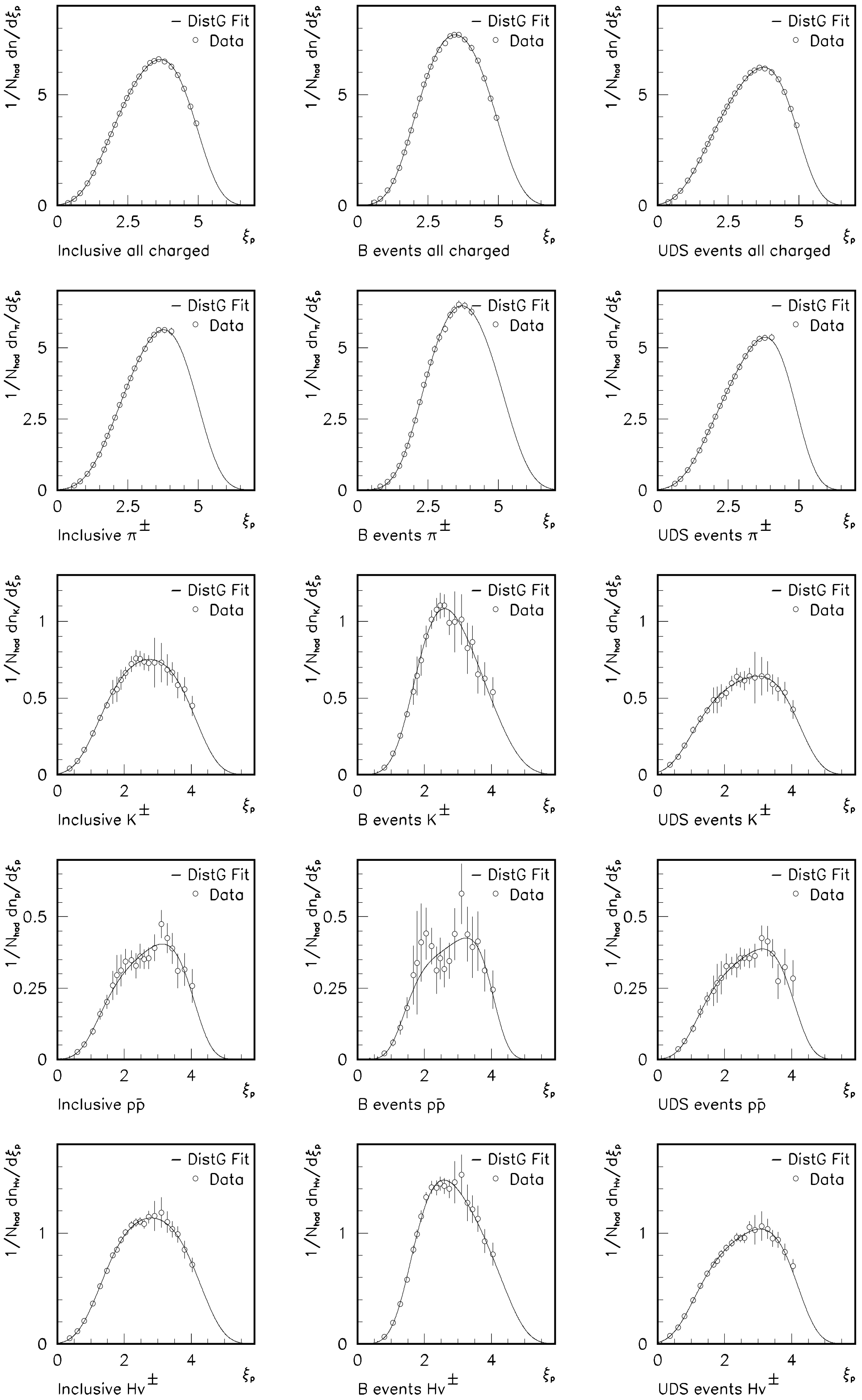

Figure 9.18: The $\pi^{\pm}$, $K^{\pm}$, $p\overline{p}$ ξ_p fitted distributions for $Z^0 \to q\overline{q}$,$Z^0 \to b\overline{b}$ and $Z^0 \to u\overline{u}, d\overline{d}, s\overline{s}$.

$Z^0 \to q\overline{q}$	DELPHI	$\epsilon_{\rm stat}$	$\epsilon_{\rm syst}$	$\epsilon_{\rm tot}$	JS74PS	HW58C
$< n_q >$	20.43	± 0.09	± 0.14	± 0.17	20.81	20.92
$< \pi^{\pm} >$	17.00	± 0.10	± 0.42	± 0.43	17.09	17.66
$< {\rm K}^{\pm} >^{*}$	2.11	± 0.06	± 0.05	± 0.08	2.23	2.11
$< {\rm p}\overline{\rm p} >^{*}$	1.04	± 0.04	± 0.02	± 0.04	0.97	0.78
$< {\rm Hv}^{\pm} >^{**}$	3.27	± 0.06	± 0.05	± 0.08	3.20	3.03
$Z^0 \to b\overline{b}$	DELPHI	$\epsilon_{\rm stat}$	$\epsilon_{\rm syst}$	$\epsilon_{\rm tot}$	JS74PS	HW58C
$< n_b >$	23.42	± 0.10	± 0.33	± 0.35	23.3	22.9
$< \pi^{\pm} >^{**}$	18.47	± 0.12	± 1.05	± 1.06	19.6	18.6
$< {\rm K}^{\pm} >^{*}$	2.54	± 0.09	± 0.13	± 0.16	2.66	2.85
$< {\rm p}\overline{\rm p} >^{*}$	1.03	± 0.06	± 0.01	± 0.06	0.94	0.61
$< {\rm Hv}^{\pm} >^{**}$	3.71	± 0.08	± 0.05	± 0.09	3.60	3.46
$Z^0 \to u\overline{u}, d\overline{d}, s\overline{s}$	DELPHI	$\epsilon_{\rm stat}$	$\epsilon_{\rm syst}$	$\epsilon_{\rm tot}$	JS74PS	HW58C
$< n_{uds} >$	19.44	± 0.09	± 0.19	± 0.21	19.9	18.6
$< \pi^{\pm} >^{**}$	16.56	± 0.10	± 0.81	± 0.82	16.5	16.1
$< {\rm K}^{\pm} >^{**}$	1.88	± 0.06	± 0.08	± 0.10	2.15	1.80
$< {\rm p}\overline{\rm p} >^{**}$	1.02	± 0.04	± 0.03	± 0.05	1.06	0.70
$< {\rm Hv}^{\pm} >^{**}$	2.93	± 0.06	± 0.09	± 0.11	3.21	2.50

Table 9.15: The measured particle production rates in $Z^0 \to q\overline{q}$, $Z^0 \to b\overline{b}$, $Z^0 \to u\overline{u}, d\overline{d}, s\overline{s}$ compared to the JETSET and HERWIG prediction. Results with an improved accuracy compared to previous measurements are indicated by a '$*$'. New results are indicated by '$**$'.

The extrapolation uncertainty has been estimated from the JETSET generator and is on average responsible for $\sim 50\%$ of the total systematic uncertainty. Results with an improved accuracy compared to previous measurements are indicated by a '$*$' in the left hand column of the table and will be discussed in the next section. New results are indicated by a '$**$'.

The results in table 9.15 are very much consistent within their uncertainties. For example, in $Z^0 \to q\overline{q}$, comparing the $< n_q >$ with the the sum of $<\pi^{\pm} + {\rm K}^{\pm} + {\rm p}\overline{\rm p}>$ leaves 0.28 ± 0.47 for light leptons i.e. $<e^{\pm} + \mu^{\pm}>$. For uds-events, the difference between $< n_{uds} >$ and $<\pi^{\pm} + {\rm K}^{\pm} + {\rm p}\overline{\rm p}>$ is 0.02. This simply means that most leptons in hadronic Z^0 decays are produced in heavy flavour events through the semi-leptonic decay of heavy flavour hadrons. For b-events, $<n_b> = 23.42 \pm 0.35$ and $<\pi^{\pm} + {\rm K}^{\pm} + {\rm p}\overline{\rm p}> = 22.04 \pm 1.07$, leaving 1.38 ± 1.13 for $<e^{\pm} + \mu^{\pm}>$. The same exercise holds also for HERWIG but is not clear for JETSET (in b-events).

Similarly, the comparisons between the sum of $<{\rm K}^{\pm} + {\rm p}\overline{\rm p}>$ and the results obtained for the heavy particle distributions $<{\rm Hv}^{\pm}>$ are in good agreement.

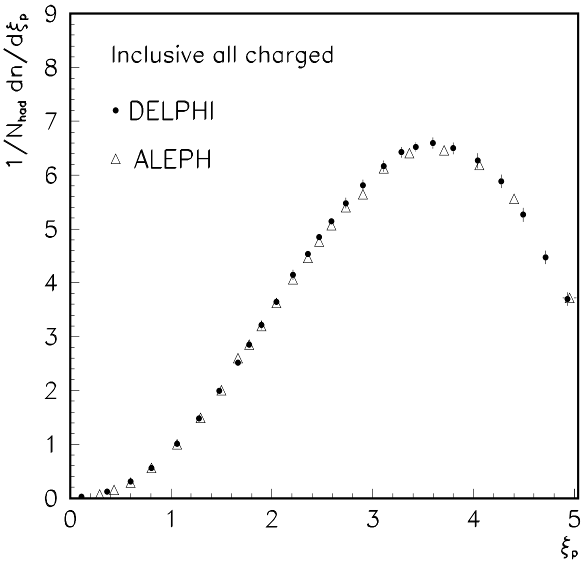

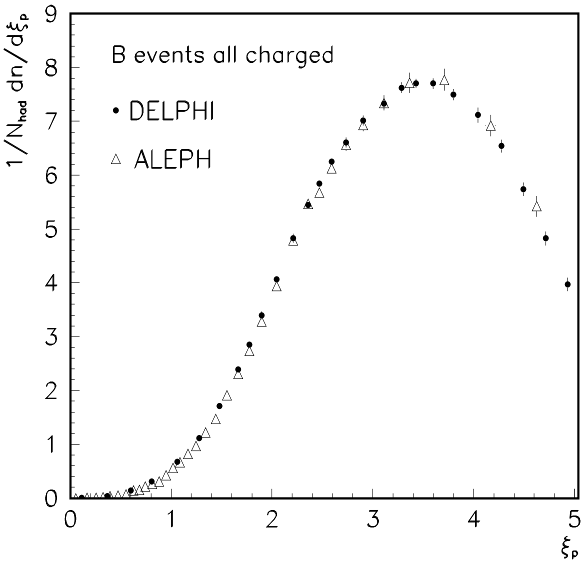

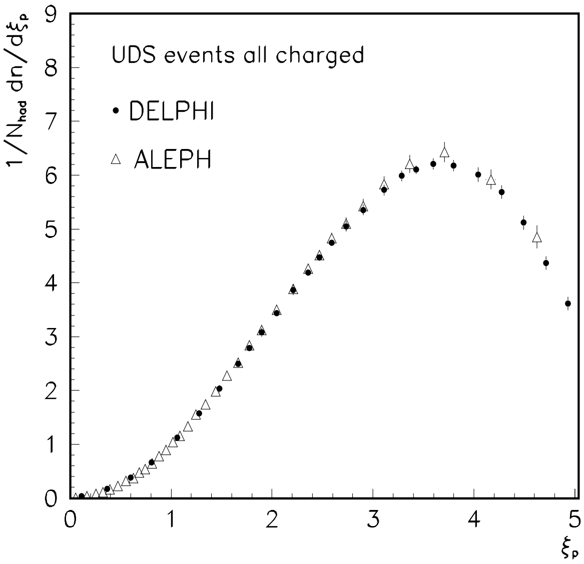

Figure 9.19: The charged particle distributions of DELPHI compared to the ALEPH results for $Z^0 \to q\overline{q}$ (top left), $Z^0 \to b\overline{b}$ (top right) and $Z^0 \to u\overline{u}, d\overline{d}, s\overline{s}$ (right). The ALEPH distributions versus ξ_p are obtained from X_p distributions ($\xi_p = \ln(1/X_p)$) published in reference [78].

9.8 Comparison with Other Experimental Results

For the three event samples, figure 9.19 illustrates the good agreement of the total charged particles distributions versus ξ_p obtained from this analysis in comparison with results obtained by the ALEPH Collaboration. The ALEPH distributions versus ξ_p are obtained from X_p distributions ($\xi_p = \ln(1/X_p)$) published in reference [78].

For comparison, published results obtained from other sources i.e. previous measurements of the particle multiplicities, are enlisted in table 9.16. The total charge multiplicity $<n_q>$ in $Z^0 \to q\overline{q}$ shows a small discrepancy with the LEP average from [21]. For $Z^0 \to q\overline{q}$, $<\pi^{\pm}>$ from this analysis is very much compatible with other results. However, the outcome is slightly lower for $<K^{\pm}>$ and slightly higher for $<p\overline{p}>$.

$Z^0 \to q\overline{q}$	DELPHI	$\epsilon_{\rm tot}$	OTHERS	$\epsilon_{\rm tot}$	
$< n_q >$	20.43	± 0.17	20.92	± 0.24	LEP Av. [21]
$< \pi^\pm >$	17.00	± 0.43	17.1	± 0.4	PDG'96 [6]
			17.052	± 0.429	OPAL [79]
$< \mathrm{K}^\pm >$	2.11	± 0.08	2.39	± 0.12	PDG'96 [6]
			2.421	± 0.133	OPAL [79]
			2.26	± 0.18	DELPHI [80]
$< \mathrm{p}\overline{\mathrm{p}} >$	1.04	± 0.04	0.964	± 0.102	PDG'96 [6]
			0.916	± 0.111	OPAL [79]
			1.07	± 0.14	DELPHI [80]
$Z^0 \to b\overline{b}$	DELPHI	$\epsilon_{\rm tot}$ ($\epsilon_{\rm stat}$)	OTHERS	$\epsilon_{\rm tot}$ ($\epsilon_{\rm stat}$)	
$< n_b >$	23.42	± 0.35 (± 0.10)	23.32	± 0.51 (± 0.08)	DELPHI [81]
			23.62	± 0.48 (± 0.02)	OPAL [84]
			23.14	± 0.39 (± 0.10)	SLD [85]
$< \mathrm{K}^\pm >$	2.54	± 0.16 (± 0.09)	2.74	± 0.50 (± 0.10)	DELPHI [81]
$< \mathrm{p}\overline{\mathrm{p}} >$	1.03	± 0.06 (± 0.06)	1.13	± 0.26 (± 0.05)	DELPHI [81]
$Z^0 \to u\overline{u}, d\overline{d}, s\overline{s}$	DELPHI	$\epsilon_{\rm tot}$ ($\epsilon_{\rm stat}$)	OTHERS	$\epsilon_{\rm tot}$ ($\epsilon_{\rm stat}$)	
$< n_{uds} >$	19.44	± 0.21 (± 0.09)	20.21	± 0.24 (± 0.10)	SLD [85]

Table 9.16: The production rates from this analysis compared to published results from other sources. The measurements of $\pi^\pm$, $\mathrm{K}^\pm$ and $\mathrm{p}\overline{\mathrm{p}}$ multiplicities in b- and uds- at LEP have so far only been published by DELPHI.

The improvements in accuracy for $< \mathrm{K}^\pm >$ ($< \mathrm{p}\overline{\mathrm{p}} >$) in $Z^0 \to q\overline{q}$ may be understood from figure 9.20. The left hand column compares the DELPHI (RICH) $\pi^\pm$, $\mathrm{K}^\pm$, $\mathrm{p}\overline{\mathrm{p}}$ distributions from this analysis with the measurements obtained by the OPAL [79] and ALEPH [82] $\mathrm{d}E/\mathrm{d}x$ identification. DELPHI is also able to measure the uncovered areas. In covering a more complete area of the distributions, the uncertainties introduced by extrapolations are reduced.

The right hand side column of the figure shows the comparison between the DELPHI-RICH and SLD-CRID [83]. The latter does not (yet) apply veto-identification. Also in a previously published DELPHI analysis for $< \mathrm{K}^\pm >$ and $< \mathrm{p}\overline{\mathrm{p}} >$ in $Z^0 \to q\overline{q}$ (on 1992 data [80]) the veto-identification was not applied. In addition, the data sample was about a factor 8 smaller compared to this analysis.

The DELPHI measurement on $< \mathrm{K}^\pm >$ ($< \mathrm{p}\overline{\mathrm{p}} >$) in b-events was previously performed using 1992 and 1993 data [81]. For the same reasons mentioned above, this analysis provides an improvement in accuracy for $\mathrm{K}^\pm$ ($\mathrm{p}\overline{\mathrm{p}}$) of a factor ~ 3 (~ 4).

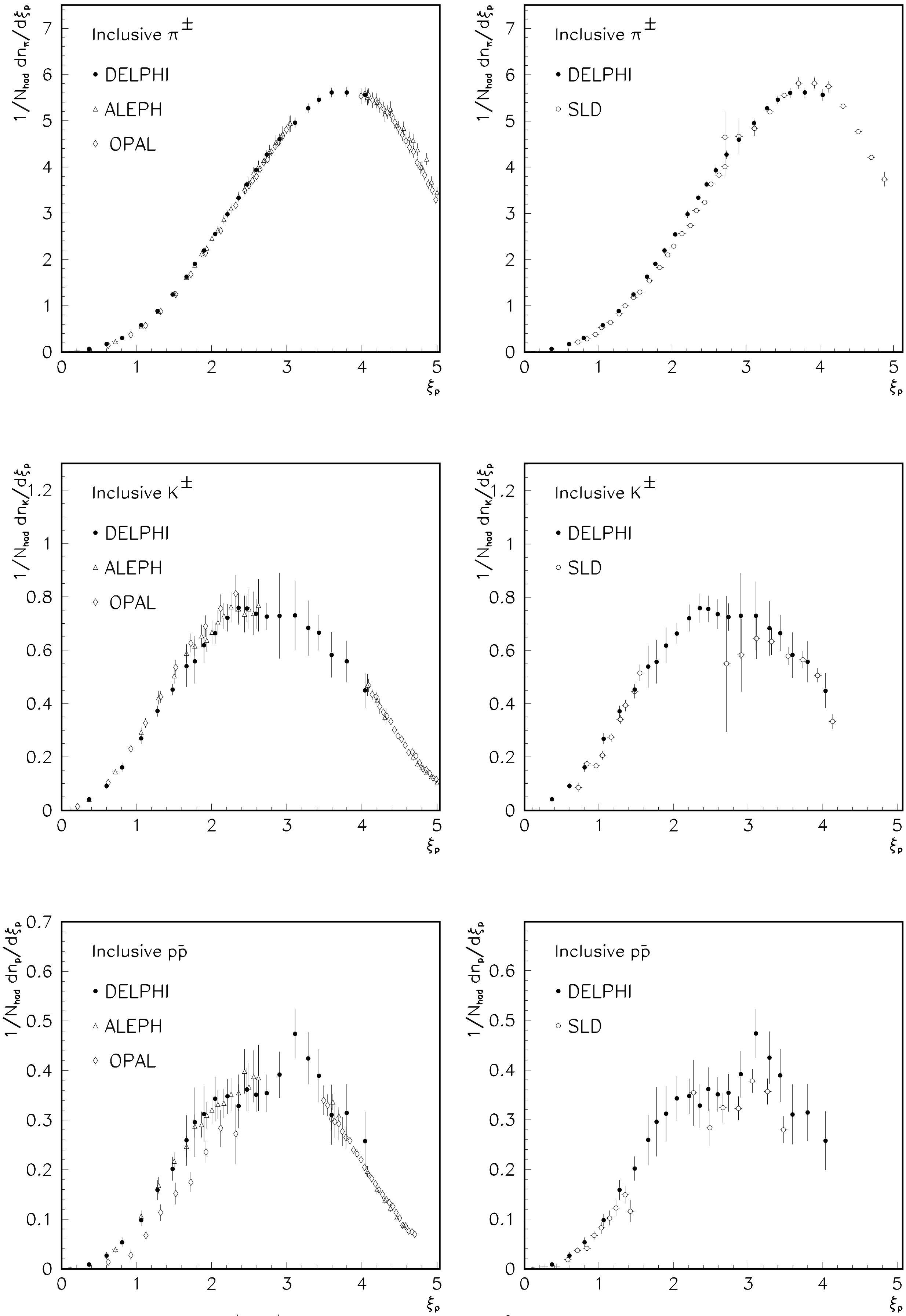

Figure 9.20: The $\pi^{\pm}$, $\mathrm{K}^{\pm}$, $\mathrm{p\bar{p}}$ ξ_p distributions in $\mathrm{Z}^0 \to q\bar{q}$, Delphi vs Aleph, Opal and SLD.

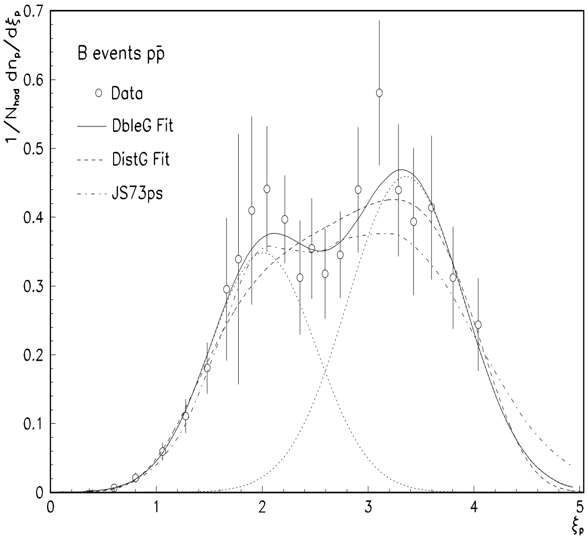

Figure 9.21: The distorted Gaussian (DistG) fit and a double Gaussian (DbleG) fit for protons in b-events compared to the JETSET prediction.

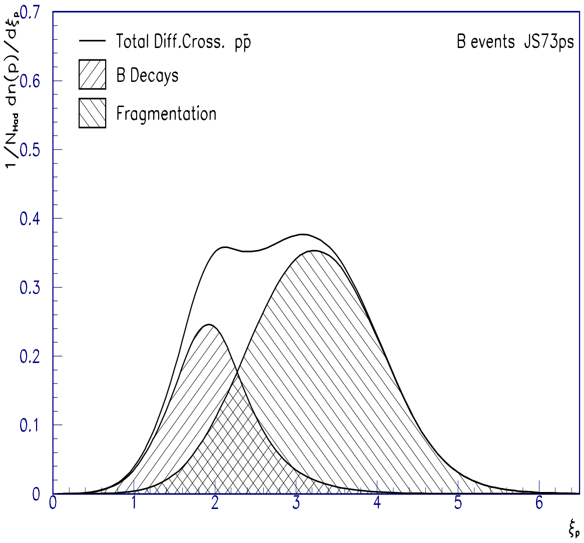

Figure 9.22: The JETSET prediction in b-events for protons originating from fragmentation and from B-decays.

9.9 Fragmentation versus Decays in Flavour Tagged Events

As has been mentioned before, the ξ_p distribution for protons, especially in b-events, shows two local maxima. JETSET predicts a more or less identical shape, but less pronounced. Similar effects can be observed in the distributions of the (normalised) proton production rate in b-events (figs. 9.13, 9.15).
The fit procedure based on the distorted Gaussian approximation in equation 9.13 does not seem to perform very well (a possible explanation may be that the LPHD-MLLA assumes particles to originate from fragmentation only). Instead, a double Gaussian fit appears to be quite successful in describing the data. Figure 9.21 shows the result of a double Gaussian fit (full line). The two constituent single Gaussians (dotted lines) take $\sim$40% and $\sim$60% of the total distribution i.e. multiplicity. The two-Gaussian composition may indicate a possible different nature of protons in b-events. For protons with low ξ_p values (thus having high momenta) it may be more likely that they originate from B-decays whereas protons with high ξ_p values might be produced during the fragmentation process. This can be verified using JETSET, by tracing back their production history. To be compared to figure 9.21, figure 9.22 shows the breakdown of the JETSET prediction for protons in b-events into two parts. One part being the protons originating from the decay of the particle which initially contained the primary quark. The other part being the protons originating – directly or indirectly[6] – from the fragmentation process. Both parts show Gaussian-like shapes, very much equivalent to the constituent single Gaussian distributions resulting from the double Gaussian fit performed on the data. In the JETSET prediction however, the two constituent Gaussian distributions take $\sim$30% and $\sim$70% of the total distribution.

To illustrate why this effect may only become visible for protons produced in b-events, figure 9.23 shows the same breakdown of the JETSET prediction as function of ξ_p, for

[6]the parent particle (or parents-parent etc.) may originate from the fragmentation e.g. $\Lambda^0 \rightarrow p\pi^-$.

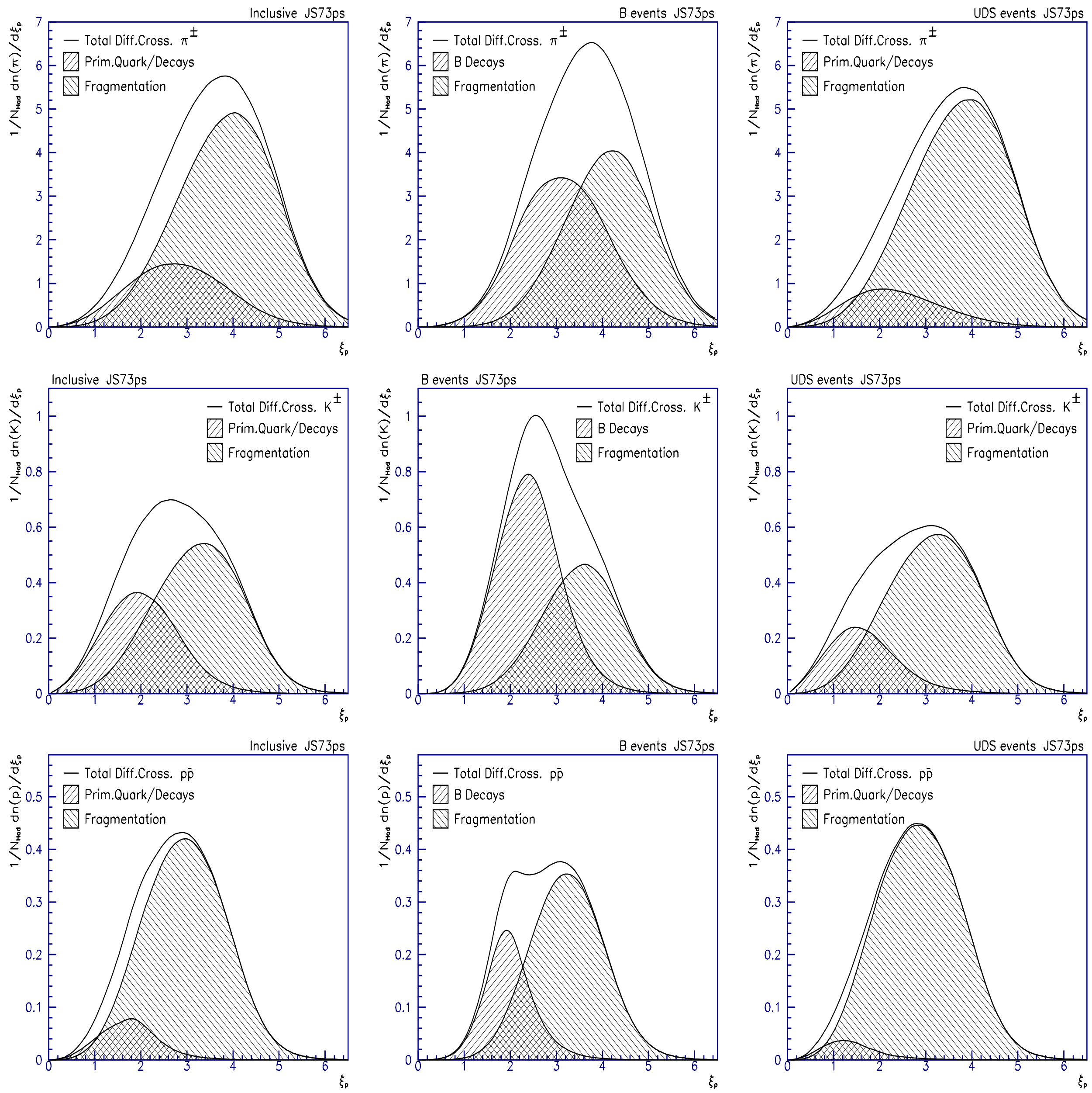

Figure 9.23: The JETSET 7.3 PS prediction for $Z^0 \to q\overline{q}$, $Z^0 \to b\overline{b}$ and $Z^0 \to u\overline{u}, d\overline{d}, s\overline{s}$ of the differential cross-section versus ξ_p for $\pi^{\pm}$, K$^{\pm}$, p$\overline{\rm p}$ originating from fragmentation and from (decays of) particles containing the primary quark. The inclusive- and uds-distributions are obtained from 5 million generated $q\overline{q}$-events. For the $b\overline{b}$ distributions 10 million events have been generated.

the complete set of identified particle spectra studied for this analysis. In the case of the inclusive- and the uds-distributions, the part Prim. Quark/Decays includes particles produced directly from the primary quark as well as particles produced indirectly i.e. produced from a decaying particle which contained the primary quark.

In making the comparison between the $\pi^{\pm}$, K$^{\pm}$, p$\overline{\rm p}$ decay- and fragmentation-distributions for b- and uds-events, figure 9.23 also shows that decays and fragmentation take about equal share in the total particle production in b-events whereas in uds-events particle production is clearly dominated by the fragmentation process.

Figure 9.24 shows the equivalent distributions for the normalised production rates as a function of momentum. As has been suggested from the measurements in section 9.5, in comparing the $K^{\pm}$ distributions for the different event samples, indeed a large fraction of the high momentum kaons ($p > 20$ GeV/c) in uds - events originates from the primary quark.

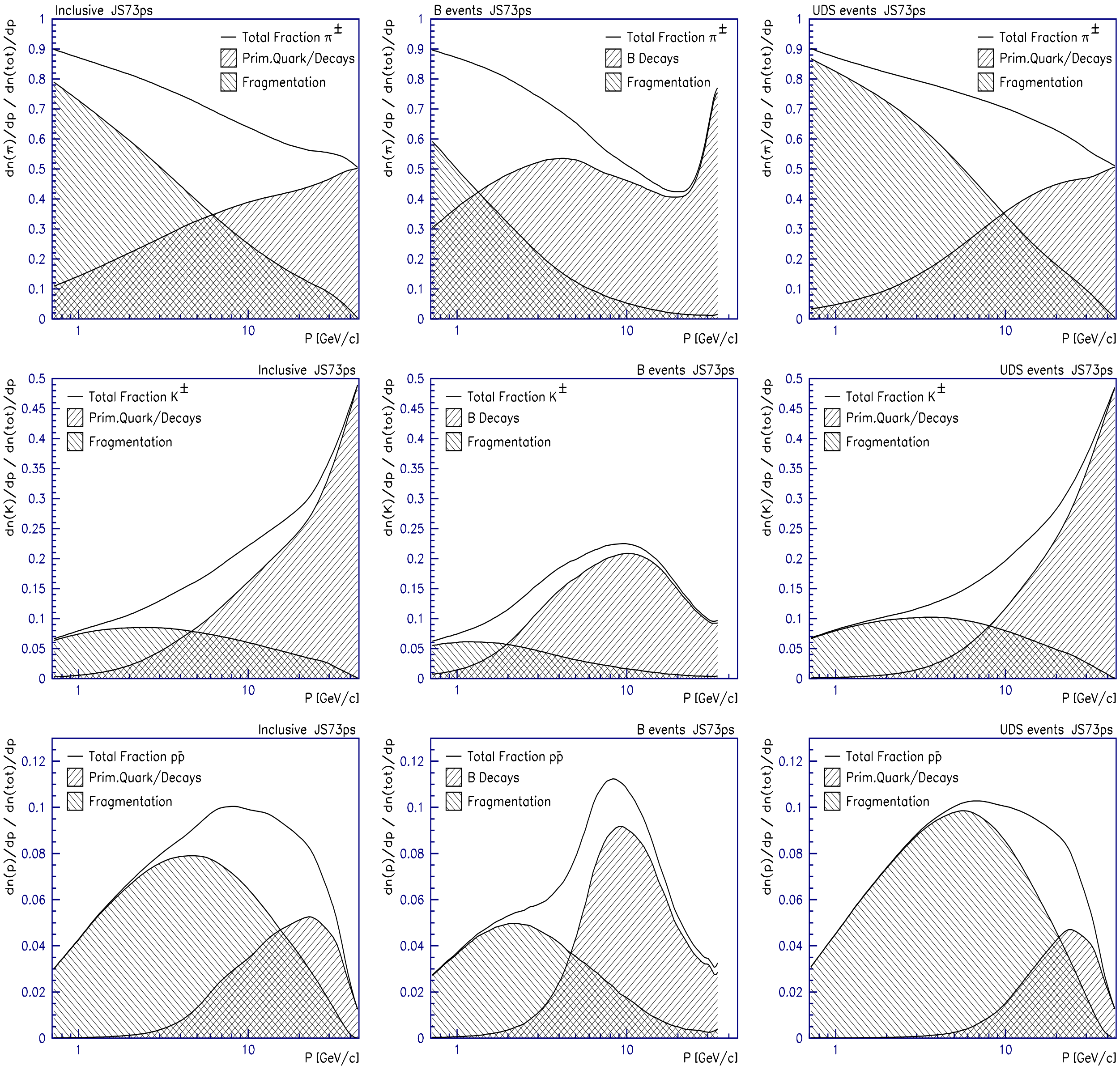

Figure 9.24: The JETSET 7.3 PS prediction for for $Z^0 \to q\overline{q}$, $Z^0 \to b\overline{b}$ and $Z^0 \to u\overline{u}, d\overline{d}, s\overline{s}$ of the normalised production rates versus p for $\pi^{\pm}$, $K^{\pm}$, $p\overline{p}$ originating from fragmentation and from (decays of) particles containing the primary quark.

Chapter 10

Summary and Outlook

The physics results presented in this thesis have been obtained through the extensive use of the DELPHI particle identification. The performance of the RICH detectors, both from the technical and from the physics point of view, has been illustrated and discussed at length. With the study of the behaviour of the detector parameters and the tracing of different sources of background, the understanding of the detector has been significantly increased. This is supported by the fact that the detector simulation gives a good description of the real data. From the measurement of the $\pi^{\pm}$, $\mathrm{K}^{\pm}$ and $\mathrm{p\overline{p}}$ spectra, covering the full momentum window from $0.7 < p < 45.6$ GeV/c, one may draw the conclusion that the RICH detectors accomplish what they were designed for: to be the backbone of the DELPHI particle identification.

The DELPHI particle identification enables high statistics precision measurements as well as the detection (i.e. reconstruction) of very weak physics signals, both of which have been discussed in detail in this thesis.

Concerning the high statistics measurements, the $\pi^{\pm}$, $\mathrm{K}^{\pm}$, $\mathrm{p\overline{p}}$ spectra obtained in $\mathrm{Z}^0 \to q\overline{q}$, $\mathrm{Z}^0 \to b\overline{b}$ and $\mathrm{Z}^0 \to u\overline{u}, d\overline{d}, s\overline{s}$, selected from 1 400 000 Z^0 decays, have been compared to the predictions from the JETSET parton shower model and the HERWIG cluster fragmentation model. The JETSET model prediction in general gives a better description of the measured spectra than HERWIG, especially in the case of proton spectra, where HERWIG seems to fail. JETSET and HERWIG are equally good in predicting the inclusive $\pi^{\pm}$ and $\mathrm{K}^{\pm}$ differential cross sections as a function of ξ_p. However, HERWIG seems to over-estimate the measurement for $\mathrm{Z}^0 \to b\overline{b}$ and under-estimates the measurement for $\mathrm{Z}^0 \to u\overline{u}, d\overline{d}, s\overline{s}$.

The prediction of the shape of the ξ_p distributions, based on the modified leading logarithm approximation MLLA while assuming local hadron parton duality LPHD, has been tested on all the measured distributions. The conclusion is drawn that the LPHD-MLLA provides a good description of the shape of the distributions. Only for protons in b- events, where the contribution from B-decays becomes explicitly visible, the LPHD-MLLA clearly fails. It has been shown that in this specific case, a double-Gaussian approach performs better, assuming one Gaussian for protons from fragmentation and one Gaussian for protons from B-decays.

	$Z^0 \to q\overline{q}$		$Z^0 \to b\overline{b}$		$Z^0 \to u\overline{u}, d\overline{d}, s\overline{s}$	
$< n_{tot} >$	20.43	± 0.17	23.42	± 0.35	19.44	± 0.21
$< \pi^{\pm} >$	17.00	± 0.43	**18.47	± 1.06	**16.56	± 0.82
$< \mathrm{K}^{\pm} >$	*2.11	± 0.08	*2.54	± 0.16	**1.88	± 0.10
$< \mathrm{p\overline{p}} >$	*1.04	± 0.04	*1.03	± 0.06	**1.02	± 0.05
$< \mathrm{Hv}^{\pm} >$	**3.27	± 0.08	**3.71	± 0.09	**2.93	± 0.11

Table 10.1: The measured particle production rates in $Z^0 \to q\overline{q}$, $Z^0 \to b\overline{b}$, $Z^0 \to u\overline{u}, d\overline{d}, s\overline{s}$. Results with an improved accuracy compared to previous measurements are indicated by a '$*$'. New results are indicated by '$**$'. $<\mathrm{Hv}^{\pm}>$ indicates the result obtained for heavy particles i.e. $m > m_{\pi}$.

An overview of the particle multiplicities in $Z^0 \to q\overline{q}$, $Z^0 \to b\overline{b}$ and $Z^0 \to u\overline{u}, d\overline{d}, s\overline{s}$, is given in table 10.1. The results are obtained by integration of the outcome of the LPHD-MLLA performed on the measured distributions. It has been shown that the $\pi^{\pm}$, $\mathrm{K}^{\pm}$, $\mathrm{p\overline{p}}$ multiplicities are very much consistent within themselves, e.g. $<\mathrm{K}^{\pm}>+<\mathrm{p\overline{p}}>\approx<\mathrm{Hv}^{\pm}>$ or $<n_{uds}>\approx<\pi^{\pm}>+<\mathrm{K}^{\pm}>+<\mathrm{p\overline{p}}>$. Additionally, the results are in good agreement with previous measurements, even though the uncertainties of this measurement are in some cases significantly smaller. The accuracy has been improved by a factor 1.5 (2.5) for $<\mathrm{K}^{\pm}>$ ($<\mathrm{p\overline{p}}>$) in $Z^0 \to q\overline{q}$, and by a factor 3 (4) for $<\mathrm{K}^{\pm}>$ ($<\mathrm{p\overline{p}}>$) in $Z^0 \to b\overline{b}$, indicated by a '$*$' in the table. Newly obtained results are indicated by a '$**$'.

The DELPHI particle identification is also very powerful with respect to the reconstruction of the different decay channels. This has been illustrated by the reconstruction of $\phi(1020) \to \mathrm{K}^+\mathrm{K}^-$. By applying different degrees of kaon tagging, it has been shown that one can obtain a ratio signal to like-sign background varying from ~ 1.6 up to more than 8. For the reconstruction of $\Lambda^0 \to \mathrm{p}\pi^-$, with the simultaneous application of the DELPHI V^0 reconstruction and the combined RICH-TPC particle identification, one can obtain Λ^0 samples of 97% purity.

Furthermore, the DELPHI particle identification allows the detection of rather weak physics signals. This has been illustrated by the positive identification of high momentum protons ($16 < p < 45.6$ GeV/c), of which the production rate in Z^0 decays is only a very small fraction of the total particle production. Moreover, the combination of the RICH-TPC particle identification enables to cover the momentum window from $0.3 < p < 45.6$ GeV/c, allowing the reconstruction of $\Lambda^0(1520) \to \mathrm{pK}^-$. This is illustrated in figure 10.1, which contains ~ 120 signal events reconstructed out of $\sim 1\,000\,000$ hadronic Z^0 decays. Without good particle identification the reconstruction of the $\Lambda^0(1520)$ would be impossible.

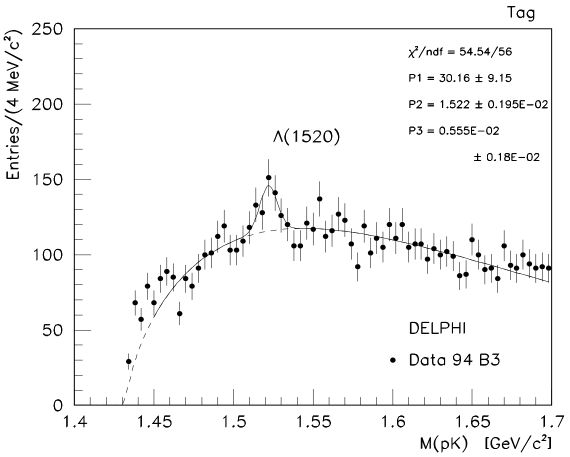

Figure 10.1: M(pK$^-$) obtained from the 94-B3 data processing, containing $\sim$120 signal events.

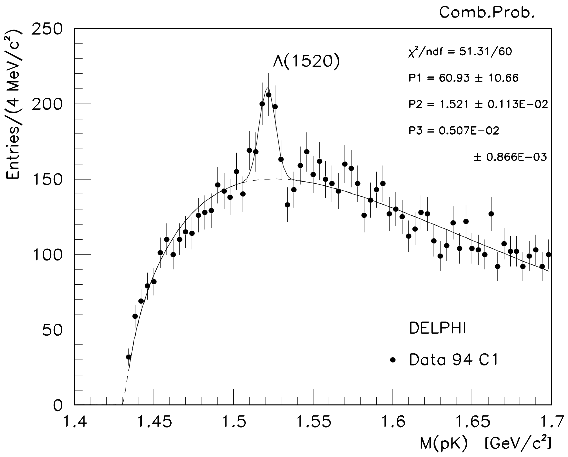

Figure 10.2: M(pK$^-$) obtained from the 94-C1 (tracking and dE/dx improved) reprocessed data, containing $\sim$250 signal events.

The DELPHI data analysis chain has recently undergone interventions, amongst others to upgrade the combined tracking and to improve the accuracy on the dE/dx measurement. The 1994 data were reprocessed after the intervention (94-C1). Preliminary studies [86] have shown that the newly achieved tracking decreases the Cherenkov angle resolution for low momentum particles ($p \lesssim 3$ GeV/c, liquid radiator domain) by $\sim$20%, which illustrates the dependence of the RICH particle identification on accurate track reconstruction. Also, with the combined RICH-TPC particle identification, through the combination of the identification probabilities, detection efficiencies over 90% can be obtained.

The reconstruction of resonances such as $\Lambda^0(1520) \to \mathrm{pK}^-$ clearly profits from these new achievements. For the reprocessed 1994 data (94-C1), this is illustrated in figure 10.2, where the combined RICH-TPC particle identification is applied, each of which covering large momentum windows: $0.7 < p < 45.6$ GeV/c for RICH, and $0.3 < p < 45.6$ GeV/c for TPC-dE/dx. Out of $\sim$1 200 000 hadronic Z^0 decays, $\sim$250 signal events are reconstructed. For the near future, it may be expected that the improved dE/dx measurement allows the lower momentum limit for particle identification to be decreased from 0.3 GeV/c to $\sim$0.1 GeV/c.

Particle identification based on the RICH technique has delivered outstanding contributions to many DELPHI physics analyses. It has been shown that the detector performance is well understood and can be accurately simulated. With the reprocessed data, the DELPHI particle identification offers the opportunity to maximally exploit the Z^0 data set for interesting physics analyses, for example in the field of charm and bottom physics, precision measurements in $\mathrm{Z}^0 \to c\bar{c}$, event flavour tagging with identified particles or studies on baryon production mechanisms.

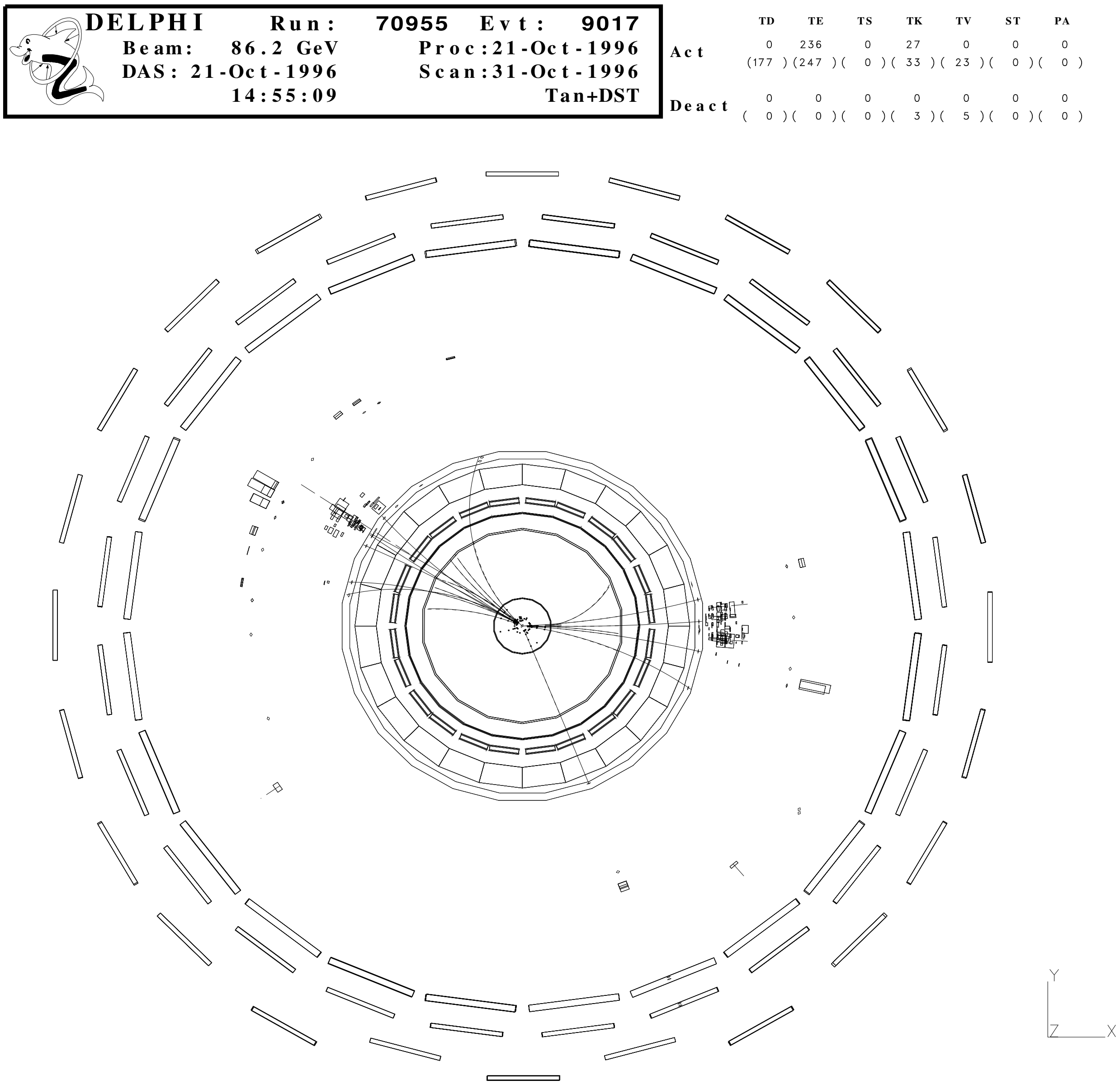

Figure 10.3: A W-event $e^+e^- \to \mathrm{W}^+\mathrm{W}^- \to q\overline{q}\,l\nu$ recorded by DELPHI. The event, showing two hadronic jets and a high momentum lepton, occurred inside the acceptance of the TPC and the BRICH.

Since November 1995, the LEP energies have been increased to move away from the Z^0 production. The beam energy has been doubled to allow the pair production of $\mathrm{W}^\pm$ bosons, the charged counterparts of the Z^0. Figure 10.3 shows a two-dimensional graphical display of an event $e^+e^- \to \mathrm{W}^+\mathrm{W}^- \to q\overline{q}\,l\nu$ recorded by DELPHI. The event, showing two hadronic jets and a high momentum lepton, occurred inside the full acceptance of the TPC and the BRICH. The production of W-pairs opens a new domain of investigations, 'standard model' tests and searches for new particles. Also these studies may profit greatly from the excellent DELPHI particle identification.

Appendix A

RIBMEAN Quality Bits

```
FLARIL LIQUID bits:
 quality flag:         RING                      VETO

           BRICH      good photons > 3          else
           FRICH      good photons > 2          else

 flaril(itk) bits: 1=extrapolation to RICH      idem
                   2=acceptance z < 115         idem
                   3=acc,runselection no trip   idem
                   4=good ring cut 1-5          see below....
                   5=tight ring 1-5             see below....
                   6=hits on track(s) in chamber  idem
 VETO
                   4=inside acceptance and hits or gas photons
                     in chamber or GAS photons
                   5=4 and chi2<9
FLARIG GAS bits:
 quality flag:         RING                     VETO

                      good photons > 1          else

 flarig(itk) bits: 1=extrapolation to RICH      idem
                   2=acceptance z < 115         idem
                   3=runselection no trip       idem
                   4=good ring cut 1-4          see below....
                   5=tight ring 1-4             see below....
                   6=hits on track(s) in chamber  idem
 VETO
                   4=less eq 3 photons in bands, inside acceptance
                   hits or gas photons in chamber or liquid photons
                   5=4 and no trip
```

Appendix B

Differential Cross-sections in $Z^0 \to q\overline{q}$

Momentum GeV/c	DELPHI $\frac{1}{N_{\rm had}}\frac{\rm dn_{tot}}{\rm dp}$	$\sigma_{\rm stat}$	$\sigma_{\rm syst}$	Xp	DELPHI $\frac{1}{N_{\rm had}}\frac{\rm dn_{tot}}{\rm dx_p}$	$\sigma_{\rm tot}$	JS73PS $\frac{1}{N_{\rm had}}\frac{\rm dn_{tot}}{\rm dx_p}$
0.30 - 0.36	11.22	± 0.47	± 0.74	0.007 - 0.008	511.8	± 39.8	510.5
0.36 - 0.46	10.95	± 0.30	± 0.52	0.008 - 0.010	499.4	± 27.4	498.9
0.46 - 0.57	10.30	± 0.16	± 0.24	0.010 - 0.012	470.0	± 13.0	468.9
0.57 - 0.70	9.25	± 0.16	± 0.23	0.012 - 0.015	422.1	± 12.8	424.6
0.70 - 0.91	7.79	± 0.15	± 0.22	0.015 - 0.020	355.1	± 12.1	361.1
0.91 - 1.14	6.360	± 0.062	± 0.082	0.020 - 0.025	290.08	± 4.67	295.22
1.14 - 1.37	5.273	± 0.065	± 0.079	0.025 - 0.030	240.50	± 4.67	243.31
1.37 - 1.60	4.412	± 0.035	± 0.041	0.030 - 0.035	201.22	± 2.43	203.35
1.60 - 1.82	3.764	± 0.035	± 0.039	0.035 - 0.040	171.70	± 2.41	172.46
1.82 - 2.28	3.018	± 0.028	± 0.030	0.040 - 0.050	137.68	± 1.88	138.12
2.28 - 2.74	2.325	± 0.023	± 0.024	0.050 - 0.060	106.03	± 1.50	106.25
2.74 - 3.19	1.853	± 0.021	± 0.021	0.060 - 0.070	84.52	± 1.35	83.96
3.19 - 3.65	1.506	± 0.019	± 0.019	0.070 - 0.080	68.71	± 1.22	67.79
3.65 - 4.10	1.253	± 0.018	± 0.017	0.080 - 0.090	57.15	± 1.13	56.06
4.10 - 4.56	1.049	± 0.017	± 0.016	0.090 - 0.100	47.84	± 1.04	46.96
4.56 - 5.47	0.830	± 0.015	± 0.014	0.100 - 0.120	37.86	± 0.93	36.88
5.47 - 6.38	0.616	± 0.013	± 0.011	0.120 - 0.140	28.09	± 0.76	27.23
6.38 - 7.29	0.471	± 0.011	± 0.009	0.140 - 0.160	21.48	± 0.63	20.72
7.29 - 8.21	0.3684	± 0.0090	± 0.0074	0.160 - 0.180	16.80	± 0.53	16.10
8.21 - 9.12	0.2907	± 0.0074	± 0.0060	0.180 - 0.200	13.26	± 0.43	12.68
9.12 - 11.9	0.1911	± 0.0055	± 0.0043	0.200 - 0.260	8.72	± 0.32	8.33
11.9 - 13.7	0.1159	± 0.0036	± 0.0027	0.260 - 0.300	5.29	± 0.20	5.00
13.7 - 18.2	0.0635	± 0.0021	± 0.0015	0.300 - 0.400	2.90	± 0.12	2.72
18.2 - 22.8	0.0273	± 0.0011	± 0.0007	0.400 - 0.500	1.243	± 0.058	1.170
22.8 - 27.4	0.01216	± 0.00057	± 0.00037	0.500 - 0.600	0.554	± 0.031	0.517
27.4 - 36.5	0.00384	± 0.00039	± 0.00027	0.600 - 0.800	0.175	± 0.022	0.161
36.5 - 45.6	0.000530	± 0.000096	± 0.000050	0.800 - 1.000	0.0242	± 0.0050	0.0227

Table B.1: Differential cross-section for charged particles in $Z^0 \to q\overline{q}$

Momentum GeV/c	DELPHI $\frac{1}{N_{had}} \frac{dn_\pi}{dp}$	σ_{stat}	σ_{syst}	Xp	DELPHI $\frac{1}{N_{had}} \frac{dn_\pi}{dx_p}$	σ_{tot}	JS73PS $\frac{1}{N_{had}} \frac{dn_\pi}{dx_p}$
0.70 - 0.91	6.908	± 0.039	± 0.239	0.015 - 0.020	315.1	± 11.1	321.1
0.91 - 1.14	5.495	± 0.032	± 0.101	0.020 - 0.025	250.66	± 4.83	256.60
1.14 - 1.37	4.486	± 0.030	± 0.095	0.025 - 0.030	204.61	± 4.54	207.63
1.37 - 1.60	3.688	± 0.027	± 0.055	0.030 - 0.035	168.23	± 2.79	170.77
1.60 - 1.82	3.088	± 0.025	± 0.051	0.035 - 0.040	140.85	± 2.61	142.88
1.82 - 2.28	2.426	± 0.018	± 0.046	0.040 - 0.050	110.65	± 2.23	112.35
2.28 - 2.74	1.839	± 0.016	± 0.043	0.050 - 0.060	83.88	± 2.10	84.44
2.74 - 3.19	1.443	± 0.010	± 0.027	0.060 - 0.070	65.83	± 1.33	65.28
3.19 - 3.65	1.1517	± 0.0083	± 0.0257	0.070 - 0.080	52.53	± 1.23	51.71
3.65 - 4.10	0.9364	± 0.0072	± 0.0216	0.080 - 0.090	42.71	± 1.04	42.04
4.10 - 4.56	0.7714	± 0.0065	± 0.0183	0.090 - 0.100	35.19	± 0.89	34.63
4.56 - 5.47	0.5961	± 0.0042	± 0.0157	0.100 - 0.120	27.19	± 0.74	26.62
5.47 - 6.38	0.4306	± 0.0036	± 0.0124	0.120 - 0.140	19.64	± 0.59	19.08
6.38 - 7.29	0.3211	± 0.0032	± 0.0101	0.140 - 0.160	14.65	± 0.48	14.13
7.29 - 8.21	0.2464	± 0.0030	± 0.0082	0.160 - 0.180	11.24	± 0.40	10.76
8.21 - 9.12	0.1877	± 0.0024	± 0.0070	0.180 - 0.200	8.56	± 0.34	8.30
9.12 - 11.9	0.1194	± 0.0012	± 0.0045	0.200 - 0.260	5.45	± 0.21	5.30
11.9 - 13.7	0.06922	± 0.00096	± 0.00277	0.260 - 0.300	3.16	± 0.13	3.06
13.7 - 18.2	0.03661	± 0.00066	± 0.00154	0.300 - 0.400	1.670	± 0.077	1.612
18.2 - 22.8	0.01490	± 0.00042	± 0.00071	0.400 - 0.500	0.680	± 0.038	0.664
22.8 - 27.4	0.00673	± 0.00030	± 0.00037	0.500 - 0.600	0.307	± 0.022	0.289
27.4 - 36.5	0.00214	± 0.00020	± 0.00024	0.600 - 0.800	0.097	± 0.014	0.089
36.5 - 45.6	0.000298	± 0.000084	± 0.000056	0.800 - 1.000	0.0136	± 0.0046	0.0121

Table B.2: Differential cross-section for pions in $Z^0 \rightarrow q\bar{q}$

Momentum GeV/c	DELPHI $\frac{1}{N_{had}} \frac{dn_K}{dp}$	σ_{stat}	σ_{syst}	Xp	DELPHI $\frac{1}{N_{had}} \frac{dn_K}{dx_p}$	σ_{tot}	JS73PS $\frac{1}{N_{had}} \frac{dn_K}{dx_p}$
0.70 - 0.91	0.558	± 0.031	± 0.077	0.015 - 0.020	25.46	± 3.77	25.51
0.91 - 1.14	0.546	± 0.021	± 0.073	0.020 - 0.025	24.90	± 3.46	23.70
1.14 - 1.37	0.466	± 0.018	± 0.066	0.025 - 0.030	21.27	± 3.13	21.32
1.37 - 1.60	0.450	± 0.020	± 0.040	0.030 - 0.035	20.54	± 2.05	19.09
1.60 - 1.82	0.400	± 0.022	± 0.056	0.035 - 0.040	18.26	± 2.76	17.15
1.82 - 2.28	0.357	± 0.016	± 0.061	0.040 - 0.050	16.30	± 2.87	14.83
2.28 - 2.74	0.292	± 0.015	± 0.063	0.050 - 0.060	13.31	± 2.94	12.54
2.74 - 3.19	0.2455	± 0.0080	± 0.0154	0.060 - 0.070	11.20	± 0.79	10.76
3.19 - 3.65	0.2157	± 0.0061	± 0.0154	0.070 - 0.080	9.84	± 0.76	9.30
3.65 - 4.10	0.1953	± 0.0054	± 0.0120	0.080 - 0.090	8.91	± 0.60	8.14
4.10 - 4.56	0.1754	± 0.0052	± 0.0121	0.090 - 0.100	8.00	± 0.60	7.19
4.56 - 5.47	0.1443	± 0.0035	± 0.0097	0.100 - 0.120	6.58	± 0.47	6.00
5.47 - 6.38	0.1123	± 0.0040	± 0.0060	0.120 - 0.140	5.12	± 0.33	4.79
6.38 - 7.29	0.0906	± 0.0052	± 0.0083	0.140 - 0.160	4.13	± 0.45	3.89
7.29 - 8.21	0.0720	± 0.0060	± 0.0090	0.160 - 0.180	3.29	± 0.49	3.19
8.21 - 9.12	0.0624	± 0.0033	± 0.0086	0.180 - 0.200	2.85	± 0.42	2.65
9.12 - 11.9	0.04344	± 0.00082	± 0.00204	0.200 - 0.260	1.98	± 0.10	1.86
11.9 - 13.7	0.02917	± 0.00073	± 0.00155	0.260 - 0.300	1.331	± 0.078	1.209
13.7 - 18.2	0.01699	± 0.00044	± 0.00115	0.300 - 0.400	0.775	± 0.056	0.708
18.2 - 22.8	0.00791	± 0.00033	± 0.00079	0.400 - 0.500	0.361	± 0.039	0.337
22.8 - 27.4	0.00364	± 0.00025	± 0.00036	0.500 - 0.600	0.166	± 0.020	0.164
27.4 - 36.5	0.00130	± 0.00017	± 0.00027	0.600 - 0.800	0.059	± 0.015	0.060
36.5 - 45.6	0.000147	± 0.000082	± 0.000108	0.800 - 1.000	0.0067	± 0.0062	0.0100

Table B.3: Differential cross-section for kaons in $Z^0 \rightarrow q\bar{q}$

Momentum GeV/c	DELPHI $\frac{1}{N_{had}}\frac{dn_p}{dp}$	σ_{stat}	σ_{syst}	Xp	DELPHI $\frac{1}{N_{had}}\frac{dn_p}{dx_p}$	σ_{tot}	JS73PS $\frac{1}{N_{had}}\frac{dn_p}{dx_p}$
0.70 - 0.91	0.320	± 0.016	± 0.072	0.015 - 0.020	14.61	± 3.37	12.44
0.91 - 1.14	0.308	± 0.018	± 0.053	0.020 - 0.025	14.06	± 2.58	12.96
1.14 - 1.37	0.249	± 0.022	± 0.043	0.025 - 0.030	11.34	± 2.22	12.53
1.37 - 1.60	0.263	± 0.021	± 0.030	0.030 - 0.035	12.01	± 1.66	11.73
1.60 - 1.82	0.249	± 0.015	± 0.027	0.035 - 0.040	11.35	± 1.40	10.78
1.82 - 2.28	0.232	± 0.012	± 0.021	0.040 - 0.050	10.58	± 1.10	9.40
2.28 - 2.74	0.1566	± 0.0062	± 0.0175	0.050 - 0.060	7.14	± 0.85	7.87
2.74 - 3.19	0.1198	± 0.0034	± 0.0123	0.060 - 0.070	5.46	± 0.58	6.64
3.19 - 3.65	0.1028	± 0.0036	± 0.0097	0.070 - 0.080	4.69	± 0.47	5.60
3.65 - 4.10	0.0934	± 0.0036	± 0.0108	0.080 - 0.090	4.26	± 0.52	4.79
4.10 - 4.56	0.0758	± 0.0035	± 0.0097	0.090 - 0.100	3.46	± 0.47	4.16
4.56 - 5.47	0.0695	± 0.0027	± 0.0066	0.100 - 0.120	3.17	± 0.32	3.39
5.47 - 6.38	0.0579	± 0.0036	± 0.0069	0.120 - 0.140	2.64	± 0.35	2.63
6.38 - 7.29	0.0457	± 0.0054	± 0.0062	0.140 - 0.160	2.08	± 0.37	2.06
7.29 - 8.21	0.0382	± 0.0065	± 0.0063	0.160 - 0.180	1.74	± 0.41	1.62
8.21 - 9.12	0.0299	± 0.0038	± 0.0046	0.180 - 0.200	1.37	± 0.27	1.27
9.12 - 11.9	0.0193	± 0.0010	± 0.0021	0.200 - 0.260	0.88	± 0.11	0.83
11.9 - 13.7	0.01246	± 0.00076	± 0.00140	0.260 - 0.300	0.569	± 0.073	0.486
13.7 - 18.2	0.00616	± 0.00036	± 0.00065	0.300 - 0.400	0.281	± 0.034	0.255
18.2 - 22.8	0.00260	± 0.00021	± 0.00044	0.400 - 0.500	0.119	± 0.022	0.102
22.8 - 27.4	0.00106	± 0.00015	± 0.00023	0.500 - 0.600	0.048	± 0.013	0.040
27.4 - 36.5	0.000269	± 0.000084	± 0.000107	0.600 - 0.800	0.0123	± 0.0062	0.0097
36.5 - 45.6	0.000046	± 0.000059	± 0.000028	0.800 - 1.000	0.0021	± 0.0030	0.0006

Table B.4: Differential cross-section for protons in $Z^0 \to q\overline{q}$

Momentum GeV/c	DELPHI $\frac{1}{N_{had}}\frac{dn_{Hv}}{dp}$	σ_{stat}	σ_{syst}	Xp	DELPHI $\frac{1}{N_{had}}\frac{dn_{Hv}}{dx_p}$	σ_{tot}	JS73PS $\frac{1}{N_{had}}\frac{dn_{Hv}}{dx_p}$
0.70 - 0.91	0.887	± 0.034	± 0.077	0.015 - 0.020	40.47	± 3.85	37.96
0.91 - 1.14	0.832	± 0.024	± 0.074	0.020 - 0.025	37.95	± 3.54	36.66
1.14 - 1.37	0.791	± 0.023	± 0.055	0.025 - 0.030	36.06	± 2.71	33.84
1.37 - 1.60	0.700	± 0.024	± 0.044	0.030 - 0.035	31.92	± 2.29	30.82
1.60 - 1.82	0.644	± 0.025	± 0.051	0.035 - 0.040	29.38	± 2.59	27.93
1.82 - 2.28	0.580	± 0.020	± 0.063	0.040 - 0.050	26.47	± 3.03	24.23
2.28 - 2.74	0.462	± 0.016	± 0.051	0.050 - 0.060	21.07	± 2.45	20.41
2.74 - 3.19	0.3871	± 0.0083	± 0.0175	0.060 - 0.070	17.66	± 0.88	17.40
3.19 - 3.65	0.3167	± 0.0059	± 0.0114	0.070 - 0.080	14.44	± 0.59	14.90
3.65 - 4.10	0.2853	± 0.0051	± 0.0091	0.080 - 0.090	13.01	± 0.48	12.93
4.10 - 4.56	0.2531	± 0.0047	± 0.0086	0.090 - 0.100	11.55	± 0.45	11.35
4.56 - 5.47	0.2136	± 0.0030	± 0.0072	0.100 - 0.120	9.74	± 0.36	9.39
5.47 - 6.38	0.1703	± 0.0027	± 0.0059	0.120 - 0.140	7.77	± 0.29	7.41
6.38 - 7.29	0.1376	± 0.0024	± 0.0049	0.140 - 0.160	6.28	± 0.25	5.95
7.29 - 8.21	0.1101	± 0.0022	± 0.0041	0.160 - 0.180	5.02	± 0.21	4.81
8.21 - 9.12	0.0923	± 0.0018	± 0.0036	0.180 - 0.200	4.21	± 0.18	3.93
9.12 - 11.9	0.06315	± 0.00085	± 0.00258	0.200 - 0.260	2.88	± 0.12	2.68
11.9 - 13.7	0.04085	± 0.00084	± 0.00183	0.260 - 0.300	1.863	± 0.092	1.695
13.7 - 18.2	0.02291	± 0.00052	± 0.00130	0.300 - 0.400	1.045	± 0.064	0.962
18.2 - 22.8	0.01028	± 0.00037	± 0.00087	0.400 - 0.500	0.469	± 0.043	0.438
22.8 - 27.4	0.00461	± 0.00026	± 0.00039	0.500 - 0.600	0.210	± 0.021	0.204
27.4 - 36.5	0.00158	± 0.00016	± 0.00020	0.600 - 0.800	0.072	± 0.012	0.069
36.5 - 45.6	0.000244	± 0.000077	± 0.000069	0.800 - 1.000	0.0111	± 0.0047	0.0106

Table B.5: Differential cross-section for heavy particles (K/p) in $Z^0 \to q\overline{q}$

Appendix C

Differential Cross-sections in $Z^0 \rightarrow b\bar{b}$

Momentum GeV/c	DELPHI $\frac{1}{N_{\mathrm{had}}}\frac{\mathrm{dn_{tot}}}{\mathrm{dp}}$	σ_{stat}	σ_{syst}	Xp	DELPHI $\frac{1}{N_{\mathrm{had}}}\frac{\mathrm{dn_{tot}}}{\mathrm{dx_p}}$	σ_{tot}	JS73PS $\frac{1}{N_{\mathrm{had}}}\frac{\mathrm{dn_{tot}}}{\mathrm{dx_p}}$
0.30 - 0.36	12.05	± 0.46	± 0.74	0.007 - 0.008	549.5	± 39.7	542.2
0.36 - 0.46	11.80	± 0.30	± 0.52	0.008 - 0.010	538.4	± 27.3	534.4
0.46 - 0.57	11.23	± 0.16	± 0.24	0.010 - 0.012	512.3	± 13.0	507.7
0.57 - 0.70	10.28	± 0.16	± 0.23	0.012 - 0.015	469.1	± 12.8	466.8
0.70 - 0.91	8.84	± 0.16	± 0.22	0.015 - 0.020	403.2	± 12.3	403.6
0.91 - 1.14	7.336	± 0.064	± 0.082	0.020 - 0.025	334.61	± 4.73	333.93
1.14 - 1.37	6.159	± 0.065	± 0.079	0.025 - 0.030	280.93	± 4.68	276.66
1.37 - 1.60	5.208	± 0.034	± 0.041	0.030 - 0.035	237.57	± 2.42	231.68
1.60 - 1.82	4.466	± 0.034	± 0.040	0.035 - 0.040	203.70	± 2.38	196.91
1.82 - 2.28	3.586	± 0.027	± 0.030	0.040 - 0.050	163.57	± 1.84	157.90
2.28 - 2.74	2.806	± 0.021	± 0.024	0.050 - 0.060	127.98	± 1.46	121.90
2.74 - 3.19	2.235	± 0.019	± 0.021	0.060 - 0.070	101.95	± 1.29	96.61
3.19 - 3.65	1.831	± 0.017	± 0.019	0.070 - 0.080	83.53	± 1.16	78.50
3.65 - 4.10	1.510	± 0.016	± 0.017	0.080 - 0.090	68.89	± 1.07	64.74
4.10 - 4.56	1.259	± 0.015	± 0.016	0.090 - 0.100	57.43	± 0.98	53.87
4.56 - 5.47	0.966	± 0.013	± 0.014	0.100 - 0.120	44.04	± 0.86	41.31
5.47 - 6.38	0.687	± 0.011	± 0.011	0.120 - 0.140	31.32	± 0.70	29.33
6.38 - 7.29	0.4967	± 0.0086	± 0.0092	0.140 - 0.160	22.66	± 0.57	21.28
7.29 - 8.21	0.3681	± 0.0070	± 0.0077	0.160 - 0.180	16.79	± 0.46	15.74
8.21 - 9.12	0.2764	± 0.0057	± 0.0063	0.180 - 0.200	12.61	± 0.38	11.85
9.12 - 11.9	0.1637	± 0.0043	± 0.0047	0.200 - 0.260	7.46	± 0.28	7.17
11.9 - 13.7	0.0882	± 0.0028	± 0.0034	0.260 - 0.300	4.02	± 0.18	3.87
13.7 - 18.2	0.0431	± 0.0022	± 0.0025	0.300 - 0.400	1.96	± 0.12	1.91
18.2 - 22.8	0.0152	± 0.0012	± 0.0021	0.400 - 0.500	0.694	± 0.064	0.714
22.8 - 27.4	0.00577	± 0.00071	± 0.00203	0.500 - 0.600	0.263	± 0.037	0.261
27.4 - 36.5	0.00120	± 0.00041	± 0.00202	0.600 - 0.800	0.055	± 0.022	0.048
36.5 - 45.6	0.0000201	± 0.0000085	± 0.0020006	0.800 - 1.000	0.0009	± 0.0023	0.0006

Table C.1: Differential cross-section for charged particles in $Z^0 \rightarrow b\bar{b}$

Momentum GeV/c	DELPHI $\frac{1}{N_{\mathrm{had}}}\frac{\mathrm{dn}_\pi}{\mathrm{dp}}$	σ_{stat}	σ_{syst}	Xp	DELPHI $\frac{1}{N_{\mathrm{had}}}\frac{\mathrm{dn}_\pi}{\mathrm{dx_p}}$	σ_{tot}	JS73PS $\frac{1}{N_{\mathrm{had}}}\frac{\mathrm{dn}_\pi}{\mathrm{dx_p}}$
0.70 - 0.91	7.781	± 0.096	± 0.246	0.015 - 0.020	354.9	± 12.0	358.3
0.91 - 1.14	6.334	± 0.078	± 0.102	0.020 - 0.025	288.90	± 5.87	290.00
1.14 - 1.37	5.205	± 0.072	± 0.098	0.025 - 0.030	237.41	± 5.55	235.49
1.37 - 1.60	4.280	± 0.066	± 0.060	0.030 - 0.035	195.20	± 4.09	193.52
1.60 - 1.82	3.595	± 0.063	± 0.056	0.035 - 0.040	163.96	± 3.84	161.31
1.82 - 2.28	2.768	± 0.044	± 0.047	0.040 - 0.050	126.27	± 2.96	125.92
2.28 - 2.74	2.140	± 0.039	± 0.047	0.050 - 0.060	97.59	± 2.76	93.88
2.74 - 3.19	1.674	± 0.025	± 0.031	0.060 - 0.070	76.35	± 1.83	71.74
3.19 - 3.65	1.312	± 0.020	± 0.027	0.070 - 0.080	59.83	± 1.55	56.59
3.65 - 4.10	1.049	± 0.017	± 0.022	0.080 - 0.090	47.84	± 1.26	45.39
4.10 - 4.56	0.853	± 0.015	± 0.019	0.090 - 0.100	38.92	± 1.10	36.76
4.56 - 5.47	0.6166	± 0.0095	± 0.0138	0.100 - 0.120	28.13	± 0.76	27.04
5.47 - 6.38	0.4124	± 0.0077	± 0.0101	0.120 - 0.140	18.81	± 0.58	18.07
6.38 - 7.29	0.2861	± 0.0066	± 0.0079	0.140 - 0.160	13.05	± 0.47	12.38
7.29 - 8.21	0.2010	± 0.0057	± 0.0058	0.160 - 0.180	9.17	± 0.37	8.79
8.21 - 9.12	0.1457	± 0.0044	± 0.0051	0.180 - 0.200	6.64	± 0.30	6.39
9.12 - 11.9	0.0810	± 0.0018	± 0.0029	0.200 - 0.260	3.70	± 0.16	3.64
11.9 - 13.7	0.0409	± 0.0014	± 0.0018	0.260 - 0.300	1.87	± 0.10	1.84
13.7 - 18.2	0.01858	± 0.00093	± 0.00088	0.300 - 0.400	0.848	± 0.058	0.849
18.2 - 22.8	0.00629	± 0.00051	± 0.00042	0.400 - 0.500	0.287	± 0.030	0.303
22.8 - 27.4	0.00252	± 0.00035	± 0.00028	0.500 - 0.600	0.115	± 0.020	0.122
27.4 - 36.5	0.00081	± 0.00030	± 0.00018	0.600 - 0.800	0.037	± 0.016	0.030
36.5 - 45.6	0.000016	± 0.000042	± 0.000013	0.800 - 1.000	0.0007	± 0.0020	0.0004

Table C.2: Differential cross-section for pions in $Z^0 \to b\bar{b}$

Momentum GeV/c	DELPHI $\frac{1}{N_{\mathrm{had}}}\frac{\mathrm{dn_K}}{\mathrm{dp}}$	σ_{stat}	σ_{syst}	Xp	DELPHI $\frac{1}{N_{\mathrm{had}}}\frac{\mathrm{dn_K}}{\mathrm{dx_p}}$	σ_{tot}	JS73PS $\frac{1}{N_{\mathrm{had}}}\frac{\mathrm{dn_K}}{\mathrm{dx_p}}$
0.70 - 0.91	0.667	± 0.090	± 0.084	0.015 - 0.020	30.42	± 5.61	26.66
0.91 - 1.14	0.612	± 0.064	± 0.083	0.020 - 0.025	27.93	± 4.80	25.15
1.14 - 1.37	0.523	± 0.060	± 0.080	0.025 - 0.030	23.84	± 4.57	23.32
1.37 - 1.60	0.585	± 0.051	± 0.050	0.030 - 0.035	26.68	± 3.27	21.56
1.60 - 1.82	0.483	± 0.061	± 0.075	0.035 - 0.040	22.02	± 4.44	20.32
1.82 - 2.28	0.494	± 0.025	± 0.076	0.040 - 0.050	22.55	± 3.67	18.59
2.28 - 2.74	0.398	± 0.016	± 0.078	0.050 - 0.060	18.17	± 3.63	16.72
2.74 - 3.19	0.335	± 0.018	± 0.020	0.060 - 0.070	15.26	± 1.22	15.03
3.19 - 3.65	0.3225	± 0.0096	± 0.0203	0.070 - 0.080	14.71	± 1.02	13.36
3.65 - 4.10	0.2845	± 0.0055	± 0.0211	0.080 - 0.090	12.97	± 0.99	11.72
4.10 - 4.56	0.249	± 0.010	± 0.015	0.090 - 0.100	11.34	± 0.81	10.20
4.56 - 5.47	0.2022	± 0.0061	± 0.0106	0.100 - 0.120	9.22	± 0.56	8.20
5.47 - 6.38	0.1526	± 0.0070	± 0.0101	0.120 - 0.140	6.96	± 0.56	6.14
6.38 - 7.29	0.109	± 0.011	± 0.010	0.140 - 0.160	4.98	± 0.68	4.60
7.29 - 8.21	0.083	± 0.011	± 0.012	0.160 - 0.180	3.79	± 0.75	3.47
8.21 - 9.12	0.0625	± 0.0050	± 0.0087	0.180 - 0.200	2.85	± 0.46	2.67
9.12 - 11.9	0.0379	± 0.0013	± 0.0017	0.200 - 0.260	1.727	± 0.099	1.600
11.9 - 13.7	0.0199	± 0.0011	± 0.0011	0.260 - 0.300	0.907	± 0.071	0.827
13.7 - 18.2	0.00868	± 0.00068	± 0.00059	0.300 - 0.400	0.396	± 0.041	0.368
18.2 - 22.8	0.00231	± 0.00041	± 0.00027	0.400 - 0.500	0.105	± 0.023	0.109
22.8 - 27.4	0.00062	± 0.00023	± 0.00006	0.500 - 0.600	0.028	± 0.011	0.032
27.4 - 36.5	0.000024	± 0.000062	± 0.000005	0.600 - 0.800	0.0011	± 0.0028	0.0049
36.5 - 45.6	0.0000007	± 0.0000036	± 0.0000009	0.800 - 1.000	0.00003	± 0.00017	0.00005

Table C.3: Differential cross-section for kaons in $Z^0 \to b\bar{b}$

Momentum GeV/c	DELPHI $\frac{1}{N_{\mathrm{had}}}\frac{\mathrm{dn_p}}{\mathrm{dp}}$	σ_{stat}	σ_{syst}	Xp	DELPHI $\frac{1}{N_{\mathrm{had}}}\frac{\mathrm{dn_p}}{\mathrm{dx_p}}$	σ_{tot}	JS73PS $\frac{1}{N_{\mathrm{had}}}\frac{\mathrm{dn_p}}{\mathrm{dx_p}}$
0.70 - 0.91	0.303	± 0.051	± 0.066	0.015 - 0.020	13.82	± 3.83	12.33
0.91 - 1.14	0.305	± 0.053	± 0.050	0.020 - 0.025	13.93	± 3.32	12.72
1.14 - 1.37	0.331	± 0.049	± 0.068	0.025 - 0.030	15.11	± 3.82	12.07
1.37 - 1.60	0.266	± 0.066	± 0.029	0.030 - 0.035	12.14	± 3.31	11.05
1.60 - 1.82	0.257	± 0.049	± 0.028	0.035 - 0.040	11.73	± 2.56	9.99
1.82 - 2.28	0.284	± 0.042	± 0.030	0.040 - 0.050	12.96	± 2.35	8.39
2.28 - 2.74	0.176	± 0.026	± 0.025	0.050 - 0.060	8.02	± 1.66	6.79
2.74 - 3.19	0.117	± 0.016	± 0.014	0.060 - 0.070	5.32	± 0.97	5.65
3.19 - 3.65	0.093	± 0.016	± 0.011	0.070 - 0.080	4.24	± 0.87	4.71
3.65 - 4.10	0.092	± 0.015	± 0.011	0.080 - 0.090	4.18	± 0.86	4.11
4.10 - 4.56	0.072	± 0.016	± 0.011	0.090 - 0.100	3.29	± 0.88	3.70
4.56 - 5.47	0.079	± 0.010	± 0.008	0.100 - 0.120	3.62	± 0.58	3.23
5.47 - 6.38	0.075	± 0.012	± 0.010	0.120 - 0.140	3.40	± 0.71	2.76
6.38 - 7.29	0.060	± 0.019	± 0.007	0.140 - 0.160	2.74	± 0.91	2.26
7.29 - 8.21	0.044	± 0.022	± 0.009	0.160 - 0.180	2.00	± 1.07	1.75
8.21 - 9.12	0.034	± 0.011	± 0.005	0.180 - 0.200	1.56	± 0.55	1.32
9.12 - 11.9	0.0173	± 0.0029	± 0.0021	0.200 - 0.260	0.79	± 0.16	0.76
11.9 - 13.7	0.0089	± 0.0018	± 0.0009	0.260 - 0.300	0.406	± 0.091	0.365
13.7 - 18.2	0.00371	± 0.00071	± 0.00037	0.300 - 0.400	0.169	± 0.037	0.145
18.2 - 22.8	0.00102	± 0.00033	± 0.00017	0.400 - 0.500	0.046	± 0.017	0.037
22.8 - 27.4	0.00027	± 0.00019	± 0.00007	0.500 - 0.600	0.0124	± 0.0092	0.0110
27.4 - 36.5	0.000083	± 0.000074	± 0.000077	0.600 - 0.800	0.0038	± 0.0049	0.0017
36.5 - 45.6	0.0000045	± 0.0000060	± 0.0000173	0.800 - 1.000	0.00021	± 0.00084	0.00005

Table C.4: Differential cross-section for protons in $Z^0 \to b\bar{b}$

Momentum GeV/c	DELPHI $\frac{1}{N_{\mathrm{had}}}\frac{\mathrm{dn_{Hv}}}{\mathrm{dp}}$	σ_{stat}	σ_{syst}	Xp	DELPHI $\frac{1}{N_{\mathrm{had}}}\frac{\mathrm{dn_{Hv}}}{\mathrm{dx_p}}$	σ_{tot}	JS73PS $\frac{1}{N_{\mathrm{had}}}\frac{\mathrm{dn_{Hv}}}{\mathrm{dx_p}}$
0.70 - 0.91	1.01	± 0.10	± 0.08	0.015 - 0.020	45.90	± 5.96	38.99
0.91 - 1.14	0.908	± 0.071	± 0.076	0.020 - 0.025	41.44	± 4.75	37.87
1.14 - 1.37	0.905	± 0.066	± 0.068	0.025 - 0.030	41.26	± 4.33	35.39
1.37 - 1.60	0.822	± 0.067	± 0.049	0.030 - 0.035	37.50	± 3.80	32.61
1.60 - 1.82	0.745	± 0.073	± 0.063	0.035 - 0.040	34.00	± 4.42	30.30
1.82 - 2.28	0.748	± 0.055	± 0.068	0.040 - 0.050	34.11	± 3.99	26.98
2.28 - 2.74	0.583	± 0.043	± 0.062	0.050 - 0.060	26.59	± 3.46	23.50
2.74 - 3.19	0.473	± 0.023	± 0.017	0.060 - 0.070	21.59	± 1.29	20.67
3.19 - 3.65	0.418	± 0.014	± 0.016	0.070 - 0.080	19.05	± 0.99	18.06
3.65 - 4.10	0.373	± 0.013	± 0.011	0.080 - 0.090	17.03	± 0.77	15.82
4.10 - 4.56	0.325	± 0.011	± 0.012	0.090 - 0.100	14.84	± 0.75	13.89
4.56 - 5.47	0.2821	± 0.0061	± 0.0104	0.100 - 0.120	12.87	± 0.55	11.43
5.47 - 6.38	0.2234	± 0.0060	± 0.0071	0.120 - 0.140	10.19	± 0.42	8.90
6.38 - 7.29	0.1686	± 0.0057	± 0.0056	0.140 - 0.160	7.69	± 0.36	6.87
7.29 - 8.21	0.1279	± 0.0047	± 0.0044	0.160 - 0.180	5.84	± 0.29	5.22
8.21 - 9.12	0.0984	± 0.0036	± 0.0036	0.180 - 0.200	4.49	± 0.23	3.98
9.12 - 11.9	0.0558	± 0.0015	± 0.0023	0.200 - 0.260	2.55	± 0.12	2.36
11.9 - 13.7	0.0284	± 0.0014	± 0.0013	0.260 - 0.300	1.295	± 0.088	1.192
13.7 - 18.2	0.01209	± 0.00082	± 0.00071	0.300 - 0.400	0.551	± 0.050	0.513
18.2 - 22.8	0.00311	± 0.00049	± 0.00034	0.400 - 0.500	0.142	± 0.027	0.147
22.8 - 27.4	0.00085	± 0.00024	± 0.00009	0.500 - 0.600	0.039	± 0.012	0.043
27.4 - 36.5	0.000136	± 0.000076	± 0.000034	0.600 - 0.800	0.0062	± 0.0038	0.0066
36.5 - 45.6	0.0000031	± 0.0000079	± 0.0000021	0.800 - 1.000	0.00014	± 0.00037	0.00011

Table C.5: Differential cross-section heavy particles (K/p) in $Z^0 \to b\bar{b}$

Appendix D

Differential Cross-sections in $Z^0 \to u\overline{u}, d\overline{d}, s\overline{s}$

Momentum GeV/c	DELPHI $\frac{1}{N_{\mathrm{had}}}\frac{\mathrm{dn_{tot}}}{\mathrm{dp}}$	σ_{stat}	σ_{syst}	Xp	DELPHI $\frac{1}{N_{\mathrm{had}}}\frac{\mathrm{dn_{tot}}}{\mathrm{dx_p}}$	σ_{tot}	JS73PS $\frac{1}{N_{\mathrm{had}}}\frac{\mathrm{dn_{tot}}}{\mathrm{dx_p}}$
0.30 - 0.36	10.97	± 0.47	± 0.74	0.007 - 0.008	500.6	± 40.0	497.9
0.36 - 0.46	10.69	± 0.31	± 0.52	0.008 - 0.010	487.8	± 27.5	485.6
0.46 - 0.57	10.02	± 0.16	± 0.24	0.010 - 0.012	457.0	± 13.1	454.5
0.57 - 0.70	8.95	± 0.16	± 0.23	0.012 - 0.015	408.0	± 12.8	409.6
0.70 - 0.91	7.46	± 0.15	± 0.22	0.015 - 0.020	340.5	± 12.0	346.1
0.91 - 1.14	6.046	± 0.061	± 0.082	0.020 - 0.025	275.76	± 4.64	281.34
1.14 - 1.37	4.966	± 0.063	± 0.079	0.025 - 0.030	226.53	± 4.63	230.68
1.37 - 1.60	4.124	± 0.034	± 0.041	0.030 - 0.035	188.13	± 2.41	192.00
1.60 - 1.82	3.506	± 0.034	± 0.040	0.035 - 0.040	159.91	± 2.38	162.38
1.82 - 2.28	2.801	± 0.028	± 0.030	0.040 - 0.050	127.76	± 1.87	129.70
2.28 - 2.74	2.141	± 0.023	± 0.024	0.050 - 0.060	97.66	± 1.49	99.62
2.74 - 3.19	1.708	± 0.021	± 0.021	0.060 - 0.070	77.90	± 1.34	78.78
3.19 - 3.65	1.390	± 0.019	± 0.019	0.070 - 0.080	63.39	± 1.22	63.54
3.65 - 4.10	1.156	± 0.018	± 0.017	0.080 - 0.090	52.73	± 1.14	52.58
4.10 - 4.56	0.968	± 0.017	± 0.016	0.090 - 0.100	44.15	± 1.05	44.08
4.56 - 5.47	0.774	± 0.015	± 0.014	0.100 - 0.120	35.28	± 0.93	34.88
5.47 - 6.38	0.581	± 0.013	± 0.011	0.120 - 0.140	26.52	± 0.77	26.03
6.38 - 7.29	0.451	± 0.011	± 0.009	0.140 - 0.160	20.56	± 0.64	20.08
7.29 - 8.21	0.3597	± 0.0093	± 0.0077	0.160 - 0.180	16.41	± 0.54	15.86
8.21 - 9.12	0.2877	± 0.0076	± 0.0063	0.180 - 0.200	13.12	± 0.44	12.65
9.12 - 11.9	0.1948	± 0.0058	± 0.0047	0.200 - 0.260	8.89	± 0.33	8.57
11.9 - 13.7	0.1232	± 0.0038	± 0.0034	0.260 - 0.300	5.62	± 0.21	5.35
13.7 - 18.2	0.0707	± 0.0024	± 0.0025	0.300 - 0.400	3.22	± 0.13	3.04
18.2 - 22.8	0.0324	± 0.0013	± 0.0021	0.400 - 0.500	1.477	± 0.068	1.389
22.8 - 27.4	0.01528	± 0.00076	± 0.00203	0.500 - 0.600	0.697	± 0.038	0.659
27.4 - 36.5	0.00530	± 0.00057	± 0.00202	0.600 - 0.800	0.242	± 0.029	0.230
36.5 - 45.6	0.00079	± 0.00017	± 0.00200	0.800 - 1.000	0.0360	± 0.0079	0.0366

Table D.1: Differential cross-section for charged particles in $Z^0 \to u\overline{u}, d\overline{d}, s\overline{s}$

Momentum GeV/c	DELPHI $\frac{1}{N_{\text{had}}}\frac{dn_\pi}{dp}$	σ_{stat}	σ_{syst}	Xp	DELPHI $\frac{1}{N_{\text{had}}}\frac{dn_\pi}{dx_p}$	σ_{tot}	JS73PS $\frac{1}{N_{\text{had}}}\frac{dn_\pi}{dx_p}$
0.70 - 0.91	6.65	± 0.13	± 0.20	0.015 - 0.020	303.4	± 11.1	308.3
0.91 - 1.14	5.231	± 0.065	± 0.086	0.020 - 0.025	238.58	± 4.91	244.96
1.14 - 1.37	4.245	± 0.061	± 0.080	0.025 - 0.030	193.64	± 4.58	197.31
1.37 - 1.60	3.487	± 0.043	± 0.046	0.030 - 0.035	159.03	± 2.86	161.82
1.60 - 1.82	2.902	± 0.040	± 0.043	0.035 - 0.040	132.35	± 2.70	135.31
1.82 - 2.28	2.296	± 0.031	± 0.038	0.040 - 0.050	104.73	± 2.23	106.51
2.28 - 2.74	1.729	± 0.030	± 0.037	0.050 - 0.060	78.85	± 2.15	80.40
2.74 - 3.19	1.351	± 0.019	± 0.023	0.060 - 0.070	61.63	± 1.34	62.68
3.19 - 3.65	1.101	± 0.017	± 0.023	0.070 - 0.080	50.22	± 1.29	49.94
3.65 - 4.10	0.901	± 0.014	± 0.019	0.080 - 0.090	41.09	± 1.08	40.89
4.10 - 4.56	0.747	± 0.013	± 0.016	0.090 - 0.100	34.06	± 0.94	33.90
4.56 - 5.47	0.590	± 0.010	± 0.014	0.100 - 0.120	26.91	± 0.80	26.50
5.47 - 6.38	0.4369	± 0.0083	± 0.0115	0.120 - 0.140	19.93	± 0.65	19.46
6.38 - 7.29	0.3324	± 0.0070	± 0.0094	0.140 - 0.160	15.16	± 0.53	14.77
7.29 - 8.21	0.2635	± 0.0062	± 0.0077	0.160 - 0.180	12.02	± 0.45	11.50
8.21 - 9.12	0.2037	± 0.0050	± 0.0066	0.180 - 0.200	9.29	± 0.38	9.03
9.12 - 11.9	0.1333	± 0.0031	± 0.0043	0.200 - 0.260	6.08	± 0.24	6.00
11.9 - 13.7	0.0812	± 0.0022	± 0.0027	0.260 - 0.300	3.70	± 0.16	3.64
13.7 - 18.2	0.0449	± 0.0014	± 0.0015	0.300 - 0.400	2.046	± 0.094	2.002
18.2 - 22.8	0.01938	± 0.00084	± 0.00073	0.400 - 0.500	0.884	± 0.051	0.868
22.8 - 27.4	0.00930	± 0.00057	± 0.00037	0.500 - 0.600	0.424	± 0.031	0.394
27.4 - 36.5	0.00290	± 0.00040	± 0.00028	0.600 - 0.800	0.132	± 0.022	0.129
36.5 - 45.6	0.00042	± 0.00015	± 0.00006	0.800 - 1.000	0.0194	± 0.0075	0.0195

Table D.2: Differential cross-section for pions in $Z^0 \to u\overline{u}, d\overline{d}, s\overline{s}$

Momentum GeV/c	DELPHI $\frac{1}{N_{\text{had}}}\frac{dn_K}{dp}$	σ_{stat}	σ_{syst}	Xp	DELPHI $\frac{1}{N_{\text{had}}}\frac{dn_K}{dx_p}$	σ_{tot}	JS73PS $\frac{1}{N_{\text{had}}}\frac{dn_K}{dx_p}$
0.70 - 0.91	0.527	± 0.047	± 0.061	0.015 - 0.020	24.06	± 3.51	25.05
0.91 - 1.14	0.524	± 0.037	± 0.058	0.020 - 0.025	23.88	± 3.15	23.10
1.14 - 1.37	0.447	± 0.033	± 0.052	0.025 - 0.030	20.37	± 2.84	20.51
1.37 - 1.60	0.398	± 0.031	± 0.031	0.030 - 0.035	18.16	± 2.00	18.14
1.60 - 1.82	0.374	± 0.036	± 0.045	0.035 - 0.040	17.07	± 2.64	15.98
1.82 - 2.28	0.314	± 0.040	± 0.047	0.040 - 0.050	14.33	± 2.80	13.44
2.28 - 2.74	0.253	± 0.045	± 0.049	0.050 - 0.060	11.55	± 3.04	10.98
2.74 - 3.19	0.217	± 0.014	± 0.012	0.060 - 0.070	9.91	± 0.83	9.14
3.19 - 3.65	0.180	± 0.014	± 0.013	0.070 - 0.080	8.19	± 0.85	7.70
3.65 - 4.10	0.160	± 0.010	± 0.009	0.080 - 0.090	7.30	± 0.62	6.65
4.10 - 4.56	0.147	± 0.010	± 0.009	0.090 - 0.100	6.72	± 0.63	5.83
4.56 - 5.47	0.1189	± 0.0078	± 0.0068	0.100 - 0.120	5.43	± 0.47	4.86
5.47 - 6.38	0.0901	± 0.0064	± 0.0043	0.120 - 0.140	4.11	± 0.35	3.91
6.38 - 7.29	0.0756	± 0.0088	± 0.0063	0.140 - 0.160	3.45	± 0.49	3.23
7.29 - 8.21	0.0629	± 0.0093	± 0.0065	0.160 - 0.180	2.87	± 0.52	2.73
8.21 - 9.12	0.0561	± 0.0071	± 0.0069	0.180 - 0.200	2.56	± 0.45	2.32
9.12 - 11.9	0.0401	± 0.0015	± 0.0017	0.200 - 0.260	1.83	± 0.10	1.71
11.9 - 13.7	0.0287	± 0.0013	± 0.0015	0.260 - 0.300	1.308	± 0.090	1.189
13.7 - 18.2	0.01838	± 0.00082	± 0.00112	0.300 - 0.400	0.838	± 0.063	0.756
18.2 - 22.8	0.00927	± 0.00055	± 0.00077	0.400 - 0.500	0.423	± 0.043	0.397
22.8 - 27.4	0.00471	± 0.00036	± 0.00047	0.500 - 0.600	0.215	± 0.027	0.214
27.4 - 36.5	0.00211	± 0.00026	± 0.00033	0.600 - 0.800	0.096	± 0.019	0.087
36.5 - 45.6	0.00027	± 0.00012	± 0.00015	0.800 - 1.000	0.0125	± 0.0088	0.0162

Table D.3: Differential cross-section for kaons in $Z^0 \to u\overline{u}, d\overline{d}, s\overline{s}$

Momentum GeV/c	DELPHI $\frac{1}{N_{had}} \frac{dn_p}{dp}$	σ_{stat}	σ_{syst}	Xp	DELPHI $\frac{1}{N_{had}} \frac{dn_p}{dx_p}$	σ_{tot}	JS73PS $\frac{1}{N_{had}} \frac{dn_p}{dx_p}$
0.70 - 0.91	0.354	± 0.028	± 0.075	0.015 - 0.020	16.13	± 3.64	12.45
0.91 - 1.14	0.317	± 0.031	± 0.054	0.020 - 0.025	14.46	± 2.82	13.01
1.14 - 1.37	0.219	± 0.035	± 0.035	0.025 - 0.030	9.98	± 2.26	12.65
1.37 - 1.60	0.251	± 0.025	± 0.024	0.030 - 0.035	11.44	± 1.58	11.88
1.60 - 1.82	0.243	± 0.018	± 0.025	0.035 - 0.040	11.07	± 1.41	10.95
1.82 - 2.28	0.208	± 0.015	± 0.017	0.040 - 0.050	9.49	± 1.00	9.65
2.28 - 2.74	0.1451	± 0.0082	± 0.0145	0.050 - 0.060	6.62	± 0.76	8.16
2.74 - 3.19	0.1200	± 0.0021	± 0.0113	0.060 - 0.070	5.47	± 0.52	6.91
3.19 - 3.65	0.1043	± 0.0030	± 0.0088	0.070 - 0.080	4.76	± 0.42	5.86
3.65 - 4.10	0.0914	± 0.0041	± 0.0093	0.080 - 0.090	4.17	± 0.47	5.00
4.10 - 4.56	0.0762	± 0.0035	± 0.0091	0.090 - 0.100	3.47	± 0.44	4.32
4.56 - 5.47	0.0655	± 0.0036	± 0.0052	0.100 - 0.120	2.99	± 0.29	3.49
5.47 - 6.38	0.0552	± 0.0048	± 0.0061	0.120 - 0.140	2.52	± 0.36	2.64
6.38 - 7.29	0.0419	± 0.0066	± 0.0054	0.140 - 0.160	1.91	± 0.39	2.06
7.29 - 8.21	0.0345	± 0.0077	± 0.0045	0.160 - 0.180	1.57	± 0.41	1.62
8.21 - 9.12	0.0277	± 0.0049	± 0.0037	0.180 - 0.200	1.27	± 0.28	1.28
9.12 - 11.9	0.0204	± 0.0013	± 0.0019	0.200 - 0.260	0.93	± 0.11	0.86
11.9 - 13.7	0.0132	± 0.0010	± 0.0014	0.260 - 0.300	0.602	± 0.079	0.524
13.7 - 18.2	0.00681	± 0.00048	± 0.00065	0.300 - 0.400	0.311	± 0.037	0.285
18.2 - 22.8	0.00315	± 0.00028	± 0.00045	0.400 - 0.500	0.144	± 0.024	0.123
22.8 - 27.4	0.00143	± 0.00021	± 0.00024	0.500 - 0.600	0.065	± 0.015	0.051
27.4 - 36.5	0.00027	± 0.00014	± 0.00007	0.600 - 0.800	0.0124	± 0.0071	0.0133
36.5 - 45.6	0.00007	± 0.00029	± 0.00003	0.800 - 1.000	0.003	± 0.013	0.001

Table D.4: Differential cross-section for protons in $Z^0 \to u\overline{u}, d\overline{d}, s\overline{s}$

Momentum GeV/c	DELPHI $\frac{1}{N_{had}} \frac{dn_{Hv}}{dp}$	σ_{stat}	σ_{syst}	Xp	DELPHI $\frac{1}{N_{had}} \frac{dn_{Hv}}{dx_p}$	σ_{tot}	JS73PS $\frac{1}{N_{had}} \frac{dn_{Hv}}{dx_p}$
0.70 - 0.91	0.874	± 0.050	± 0.061	0.015 - 0.020	39.86	± 3.62	37.50
0.91 - 1.14	0.811	± 0.041	± 0.063	0.020 - 0.025	37.00	± 3.41	36.11
1.14 - 1.37	0.750	± 0.036	± 0.045	0.025 - 0.030	34.21	± 2.62	33.16
1.37 - 1.60	0.644	± 0.035	± 0.038	0.030 - 0.035	29.37	± 2.35	30.01
1.60 - 1.82	0.608	± 0.035	± 0.040	0.035 - 0.040	27.74	± 2.45	26.94
1.82 - 2.28	0.520	± 0.040	± 0.050	0.040 - 0.050	23.73	± 2.93	23.09
2.28 - 2.74	0.411	± 0.033	± 0.041	0.050 - 0.060	18.77	± 2.40	19.14
2.74 - 3.19	0.356	± 0.013	± 0.014	0.060 - 0.070	16.23	± 0.87	16.04
3.19 - 3.65	0.2801	± 0.0095	± 0.0102	0.070 - 0.080	12.78	± 0.64	13.56
3.65 - 4.10	0.2468	± 0.0075	± 0.0071	0.080 - 0.090	11.26	± 0.47	11.65
4.10 - 4.56	0.2223	± 0.0071	± 0.0070	0.090 - 0.100	10.14	± 0.46	10.15
4.56 - 5.47	0.1820	± 0.0051	± 0.0055	0.100 - 0.120	8.30	± 0.34	8.35
5.47 - 6.38	0.1463	± 0.0046	± 0.0047	0.120 - 0.140	6.67	± 0.30	6.55
6.38 - 7.29	0.1187	± 0.0040	± 0.0038	0.140 - 0.160	5.41	± 0.25	5.29
7.29 - 8.21	0.0969	± 0.0035	± 0.0032	0.160 - 0.180	4.42	± 0.21	4.35
8.21 - 9.12	0.0828	± 0.0029	± 0.0029	0.180 - 0.200	3.78	± 0.19	3.61
9.12 - 11.9	0.0608	± 0.0017	± 0.0022	0.200 - 0.260	2.77	± 0.13	2.56
11.9 - 13.7	0.0411	± 0.0015	± 0.0017	0.260 - 0.300	1.87	± 0.10	1.71
13.7 - 18.2	0.02500	± 0.00094	± 0.00124	0.300 - 0.400	1.140	± 0.071	1.042
18.2 - 22.8	0.01218	± 0.00061	± 0.00087	0.400 - 0.500	0.555	± 0.048	0.520
22.8 - 27.4	0.00603	± 0.00038	± 0.00052	0.500 - 0.600	0.275	± 0.030	0.265
27.4 - 36.5	0.00228	± 0.00027	± 0.00021	0.600 - 0.800	0.104	± 0.016	0.101
36.5 - 45.6	0.00039	± 0.00013	± 0.00009	0.800 - 1.000	0.0180	± 0.0073	0.0171

Table D.5: Differential cross-section for heavy particles (K/p) in $Z^0 \to u\overline{u}, d\overline{d}, s\overline{s}$

List of Figures

2.1 $SU(4)$ multiplets for u, d, s, and c mesons . . . 5
2.2 $SU(4)$ multiplets for u, d, s, and c baryons . . . 5
2.3 Born diagram of e^+e^- annihilation into quarks . . . 6
2.4 e^+e^- cross-section vs centre-of-mass energy . . . 6
2.5 Measurements of α_s vs Q . . . 7
2.6 Four phases in e^+e^- annihilation . . . 8
2.7 Illustration of string fragmentation and cluster fragmentation . . . 9
2.8 Illustration of string fragmentation . . . 10

3.1 Map of local area around LEP . . . 14
3.2 Overview of the LEP injection systems . . . 14
3.3 LEP time-integrated luminosity for 1993 and 1994 . . . 15
4.1 Artist's view of the DELPHI detector . . . 16

4.2 Schematic view of the DELPHI detector . . . 18
4.3 Schematic layout of the VD . . . 19
4.4 VD vertex reconstruction example . . . 20
4.5 Schematic view of the ID . . . 21
4.6 Schematic view of the TPC . . . 22
4.7 Layer structure of an HPC module . . . 25
4.8 TPC $\mathrm{d}E/\mathrm{d}x$ measurement vs momentum . . . 27
4.9 VD $\mathrm{d}E/\mathrm{d}x$ measurement vs momentum . . . 27
4.10 DELPHI offline analysis chain . . . 30

5.1 BRICH expected Cherenkov angle vs momentum . . . 35
5.2 Working principle of the BRICH . . . 37
5.3 BRICH transmission coefficients . . . 37
5.4 Location of the RICH detectors in DELPHI . . . 38
5.5 Schematic view of the BRICH detector . . . 40
5.6 BRICH electric drift field . . . 41
5.7 Schematic view of the BRICH MWPC . . . 41
5.8 BRICH drift velocity vs time and pressure . . . 43
5.9 BRICH drift velocity vs drift tube position . . . 43
5.10 Matching between TPC BRICH track extrapolation . . . 44
5.11 Mis-match between TPC BRICH track extrapolation . . . 44
5.12 RICH UV-monochromator system . . . 47
5.13 UV-transmission for liquid C_6F_{14} . . . 48
5.14 UV-transmission for liquid C_5F_{12} . . . 48

5.15 UV-transmission for gaseous C_5F_{12} 49
5.16 UV-transmission for gaseous C_4F_{10} 49
5.17 Chemical structure of TMAE 50
5.18 TMAE UV-photon conversion length 50
5.19 BRICH Cherenkov fluid systems 51
5.20 UV-transmission for raw sample C_6F_{14} 52
5.21 UV-transmission for C_6F_{14} after cleaning 52
5.22 UV-transmission for C_6F_{14} of degraded quality 53
5.23 UV-transmission for degraded C_6F_{14} after treatment 54
5.24 Distillation curves for CF-liquids 54
5.25 UV-transmission for C_4F_{10} (450 ppm water) 55
5.26 BRICH 1995 start-up schedule 56
5.27 Monitoring of the filling of the BRICH gas radiator 57

6.1 Background R_ϕ-cluster in the BRICH 59
6.2 Liquid radiator $\theta_{\check{c}}$ before and after cleaning 59
6.3 FRICH drift box alignment 59
6.4 BRICH Cherenkov angle before and after alignment 60
6.5 BRICH mirror alignment 60
6.6 Top-bottom variations due to fluid-mixing 61
6.7 Photon feedback illustration 62
6.8 Split up of $\theta_{\check{c}}^{\text{p.e.}}$ in two sectors in local ϕ 62
6.9 Local φ of signal from liquid radiator 63
6.10 RICFIX data vs Monte Carlo for single photo-electrons 63
6.11 RICFIX data vs Monte Carlo for gas rings 63
6.12 Data vs Monte Carlo before and after RICFIX 64
6.13 BRICH liquid Cherenkov angle vs p 65
6.14 BRICH gas Cherenkov angle vs momentum 65
6.15 RIBMEAN distributions of the key parameters for physics 66
6.16 RIBMEAN $1/\sqrt{N_{\text{p.e.}}}$ test 67
6.17 RIBMEAN $(\theta_{\check{c}} - \theta_\pi^{\text{exp.}})/\sigma_{\text{ring}}$ distributions 68
6.18 Liquid radiator RIBMEAN 2.5 σ_{sep} $\pi^\pm$, $K^\pm$, $p\overline{p}$ bands 69
6.19 Gas radiator RIBMEAN 2.5 σ_{sep} $\pi^\pm$, $K^\pm$, $p\overline{p}$ bands 69
6.20 Zoom liquid RIBMEAN 2.5 σ_{sep} $\pi^\pm$, $K^\pm$, $p\overline{p}$ bands 69
6.21 Zoom gas RIBMEAN 2.5 σ_{sep} $\pi^\pm$, $K^\pm$, $p\overline{p}$ bands 69
6.22 $\pi^\pm/K^\pm$, $K^\pm/p\overline{p}$, $\pi^\pm/p\overline{p}$ separation of RIBMEAN 70
6.23 $\pi^\pm$, $K^\pm$, $p\overline{p}$ probability for zero Cherenkov angle reconstruction 70

7.1 Track selection efficiency vs momentum 81
7.2 Efficiency matrix for standard NEWTAG (BRICH) 82
7.3 Purity matrix for standard NEWTAG 83
7.4 Rejection matrix for standard NEWTAG 84
7.5 Heavy particle standard NEWTAG 84
7.6 Comparison of ‘very loose’, ‘loose’, ‘standard’, ‘tight’ tagging 86

8.1 Comparison of 94B3 data-Monte Carlo (K^0, Λ^0). 88
8.2 Comparison of 94-B3 data-Monte Carlo (muons). 89

8.3 Comparison of 94-B3 data-Monte Carlo ($N_{\rm tagged}/N_{\rm tot}$). 90
8.4 XNEWTAG reconstruction of $\phi(1020) \to \mathrm{K^+K^-}$ in $\mathrm{Z^0} \to q\overline{q}$ 92
8.5 XNEWTAG reconstruction of $\phi(1020) \to \mathrm{K^+K^-}$, heavy particle tag 93
8.6 RNEWTAG reconstruction of $\phi(1020) \to \mathrm{K^+K^-}$, heavy particle tag 93
8.7 RNEWTAG reconstruction of $\phi(1020) \to \mathrm{K^+K^-}$ 94
8.8 RNEWTAG reconstruction of $\phi(1020) \to \mathrm{K^+K^-}$, $R_\phi < 3$mm 94
8.9 XNEWTAG invariant mass distributions for $\mathrm{M}(\pi^+\pi^-)$ 95
8.10 RNEWTAG invariant mass distributions for $\mathrm{M}(\pi^+\pi^-)$ with $R_\phi < 3$mm 95
8.11 XNEWTAG invariant mass distributions for $\mathrm{M}(\mathrm{K}^+\pi^-)$ 96
8.12 XNEWTAG invariant mass distributions for $\mathrm{M}(\mathrm{p}\pi^-)$ 97
8.13 XNEWTAG invariant mass distributions for $\mathrm{M(pK^-)}$ 98
8.14 XNEWTAG invariant mass distributions for $\mathrm{M(pK^-)}$ 98
8.15 XNEWTAG reconstruction of $\phi(1020) \to \mathrm{K^+K^-}$ in b-events 99
8.16 XNEWTAG distributions for $\mathrm{M}(\pi^+\pi^-)$, $\mathrm{M}(\mathrm{K}^+\pi^-)$, $\mathrm{M}(\mathrm{p}\pi^-)$ in b-events 100

9.1 Impact parameter distributions after event selection 102
9.2 Distributions for $\Delta p/p$ and selected tracks after event selection 103
9.3 Distributions in θ and ϕ after event selection 104
9.4 Distributions of significance for b-tagging 105
9.5 b-event tagging efficiency vs purity 106
9.6 b-tag probability distribution $\mathcal{P}_E$ 107
9.7 Combined RICH-TPC proton-tag 109
9.8 XNEWTAG data-Monte Carlo comparison ($\mathrm{K^0_S}$, Λ^0) 111
9.9 Track selection efficiency, ratio data-Monte Carlo 112
9.10 Ratio data-Monte Carlo for tagging $\pi^\pm$ from $\mathrm{K^0_S} \to \pi^+\pi^-$ 114
9.11 Statistical and systematic uncertainties vs momentum 119
9.12 Normalised $\pi^\pm$, $\mathrm{K}^\pm$ and $\mathrm{p\overline{p}}$ production rates in $\mathrm{Z^0} \to q\overline{q}$, $\mathrm{Z^0} \to u\overline{u}, d\overline{d}, s\overline{s}$ 122
9.13 Normalised $\pi^\pm$, $\mathrm{K}^\pm$, $\mathrm{p\overline{p}}$ production rates in $\mathrm{Z^0} \to b\overline{b}$ 123
9.14 Normalised production rates for $\pi^\pm$ and heavy particles 125
9.15 Differential cross-sections $\pi^\pm$, $\mathrm{K}^\pm$, $\mathrm{p\overline{p}}$ in $\mathrm{Z^0} \to q\overline{q}$, $\mathrm{Z^0} \to b\overline{b}$, $\mathrm{Z^0} \to u\overline{u}, d\overline{d}, s\overline{s}$ . . . 128
9.16 Differential cross-sections $\pi^\pm$ and heavy particles 130
9.17 $\pi^\pm$, $\mathrm{K}^\pm$, $\mathrm{p\overline{p}}$ ξ_p distributions vs JETSET and HERWIG 132
9.18 ξ_p fitted particle distributions for $\mathrm{Z^0} \to q\overline{q}$, $\mathrm{Z^0} \to b\overline{b}$, $\mathrm{Z^0} \to u\overline{u}, d\overline{d}, s\overline{s}$ 133
9.19 Charged particle ξ_p distributions, DELPHI vs ALEPH 135
9.20 ξ_p distributions in $\mathrm{Z^0} \to q\overline{q}$, DELPHI vs ALEPH, OPAL and SLD 137
9.21 Protons in b-events, double Gauss. fit vs distorted Gauss. fit 138
9.22 Protons in b-events, fragmentation vs decays 138
9.23 JETSET ξ_p prediction for $\pi^\pm$, $\mathrm{K}^\pm$, $\mathrm{p\overline{p}}$ from decays and fragmentation 139
9.24 JETSET $f_i(p)$ prediction for $\pi^\pm$, $\mathrm{K}^\pm$, $\mathrm{p\overline{p}}$ from decays and fragmentation 141

10.1 $\mathrm{M(pK^-)}$ obtained from the 94-B3 data processings 144
10.2 $\mathrm{M(pK^-)}$ obtained from the 94-C1 data processings 144
10.3 Two-dimensional view of a LEP-II event 145

List of Tables

2.1 Fundamental forces in the Standard Model . . . 4
2.2 Fermions and their electroweak quantum numbers . . . 4

5.1 Properties of DELPHI Cherenkov fluids . . . 37
5.2 Monitoring and control of RICH parameters . . . 43

6.1 RICH resolutions after alignment . . . 60

7.1 NEWTAG output values . . . 74
7.2 NEWTAG mean efficiency, purity and rejection . . . 85

9.1 b-tag event probability vs purity . . . 116
9.2 Sources of systematic uncertainty . . . 120
9.3 Normalised production rates for $\pi^{\pm}$ in $Z^0 \rightarrow q\overline{q}$ . . . 124
9.4 Normalised production rates for $K^{\pm}$ in $Z^0 \rightarrow q\overline{q}$ . . . 124
9.5 Normalised production rates for $p\overline{p}$ in $Z^0 \rightarrow q\overline{q}$ . . . 124
9.6 Normalised production rates for heavy charged particles in $Z^0 \rightarrow q\overline{q}$ . . . 124
9.7 Normalised rates for $\pi^{\pm}$ in $Z^0 \rightarrow b\overline{b}$ . . . 126
9.8 Normalised rates for $K^{\pm}$ in $Z^0 \rightarrow b\overline{b}$ . . . 126
9.9 Normalised rates for $p\overline{p}$ in $Z^0 \rightarrow b\overline{b}$ . . . 126
9.10 Normalised rates for heavy particles in $Z^0 \rightarrow b\overline{b}$ . . . 126
9.11 Normalised rates for $\pi^{\pm}$ in $Z^0 \rightarrow u\overline{u}, d\overline{d}, s\overline{s}$ . . . 127
9.12 Normalised rates for $K^{\pm}$ in $Z^0 \rightarrow u\overline{u}, d\overline{d}, s\overline{s}$ . . . 127
9.13 Normalised rates for $p\overline{p}$ in $Z^0 \rightarrow u\overline{u}, d\overline{d}, s\overline{s}$ . . . 127
9.14 Normalised rates for heavy particles in $Z^0 \rightarrow u\overline{u}, d\overline{d}, s\overline{s}$ . . . 127
9.15 DELPHI multiplicities in $Z^0 \rightarrow q\overline{q}$, $Z^0 \rightarrow b\overline{b}$, $Z^0 \rightarrow u\overline{u}, d\overline{d}, s\overline{s}$ vs generators . . . 134
9.16 DELPHI multiplicities in $Z^0 \rightarrow q\overline{q}$, $Z^0 \rightarrow b\overline{b}$, $Z^0 \rightarrow u\overline{u}, d\overline{d}, s\overline{s}$ vs others . . . 136

10.1 DELPHI multiplicities in $Z^0 \rightarrow q\overline{q}$, $Z^0 \rightarrow b\overline{b}$, $Z^0 \rightarrow u\overline{u}, d\overline{d}, s\overline{s}$ . . . 143

B.1 Differential cross-section for charged particles in $Z^0 \rightarrow q\overline{q}$ . . . 147
B.2 Differential cross-section for pions in $Z^0 \rightarrow q\overline{q}$ . . . 148
B.3 Differential cross-section for kaons in $Z^0 \rightarrow q\overline{q}$ . . . 148
B.4 Differential cross-section for protons in $Z^0 \rightarrow q\overline{q}$ . . . 149
B.5 Differential cross-section for heavy particles in $Z^0 \rightarrow q\overline{q}$ . . . 149

C.1 Differential cross-section for charged particles in $Z^0 \rightarrow b\overline{b}$ . . . 150
C.2 Differential cross-section for pions in $Z^0 \rightarrow b\overline{b}$ . . . 151
C.3 Differential cross-section for kaons in $Z^0 \rightarrow b\overline{b}$ . . . 151
C.4 Differential cross-section for protons in $Z^0 \rightarrow b\overline{b}$ . . . 152
C.5 Differential cross-section for heavy particles in $Z^0 \rightarrow b\overline{b}$ . . . 152

D.1 Differential cross-section for charged particles in $Z^0 \rightarrow u\overline{u}, d\overline{d}, s\overline{s}$ . . . 153
D.2 Differential cross-section for pions in $Z^0 \rightarrow u\overline{u}, d\overline{d}, s\overline{s}$ . . . 154
D.3 Differential cross-section for kaons in $Z^0 \rightarrow u\overline{u}, d\overline{d}, s\overline{s}$ . . . 154
D.4 Differential cross-section for protons in $Z^0 \rightarrow u\overline{u}, d\overline{d}, s\overline{s}$ . . . 155
D.5 Differential cross-section for heavy particles in $Z^0 \rightarrow u\overline{u}, d\overline{d}, s\overline{s}$ . . . 155

References

[1] S.L. Glashow, Nucl. Phys. 22 (1967) 597.

[2] A. Salam, Proc. 8th Nobel Symposium, (Almquist & Wiksell, Stockholm 1968).
A. Salam, J.C. Ward, Phys. Lett. 13 (1964) 168.

[3] S. Weinberg, Phys. Rev. Lett. 19 (1967) 1264.

[4] M. Gell-Mann, Phys. Lett. 8 (1964) 214.

[5] G. Zweig, CERN–Reports/8182/TH401 (1964),
G. Zweig, CERN–Reports/8419/TH412 (1964).

[6] Particle Data Group, R. Barnett et al., Phys. Rev. D54, (1996) 1.

[7] N. Cabibbo, Phys. Rev. Lett. 12 (1964) 62,
M. Kobayashi and K. Maskawa, Prog. Theor. Phys. Rev. D2 (1973) 652.

[8] M. Schmelling, Phys. Scripta. 51 (1995) 683.

[9] G. Sterman et al., Rev. of Mod. Phys. Vol.67 No.1 (1995) 157.

[10] Ch. Berger, Teilchenphysik (Springer-Verlag, Berlin, 1992).

[11] S. Gorishny, A. Kataev and S. Larin, Phys. Lett. B212 (1991) 144,
L. Surguladze and M. Samuel, Phys. Rev. Lett. 66 (1991) 560, 2416 (E).

[12] S. Larin, T. van Tinbergen and J. Vermaseren, Phys. Lett. B320 (1994) 159.

[13] S. Bethke, Nucl. Phys. B39 (Proc. Suppl.) B, C (1995) 198.

[14] S. Catani, G. Turnock and B. Webber, Phys. Lett. B272 (1991) 368-372.

[15] R. Field and R. Feynman, Nucl. Phys. B1336 (1978) 1.

[16] B. Andersson et al., Phys. Rep. 97 (1983) 31.

[17] T. Sjöstrand, Comp. Phys. Comm. 39 (1986) 347.
T. Sjöstrand, M. Bengtsson, Comp. Phys. Comm. 43 (1987) 367.
T. Sjöstrand, Comp. Phys. Comm. 82 (1994) 74. T. Sjöstrand, JETSET manual CERN–TH/7112/93 (1994).

[18] C. Peterson et al., Phys. Rev. D27 (1983) 105.

[19] G. Marchesini and B. Webber, Nucl. Phys. B310 (1988) 461.

[20] G. Marchesini and B. Webber, Nucl. Phys. B238 (1984) 1,
G. Marchesini et al., Comp. Phys. Comm. 67 (1992) 465. G. Marchesini et al., HERWIG 5.8c manual.

[21] DELPHI Collaboration, P. Abreu et al., Z. Phys. C73 (1996) 11.

[22] Y. Azimov, Y.Dokshitzer, V. Khoze and S. Troyan, Z. Phys. C31 (1986) 213-218, and references therein.

[23] C.P. Fong and B.R. Webber, Phys. Lett. B229 (1989) 289.
C.P. Fong and B.R. Webber, Nucl. Phys. B355 (1991) 54.

[24] Y.Dokshitzer, V. Khoze and S. Troyan, Z. Phys. C55 (1992) 107, and ref. [19] therein.

[25] A. Böhrer, Inclusive hadron production in hadronic decays of the Z^0 boson at LEP-I, University of Siegen, Germany, SI-96-15 (1996), submitted to Phys. Rep. .

[26] LEP design report, CERN-LEP/84-01 (1984).
V.Hatton et al., LEP performance Note 12 (1990).
R.Baily et al., CERN-SL/90-95 (1990).

[27] L.Arnaudon et al., CERN–PPE/92-125 (1992).

[28] URL: http://www.cern.ch, LEP statistics.

[29] The LEP collaborations and the LEP Electroweak Working Group. CERN–PPE/95-172 (1995).

[30] Delphi Collaboration, Delphi Technical Proposal, CERN-LEPC/83-3 (1983).

[31] Delphi Collaboration, The Delphi detector at LEP, Nucl. Instr. and Meth. A303 (1991) 233-276.

[32] Delphi Collaboration, P. Abreu et al., Performance of the Delphi detector, Nucl. Instr. and Meth. A378 (1996) 57-100, and most references therein.

[33] V.Chabaud et al., CERN–PPE/95-86 (1995).
N.Bingefors et al., Nucl. Instr. and Meth. A328 (1993) 447.

[34] P.Antilogus et al.,Nucl. Instr. and Meth. A283 (1989) 567.

[35] Delphi Collaboration, Delphi Data Analysis Program (delana) User's guide, Delphi-Note 89-44 PROG 137 (1989).

[36] URL: http://wwwcn.cern.ch/~offline/analysis/analysis.html.

[37] Delphi Collaboration, delsim– Delphi Event Generation and Detector Simulation, Delphi-Note 89-15 PROG 130 (1989).

[38] P.A. Cherenkov, Dokl. Akad. Nauk SSSR, 2 (1934) 415.
P.A. Cherenkov, Phys. Rev. 52 (1937) 378.

[39] I. Frank and I. Tamm, Dokl. Akad. Nauk SSSR, 14 (1938) 107.

[40] J. Séguinot and T. Ypsilantis, Nucl. Instr. and Meth. 142 (1977) 377-391.

[41] See for example L.I. Schiff, Quantum Mechanics, McGraw-Hill, 1955.

[42] J. Séguinot, CERN-EP/89-02, LPC/89-25, 31 July 1989.

[43] E.G. Anassontzis et al., Nucl. Instr. and Meth. A323 (1992) 351.
W. Adam et al., Nucl. Instr. and Meth. A343 (1994) 68.
Delphi rich Collaboration, contributions to the Second Workshop on rich Detectors, Uppsala 1995. Nucl. Instr. and Meth. A371 (1996).

[44] G. Lenzen, E. Schyns, J. Thadome, J. Werner, Nucl. Instr. and Meth. A343 (1994) 268-272, and references [7-14] therein.

[45] P. Baillon, Production of 300 paraboloidal mirrors with high reflectivity for use in the Barrel RICH counter of DELPHI at LEP. DELPHI-Note 88-84 RICH 35 (1989).

[46] D. Bloch et al., Nucl. Instr. and Meth. A273 (1988) 847.
E. Schyns, Multiwire Proportional Chambers for the DELPHI Barrel RICH; tests with single electrons, Graduation thesis, NIKHEF Amsterdam.

[47] W. Adam et al., Nucl. Instr. and Meth. A338 (1994) 284.

[48] W. Adam et al., Experience with the Ring Imaging Cherenkov Detector of DELPHI. ICHEP 94 Ref. gls0206.

[49] S. Maltesos, A Filippas, and E. Fokitis, A method for determination of Gaseous Refractivity based on the Interferogram discrete Fourier Transform (GRIFT), DELPHI-Note 96-65 RICH 87 (1996), submitted to Nucl. Instr. and Meth. .

[50] J. Werner, Diploma thesis WUB-89-3 (1989).

[51] W. Adam et al., Nucl. Instr. and Meth. A360 (1995) 416-422.

[52] M. Davenport and E. Schyns, Internal Report (1993), unpublished.

[53] S. Ilie and G. Lenzen, Perfluorocarbon Liquid. Specific Chemical Aspects for the use within the DELPHI RICH. DELPHI-Note 93-33 RICH 54 (1993).

[54] M. Bosteels and S. Ilie, Technical note MT-SM/93-02, CERN (1993).

[55] M. Danielsson and H-J. Gerber, Nucl. Instr. and Meth. A334 (1993) 339.

[56] Ch. Joram, A distillation plant for C_5F_{12}/C_6F_{14} separation in the BRICH radiator systems. Internal Report (Nov. 1995) unpublished.

[57] H. Fürstenau et al., Nucl. Instr. and Meth. A371 (1996) 263-267.

[58] D. Bloch, M.Dracos and S. Tzamarias, Nucl. Instr. and Meth. A371 (1996) 236-240.

[59] M. Berggren, ERA, the RICH alignment software package, DELPHI-Note 89-81 PROG 146 (1989).

[60] S. Haider, PhD thesis, University of Leiden, The Netherlands (June 1995).

[61] W. Adam et al., Nucl. Instr. and Meth. A371 (1996) 228-231.

[62] B. Erzen et al., DELPHI-Note in preparation.

[63] W. Adam et al., Nucl. Instr. and Meth. A371 (1996) 240-243.

[64] P. Baillon, Nucl. Instr. and Meth. A238 (1985) 341.

[65] M. Dracos, A particle identification method for Ring Imaging Cherenkov detectors, CRN-95-21.

[66] F. Hahn, PhD thesis, Wuppertal University WUB-DIS 95-2.

[67] W.L.G. Koontz and K. Fukunaga, IEEE Trans. Computers C21 (1972) 11.

[68] G. Piana, Tau decays in three prongs with kaons, DELPHI-Note in preparation.

[69] M. Battaglia and P.M. Kluit, The RIBMEAN Clustering Package for DELPHI RICHes. DELPHI-Note 96-133 RICH 90 (1996).

[70] E. Schyns, NEWTAG - π, K, p Tagging for DELPHI RICHes. DELPHI-Note 96-103 RICH 89 (1996).

[71] DELPHI Collaboration, P. Abreu et al., Z. Phys. C73 (1996) 61.

[72] OPAL Collaboration, R. Akers et al., Z. Phys. C68 (1995) 1.

[73] M. Blume, PhD thesis, Wuppertal University WUB-DIS 96-19.

[74] DELPHI Collaboration, P. Abreu et al., CERN–PPE/97-27, to be submitted to Z. Phys. .

[75] DELPHI Collaboration, P.Abreu et al., Z. Phys. C65 (1995) 555.
G.V. Borisov, Lifetime Tag of Events $Z^0 \rightarrow b\bar{b}$ with the DELPHI detector, DELPHI-Note 94-125 PROG 208 (1994).
G.V. Borisov and C. Mariotti, Fine tuning of the impact parameter resolution in the DELPHI detector, DELPHI-Note 95-140 PHYS 565 (1995).

[76] ALEPH Collaboration, Phys. Lett. B313 (1993) 535.

[77] DELPHI Collaboration, J. Dahm, M. Reale, E. Schyns, Production of $\pi^{\pm}$, $K^{\pm}$ and $p\overline{p}$ in hadronic Z^0 decays, uds- and b-quark events. ICHEP'96 Ref.pa01-037, DELPHI-Note 96-86 CONF 15, June 25 1996.

[78] ALEPH Collaboration, Phys. Lett. B357 (1995) 487.

[79] OPAL Collaboration, R. Akers et al., Z. Phys. C63 (1994) 181-195.

[80] DELPHI Collaboration, P. Abreu et al., Phys. Lett. B444(1995) 3.

[81] DELPHI Collaboration, P. Abreu et al., Phys. Lett. B347(1995) 447-466.

[82] ALEPH Collaboration, D. Buskulic et al., Z. Phys. C66 (1995) 355.

[83] SLD Collaboration, K. Abe et al., Production of $\pi^{\pm}$, $K^{\pm}$, $p\overline{p}$, K^0_S, Λ^0 in hadronic Z^0 decays, SLAC-PUB-95-6920.

[84] OPAL Collaboration, R. Akers et al., A Measurement of Charged Particle multiplicity in $Z^0 \rightarrow c\bar{c}$ and $Z^0 \rightarrow b\bar{b}$ Events, CERN–PPE/95-038, submitted to Phys. Lett. .

[85] SLD Collaboration, K. Abe et al., Measurement of the Charged Multiplicities in *b, c* and light Quark Events from Z^0 Decays, SLAC-PUB-96-7172.

[86] E. Schyns, DELPHI Particle Identification with 1994C (review on behalf of HADIDENT task), DELPHI Plenary, Feb. 1997.

DIESES ist das Bild der Welt,
Das man für das beste hält:
Fast wie ein Kinderspiel,
Fast wie eine Schnecke vor dem Ziel,
Fast wie eine krumme Uhr,
Fast wie ein Stier so stur,
Fast wie ein Kartenhaus,
Fast wie die Katze und die Maus,
Fast wie lange, schwere Reisen,
Fast wie guter Wein und Speisen,
Fast wie es sich gehört,
Fast im Ganzen total gestört,
Fast so wie kein Gott es führt im Schilde,
Sieht es aus, im besten Bilde.
(Vanum est vobis ante lucem surgere [HWV 238].)

Es spürt der Mensch, wenn er Wissen schafft,
So eine ungewisse (!) starke Kraft.
Die Stärke vermag nicht nur einen Held,
Denn sie zieht sehr viele herein ins Feld.
Drum schreib ich allhier ein:
Mit Wissenskraft ist man nie allein!

CERN am Genfer See den 29. Februar 1997.

Emile Schyns

Acknowledgements

First and foremost, I wish to express my utmost gratitude to Prof. Dr. Jürgen Drees, who enabled my stay at CERN to work on this thesis and to contribute to the exciting research at the frontier lines of high energy physics. Without his constant support and the inspiring discussions, it would have been impossible to produce this work. It is such an enormous pleasure to be enabled to work on a thesis containing both detailed detector hardware topics and precise physics measurements.

During my work on DELPHI and its RICH detectors, I had the privilege to collaborate with many people and to learn from their experience and knowhow in physics and computing. Through learning by doing and through learning by being there, I gained a lot of experience which hardly can be found in text books. I am most grateful to Dr. Ettore Rosso from whom I learned that also in detector physics one often can apply the expression: 'Der Teufel sitzt im Detail'. I am also most grateful to Dr. Olav Ullaland, who taught me the different phases of character building which an experimental physicist can go through. Many special thanks go to my good friend Dr. Martyn Davenport. I appreciate very much to have learned from him that one has to work with optimal precision, but even then, with the Helium detector one always comes to the conclusion, which is true in general: everything leaks. Many special thanks also go to my good friend Dr. Hermann Fürstenau, who patiently introduced me to the DELPHI offline software. From him I learned to answer the question: how many errors are user-errors?

I am most grateful to Dr. Jean-Eudes Augustin and Dr. Daniel Treille for their continuous and reassuring interest in my work and the different milestones which were obtained. Furthermore, I greatly appreciate the excellent cooperation of Dr. Peter Kluit and the daily resolving coffee break discussions, to speed up the progress of my analysis. Many thanks go to Borut Erzen for the very pleasant collaboration during the testing of numerous versions of our software, and to Wolfgang Adam for his efficient and rapid help. Many thanks go also to Dr. Børge Nielsen for his valuable comments and to Dr. Dirk Toet for the inspiring motivations. I thank Dr. Georg Lenzen for his support and Jocelyn Thadome for his large contribution to the technical realisation of the DELPHI monochromator systems.

I especially thank my friends and former office mates Dr. Ferdinand Hahn, Dr. Rolf Lindner and Dr. Matthias Blume for the good teamwork and for helping me to find foxy solutions for technical problems. In this respect I also want to thank Dr. Jochen Dahm, Dr. Mario Reale, Dr. Wulf Oberschulte-Beckmann and Christian Weiser. I appreciate very much the help I got from Dr. Fabio Cossutti concerning the technical problems with the simulation code which I needed for the final stage of my analysis. I thank Dr. Klaus Hamacher and Dr. Alessandro de Angelis for their opinions and fruitful discussions on the different physics topics related to this thesis.

I am specially grateful to my friends and colleagues Dr. Ariella Cattai, Dr. Martyn Davenport, Prof. Dr. Alex Firestone, Dr. Hermann Fürstenau and Dr. Olav Ullaland. When I need them, they are always there, either to cheer the achievement of good results or to discuss urgent and serious matters.

Many great thanks go to my parents and my brothers and sister, for their continuous long distance support. Finally, I am utmost grateful to my dearest Esther for her permanent mental support and her incredible patience, especially during the analysis and writing phase of this thesis.

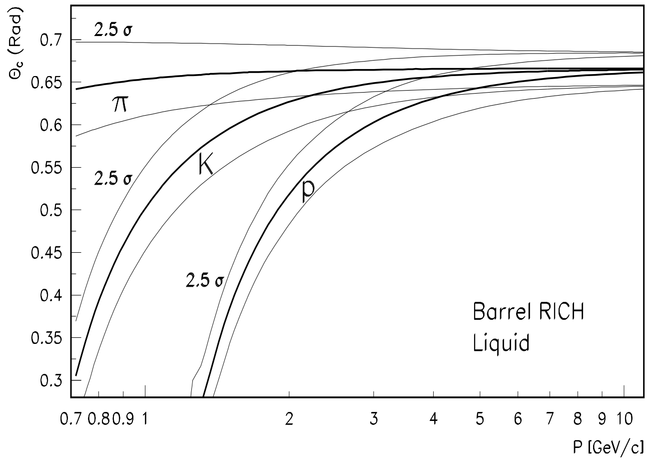

The 2.5 sigma bands for $\pi^{\pm}$, $K^{\pm}$ and $p\overline{p}$ identification in the Barrel RICH liquid radiator (Fig. 6.18, page 69).

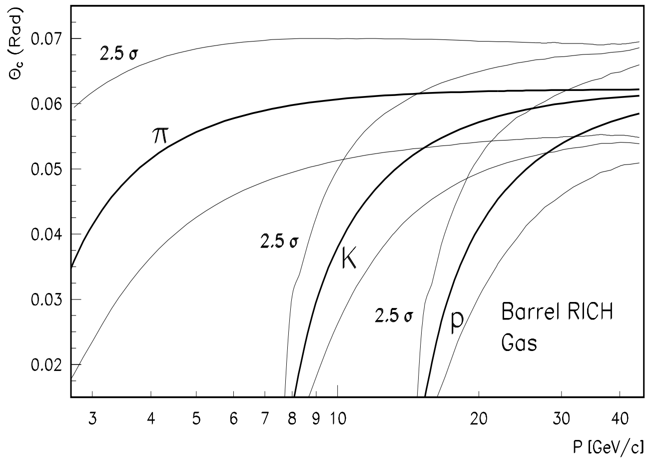

The 2.5 sigma bands for $\pi^{\pm}$, $K^{\pm}$ and $p\overline{p}$ identification in the Barrel RICH gas radiator (Fig. 6.19, page 69).

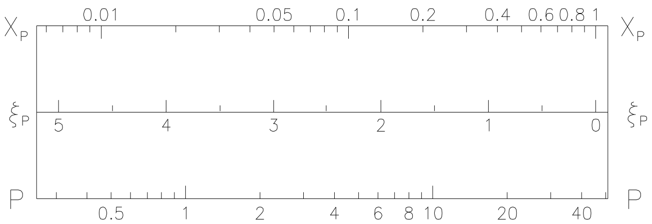

Conversion figure: $\xi_p = \ln(1/X_p) = \ln(E_{\mathrm{beam}}/p)$.